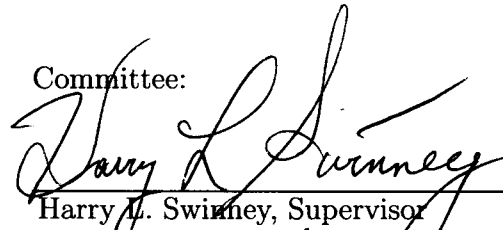The Dissertation Committee for Daniel Ivan Goldman
Certifies that this is the approved version of the following dissertation:

Pattern formation and fluidization in vibrated granular layers, and grain dynamics and jamming in a water fluidized bed
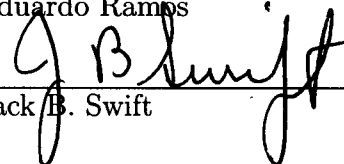
Committee:

Harry L. Swinney, Supervisor

Philip J. Morrison

Ronald L. Panton

Eduardo Ramos

Jack B. Swift

Pattern formation and fluidization in vibrated granular layers, and grain dynamics and jamming in a water fluidized bed

by

Daniel Ivan Goldman, B.S.

DISSERTATION

Presented to the Faculty of the Graduate School of

The University of Texas at Austin

in Partial Fulfillment

of the Requirements

for the Degree of

DOCTOR OF PHILOSOPHY

THE UNIVERSITY OF TEXAS AT AUSTIN

August 2002

Dedicated to my parents, who made all of this possible.

Acknowledgments

Outside of the laboratory, my family has been a source of inspiration and support over these many years. I thank them for allowing and encouraging me to pursue my dream, with only a minimum of nagging. I also thank my friends who have allowed for the slightly odd behavior induced by scientific inquiry. In the world on physics, I would like to thank Prof. John King at MIT for introducing me to the intoxicating world of experimental physics. Special thanks to Gene DiSalvatore, without whom I would never have found Texas. I would like to thank the many people in the physics department and Center for Nonlinear Dynamics I've collaborated with and pestered during these years. Norma Kotz, Dorothy Featherling, Rosie Tovar, Olga Vera have solved many administrative and logistical problems which would have certainly forced me out on the street. Ed McKnight, Jack Clifford, Billy Kilgore all provided excellent advice and training in the machine shop. Thanks to Robert Hasdorff and John England for electronics help. Thanks to John DeBruyn, Brendan Plapp, and Anna Lin who all helped me so much during my qualifying exam. Special thanks to Mark Shattuck for helping to guide me in the early days in the CNLD. Without his patience for my questions and constant interest in my research, my experience would have been much less enjoyable. I owe a great debt to Paul Umbanhowar, without whom I would not be in the CNLD. His interest, support and friendship over the years has been invaluable. I would also like to thank Prof. Jack Swift for his interest and many discussions over the years. Finally, I must thank Prof. Harry Swinney, from whom I've learned the correct way to do physics, on a scientific as well as personal level. I cannot thank him enough for his kindness and support over the years.

Pattern formation and fluidization in vibrated granular layers, and grain dynamics and jamming in a water fluidized bed

This work examines the behavior of granular materials forced away from equilibrium in two different experimental systems. We study pattern formation in vibrated granular layers, and fluidization of grains near the onset of fluidization in a water fluidized bed.

When a thin layer of grains is subject to sufficiently strong vertical vibration of frequency f_d, standing wave patterns are excited and oscillate subharmonically at $f_d/2$. The patterns form when Γ, the peak plate acceleration normalized by gravity, exceeds a critical value, $\Gamma \approx 2.5$. To gain understanding of this transition, we studied the behavior of the layer near the onset of patterns. Below onset, for $\Gamma < 2.5$, we found that although no visible patterns were excited, the noisy state contained spatial structure. In addition, we studied the formation and the evolution of order in square patterns after a rapid change in Γ from below to above onset. We found that the pattern formed in two distinct stages: a rapid ordering with universal properties, followed by a slower non-universal ordering. We also examined the behavior of the average wavelength of the patterns during the first stage ordering, and found that the evolution of the wavelength was accompanied by a change in the effective fluid depth of the layer. The condition for a rapid layer fluidization was shown to be governed by a previously studied grain mobility transition. In the asymptotically formed square patterns, we found that the dynamics of the nodes of the patterns displayed normal modes and dispersion relations analogous to those of a two-dimensional crystal lattice. In addition, the normal modes could be resonantly excited; if the amplitude of a mode became large enough, the crystal melted, in accord with the Lindemann criterion for 2D melting. At higher values of Γ, we performed experiments on patterns that displayed phase discontinuities, called kinks. We observed that localized transient kinks called phase bubbles prevented the formation of stable patterns that would oscillate at $f_d/6$. By preparing the system with a uniform initial condition, we were able to observe transient $f_d/6$ patterns. In addition, we found that

a convective motion associated with kinks led to segregation of different-sized particles: large particles were pulled into the kink and remained trapped.

Fluidization in a water fluidized bed occurs when the pressure drop ΔP developed by the flow Q through packed grains balances the buoyant weight of the grains, $(\rho_p - \rho_f)gh$, where ρ_p and ρ_f are the solid and fluid densities and h is the height of the grains. For increasing Q, fluidization is characterized by an increase in void fraction, $1-\Phi$, where Φ is the solid particle fraction. Using a light scattering technique called Diffusing Wave Spectroscopy, we studied the dynamics of grains for smooth increases and decreases of Q near the onset of fluidization. We found that the behavior was strongly influenced by the initial packing fraction of the grains. Loosely packed grains near Random Loose Packed (RLP), with $1-\Phi \approx 0.45$, moved immediately at the onset of fluidization and remained in motion. In contrast, tightly packed grains displayed a range in Q above onset during which voidage changes were followed by a rapid settling into a motionless state. We found that this was a result of yield stresses developed in the packed material due to the creation of a stress-bearing network; the network resulted from jamming of the grains due to frictional contacts between the grains and the walls of the cell. We also found that behavior of the bed upon defluidization was analogous to the behavior of a supercooled liquid near the glass transition: for $1-\Phi > 0.45$, the bed resembled a liquid. For $1-\Phi < 0.45$, motion in the bed was hindered due to local regions of largely immobile particles. These regions grew in size as Q was decreased until $\Delta P < (\rho_p - \rho_f)gh$, at which point all translational dynamics of the grains ceased.

Table of Contents

List of Tables

List of Figures

xix

xxiii

Chapter 1

Introduction

1.1 Motivation and problems to be studied

Granular materials are typically defined as a collection of macroscopic particles which interact dissipatively upon collision and for which the thermal energy $k_B T$ is small compared to any energy scale in the problem. Concealed in this rather mundane description are systems that mimic the behavior of matter in many different regimes, see Figure 1.1. These regimes can be high Knudsen number collisionless flow, shock waves propagating with Mach number much greater than one, or solids which can support a yield stress. Importantly, all regimes can be seen and studied in detail in a single-person laboratory experiment.

As an example, imagine pouring sand, a common granular material, out of a jar over a pencil and onto the ground. As the grains leave the jar, their flow resembles a fluid. In fact, due to the large mean-flow velocity relative to the fluctuating component of flow velocity (a factor of 10), the grains strike the pencil at high Mach number. Consequently, an oblique shock forms. When the flow hits the ground it solidifies due to dissipative collisions, coming to rest in the form of a pile. Unlike the fluid-like flow above it, the pile can support stress. Thus, this simple experiment exhibits physical phenomena and properties of matter that are typically studied only at great cost and almost never in the same experiment. In this spirit, we explore the behavior of granular materials in different regimes in this dissertation.

The problems that will be described cover a fairly wide range of behavior of a collection of grains. In a single thesis I am able to describe systems which display peculiar clustering effects in gas-like behavior, time dependence of wave patterns which form in a granular fluid, the effects of fluctuations in the granular temperature on this fluid, fluid-like behavior in a collection of grains forced by water, and solid, glassy behavior of a packed set of grains where inter-particle forces and stress chains dominate the behavior

1.1.1 Overview of the Dissertation

The work in this dissertation deals with transitions between different regimes of granular behavior as control parameters are changed. Two main systems will be
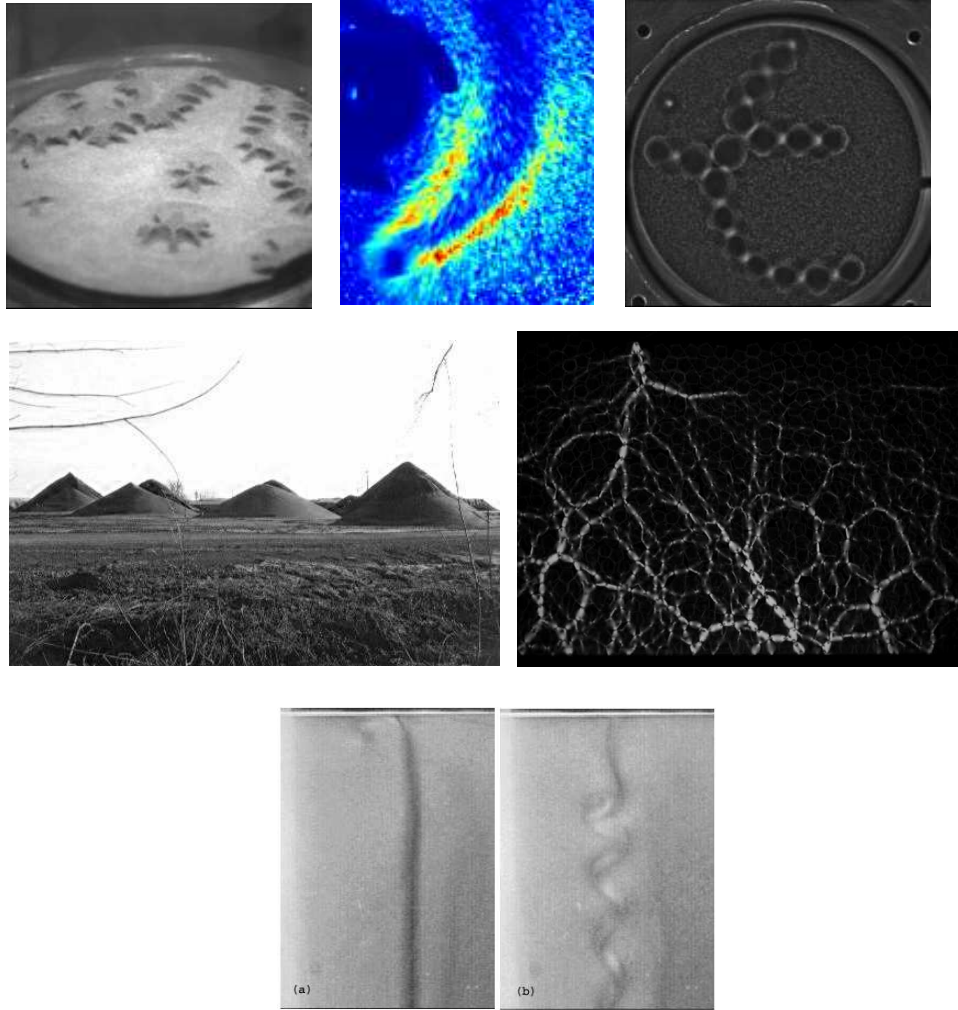
Figure 1.1: Different behavior displayed by granular materials, left to right and down the page: surface waves in a vibrated layer, Cerenkov wave radiation of a rod moving in a thin layer, localized structures (oscillons) in a vibrated layer, sand piles on the Petrie Islands, Ottawa (from website of The Friends of Petrie Island), stress chain backbone in a solid granular pile of disks (from website of B. Behringer), the wake of a 1 mm sphere falling in water (from E. Ramos)

studied, and both are effectively designed to maintain a set of grains out of the motionless equilibrium state. Wave phenomena in thin vibrated layers will be discussed in Chapters 4-6. Chapter 7 discusses a problem in granular gases called inelastic collapse. Chapters 8-9 will deal with fluidization phenomena in a water fluidized bed, including behavior of grains at onset of fluidization and analogies to glasses. Chapter 2 will review the behavior of granular materials in regimes which are relevant to the problems discussed

in the dissertation, and Chapter 10 will conclude.

The remainder of Chapter 1 introduces the two main systems that will be studied.

1.1.2 Wave patterns in vibrated layers

We study a system in which thin granular layers (up to about 15 particle diameters deep) are vibrated vertically sinusoidally such that the position of the plate obeys,

$$y = A\sin(2\pi f_d t) \tag{1.1}$$

where f_d is the drive frequency of the plate, typically between $10 - 200$ Hz, and A is the amplitude of the plate. The state of the system is characterized by the peak plate acceleration relative to gravity, $\Gamma = A(2\pi f_d)^2/g$. Since chapters 4-6 review the literature of vibrated granular layers relevant to the specific problems studied, in this section we will only briefly introduce the basic features of the system which have already been well described in [129, 179–181].

Behavior of the layer for increasing Γ

As an example of the basic phenomena encountered in vibrated granular layers, we summarize transitions displayed in a thin layer of 100 μm bronze, 15 particle diameters deep [137]. For $\Gamma < 1.0$, the plate never accelerates greater than $-g$ and the layer rests on the plate as a solid clump. For $1.0 < \Gamma <\approx 2.0$, the layer leaves and strikes the plate every oscillation but the energy input by the shaking plate is completely dissipated and the grains remain in a compact solid state. The regime from $2.0 < \Gamma < 2.5$ has been studied in depth in [137]. In this regime for f_d smaller than $f_d \approx 70$ Hz, the layer is in a dilated state during some fraction of the cycle and this dilation is large enough for grains to slip past each other–the layer becomes fluidized. For $f_d > 70$, the layer is dilated but there is not enough room for grains to move past each other; however the top of the layer remains fluidized. For $f_d > 200$, the dilation becomes so small that the layer remains in a compact solid state.

Above $\Gamma = 2.5$ for $f_d < 200$ hydrodynamic wave patterns oscillating at $f_d/2$ form (see Figure 1.2), and a phase diagram of the types of patterns is shown in Figure 1.3. Here f_d is normalized $f_d^* = f_d/\sqrt{(g/H)}$, where H is the layer depth. In the presentation of experimental results, we give layer depth in dimensionless form, $N = H/d$, where d is the particle diameter. The system forms stripes for high frequency ($f_d^* > 0.33$) [181] and squares for $f_d^* < 0.33$. Hexagon patterns oscillating at $f_d/2$ form above $\Gamma \approx 4.0$ due to a temporal symmetry breaking in the collision with the plate.
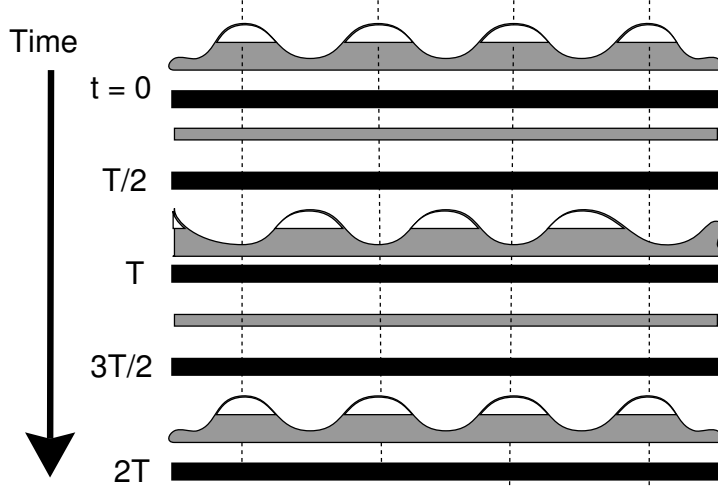
Figure 1.2: Patterns that form in a vibrated granular layer oscillate subharmonically to the plate oscillation. Under low angle illumination, peaks are visible and valleys are in shadow.

The patterns that oscillate at $f_d/2$ exist for $\Gamma < 4.5$. Above 4.5, the flat state returns and now strikes the plate every other plate oscillation, allowing phase discontinuities in the layer to form (for discussion, see Chapter 6). Above $\Gamma \approx 5$, the flat state bifurcates into patterns that oscillate at $f_d/4$ again forming squares and stripes and hexagons. Above $\Gamma > 7.5$, a qualitative change in the layer dynamics occurs; a spatiotemporally chaotic state called a phase bubble state forms and prevents the $f_d/6$ patterns which would be in the series of bifurcations $f_d/2 \rightarrow f_d/4 \rightarrow f_d/6$ from forming. Details are discussed in Chapter 6.

In this dissertation, we will explore the behavior of the vibrated layers in different regions of the $\Gamma - f_d$ parameter space. In Chapter 4 we study the time evolution of order in square patterns following a rapid change in Γ from a flat featureless state. We find that the patterns form in two distinct stages: in the first stage, which lasts on the order of 10 plate oscillations, the amplitude of the pattern rapidly grows and the pattern displays ordering dynamics that are universal. In the second stage, which can last 10^4 plate oscillations, the pattern evolves through growth of large domains which eventually coarsen to a perfectly ordered square pattern; the ordering dynamics in this stage are not-universal. In chapter 5, we study the dynamics of the square patterns and find that the elements of the patterns act as if they are coupled by Hookian springs. The dynamics of the square patterns thus resemble a two-dimensional crystal lattice and we find that the normal modes of this crystal can be resonantly excited. The amplitude of excitation can be made large enough to melt the lattice, and the melting transition is in agreement

4
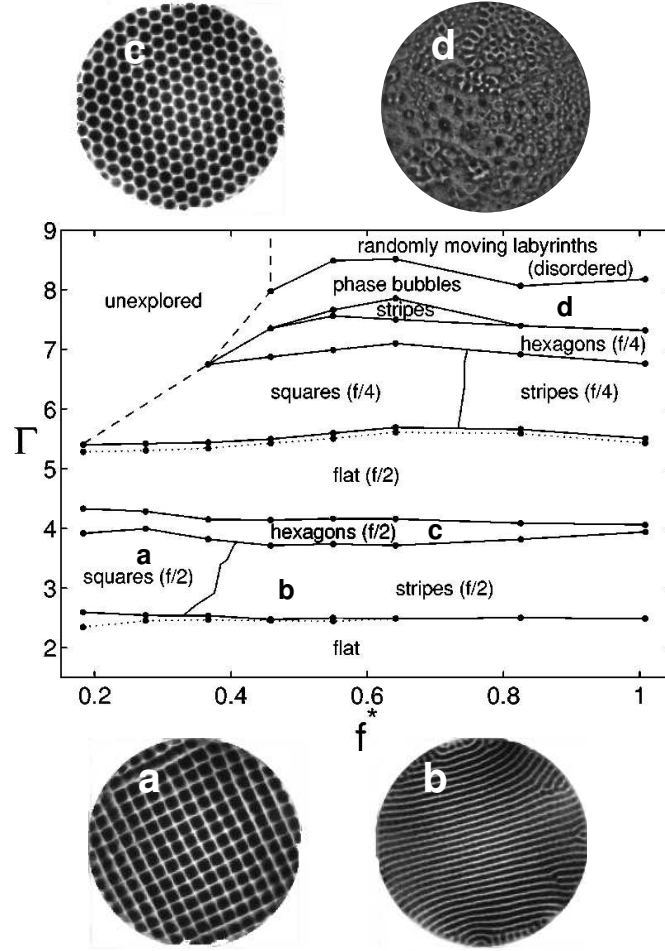
Figure 1.3: Phase diagram for a layer 11 particle diameters deep. Samples of the patterns seen in the phase diagram are shown for points a-d. f_d^* is the normalized drive frequency, with $f_d^* = f_d/\sqrt{(g/H)}$ where H is the layer depth and g is the gravitational acceleration.

with a criterion used to predict melting in real crystals. Thus, we have developed a new description of nonequilibrium patterns.

In Chapter 6, we discuss further the dynamics of patterns following a change in Γ. We study the evolution of the average wavelength of the pattern and find that the evolution of the pattern wavelength is related to a fluidization transition in the layer. We also study the properties of the vibrating layer below the onset of patterns and find that there is a characteristic length scale in the seemingly randomly excited "flat" state. Finally, we examine the dynamics of phase discontinuities called kinks and phase bubbles. We find that these discontinuities mask patterns which are predicted to oscillate at $f_d/6$ and we have observed transient $f_d/6$ patterns. In addition, we present results in which

5

convection roll structures associated with the kinks are able to transport and segregate grains of different size added to the vibrating layer.

1.1.3 Dynamics of grains at the onset of fluidization

We study a water fluidized bed near the onset of fluidization. In a fluidized bed, grains are subject to a flow of fluid against the direction of gravity. At a critical volume flow rate Q_f, the grains make a transition from solid to liquid like behavior. The fluidized bed system differs from the vibrated layer due the presence of the water. Interaction between the grains is no longer due solely to inelastic contact collisions; grains now interact by hydrodynamic effects which can operate at a distance greater than a grain diameter. The grains that will be used in the experiments in this dissertation are glass spheres and an image of the side of a fluidized bed is shown in Figure 1.4.

Figure 1.4: 335 μm glass spheres in water

Schematics of the fluidization transition are shown in Figure 1.5 and Figure 1.6. We now describe the basic process of fluidization. Fluid is forced through a collection of grains occupying a solid volume fraction Φ at a constant volume flow rate Q. In fluidized bed research it is customary to instead use $1 - \Phi$, the voidage of the bed[1]. At low flow rates (small Reynolds number for the pore), flow through porous media of voidage $1 - \Phi$ follows an empirical relation called Darcy's law; for higher flow rates Darcy's law must be corrected and these corrections are called Ergun's relation [160]. Darcy's law says that the

---

[1]Note that for identical spheres, the voidage cannot be smaller than the value for FCC crystal packing, $1 - \Phi \geq 1 - \pi/(3\sqrt{2}) \approx 0.26$. This was conjectured by Kepler in 1609 and proved by Hales in 1998 [84]. However, practically, the voidage never reaches a value lower than Random Close Packed (RCP), $1 - \Phi \approx 0.37$. The maximum possible voidage occurs when the solid volume fraction goes to zero, or $1 - \Phi = 1$.
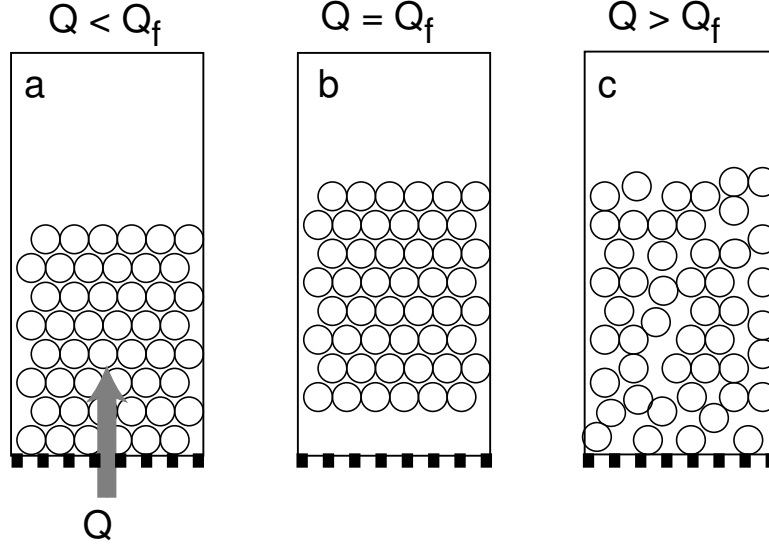
Figure 1.5: A schematic illustrating the behavior of grains at three points a-c as the volume flow rate, Q is increased through fluidization.

pressure drop developed by the fluid, ΔP is proportional to Q and inversely proportional to a monotonically increasing function of $1 - \Phi$ called the permeability[2]. To make an analogy to electrical current flow, the permeability can be thought of as the inverse of the resistivity of the medium. Thus, for fixed $1 - \Phi$, ΔP increases with increasing Q. When Q is increased so that that ΔP equals the buoyant weight of the bed normalized by cross sectional container area A, a force balance occurs. The system can respond by allowing all grains to be translated up the container at once. However, the fluidization velocity, Q/A, is roughly a factor of 50-100 times smaller than the sedimentation velocity of a single particle (see below). Thus when the bottom becomes exposed, particles fall, filling in the space that was free of particles. This has the effect of increasing the voidage of the sample as illustrated in Figure 1.5. By Darcy's law, this restores the force balance. Thus the net effect is that the system responds to fluidization by increasing its voidage, and this is plotted in Figure 1.6.

Above fluidization, the relationship between the voidage of the bed and the flow velocity of fluid $v_f = Q/A$ has been extensively studied, and different empirical rules have been proposed [32, 109]. The formula of Richardson and Zaki [152] is perhaps the best known of these fits, and proposes a power law scaling,

---

[2]In the Kozeny theory of porous media, the permeability is proportional to $(1 - \Phi)^3$ [160]
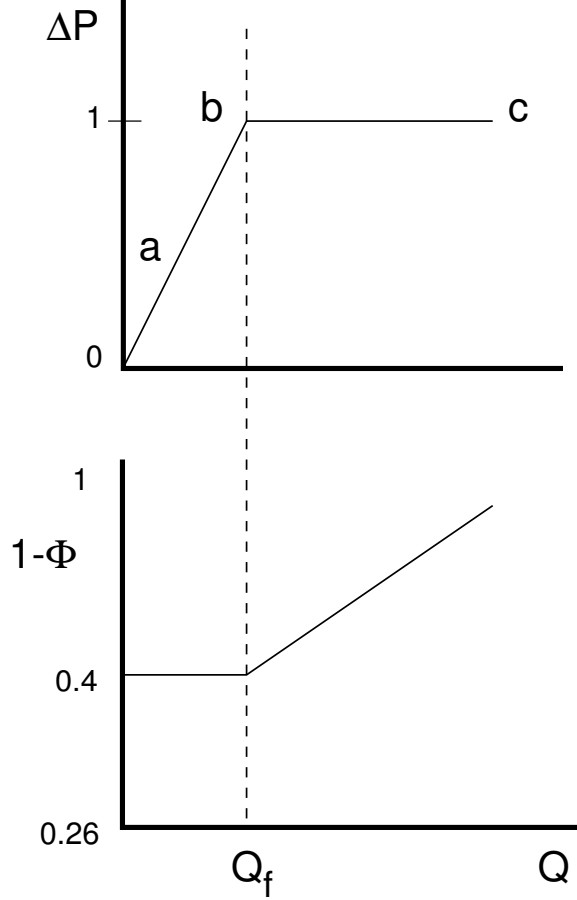
Figure 1.6: Schematic plots of the basic measurements and phenomena in fluidization for slow increases of Q. Top panel: ΔP, the pressure drop of fluid through the grains normalized by the buoyant weight of the grains. Bottom panel: the average void fraction (voidage) of the particles, $1 - \Phi$. Voidages at fluidization are typically between $0.37 < 1 - \Phi < 0.45$. Points a-c refer to the diagrams in Figure 1.5.

$$\frac{v_f}{v_s} = (1 - \Phi)^n \tag{1.2}$$

where v_s is the terminal sedimentation velocity of a single sphere falling in the tube of diameter $D = \sqrt{A}$. This rule applies to non-bubbling fluidized particles of diameter d with $0.1 < d < 6$ mm and particle density ρ_p between approximately $1 < \rho_p < 11$ g/cm^3 for fluids with densities between approximately $0.8 < \rho_f < 3$ g/cm^3. The Richardson-Zaki power law is actually quite complicated: the exponent n depends on D, the particle diameter d, and the Reynolds number at the terminal velocity of the sedimenting sphere in an infinite fluid, $\mathrm{Re}_t = dv_t \rho_f / \mu$, where ρ_f is the fluid density and μ the fluid viscosity.

9

Due to wall effects, v_s is slightly smaller than v_t and is related to v_t as $\log v_s = \log v_t - d/D$. The expression given for n is shown in the table,

Exponent	Range
$n = 4.65 + 20\frac{d}{D}$	$\mathrm{Re}_t < 0.2$
$n = \left(4.4 + 18\frac{d}{D}\right)\mathrm{Re}_t^{-0.03}$	$0.2 < \mathrm{Re}_t < 1$
$n = \left(4.4 + 18\frac{d}{D}\right)\mathrm{Re}_t^{-0.01}$	$1 < \mathrm{Re}_t < 200$
$n = 4.4\mathrm{Re}_t^{-0.1}$	$200 < \mathrm{Re}_t < 500$
$n = 2.4$	$\mathrm{Re}_t > 500$

Table 1.1: The expression for n in Equation 1.2 for different parameters

For particles used in the experiments that will be described in Chapter 9, typical $\mathrm{Re}_t \approx 10$ giving a value of $n \approx 4.5$. We find good agreement with Equation 1.2 below the onset of bubbling. Thus, for our experiments near onset at $1 - \Phi \approx 0.42$, fluidization velocities are typically a factor of 50 smaller than single particle sedimentation velocities.

Despite the complicated dependence of n, Equation 1.2 is a useful predictor of bed height as a function of flow rate for non-bubbling beds (See Figure 8.28 in Chapter 8). However, there is no theoretical derivation of this power law behavior.

Fluidized bed dynamics at onset

While the bulk behavior of fluidized beds is well characterized, the dynamical behavior at the onset of fluidization is not as well understood. The first systematic study of gas fluidized bed behavior was due to Geldart [63]. Existing data were used to create a classification scheme of four types of onset behavior. This scheme relates onset behavior to particle diameter and particle-fluid density difference. The so-called Geldart diagram is shown in Figure 1.7. We note that there is no similar diagram for water fluidized beds.

There are four regions of behavior on the diagram, A-D. Behavior of Geldart A "aeratable" particles is defined by a smooth expansion of the bed at the onset of fluidization. Geldart A particles are typically small in size and have densities less than roughly $1.4\,\mathrm{g/cm^3}$. The smooth expansion of the bed exists for a range in flow rate, above

10
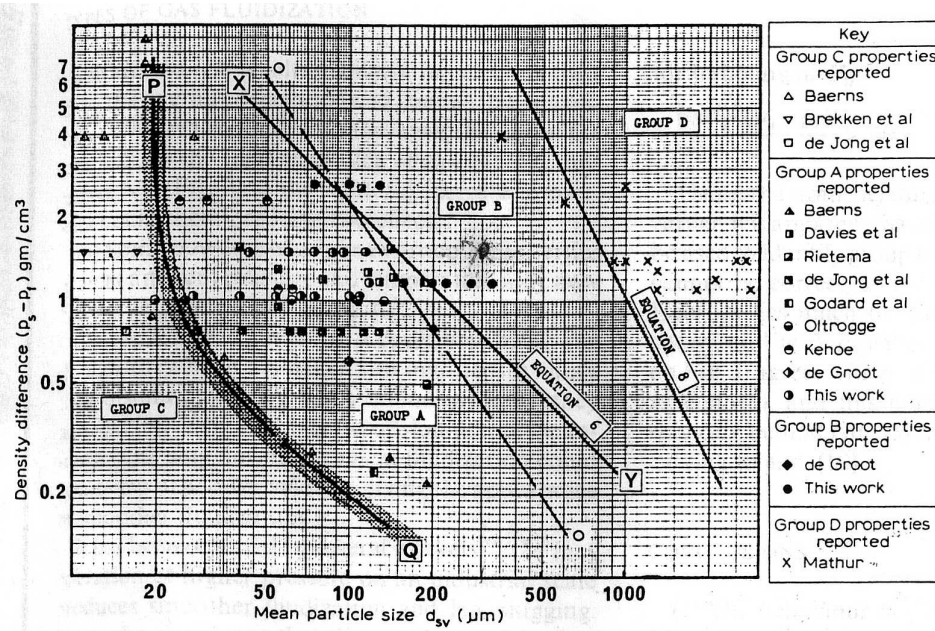
Figure 1.7: The Geldart classification scheme for air fluidized particles.

which the system becomes unstable to traveling structures of low particle density [156]. This is called bubbling and is ubiquitous in gas fluidized beds. Examples of bubbles are shown in Figure 1.8. Geldart B particles differ from those in A, in that bubbling begins immediately at the onset of fluidization.

We note that in liquid fluidized beds, the bubbling takes the form of regular traveling waves of low particle density which span the entire cross sectional area, Figure 1.9. This is one of the main differences between the behaviors of gas and liquid fluidized beds. Many studies of bubbling and stability of the fluidized state to density waves have been made [57, 97]. Much work has gone into stability analysis of the two-fluid models with some success in the prediction of onset [4, 93] of bubbling. Two-fluid models predict that the bubble is a secondary instability on the wave structure, but experimental studies are lacking.

Very small particles for which interparticle interaction is important are grouped in Geldart C. These beds display cohesive behavior at onset without a transition to a uniformly fluidized state. D refers to spouting beds and will not be discussed here.

As noted, the Geldart diagram was compiled for gas fluidization and no similar classification has been made for water fluidized beds. However, water fluidized beds are a convenient experimental tool; unlike in gas fluidization, it is straightforward to vary working fluid parameters like fluid density and viscosity. With that in mind, in Chapter 8, we study a water fluidized bed in what we might think to be the simplest

11
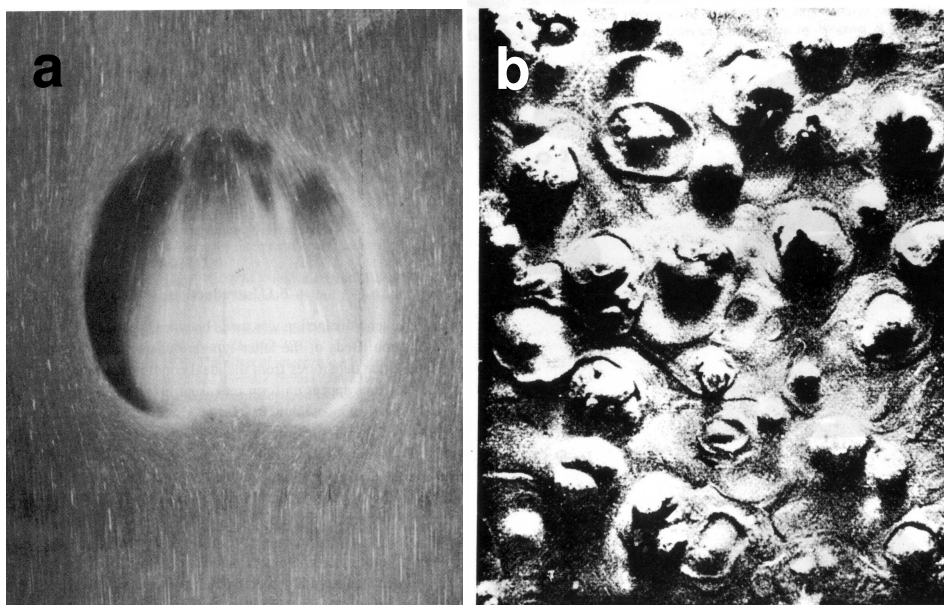
Figure 1.8: (a) A streak photograph showing a side view of a bubble in a two dimensional gas fluidized bed, from [97] (b) A top view of a bubbling gas fluidized bed. The surface of the bed resembles a boiling liquid, from [42].

situation, water fluidized glass spheres which display uniform fluidization at onset. Our results demonstrate that the dynamics of grains between 0.1 and 1 mm at the onset of fluidization are strongly dominated by friction contact forces. We will describe the motion of the grains at onset using a variety of techniques that will be described in Chapter 3. We will also compare our results to previous onset studies of gas fluidization of Geldart A particles.
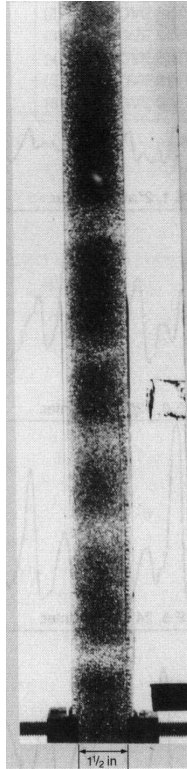
Figure 1.9: Liquid fluidized beds are unstable to low density waves of frequency roughly 1 Hz. Shown are upward traveling waves in 2 mm glass beads in a tube 3 cm in diameter. From [97].

Chapter 2

Review of phenomena in granular materials

The problems that will be discussed in Chapters 4-9 deal with granular materials in the fluid and solid regimes. We will study such phenomena as collisional dynamics of a dense inelastic gas, waves in a granular liquid, fluidization transitions from solid to liquid behavior in a vibrating layer, and sub-micron motions of a granular solid forced by water. Therefore, in this chapter I give a review of basic phenomena in granular materials, dry and wet. I save more specific introductions to different experiments for their respective chapters. I begin with the gas and fluid-like aspects of strongly forced grains, often called rapid granular flow.

2.1 Rapid granular flow–granular gases and liquids
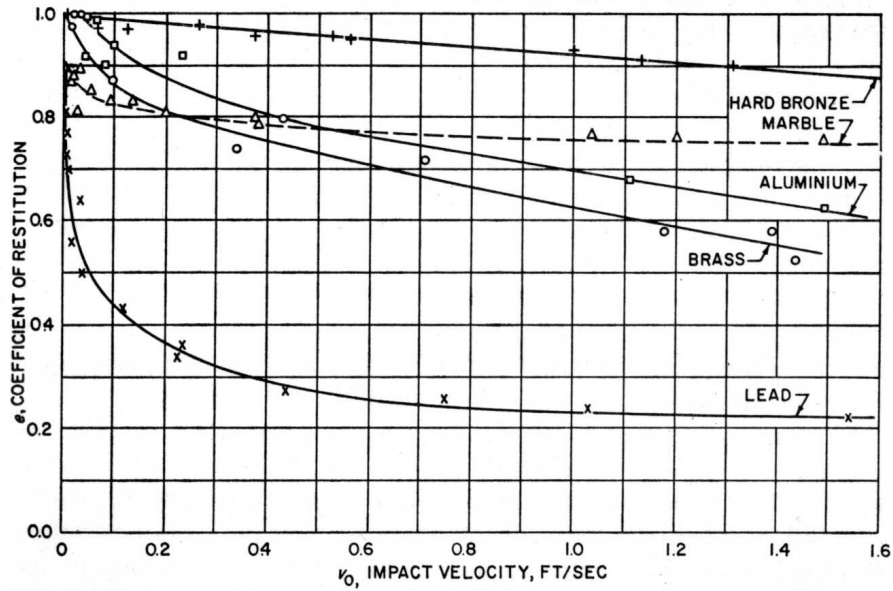
Figure 2.1: The coefficient of restitution for normal impact between two spheres as a function of velocity for different materials. Plot taken from compiled data in [75].

A collection of grains must be continuously forced to be maintained away from the equilibrium pile on the table. This is due to the dissipative nature of the collisions. This inelasticity is typically included in the description of granular materials by a coefficient of restitution, r, which models the dissipation of energy at each collision, such that,

$$\Delta v_n^{'} = -r\Delta v_n \tag{2.1}$$

where $\Delta v_n^{'}$ and and Δv_n denote the relative collision velocities of the spheres before and after the collision. The value of r is usually taken to be a constant. However, event-driven molecular dynamics simulations of granular materials which use a constant r suffer from a severe problem. For sufficiently high particle densities and low enough r, the gas can suffer inelastic collapse: certain particles experience an infinite number of collisions in a finite time and this overwhelms any computation as all of the time is spent computing trajectories in these highly clustered regions. The collapse phenomenon was thought to provide a mechanism for the formation of clusters of high density regions in a freely cooling granular gas. However, we have shown (see Chapter 7) that inelastic collapse is an artifact of the constant r model. In reality, r is velocity dependent, as seen in Figure 2.1. When a velocity dependent r is used, this collapse phenomenon disappears. Thus inelastic collapse creates a pathological form of clustering. However, the absence of inelastic collapse does not imply the absence of clustering. Using a collision model in which r was held constant but collapse was prevented by a cutoff in collision time, Luding and Hermann found that a freely cooling granular still demonstrated clustering, forming a growing set of filamentous structures, see Figure 2.2 [122]. Although it has been shown that a velocity dependent r modifies the cooling rate [162] of the gas, to date, no studies have been done to carefully examine clustering with a physical form of r.

The idea of rapid granular flow says that a collection of grains that is forced away from its equilibrium state by suitable agitation can be thought of as a fluid and described by hydrodynamic equations. The equations which govern this fluid-like behavior can be derived from a kinetic theory of hard-sphere inelastic gases [51]. This theory starts from the Boltzmann-Enskog equation whose collision operator is modified to include inelastic collisions.

A snapshot of a granular gas is shown in Figure 2.3. When the collection of grains is continuously agitated so that the cooling state is not reached [15, 133], the system reaches a steady state. Using the kinetic theory, distribution functions for particle velocities at small inelasticity have been calculated for these steady states. Due to inelasticity, these deviate from Maxwellian and compare well with molecular dynamics simulations [133, 187]. In addition to changing the local velocity distribution function by over-populating the tails, the inelasticity of the grains produces non-trivial effects such as long range correlations in particle velocities. In the uniformly heated case, these
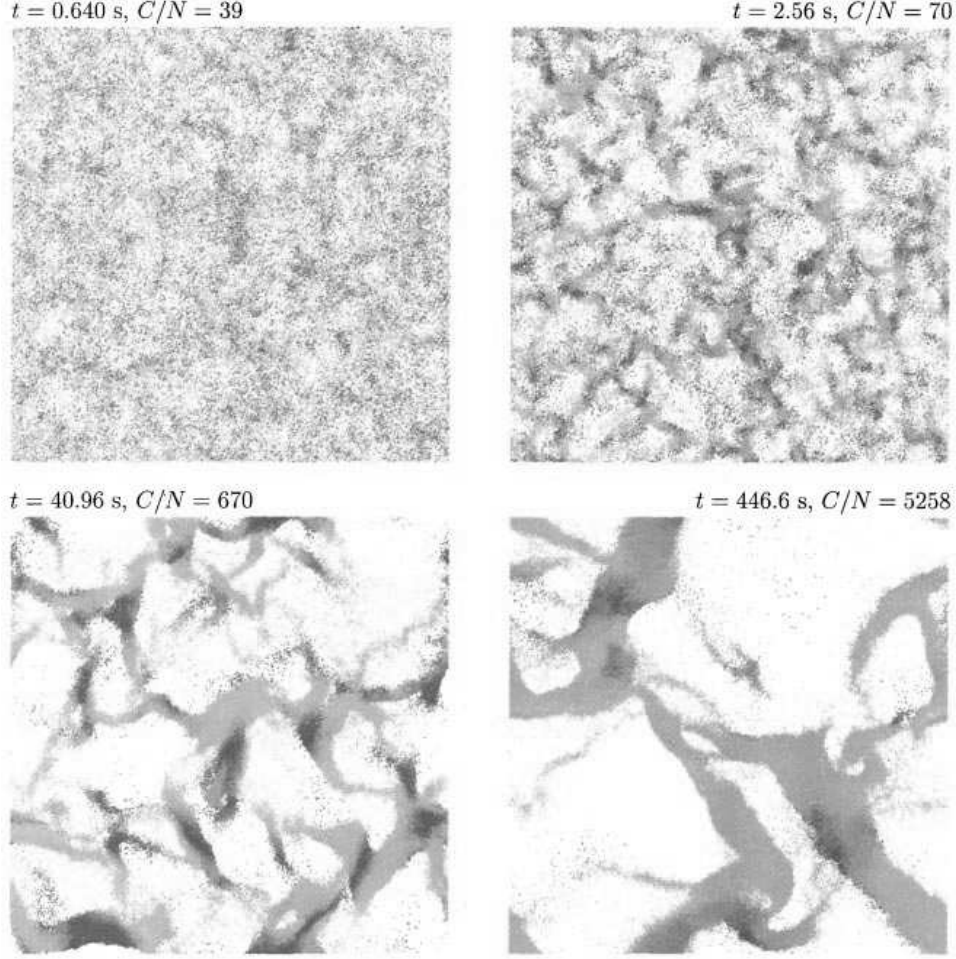
Figure 2.2: The clustering seen in a three dimensional molecular dynamics simulation of a freely cooling granular gas with a constant r model modified to prevent inelastic collapse. As time increases the clusters grow in size and the average number of collisions per particle C/N increases. Figure reproduced from [122]

correlations are not so severe as to produce the strong clustering as in the freely cooling case but instead produce system wide circulation [15].

2.1.1 Hydrodynamics and continuum equations

For small inelasticity and density, the velocity particle distribution function given by the Enskog-Boltzmann single particle distribution function is nearly Maxwellian. Expansion of the equation around this solution yields a set of Navier-Stokes like equations, the Jenkins-Richman equations. For completeness, these are given in Appendix B. These
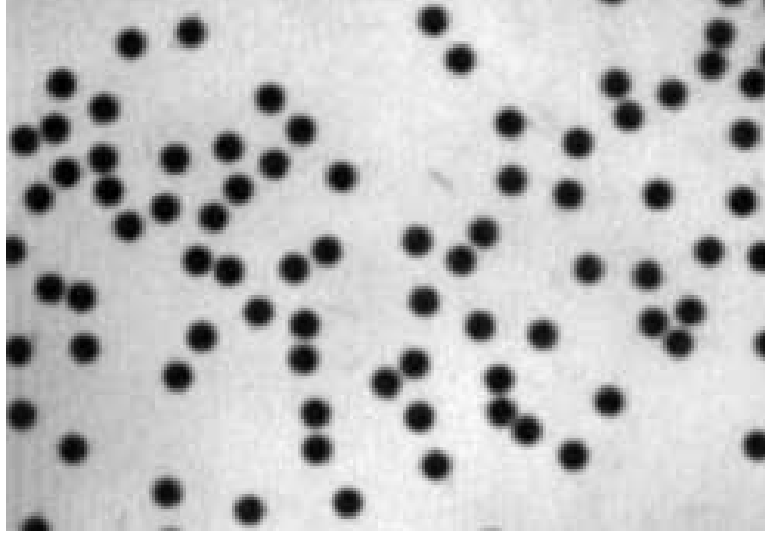
Figure 2.3: A collection of vibrated 1.65 mm steel spheres is an inelastic gas. The spheres are confined between two plates and the container is subject to vertical vibration. Courtesy D. Miracle

equations and the expressions for the transport coefficients are computed from the kinetic theory of inelastic hard spheres and they differ from a ideal compressible gas only by the addition of an energy loss term due to the inelasticity of the collisions. The Jenkins-Richman equations compare well to hard sphere molecular dynamics simulations [150], and also have produced wave patterns such as those that will be discussed in the next section. In fact, while there has been much debate on the ability of hydrodynamic-like equations to describe granular flows [49, 51, 69, 100, 165, 175], it now seems clear that the Jenkins-Richman equations can capture much of the behavior of simple vibrating flows and the behavior of rapid granular flows [19, 150][1].

It should be noted that typical granular flows are supersonic as the speed of the flow is usually much greater than the speed of the fluctuations around that flow. This causes shocks to form when a flow impinges on an object. The hydrodynamic equations agree well with molecular dynamics simulations in this regime [19, 150]. However, there can be other effects such as size segregation and heaping which would seem to defy hydrodynamic description. I will not in this thesis comment on the applicability of hydrodynamics to granular flows.

Fluid-like phenomena in granular materials occur when the collision frequency is

---

[1]The wave phenomena I will describe have not been quantitatively compared to the Jenkins-Richman equations, although there is evidence that the equations can reproduce $f_d/2$ patterns. Private communication from J. Bougie.

much larger than any frequency in the problem and the time of contact of the grains is very small. In this thesis, we will also explore problems in the opposite regime, when the time of contact is very large and collision rates are low. This is a situation when the static aspects of granular materials come into play and will now be discussed.

2.2 Solid-like behavior

When the density of a granular material becomes so large that the grains do not have enough room to slip past each other and the input energy becomes small enough so that they don't have enough energy to create the space to slip by each other, the granular material displays the characteristics of a solid. In this regime, contact forces between the grains dominate the behavior and collisional momentum transfer is unimportant. Under shear, a dense packing will develop a yield stress and only flow by plastic deformation— local grain rearrangement. This plastic behavior depends on the volume fraction of the grains, applied shear and normal stresses and the shear stress rate. This behavior has direct relevance to our studies of fluidized beds in the tightly packed states near onset where the grains are in contact and slowly sheared.

Different theories have been developed to account for the behavior of these solids under shear. A theory of solid-fluid transitions in granular materials called dilatancy was proposed by Reynolds in 1885 [151]. Reynolds argued that for a shear stress to induce flow, a collection of grains must dilate sufficiently to allow grains to slip by each other. If the grains are confined, this creates stresses at the boundaries and thus the material will develop a yield stress.

Since Reynolds, much work has been done in the field of soil mechanics with the goal to find constitutive relations between stresses and strains on a granular sample [97]. We will give a qualitative picture of the surprisingly complicated behavior of different grain packings under shear. Such a picture will be useful in interpreting results in Chapters 8 and 9

2.2.1 Shear and stress-strain relations for granular packings

The basic processes for very slowly deforming granular piles is shown in Figure 2.4 and the description we give here has been adapted from Jackson [97]. A collection of grains packed with solid volume fraction Φ_0 is enclosed by two infinite plates that are free to move in the plane of shear and also normal to this (an idealized Couette shear apparatus). A shear stress T is slowly applied tangential to the upper plate and at the same time a normal stress N is applied normal to this plate. Upon shear the plates displace an amount s, and the relationship between T and s is shown in Figure 2.5 for
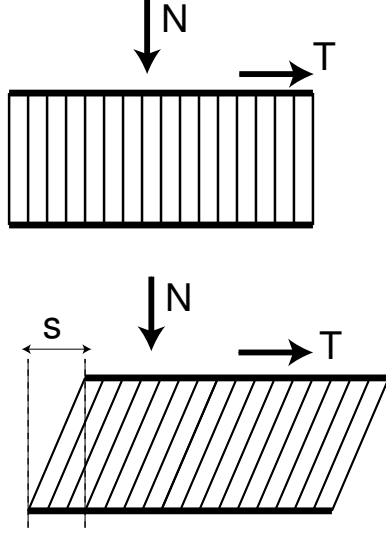
Figure 2.4: A schematic of an experiment to shear a quasi-infinite packed collection of grains. The plates are free to move in all dimensions.

two cases, a loose packing with a large normal force (small Φ_0, large N) and a tight packing with a small normal force (large Φ_0, small N)
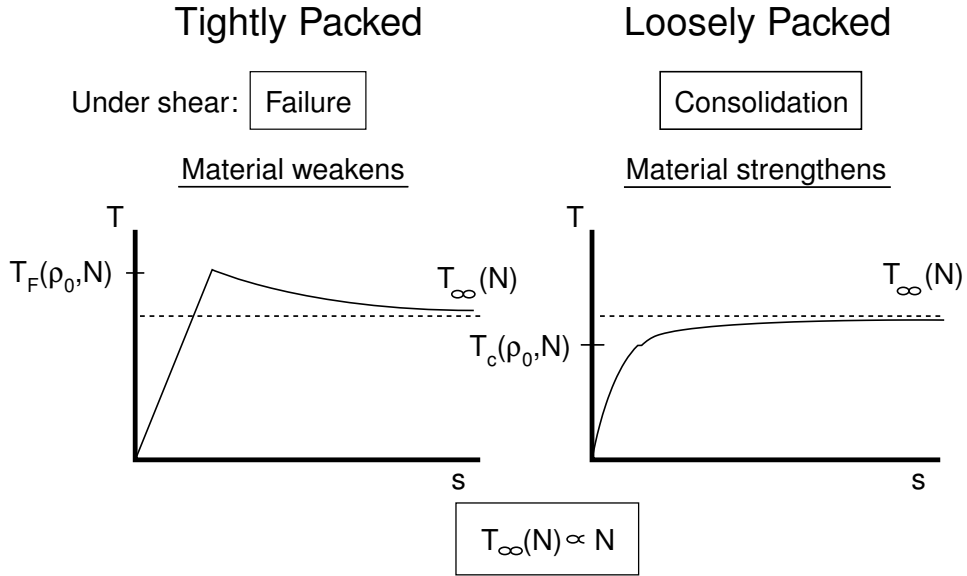
Figure 2.5: The stress-strain relations for shear of two different packings.

For both cases, for small enough displacements, the stress is proportional to the strain and the system can be reversibly deformed–this is due to the elastic behavior of the

grains. However, there exists a yield stress above which the material no longer behaves elastically and plastic deformation occurs. The qualitative behavior of the grains depends on Φ_0 and N and we discuss what happens when the shear stress goes beyond the yield stress in both cases.

For the tightly packed state under a small normal force, the yield stress is denoted by $T_F(\Phi_0, N)$, and is called the failure stress–the behavior of the material when it reaches this value is called failure. This is apparent from Figure 2.5. When the stress reaches T_F, it suddenly decreases and the stress needed to increase s continues to decrease as s increases reaching an asymptotic value $T_{\mathrm{inf}}(N)$ for large displacement. The material has failed and has become weaker.

Contrast this to the loosely packed case with a large normal force, whose stress-strain relationship shown in Figure 2.5 right panel. Here, the yield stress is denoted $T_C(\Phi_0, N)$ and the behavior of the material when it reaches this stress is called consolidation. Beyond T_C, the stress needed to maintain a separation s increases with increasing s and reaches the same asymptotic value $T_{\mathrm{inf}}(N)$ for large displacement. The material has become stronger under shear.

Dilation and consolidation (compaction)

Tightly Packed   Loosely Packed

| Dilation accompanies shear | Compaction accompanies shear |

Shear confined to thin region   Shear spreads throughout
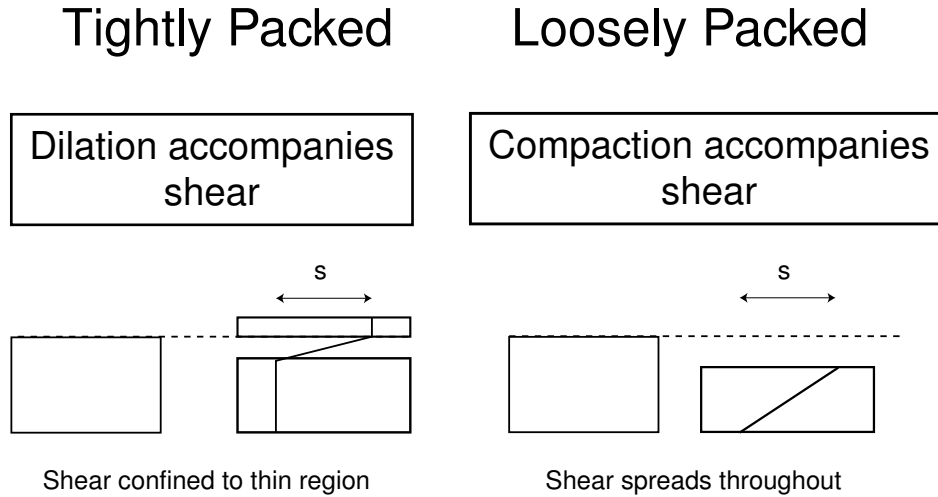
Figure 2.6: The relative change in volume fraction for granular packings under shear. Tightly packed grains dilate while loosely packed grains undergo compaction

The consequences of shear on the volume fraction of the grains are shown in Figure 2.6. As argued, in the tightly packed case the material weakens at failure. Suppose it weakens locally in a thin layer. This thin layer is now weaker than the rest of the

material, so any further shearing will occur there. Thus the shear layer remains localized. As the material has weakened, in the shear layer the density is lower and the grains are further apart. Thus the material has expanded and the plate separation has increased in the direction parallel to N. This is the phenomenon of dilation discussed by Reynolds.

As the name implies, the opposite occurs for the loosely packed case. Here when the yield stress is reached, the material begins to strengthen. In this case, yield will occur throughout the material. We can see this with the following argument: suppose the material strengthens in a thin local layer. This material in this layer is now stronger, so any continued strain will now deform the rest of the material which is weaker. Thus, the material will continue to deform outside the layer until the strength catches up to the strength of the initially deformed layer. In this way the entire material deforms in unison. The source of the increased strength of the material is due to its consolidation: the density is now higher and thus the plates are closer together[2].

Yield stress as a function of Φ_0 and N
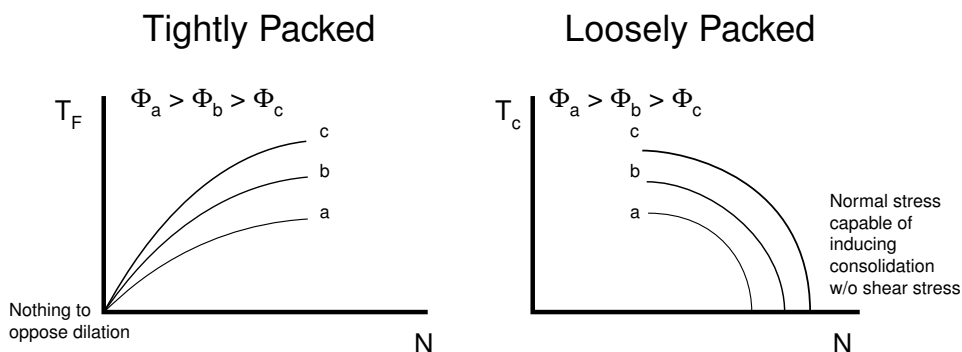
Figure 2.7: Yield stress in a granular packing as a function of normal stress. The curves in the tightly packed case are called yield loci, while those in the loosely packed state are called consolidation loci.

The values of the yield stresses are functions of Φ_0 and N, and these are plotted in Figure 2.7. They are called the failure and consolidation loci, and the goal of any theory of soil mechanics is to predict these curves for a given packing and set of stresses [97]. In the tightly packed case, for a fixed Φ, the yield stress, T_F increases as N increases. This is reasonable, as the material must be dilated in order to fail and any normal force will resist this dilation. For a given N, T_F increases as Φ increases: the system must dilate a

---

[2]Under gravity, piles of grains naturally consolidate, and the process of consolidation is difficult to observe [97]. However, poor flow distribution in our fluidized bed experiments (see Chapter 8) produces local stresses that lead to (often unwanted) consolidation effects.

sufficient amount to move past the elastic limit and this requires more force to move the grains for a tighter packing (larger Φ, stronger material).

Again, we contrast this with the loosely packed case. The values of yield stress display a different behavior. For fixed Φ, the value of the yield stress is 0 for finite N. This is reasonable, as at T_C, the material will compact, and the normal stress is already supplying a force which would seek to increase Φ. The value of N needed to begin consolidation in the absence of shearing force decreases as Φ decreases because the looser packing is weaker and needs less force to begin the consolidation. For a given Φ, as N decreases, it takes a corresponding a greater amount of shear force to begin the consolidation. This is also reasonable, as the normal force seeking to consolidate is less and therefore must now be supplemented with another shear force.

Discussion

As mentioned, theories in soil mechanics are developed to calculate the yield and consolidation loci, seeking to find constitutive relations for the stress tensor [68]. The theories are based on theories of plasticity of materials. A discussion of these theories is well beyond the scope of this dissertation. It is unclear whether hydrodynamic theories like those of Jenkins and Richman can be applied to slowly deforming solid-like granular piles. Much of the behavior of granular materials in this regime is dominated by interparticle contact forces and will play a significant role in the behavior of the grains in the fluidized bed. However, there have been efforts to describe [89] the slowly shearing solid state with hydrodynamic equations with suitably modified constitutive relations [16, 89, 117, 118]

We also point out that no values of Φ have been mentioned in this section. What defines a tightly packed versus a loosely packed state? One answer to this question, using the concept of the "dilatancy onset", was provided in a study by Onoda and Liniger [139]. They showed that the dilatancy onset, the packing density at which a shear does not promote dilation, occurred at a state called random loose packing (RLP), $\Phi \approx 0.55$. RLP is loosely defined as the lowest Φ that can support an external load. Thus, a "tight" packing with $\Phi > 0.55$ will dilate and weaken in response to a shear, whereas a "loose" packing with $\Phi < 0.55$ will consolidate and strengthen. We will return to this important concept in Chapter 8, when we examine the fluidization behavior of different packings.

The theory described in the previous sections is a continuum theory. However, careful examination of static and slowly deforming piles of grains reveals that stress is distributed inhomogeneously throughout the material along preferred network of chains (see the image in Figure 1.1) and these have been shown to play a role in the stress-strain relations. Thus, the discrete nature of the grains becomes important and we now discuss some of these results.

2.2.2 Force chains and contact forces

Careful examination of the stress-strain of a granular layer in a Couette shear apparatus shows that there are large fluctuations in the stress as strain is increased [132]. These fluctuations have been shown to be associated with the stress chains [95], see Figure 2.8. The stress chains were directly observed in two dimensions by measuring the change in polarization of photoelastic disks placed between cross-polarizers. This technique reveals that the stress is concentrated along a network of paths. Below a critical value of the packing, the stress fluctuations are small and above this critical value they can become very large. Thus the system organizes the stress into a backbone of chains which have a strong influence on the dynamics.
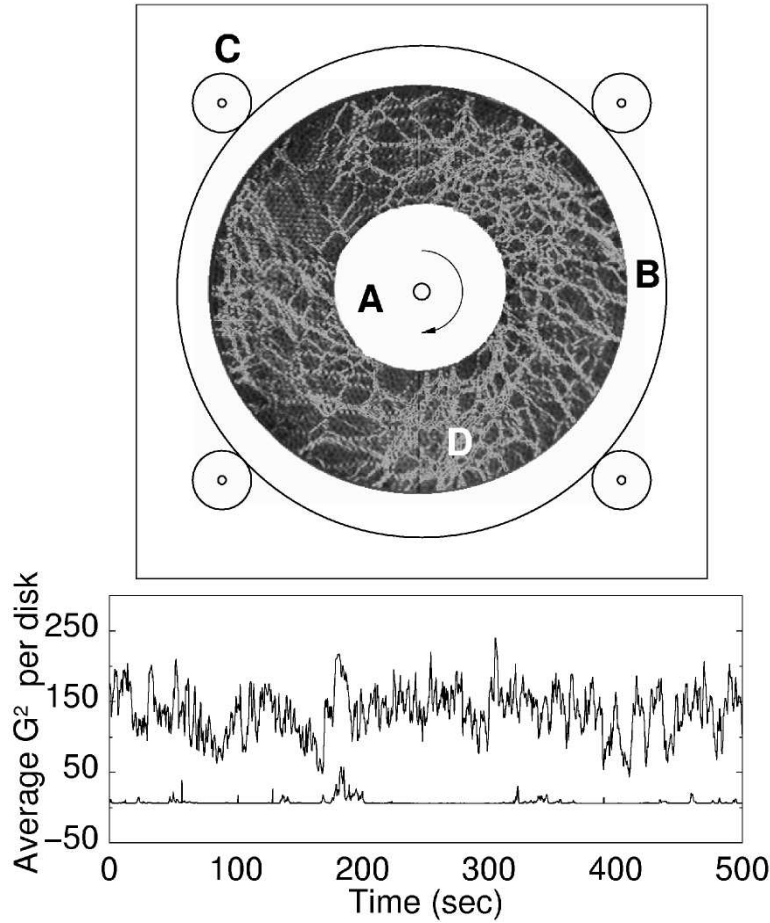
Figure 2.8: Upper panel: A sheared collection of photoelastic disks between cross polarizers reveals the existence of stress chains. Under shear, the stress on the disks, G^2 displays large fluctuations for tight packings (upper curve) and small fluctuations for loosely packed state (lower curve). From [95]

This backbone can be amazingly dynamic and experiments have been done to probe its properties in response to small perturbations. As the stress is distributed inhomogeneously, a large response in the material properties can occur for a local perturbation. Inserting a sound transmitter and detector in a granular pile of 5 mm glass grains and locally heating a grain so that it changed linear dimension by 300 nm resulted in a drop in sound received by 20%, see Figure 2.9 [113, 115, 116]. At other positions, the heat pulse did not produce any effect. The interpretation is that the heat pulse deforms the grains and if the deformed grains are members of a chain, significant re-organization can occur. Since sound is traveling on stress paths, this re-organization can have a huge effect. Such effects have also been seen in thermally heated beads using conductivity measurements and the fluctuation properties of the medium were characterized in response to perturbation [18]. We will see a similar effect in Chapter 8 and characterize the response of the material using a less invasive light scattering techniques.
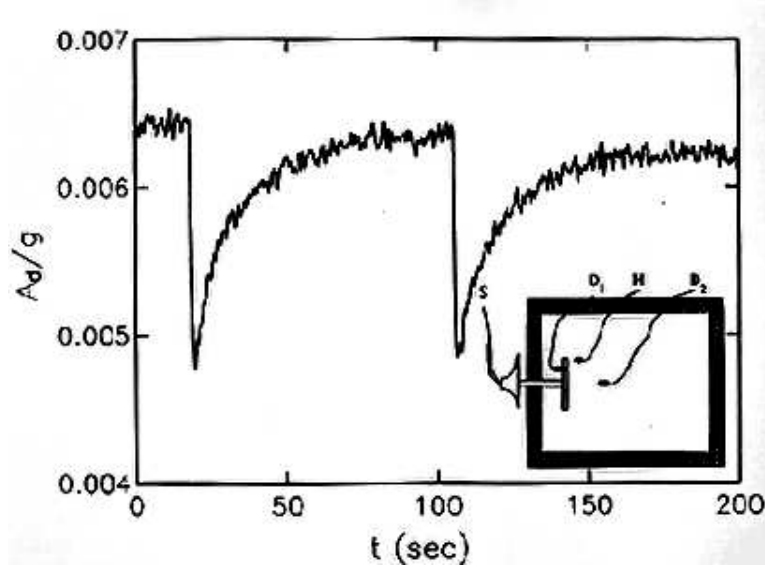
Figure 2.9: The response of a small detector (D) to sound emitted from a speaker (S) after heat pulses are locally applied to grains in the box. Two successive pulses from a heater (H) are applied at $t = 0$ and $t = 88$ sec. Each creates a thermal expansion $\Delta l \sim 300$ which dramatically changes the amplitude of the detected sound. From [113]

The presence of a stress chain backbone has a strong influence on the static properties of granular packings. For example, unlike a true liquid, the pressure in a column of grains is independent of depth below a certain depth. This is due to the stress chains which support the weight of the column. [188].

One way to approach the influence of chains is to study the the distribution of force at contact between grains, $P(F)$. The presence of particles that are more signifi-
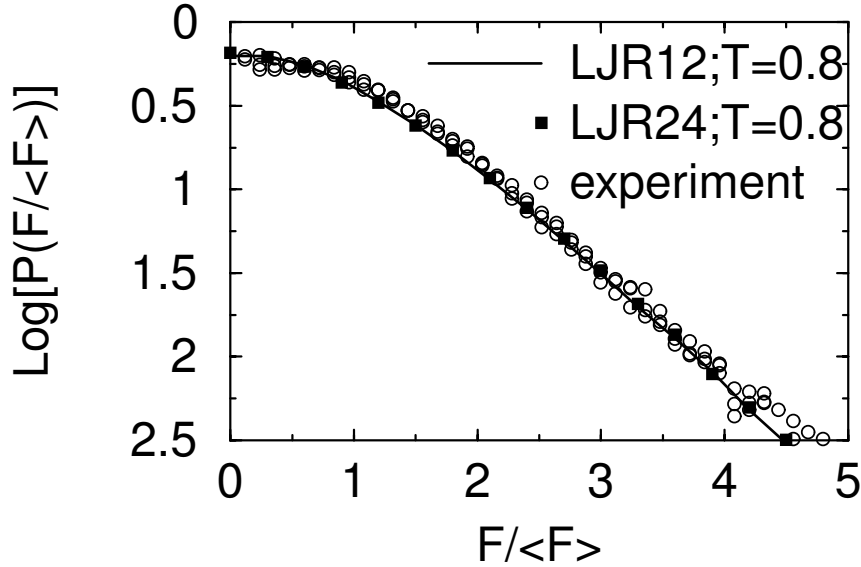
Figure 2.10: The appearance of a plateau in the grain contact force distribution has been observed in glass simulations and may occur in a jamming system or in a system undergoing a glass transition. The ∘ points are from an experiment on granular materials [136], while the other curves are for molecular dynamics simulations of particles interacting with Lennard-Jones potential. Taken from [138]

cantly stressed than others should play a role in this distribution. Groups have [114, 136] measured the force distribution between grains in a packed container and found it decayed exponentially for forces above the mean force and was almost constant for forces below the mean–a small plateau appears at low forces, see Figure 2.10. The plateau is thought to be a consequence of the inhomogeneous distribution of stress due to the force chains. In fact, it was proposed that the plateau indicates a more general jamming transition, when a system develops a yield stress as a parameter is changed. We now discuss the basic principles of jammed systems.

2.2.3   Jamming and Fragile Matter

A unifying picture has been proposed for systems that display a dramatic change in material properties as a parameter is varied. It is called the jamming picture and notes that very different systems often display similar behavior upon change of parameters. For example, colloids and foams change viscosity by many orders of magnitude upon a small increase in volume fraction or applied shear. Systems like supercooled liquids display similar slow-down behavior upon decrease of system temperature to become a glass. It has been proposed that these common behaviors can be unified in a jamming

diagram [112], see Figure 2.11.
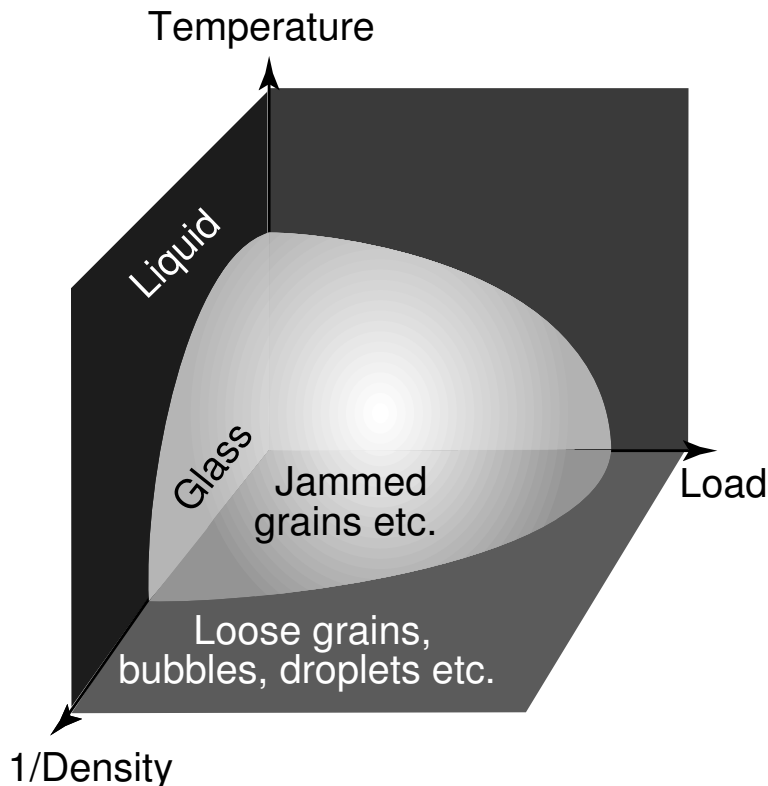
Figure 2.11: The proposed jamming diagram. Jammed states can be reached by cooling, change in volume fraction, or application of a shear. Taken from [112]

Different definitions of jamming have been proposed, for example "A system jams when it develops a yield stress or extremely long stress relaxation time in a disordered state" [138]. This is a very broad definition; we would like to understand the common features that systems which are jamming display. Molecular dynamics studies of glass-forming molecules showed that the appearance of a plateau in $P(F)$ coincided with the temperature of the glass transition in this system [138], see Figure 2.10. In addition, models of foams known to produce jamming were studied, and also displayed a plateau at the jamming transition. Thus, it was speculated that the jamming transition could be a more general form of a glass transition (we will discuss the glass transition in Chapter 9). Features of a jamming transition would include the development of a plateau in $P(F)$ and the development of a yield stress. It was speculated that the appearance of a plateau in the interparticle force curve could be related to the appearance of the stress chains. In such a picture, the system jams when the force chain network has enough participants. Formation of such a state has been called fragile matter, and is schematically illustrated in Figure 2.12.
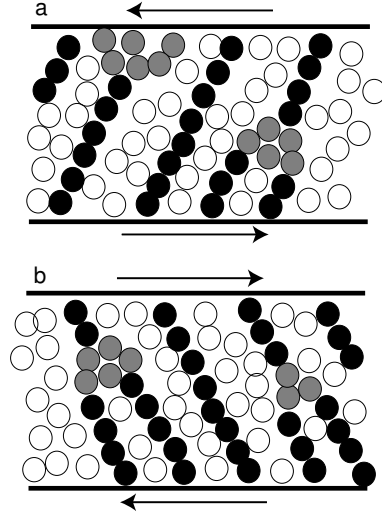
Figure 2.12: A schematic of a jammed system. The system is strong in the direction of the applied shear, but will reorganize when the shear is applied in the opposite direction. Adapted from [27].

Fragile matter is defined as a system that is strong in the direction of applied shear, but weak when the shear is reversed [27]. Such behavior is thought to be due to the network of force chains that is set up in response to the applied shear. This is illustrated in Figure 2.12. For applied stresses that aren't strong enough to fluidize, the grains may lock into place by development of a force network. This network now has a yield stress and is jammed. The system responds elastically to further small stress in this direction without the need for plastic deformation. However, this jammed state is *fragile* in the sense that it is strong only in the direction of the previously applied shear. If the shear is reversed, given what is called an *incompatible load*, the network will break and the system will deform plastically to create a new network, unlike a regular solid. There are chain particles and spectator particles in this description and the spectator particles don't participate in the main jamming chains. We will interpret our fluidized bed results in terms of the jamming picture in Chapter 8.

It has also been proposed that dense packings of granular materials that can jam share properties in common with glasses below the glass transition temperature [38, 39, 56]. In Chapter 9 we discuss these results in relation to the slow dynamics of the fluidized bed.

2.3 Multiphase flow

Describing the many different behaviors of dry granular materials is extremely challenging. When fluid is added to the grains the properties of the system can change radically. The problem are more difficult than in dry granular materials due to the extended interaction range. Dry grains only interact at collision but grains in water interact at a distance. Furthermore, the form of the interaction is governed by the Navier-Stokes equation and changes for different particle Reynolds numbers, $Re = vd\rho/\mu$, where v is a typical velocity, d is a typical particle size, μ is the viscosity and ρ is the density of the fluid. The boundary conditions also play a role. As an example, we present the work of Ramos[3] who has shown that even the motion a single particle in a fluid can be complicated, as shown in Figure 2.13. Here a ball is dropped at $Re \approx 230$ between two plates filled with water and the wake is visualized by Kaliroscope. For narrow gap, vortices are shed similar to flow past a infinite cylinder. As the gap size is increased, the wake changes character, becoming more like the wake behind a moving sphere.
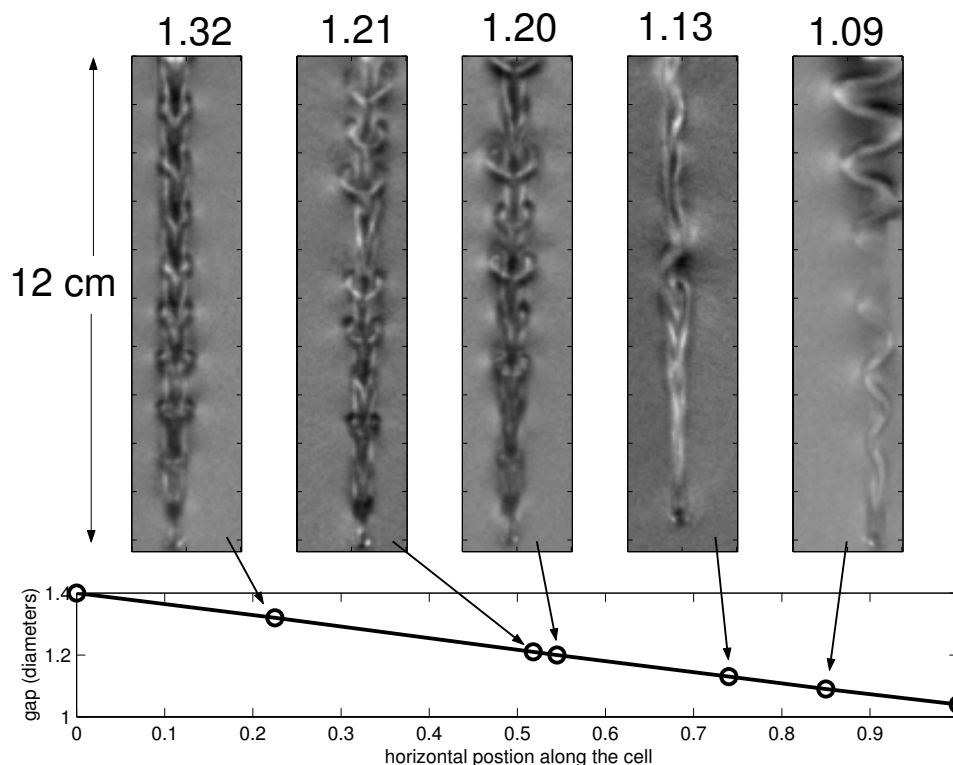
Figure 2.13: The wake behind a 3 mm acrylic sphere falling in water between two plates is a function of the ratio of gap thickness to the ball diameter. In all cases, $Re \approx 230$.

---

[3]Private communication, unpublished work.

28

2.3.1 Few particle dynamics

At low Reynolds numbers, where inertial terms are unimportant, particles interact by Stokes forces [86]. At moderate Reynolds numbers, dynamics becomes more complicated. The two-body sedimentation problem has been studied in [60] and displays interesting dynamics, seen in Figure 2.14. If two particles are dropped near each other, the particle which is behind (the second particle) is pulled into the wake of the particle which is ahead (the first particle). The second particle is then accelerated along the line joining the centers of the particles. They briefly come into contact and the first particle is sent tumbling off to the side. This process has been called drafting, kissing and tumbling [60], and is a mechanism by which vertical particle momentum is transfered into horizontal momentum. However, most of the studies to date have been qualitative and careful experiments should be done to describe the two-body problem as a function of particle Reynolds number and to also clarify the roles of the boundaries.
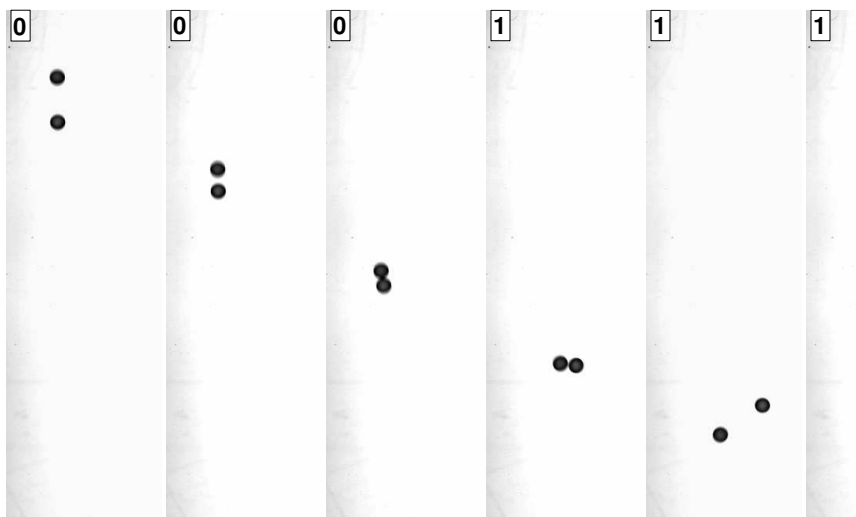
Figure 2.14: Two particles falling in water draft, kiss, and tumble as they fall. Images courtesy of Eduardo Ramos.

2.3.2 Multi-particle dynamics

While dynamics in systems composed of only a few particle are very complicated, systems of many particles have received much more attention. The first treatment of the effects of many particles on the properties of a fluid was the calculation of the viscosity as a function of particle concentration by Einstein in 1905. Since then, the most carefully studied and characterized multi-particle system has been that of sedimentation of spheres with very small particle Reynolds number ($\mathrm{Re}_p \approx 10^{-4}$ in typical experiments). These

systems have the advantage that due to the slow sedimentation rate, they can be observed for long times in a steady state.

Even at these Reynolds number, sedimentation of tiny spheres is still not understood theoretically: prediction of the sedimentation velocity for a collection of spheres as a function of particle concentration is still an unsolved problem [22, 148]. There has been considerable effort to calculate this sedimentation velocity beginning with Smoluchowski in 1912 [168]. Thirty years ago, Batchelor gave a formula which works well at low particle Reynolds number [11]. He proposed that the sedimentation velocity, v_s for a collection of spheres with volume fraction Φ should be related to the terminal velocity of a single sphere slowly falling in an infinite medium, v_t by

$$\frac{v_s}{v_t} = 1 - 6.55\Phi + O(\Phi^2) \tag{2.2}$$

Experiments have confirmed the linear correction to the sedimentation velocity, but find a prefactor smaller than 6.55 [22]. For larger velocities and higher volume fractions, the Richardson-Zaki equations (Equation 1.2) give good predictions for sedimentation rates, but in this regime there is no theoretical derivation of the power scaling of v_s with Φ.

Recently, experiments have been done to monitor the actual particle trajectories during sedimentation. The dynamics of the flows even at these low Reynolds numbers is surprisingly complicated, see Figure 2.15, and includes fluctuations of correlated regions of motions which resemble turbulence even though particle Re is so small [176]. Correlations of the velocity fluctuations have been extensively studied using PIV and light spectroscopy techniques [111, 163, 164] and found to obey scaling laws.

At yet larger particle Reynolds number, Re $\approx$ 1 with bigger particles, the work is much more sparse although new techniques are being developed to study these cases [34, 140, 141]. At these larger Reynolds numbers, the sedimentation steady state isn't reached as in lab size apparatus the sedimentation only lasts for a short time. Also, with larger particle size, container size becomes important. It has been shown that fluidized beds are useful to study a system with larger Re [34]. The fluidized bed allows the system to reach a steady state, effectively sedimenting forever[4]. Fluidized beds also allow control of the average volume fraction by changes in flow rate. Using a form of spectroscopy based on the detection of multiply scattering sound, Cowan *et al.* studied the correlations present in fluidization of 0.438 mm spheres in a container 120x200x12 mm^3, and found that there were correlations of the type found in smaller Re [34].

---

[4]However, there should be differences due to imposed flow profile; the sedimenting suspension is allowed its own "imposed" flow
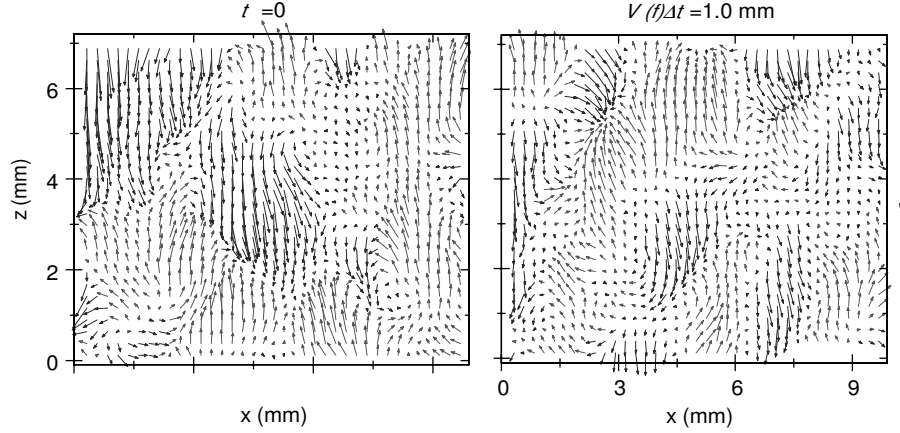
Figure 2.15: The local velocity field showing fluctuating regions in a sedimenting suspension of 50μm particles particle at Re $\approx 10^{-4}$, from [164].
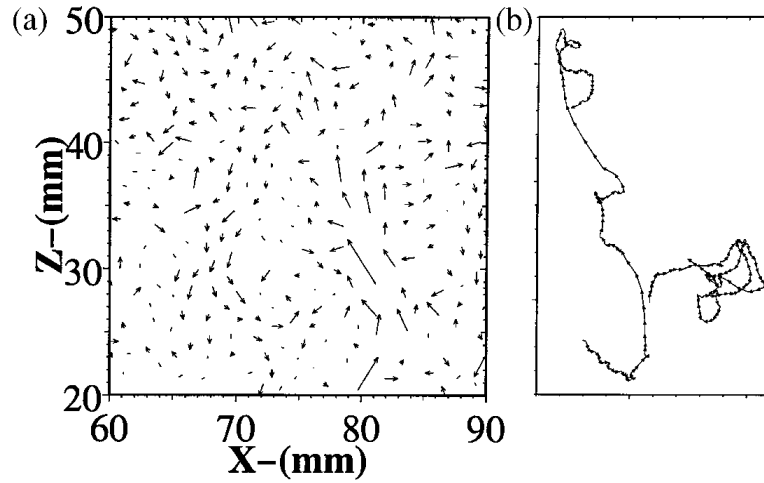
Figure 2.16: (a) A snapshot of particle velocities in a quasi-2D fluidized bed. (b) Time-traces of the motion of two different particles. The leftmost trace shows that particles can make rapid vertical excursions. From [155]

Work has been done in quasi-two dimensional fluidized beds at these Reynolds number [154, 155]. In these experiments, particle tracking was used to account for all particle positions at all times to study spatial correlations and obtain the velocity PDFs. A crossover in the shape of PDF was found as particle concentration was changed. Particles were found to behave superdiffusively in the vertical direction but obeyed normal diffusion in the horizontal direction, indicating that the particles undergo rapid vertical motions within the the fluidized state.

Work at higher Re and larger aspect ratio systems (3D beds) has been studied for over 50 years [41, 83, 93, 97, 109], but without the precision experiments which are currently being applied to sedimenting suspensions. Our experiments will help to fill that void. We will discuss 3D beds in more detail in the chapters on fluidized beds, and we postpone further discussion here.

2.3.3   Theories of multiphase flows

At low Reynolds numbers, $Re \ll 1$, theories have been developed to describe the interaction of few and many particles. Details are discussed in [86].

Interpenetrating fluids

There have been different attempts to create a hydrodynamic description of many-particle multiphase flow using interpenetrating fluids [92, 97], but none are tested with the rigor of continuum theories of dry grains. As none of the results from two-fluid models will be discussed in this dissertation, we will not discuss these theories.

Direct Numerical Simulation

Given the complication of the two-fluid models and lack of contact of with experiments, perhaps the best hope lies in direct numerical simulation. However, this is an extremely challenging problem due to the need to solve Navier Stokes with many moving boundaries. Techniques for calculation have been developed at low Reynolds numbers Stokes flows where computation called Stokesian Dynamics and have been shown very useful for simulation of colloidal particles [20, 61].

In a more sophisticated approach, a recent Grand Challenge project has developed techniques to solve Navier-Stokes equations in three dimensions in the presence of multiple moving boundaries. The goal was to develop general parallel code called particle movers. Using a numerical scheme called fictitious domain method [67], Pan *et al* have shown that a multiparticle-fluid (1000 particles) system at finite Re can be modeled [143] including fluidization and sedimentation. These results are impressive, see Figure 2.17, although quantitative comparison is in the early stages. Single particle results are promising, as seen in Figure 2.18, and should improve as computers get faster.

2.3.4   Industrial applications for multiphase flows

Finally, we should mention that fluidized beds have been studied industrially for over 50 years due to their importance in oil refining. For example, the Chevron refinery in Pascagoula, MS uses a fluidized bed catalytic cracker to process almost $200,000$
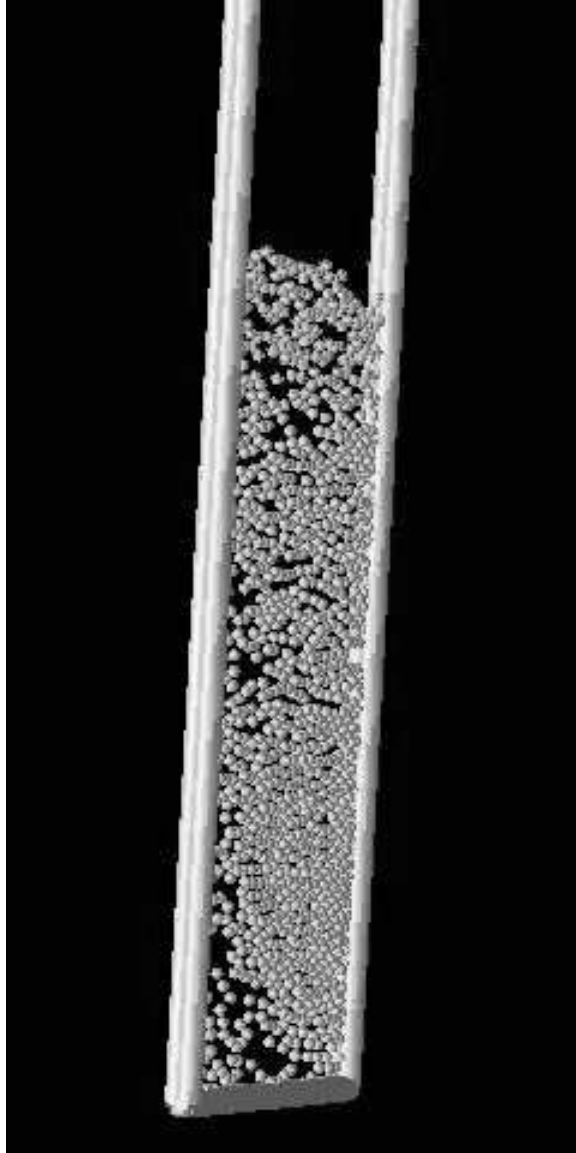
Figure 2.17: Direct numerical simulation of water fluidization of 1204 spheres confined to a narrow gap. Simulation by T.-W. Pan.

barrels/day. At 14 dollars a barrel, that is almost 10^9 dollars per year[5].

---

[5]Source: Chevron web site, `http://www.chevron.com/about/pascagoula/`
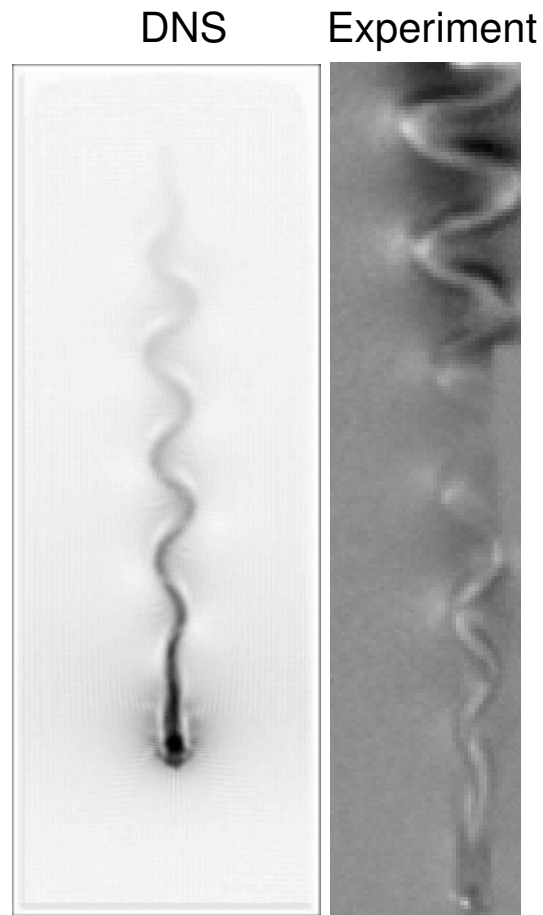
DNS   Experiment

Figure 2.18: Comparison of experiment and DNS results for the sedimentation of a single sphere within a fluid filled gap of 1.1 particle diameters. The agreement is quite good. Courtesy E. Ramos and T.-W. Pan

Chapter 3

Experimental apparatus and techniques

3.1 Introduction

This section describes the experimental equipment used to study two different problems in granular flow: the dynamics of wave patterns formed in a vibrated granular layer and the motion of grains at the onset of fluidization in a water fluidized bed. The experimental apparatus share little in common, other than that they are devices which fluidize granular materials in a controlled way. The bulk of the effort in both experiments has gone into minimizing inhomogeneity in forcing: in the vibrated layer experiment this consists of creating a system which shakes sinusoidally in only the vertical direction with minimal vibration in lateral direction while maintaining a controlled vibration acceleration. In the fluidized bed, the effort was put into ensuring a uniform flow velocity across the diameter of the column which houses the grains, without local inhomogeneities in the flow.

3.2 Vibrated granular layer experiment

In this section, I describe the system used to vibrate thin layers of granular material.

3.2.1 Mechanical details

A schematic of the shaker is shown in Figure 3.1. The system is designed to minimize lateral vibrations while ensuring precisely controlled vertical sinusoidal acceleration. I now describe the different components of the shaker.

Bronze spheres typically 165 μm are shaken in containers evacuated to 20 mTorr to avoid effects due to hydrodynamic interaction [142]. The vacuum is produced by a roughing pump and its level is monitored by a Granville-Phillips 275 Convectron convection gauge. The containers have bases made from Aluminum plates with Acrylic side-walls. As small grains can be strongly influenced by static charge effects due to the repeated rubbing against the side-walls, the walls are coated with an anti-static coating called Mar-Con developed by SciCron Technologies of Amarillo, TX. This coating con-

sists of a thin film deposited on the acrylic which contains tiny (< 1 μm) conducting spheres. For small particles, the application of the conducting film can alter the value Γ for the onset of waves. In addition, without the coating, a cloud of fluidized particles, presumably due to extra repulsion due to static effects, can appear above the surface of the waves.
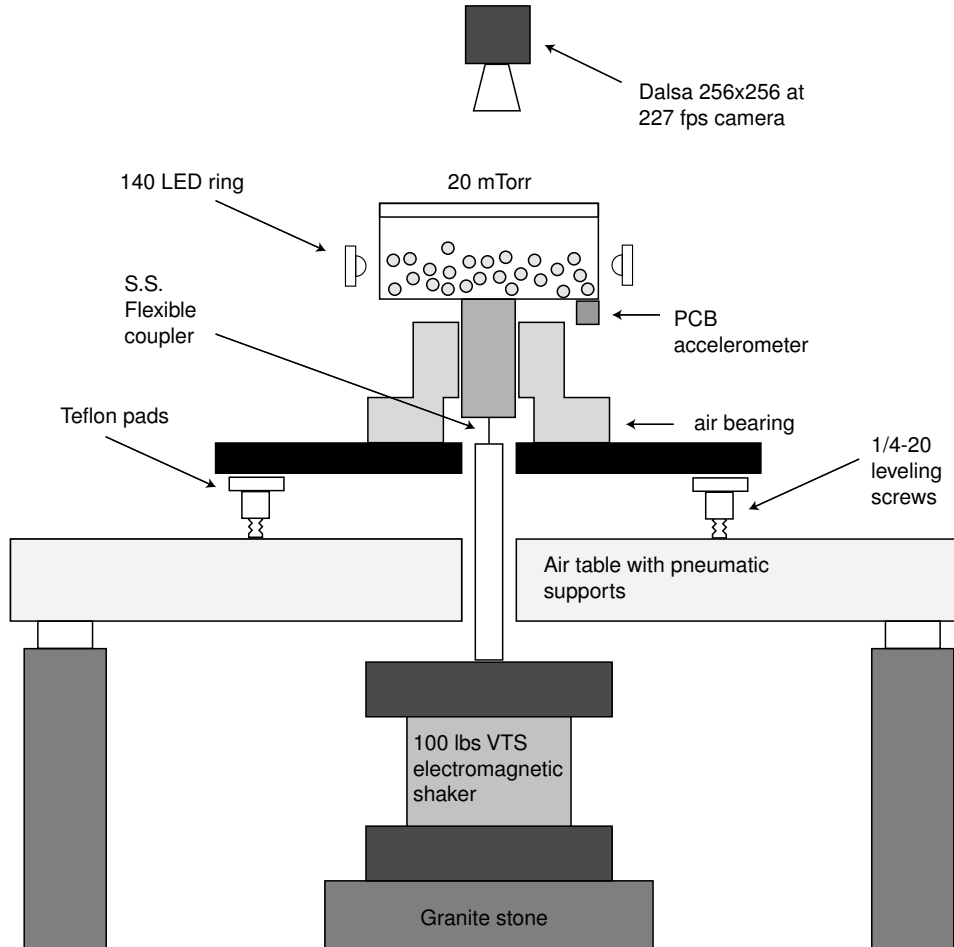
Figure 3.1: A schematic of the vertically vibrating granular layer apparatus. The diagram is not to scale. Each component is described in the text.

The heart of the system is a electromagnetic shaker (Vibration Test System 100) whose armature oscillates in a field produced by two permanent magnets and is critically damped with beryllium copper flexures: this produces undistorted sinusoidal vertical acceleration over a wide range of frequencies and accelerations. However, the small linear bearing in the VTS shaker is not sufficient to control lateral motions to the degree necessary in the experiment and thus a more sophisticated stabilization arrangement was developed.

A square-shaft low-friction square shaft air bearing (New Way Air Bearings) increases lateral stability of the shaking cell, see Figure 3.2. The cells are mounted to the bearing ram, a 10 cm long shaft with square cross section 2.54 x 2.54 cm. The ram slides in the square-bore shaft created by four precision aligned porous plates 8 cm in length. The porous plates are connected to a supply of gas (compressed dry N_2) through filters and the gas pressure is regulated to 50 Psi, although the exact pressure is not critical. The gas allows the ram to move almost frictionlessly without mechanical contact in the vertical direction while being extremely rigid in the lateral direction (70 N/μm, 0.1 μm of lateral travel per 1 cm of vertical travel).

square shaft air bearing
0.25 μm/2.54 cm
horizontal/vertical travel

Porous Al plate   2.54 cm

Dry air in
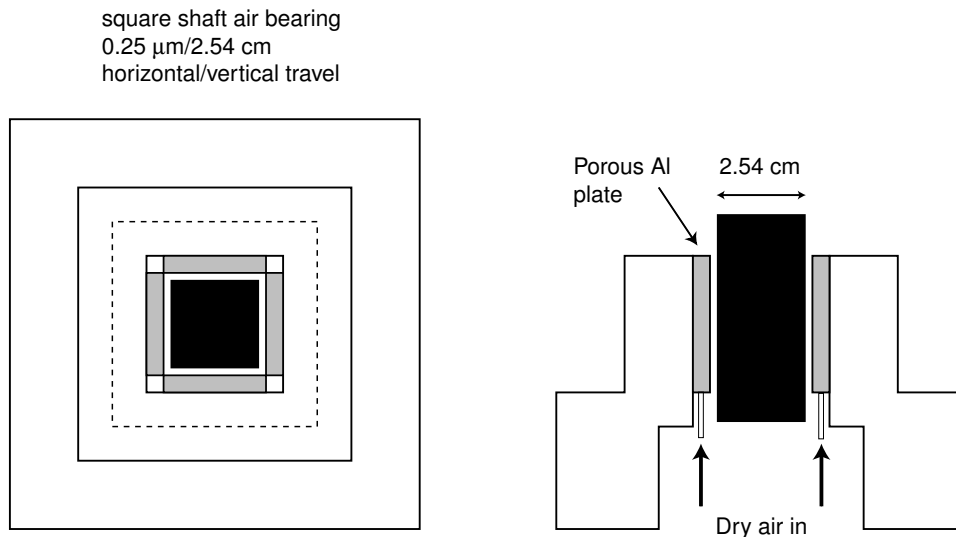
Figure 3.2: A detailed view of the air bearing assembly.

The stiffness of the shaker (flexures/linear bearing) is much lower (by a factor of approximately 10^3) than that of the air bearing. To avoid undue mechanical stress on the shaker and any lateral support of the air bearing housing, we use a flexible coupler to couple the ram to the shaker. This consists of a steel rod, 1 cm in length and 0.16 cm in diameter. The rod has a stiffness intermediate between the shaker and the ram and has a resonant frequency (10^4 Hz) which is much larger than any shaking frequency. The flexible coupler is connected from the shaker to the bearing ram and the housing of the air bearing is mounted to leveling plate which can be leveled by three screws. The screws are attached to a table which is floated on isolating pneumatic supports (Newport Corporation) to further reduce lateral coupling between the shaker and the container.

All of this aids in two problems. Without the square shaft bearing, due to lateral components of acceleration, the patterns can rotate in solid body rotation with periods

which can be less than a minute. Such rapid rotation produces boundary forcing on the pattern which can introduce defects. The addition of the air bearing increases the period of rotation to several hours, a time scale unimportant in the study of the phenomena described in Chapters 4- 6. We have also measured the lateral accelerations using a triaxial accelerometer (PCB 356A08) and the magnitudes are typically at the resolution of the device, 10 mg.

The second problem caused by lateral vibration is more severe: this is a resonance effect which causes the grains to heap in one direction toward the sidewall of the container (effectively changing their level) at higher frequencies. The current shaker design has reduced the severity of this effective de-levelling: below approximately 40 Hz, the level doesn't need to be changed once set. However above 40 Hz, the level must be adjusted as the frequency is changed. Since most of the work which will be described is below this frequency, this effect is unimportant. However, for controlled studies of patterns at higher frequencies, this problem needs to be addressed.

3.2.2 Control Electronics

A Stanford Research SRS 345 function generator drives a Techron power amplifier bridged to supply 500 Watts of power to the VTS shaker. The SRS generator generates a voltage from a lookup table and produces extremely pure sinusoidal functions. However, there can be significant drift in the output of the power amplifier and to account for this, we implement Proportional-Integral-Derivative (PID) Control on the acceleration of the container. The signal from the PCB accelerometer is input into a Metrabyte DAS-HRES A/D board digitizing with a resolution of 16 bit at 40 kHz. The computer computes the correction signal and applies a 0-5 VDC signal to a modulation input on the SRS of the form required for PID. PID control is a standard control technique and I will not describe the details of the implementation [125]. The control scheme maintains a stability of 0.1% in Γ over a period of hours.

As a side note, we control the modulation input of the SRS instead of communicating with the SRS through its serial interface. This is because the SRS uses relays to switch output ranges. When a relay switches, it creates a momentary 0 VDC. This is undesirable as it creates a short spike in the control signal. The spike disrupts the pattern and also causes the control to deviate from the set-point for a short time.

3.2.3 Frequency Modulation

In Chapter 5 we will describe experiments which study the response of square pattern to frequency modulation of the container drive frequency, f_d. We modulate the forcing of the shaker using the frequency modulation (FM) feature of the SRS shaker in

which the voltage has a form

$$y = A\sin(2\pi f_d t + \frac{f_{ms}}{f_{mr}}\sin 2\pi f_{mr}t) \tag{3.1}$$

which produces a frequency modulation of the drive signal f_d with modulation frequency (rate) f_{mr} and depth of modulation (span) f_{ms}.

As the SRS can only generate f_{ms} and f_{mr} in steps of 0.1 Hz, to conduct modulation sweeps with higher frequency resolution, we use a Intersil 8038 precision wave-generator. We drive the FM input of the 8038 with the unmodulated output of the SRS (which has resolution to 1 mv) ensuring stable frequency modulation. We do not perform PID control when the system operates in this mode, and the 8038 has a large enough thermal drift for this to be problem. However, since data are typically taken for only several hundred cycles, the acceleration can be monitored and corrected if necessary. This chip allowed us to perform high resolution "spectroscopy" of patterns, in steps of 10^{-3} Hz.

3.2.4 Illumination and imaging

The lighting in the system is controlled by a phase-locked loop circuit designed by Paul Umbanhowar, and the details of the circuit are discussed in his thesis [182]. The circuit produces output pulses of 1/100 duty cycle phase locked to the signal from the SRS generator. The phase in the oscillation cycle can be adjusted and the strobing frequency can be a multiple 2^n of the drive frequency, useful for study of patterns which respond at different multiples of the drive frequency. The phase locked loop drives a power transistor, operational amplifier feedback circuit (see Figure 3.3) which produces constant current pulses to a circular ring of 120 red LEDs wired in parallel with opening angle of 45 degrees. This ring is placed so that the grains are illuminated at low angles and causes high regions to be brightly lit and low regions to be dark.

We image the layer using a DALSA-CAD256 8 bit digital camera, 256x256 pixels at 227 frames/sec with an Imaging Technology frame-grabber. The camera has no trigger input, so it is synced to the strobe light in software by acquiring frames when a light threshold is reached in each frame. As the strobe frequency and camera pixel clock frequency are incommensurate, this can lead to frames in which there is very little light (frame straddling) and we must correct for such frames by discarding them in post-processing. All image processing is done in the Matlab development environment.
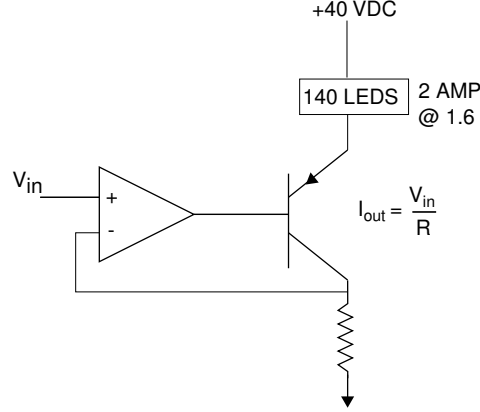
Figure 3.3: A constant current LED driver circuit. The feedback loop maintains a constant current set by the voltage of the incoming pulse, V_{in} and the load resistor, R.

3.2.5 Rapid Γ change experiments

In chapters 4- 6, we study pattern formation after a sudden change in the acceleration of the container. The experiment must jump at precise and repeatable accelerations during the cycle. Because the inductive shaker oscillates with a frequency dependent phase lag (LEAD) relative to the drive signal, we monitor the phase of the acceleration using a Schmidt trigger set to output a positive-going pulse when the acceleration signal crosses a certain threshold. These pulses are monitored by an input line on the parallel port of the PC, allowing for msec resolution of phase detection. The accelerometer signal is recorded by the A/D board, and written to disk at 40 kHz for the duration of the experiment.

3.3   Fluidized bed apparatus

In this section, I describe the experimental details of the fluidized bed experiment. The experiment requires that a collection of grains, packed into a tube of square cross section, receive a flow of water that is precisely controlled in time and spatially homogeneous. As equilibration times in the system can be long, the experiment must maintain the desired flow characteristics over a period of days. We have designed a system that satisfies these conditions and I will describe the system below. A block schematic diagram illustrating all of the elements of the experiment is shown in Figure 3.4.
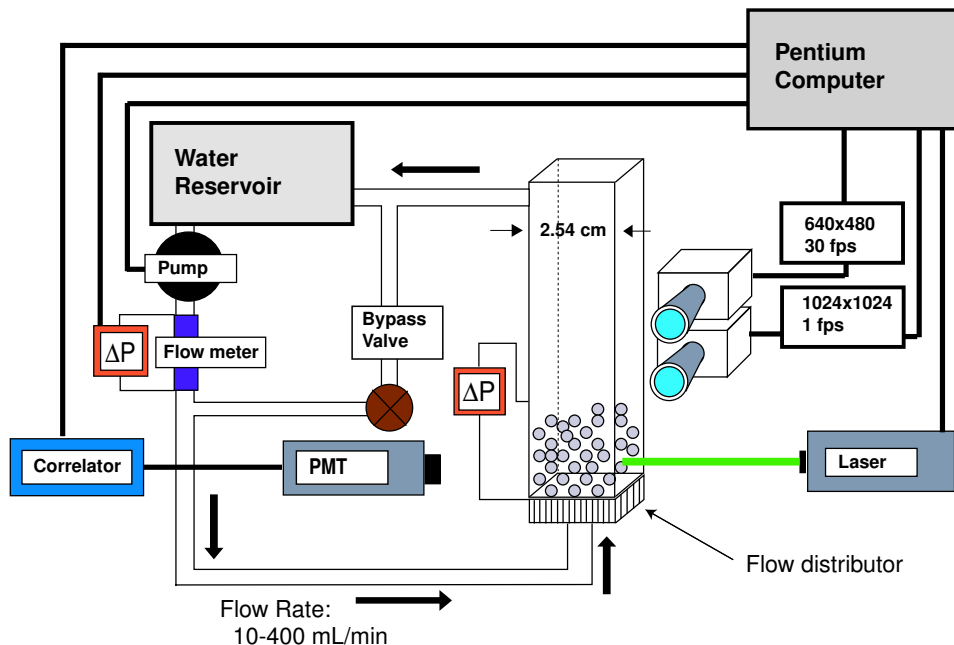
Figure 3.4: A block diagram of the fluidized bed flow apparatus. The different elements of the experiment are described in the text.

3.3.1   Flow distribution

The most important element of a fluidized bed is the flow distribution element, the distributor. The purpose of the distributor is to create a uniform flow profile at the entry to the bed. Distributors in laboratory experiments are often constructed from multiple layers of uniform mesh or single pieces of porous plate. However, the design of distributors is still more an art than a science, with different groups using different designs and materials. This artistry is unsatisfactory, as there is evidence that the distributor design can strongly influence fluidization phenomena. For example, it has been shown

that bubbling (and the size of bubbles) depends strongly on the distributor pore size [43]. In the most complete study to date, analysis and preliminary experiments were conducted to study the stability of fluidization to large scale circulation as a function of the pressure drop through a distributor [97]. However, comparison to experiment was hampered by the lack of flow distributors with sufficiently uniform flow profiles. Furthermore, these studies do not address the question of the specific designs; in recent years, very few systematic studies have been done to test different designs [43, 109]. We hope that the designs discussed below will be useful contribution. Our experiments are very sensitive to slight flow inhomogeneity and our distributor design reflects this constraint. Two designs have been used and tested, and schematics of the different fluidized bed designs are shown in Figure 3.5 and Figure 3.7. The beds and control apparatus discussed here are designed for fluidization of $0.1 - 1$ mm glass spheres with density of roughly 2.5 g/cm^3.

The design shown in Figure 3.5 uses several layers of precision mesh screening to achieve uniform flow distribution. A double layer of mesh is pulled tight by o-rings across a square opening. The o-rings are pressed on by a block which holds the square bore glass tube. The bottom mesh is nylon screen (Nitex precision mesh, Sefar America, Kansas City, MO) with 5 μm holes and 0.75% open area, (see Figure 3.6) and the top layer is 635 stainless steel mesh (TWP Inc, Berkeley, CA) with 20 μm holes and 26% open area. The nylon mesh creates the bulk of the pressure drop (up to 70 kPa) through the distributor while the stainless steel mesh supplies the rigidity. Both meshes have excellent uniformity and the only difficulty is creating a reliable joint between the mesh and the walls. We have found that the flow characteristics of the device using the mesh technique depends sensitively on the sealing between the edge of the tube and the mesh. Because of the flexibility of the mesh, a nonuniform clamping pressure around the perimeter of the tube produces fast-moving jets of water at fluidization which persist far above onset creating streaming jets in the fluidized bed.

These jets are undesirable and influence studies of the fluidization of different packings of grains near the onset of fluidization. For loose packings, the jets locally fluidized regions and allow the system to re-pack at a higher volume fraction. This produces a measurable drop in bed height before fluidization. For tight packings, the jets tend to expand the bed prior to fluidization and this produces a rounding of the fluidization transition. The location and strength of the jets are sensitive to the clamping and construction procedure and while with enough repetition a bed can be assembled which does not suffer from the above problems, we have surged ahead looking for a more robust design. We note that work on the stability of fluidized beds has shown that beds become unstable to large scale circulation if the ratio of pressure drop through the distributor to the pressure drop through the bed is less than about 10 [97]. In our fluidized beds with mesh distributors, the pressure drop across the distributor is typically 30-50 kPa, a factor of 20-40 times greater than the pressure drop across the bed.
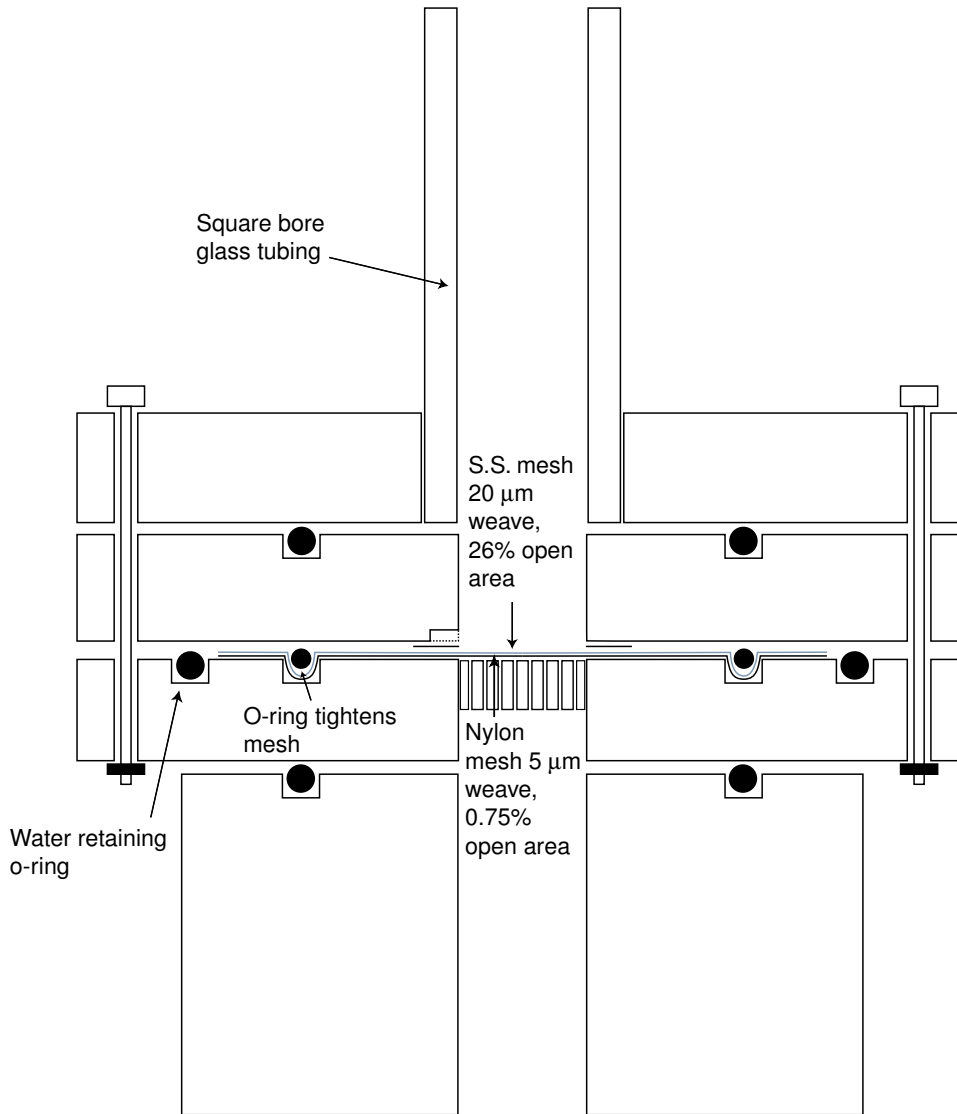
Figure 3.5: The schematic of the fluidized bed which using different meshes as flow distribution elements.

A more robust design uses a distributor made from a 2 mm thick porous glass plate manufactured by Collimated Holes, Inc. of Campbell, CA. The plate is made from an array of optical fibers which are bundled and fused together. The fibers have cores and cladding which are made of different types of glass and after bundling, the core glass is etched away leaving a hexagonal array of 10 μm holes arranged on approximately 15 μm centers. As the plate is 2 mm thick, it is very rigid. See Figure 3.8 for magnified image of the plate.

From our studies with the mesh distributors, we have found that the design of the
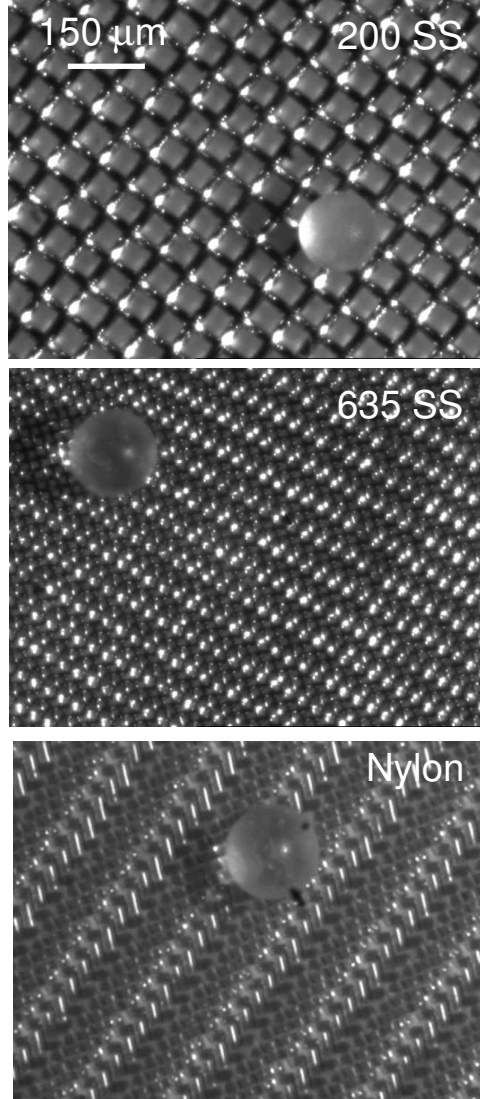
Figure 3.6: Different meshes used as flow distribution elements. A combination of stainless steel and nylon mesh produces a uniform flow distributor. A 100 μm glass sphere is shown for scale reference.

mounting of the plate is as important as the design of the plate itself. Therefore the plate is bonded between two exactly matched glass tubes, the downstream side long enough to ensure a uniform profile of fluid impinging on the distributor plate. The bonding was done using UV curing epoxy which wicked into the joint and was hardened before reaching the inner edge of the walls. All construction was done by Collimated Holes, Inc.

The entire apparatus is bonded to an acrylic flange using waterproof Devcon 2-ton epoxy. The flange mounts to another homogenizing section which is mounted to
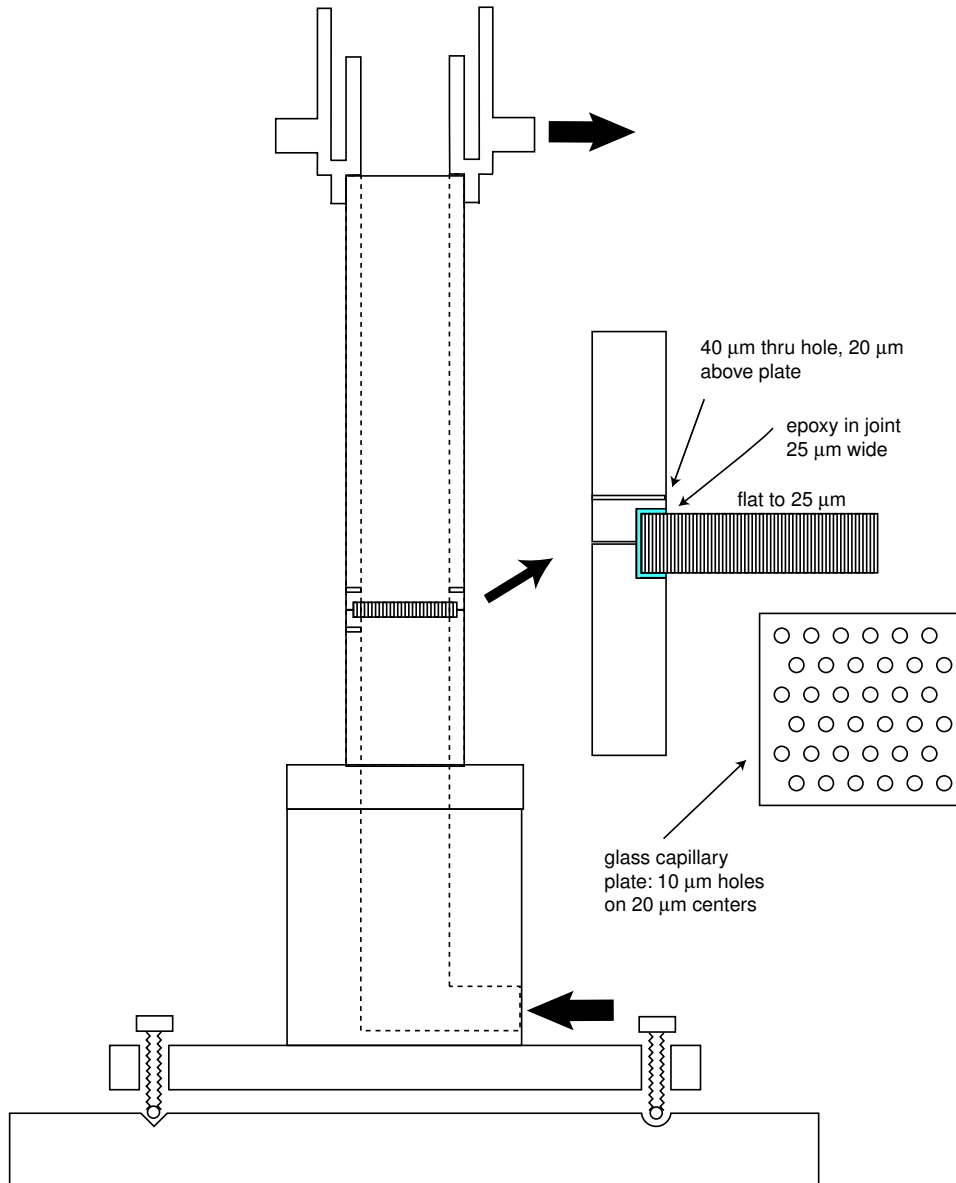
Figure 3.7: Schematic of a fluidized bed using a porous glass plate as a distributor manufactured by Collimated Holes, Inc. The plate is bonded between two matched square-bore glass tubes.

a kinematically mounted leveling plate. The flow accumulates in an overflow bucket ensuring a constant height upper boundary condition.
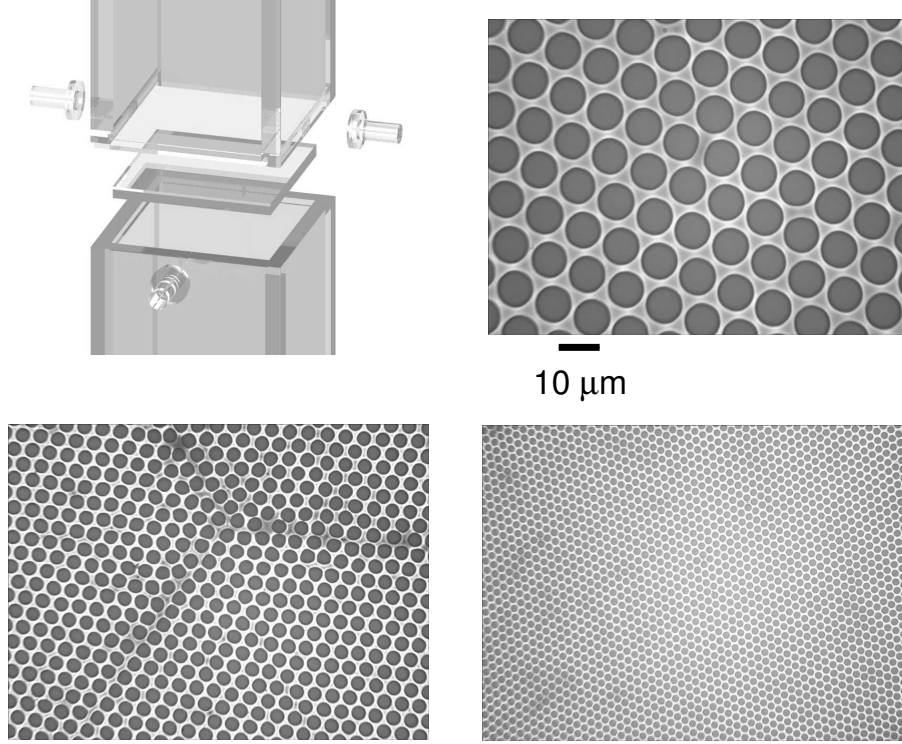
Figure 3.8: Clockwise: An exploded view of the bed with capillary plate distributor. A top view of the 2 mm thick capillary plate. A view with less resolution. A section of the plate with a defect boundary.

Possible improvements in distributor design

The pressure drop across the porous plate distributor is about a factor of two greater than the pressure needed to support the bed. As there is some debate on the effect of the pressure drop in the distributor on the stability of the fluidized state, it would be useful to be able to vary this pressure drop. A possible improvement of the design is shown in figure 3.9. This design would allow different pressure drops to be created while maintaining the rigidity and wall-plate precision of the porous plate. It would consist of two matched sections of square bore tubing sandwiching a piece of mesh and different weaves of meshes would control the pressure drop.

3.3.2 Pressure measurements

In both designs, (Figures 3.7 and Figure 3.5), the pressure drop due to fluid passing through the bed is measured by differential pressure transducers (details of the transducers are discussed below). In fluidization, the pressure drop is always less than or equal to the buoyant weight of the bed. In our experiments, this is typically 0 to 1500
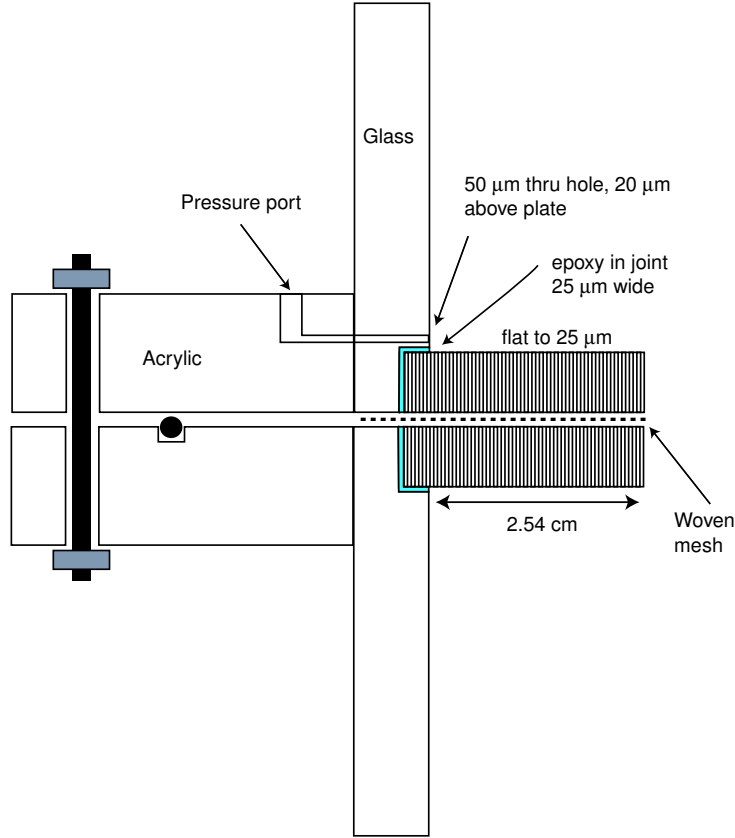
Figure 3.9: Schematic of a proposed fluidized bed using a porous glass plate to sandwich mesh. Different meshes would be used to vary pressure drop across the distributor.

Pa. In the mesh design, the pressure is measured through a 75 μm slot directly above the distributor. In the capillary plate design, the pressure directly above the distributor is measured through a 50 μm hole 20 μm above the base of the distributor.

3.3.3 Flow system

Steady stable flow in time is crucial for controlled studies near the onset of fluidization. We have developed a fluid flow control system to maintain precisely and accurately controlled steady flow rates from 0 to 200 mL/min over periods of hours. An example of the controlled flow over typical measurement times (30 seconds) is shown in Figure 3.10. Measurements over much longer times look similar. The flow is controlled by a Micropump pump which is magnetically coupled to a DC motor. To sense the flow, we use a Validyne DP-15 differential pressure transducer which measures the pressure drop across a section of pipe. The high sensitivity, stability and time response make this an ideal flow

sensing element. The transducer forms one arm of an AC bridge and measures deflection of a stainless steel diaphragm by changes in inductance in a pickup coil. The range of the transducer can be set by changing diaphragm thicknesses, but we find it more convenient to measure in different flow rate ranges by changing the length of the pipe across which the flow is measured. These elements are incorporated into a PID loop using a Pentium computer and a Metrabyte DAS-HRES A/D board. The accuracy of the pressure gauge is 0.25% and has a sensitivity of 0.6 Pa for the diaphragm used in our experiments. The length of the pipe and the sensitivity of the device determine the overall sensitivity of the flow measurement, and for a pipe of length 30 cm, we can detect flow rate changes as small as 0.05 mL/min. To convert to flow rate in mL/min, we calibrate the transducer arrangement against a McMillan 101-4TP paddle wheel-type flow meter (McMillan Company, Georgetown, TX), accurate to 1%. With the arrangement described, we can maintain high flow stability for the typical ranges in the experiments, $0 - 100$ mL/min over periods of hours and days.
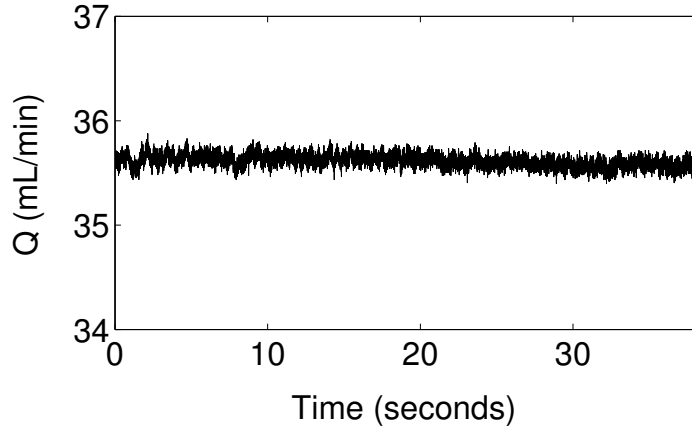
Figure 3.10: The flow measured under control at $Q = 35.61$ mL/min for 30 seconds. The RMS deviation around the mean is 0.2%.

An ASCO three way valve is used to pulse flow to the bed and create different bed packings (see Chapter 8).

3.4 Measurements and characterizations of grain behavior

We use a variety of techniques to characterize the behavior of the bed, including high resolution imaging to measure the average volume fraction, differential pressure measurements to measure the pressure drop across the bed and light scattering techniques to measure small length scale motions of the grains. In this section I describe each.

3.4.1 Pressure measurements

We measure the pressure drop developed across the bed using another Validyne pressure sensor between a port slightly above the bottom of the bed and a point above the bed. The position of the second pressure port is not critical as the effect of pressure head is canceled since the ports of the transducer at the same level. The only effect of the position of the second port is due to drag force along the square tube. We neglect this contribution as for the large bore tubing used in the bed, the drop is not a measurable within the sensitivity of our transducers.

3.4.2 Volume fraction
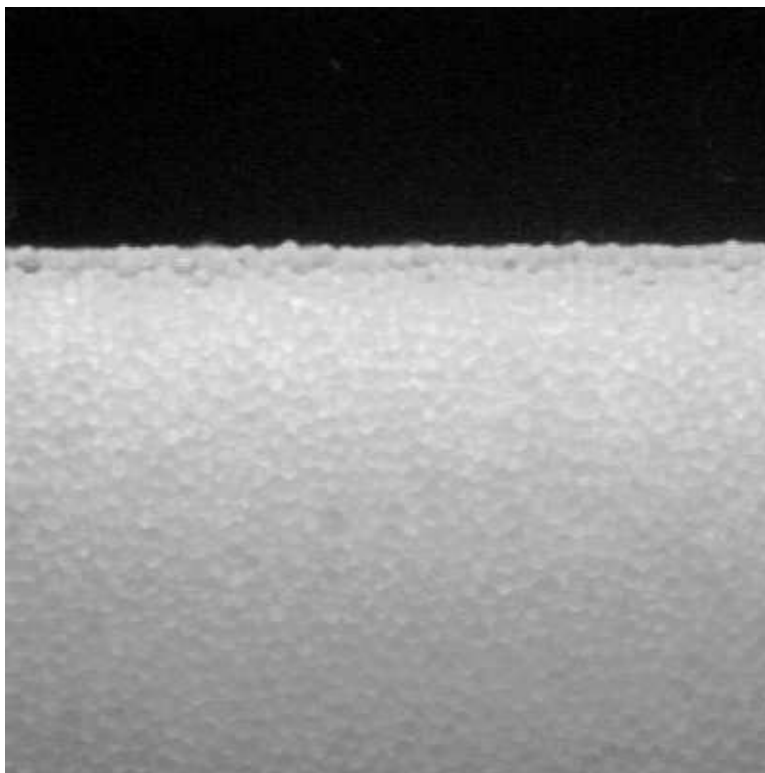
Figure 3.11: The voidage, $1 - \Phi$ is computed from high resolution images of the bed. A top section of a bed of 335 μm glass spheres, 2x2 cm^2 is shown

The average voidage of the particles $1 - \Phi$ is determined from high resolution images of a face of the bed using a 1024x1024 10 bit Xilix camera. Since the interface in the bed in our experiments is always flat (see Figure 3.11), we average horizontally. Using this technique, we can achieve resolution of 5 μm, a factor of 20 to 200 smaller than a particle diameter. For a bed of cross-sectional area A, the height of the bed h is

49

converted to volume fraction by a measurement of the total mass m_p of the particles and their density ρ_p by,

$$1 - \Phi = 1 - \frac{m_p}{\rho_p A h} \tag{3.2}$$

The average densities of the glass spheres are accurately measured by immersing particles of known mass in a tube filled with water and measuring the increase in height of the water with the high resolution camera. The density for 300μm glass spheres is 2.56 g/cm³

3.4.3   Light scattering techniques

To study the motion of the grains in the fluidized bed, we study the intensity fluctuations of laser light transmitted through the transparent particles. A schematic of the light scattering is shown in Figure 3.12. Coherent light from a laser is incident normal to one face of the glass fluidized bed chamber. The light beam is expanded by a lens to avoid local heating effects. The light enters the sample, undergoes multiple scattering events from the glass spheres, and emerges from the opposite face where it is collected by a photomultiplier or a CCD camera.

The light accumulates phase proportional to the length of the path it travels through the scattering medium. The intensity at a point in space is the square of the sum of the fields from all paths which reach that point. For a collection of random scatterers, the interference results in a spatially random pattern with regions of bright and dark. These bright and dark regions are called speckles and are analogous to the fringes in an interference pattern from regularly spaced array of scatterers. An image of a speckle pattern is shown in Figure 3.13. In the scattering experiments, the optical setups are such that a detector images a single speckle, called a coherence area.

Motion of the scatterers changes path lengths, and the interference from these changing paths creates a fluctuating speckle pattern. Thus, measurement of the the intensity fluctuations in a coherence area gives information about the motion of the scatterers. The great advantage of the multiple scattering techniques is that they are extremely sensitive to small particle motions. Since there are typically several hundred particles involved in the scattering of the light, each must only displace a small amount for the total phase of the light to change by π (the path lengths by λ). Thus, the time evolution of the speckle fluctuations gives a high resolution measurement of particle motion. For example, we can detect motions as small as 1 nm for a tube with cross section 2.54 x 2.54 cm containing 300 μm particles.

As Figure 3.12 illustrates, we study the time evolution of the speckle pattern in two ways. The first is a light scattering technique called Diffusing Wave Spectroscopy
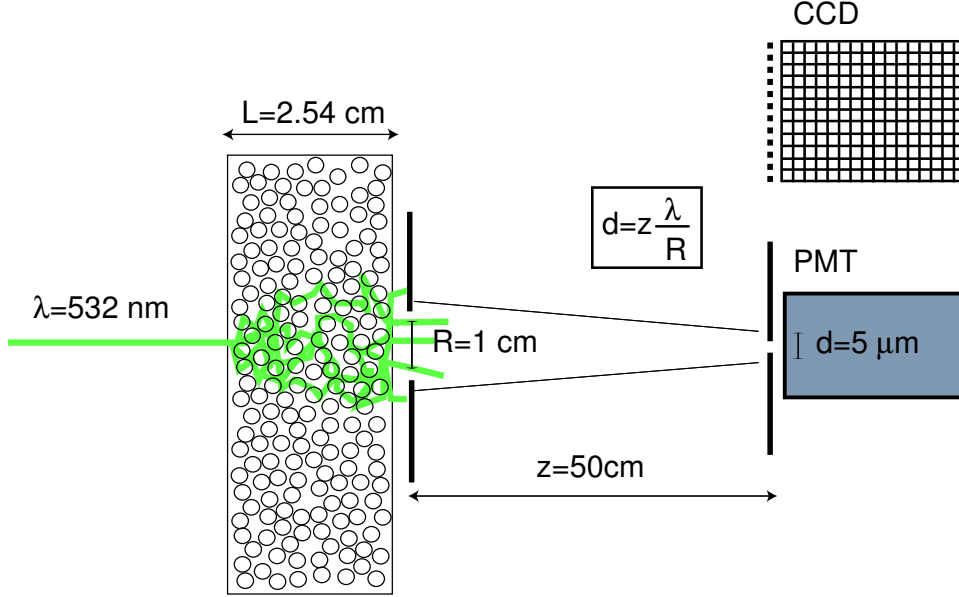
Figure 3.12: The scattered light in the experiment is detected by either a PMT or a CCD camera. The pinhole in front of the PMT images one coherence area, whereas each element of the CCD, 10x10 μm, images slightly less than one coherence area. A side-view of the CCD is shown.

(DWS) [144]. In DWS, the scattered light in a single coherence area is collected by a photomultiplier tube, shaped by a combination amplifier/discriminator and fed into a autocorrelation computer card, Flexible Instruments Flex 30. The autocorrelator calculates the intensity autocorrelation function $g^{(2)}(\tau)$ using the multiple tau method [159], filling channels spaced logarithmically in time. The correlator has time resolution (minimum bin size) of 0.1 μsecond.

The theory of DWS is used to calculate the ensemble averaged mean square displacement of the particles, MSD $= \langle \Delta R(\tau)^2 \rangle$, from the measured temporal correlation function $g^{(2)}(\tau)$. We will discuss the theory of DWS in more detail in section 3.5.

Another technique, essentially an extension of DWS, involves imaging multiple speckles onto a 8 bit 640x480 CCD [190]. In the multispeckle technique, the optics are arranged such that each CCD element (pixel) records a single speckle coherence area[1]. Each pixel records the intensity fluctuations from statistically independent scattering

---

[1]For the inspiration behind this technique, see experiments on multispeckle DLS, see [101, 195]
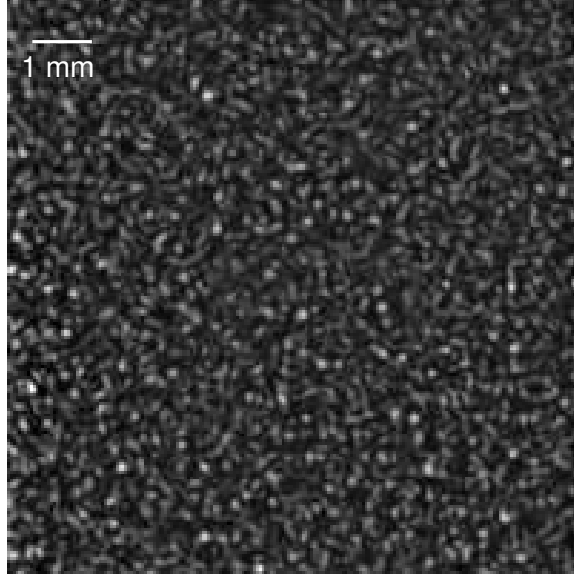
Figure 3.13: The speckle pattern created by random scattering of coherent laser light from collection of 335 μm glass spheres.

events, and thus by proper averaging, we are able to boost signal to noise at long delay times. However, due to the relatively slow speed of the CCD camera used, (30 Hz, with shutter time roughly 30 msec), we are not able to resolve the short time dynamics. However, by recording the CCD images to disk for long times (up to two hours), we can use this technique to study transient grain rearrangements and motions.

Collection optics

The mean size of the bright and dark spots is called a coherence area and can be thought of as the average size over which a region of light will be coherent. As seen in Figure 3.12, it is calculated from,

$$d = z\lambda/R \qquad (3.3)$$

where z is the distance from the scattering volume, λ is the wavelength of light and R is the characteristic dimension of the aperture. Equation 3.3 sets the geometry of the collection optics, insuring that the detector images only a single coherence area. In fact, the DWS measurements provide a measure of coherence area by the value of the correlation curve at $\tau = 0$. This will be discussed when experimental results are presented, in section 3.5.3 and Chapter 8. In our setup, the collection optics consist of a 1 cm aperture, a 30 cm long tube with a blackened interior, and a 50 μm pinhole placed

in front of the PMT. The inside of the tube is blackened to prevent the absorption of stray reflected light. The length of the tube chosen such that the speckle is the size of the pinhole. In the multispeckle technique each CCD element measures 10x10 μm, imaging slightly less then one coherence area; we simply use the aperture and the tube length to set the speckle size to be the size of the CCD element.

Practical considerations

The multiple scattering scatters light into all solid angles. Thus, to ensure good statistics, the laser source must have high enough power so that enough photons are collected in the small detector angle. We find that for DWS of colloidal particles, sampling times of 30 seconds require laser power of roughly $100mW$ to ensure smooth correlation functions. For 300 μm spheres in water, the power must be increased to 1 Watt. The high power concentrated in the 2 mm beam diameter can cause significant heating of the medium; we often expand the beam with lens to reduce this effect. The laser must also have a coherence length which is longer than any scattering path length. This ensures that the de-phasing of the light, the source of the fluctuating intensity, is only due to fluctuations in the positions of the scatterers. We use a Coherent Verdi 532 nm laser with a linewidth of less than 5 MHz. This creates a coherence length of 60 m, much greater than any path length in the sample. The power output of the laser is controlled to 1% over hours.

These multiple scattering spectrospcopy techniques are sensitive to motions as small as 1 nm. Thus, to eliminate external perturbation and vibration, the system is placed on a Newport Optical table.

3.5 Diffusing Wave Spectroscopy (DWS)–theory and measurements

As described above, DWS probes small length-scale motions over short time-scales by measurements of the autocorrelation of intensity fluctuations of transmitted photons. We now describe the theory of DWS. To test the theory and our apparatus we also present measurements of diffusive behavior of small 0.596μm colloidal particles. We will present data for application to the larger glass spheres of the fluidized bed in a Chapter 8.

3.5.1 Multiple scattering theory-essential physics

The goal of the measurement of scattered light is to relate the motion of the scatterers to the measured decay of correlation of intensity fluctuations, $g^{(2)}(\tau)$. At a given instant in time at the detector, the field is the sum of the electric fields of all light paths. This field will change (and thus the intensity fluctuate) due to changes in scattering paths by the motion of the particles. To calculate the detected field, we need to do a double sum. First, we must find an expression for the phase $\phi(t)$ accumulated by a photon traversing a path p of length $s(t)$ as it scatters N times through the medium. This requires a sum over the positions of the scatterers in the path. The second sum requires that we sum over all possible paths from source to detector. Now, the motion of the particles creates a time-dependence in the length of the path, $s(t)$, and thus the phase accumulated in the path acquires a time-dependence. Thus, we will calculate how the total phase for that path changes as the scatters move. The final sum can be thought of as the sum over the change in phase weighted by the probability that a path of length s suffers that change in phase. Therefore, we need an expression for the probability of light to travel through the medium along a path of length s. This will be denoted $P(s)$.

Each path of length s will contribute a decay to $g^{(2)}(\tau)$ which can be thought of as the characteristic time it takes for the phase of that path to change by π. If there were only one path through the medium, this would yield the decay of the correlation function immediately. However, there are many paths and each contributes a different decay rate to the electric field intensity. Thus the final decay function will account for these contributions. They will contribute in proportion to the relative probability for light to travel that path, $P(s)$. Paths which are more probable more strongly influence the time-scale of the decay.

The contribution to the decay of $g^{(2)}$ for a single path will be calculated in the next section. For diffusively moving scatterers, with trajectories which are random walks over long times, it decays almost exponentially in time. To calculate the path length probability function, DWS relies on the assumption that in a sufficiently scattering medium, the intensity of light follows a diffusion equation. To make this connection we use the

fact that the light moves *much* faster than any of the scatterers; the diffusion coefficient of diffusing light is written $D_l = vl^*/3$, where v is the average velocity of light (transport velocity) in the medium [183]. For example, in a dense colloidal suspension, D_l is typically 10^{16} larger than the diffusion coefficient of a typical colloidal particle. Thus, on a sufficiently short time-scale, we can view the problem as transmission through a collection of static scatterers. The light scatters with a mean distance between scattering events of l. After the light has undergone enough scattering events, characterized by a total path length l^*, the direction of the light is uncorrelated with its original direction. Averaged over this scale, the photons look as if they are diffusing, and the diffusion equation can be used to calculate the intensity profile of the light in the medium. Since the number of photons emerging from a point is related to the length of the path that it took for those photons to diffuse to the point, this relates $P(s)$ to the intensity calculated from the diffusion equation.

In our experiment, $l^* > l$ and $L \gg l^*$. Typically $L \sim 2.54$ cm, $l \sim 100$ μm, and $L/l^* \sim 20$. On average, light undergoes $\approx (L/l^*)^2$ scattering steps with l^*/l scattering events per step, so the light is scattered $\approx (L/l^*)^2 l^*/l$ times by the time it emerges. This multiple scattering ensures that the propagation of the light will be diffusive and this approximation is crucial for the validity of DWS.

There is an interesting difference between media which multiply scatter and those that do not. Consider the transmission coefficient, T, of a plane wave incident on scattering medium of length L. If $L < l$, most of the light is unscattered, and $T \approx \exp(-L/l)$. If $L \gg l^*$, none of the light is unscattered. It is transmitted diffusively and $T \approx l^*/L$. The transmission measurement is a useful check to determine whether we can use DWS. We will use this formula later to compute the value of l^*.

3.5.2 Multiple scattering-calculations

In this section, I outline the basic theory for calculation of the ensemble averaged MSD from temporal correlation of scattered light. The calculations in this section follow Weitz [192].

Correlation functions and changes in field

Since we seek to calculate an expression for the electric field at the detector due to scattering, it would be convenient to measure the electric field at a point and perform the correlation of the electric field, $g^{(1)}(\tau)$,

$$g^{(1)}(\tau) = \frac{\langle E^*(t)E(t+\tau)\rangle}{\langle E^*(t)E(t)\rangle} \tag{3.4}$$

However, this is difficult due to the high frequency of visible light. Instead, we detect the intensity of the scattered field, $\bar{I} = \langle E^*(t)E(t) \rangle$, where the average is taken over many cycles of the field oscillation. From this intensity signal, the intensity autocorrelation function $g^{(2)}$, called the degree of second order coherence, is calculated from

$$g^{(2)}(\tau) = \frac{\langle \bar{I}(t)\bar{I}(t+\tau) \rangle}{\bar{I}^2} \tag{3.5}$$

For intensity fluctuations which are rapid compared to the time scale of measurement, $g^{(2)}$ and $g^{(1)}$ are related by the Siegert relation,

$$g^{(2)} = 1 + \beta|g^{(1)}(\tau)|^2 \tag{3.6}$$

where β is a number related to the optical arrangement of the system: detection of one coherence area or less yields $\beta = 1$ and $g^{(2)}(0) = 2$ for polarized light, while for unpolarized light, $\beta = 0.5$ and $g^{(2)}(0) = 1.5$. We now outline the calculation $E(t)$ for light transmitted through many scatterers.

A calculation of $E(t)$ relates to the experimentally obtained $g^{(2)}$ to the mean square displacement of the particles. As described physically above, the calculated field will be a sum over the paths p which have accumulated a phase $\Phi(t) = k_0 s$ during the transit time t on a path of total length $s(t)$ through the sample. Here k_0 is the wavevector of the light, with $k_0 = 2\pi/\lambda$. At time t, the electric field at the detector $E(t)$ is the sum over all paths which reach the detector and can be written,

$$E(t) = \sum_p E_p e^{i\Phi_p(t)} \tag{3.7}$$

where E_p is the amplitude of the field from path p and $\sum_p$ represents the sum over all paths. To connect with experiment, $E(t)$ is inserted into Eq. 3.4. Assuming that photon paths are uncorrelated, it can be shown that,

$$g^{(1)}(t) = \sum_p \frac{\langle I_p \rangle}{\langle I \rangle} \langle e^{\Delta \Phi_p(t)} \rangle \tag{3.8}$$

where $\langle I_p \rangle \equiv \langle |E_p|^2 \rangle$ is the average intensity of the path p. Thus, two quantities must be calculated to turn this into a useful method. $\langle I_p \rangle$ will be calculated later using the diffusion of light approximation. $\Delta \Phi_p(t) = \Phi_p(t) - \Phi_p(0)$ is the phase shift in time due motion of the scatters and we calculate it now.
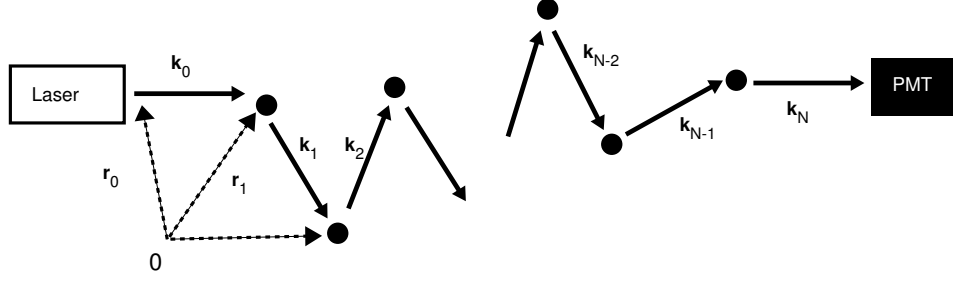
Figure 3.14: A typical scattering path used to calculate the change in phase of the light.

Phase change in a path

We must first calculate the change in phase of scattered light as a result of particle motion. Figure 3.14 shows the basic physics of the scattering. The total path length, s, of light which scatters elastically ($|k_n| = k_0 =$ constant) N times on a trip through the medium can be written,

$$s = \sum_{i=0}^{N} |\mathbf{r}_{i+1} - \mathbf{r}_i| = \sum_{i=0}^{N} (\frac{\mathbf{k}_i}{|\mathbf{k}_i|}) \cdot (\mathbf{r}_{i+1} - \mathbf{r}_i) \qquad (3.9)$$

and from this equation, we calculate the total phase change for a given path,

$$\Phi(t) = \sum_{i=0}^{N} \mathbf{k}_i \cdot [\mathbf{r}_{i+1} - \mathbf{r}_i] \qquad (3.10)$$

The main result of this calculation, obtained after averaging over many particles, is that for a path through the sample of total length $s = Nl$ with $N \gg 1$, the mean squared change in phase for the path can be written,

$$\langle \Delta\Phi_p^2(t) \rangle = \frac{2}{3} k_0^2 \langle \Delta r^2(t) \rangle \frac{s}{l^*} \qquad (3.11)$$

This equation relates the mean squared phase change of the light to the mean square displacement of the particle motion. Physically, it says that for large path lengths, the phase undergoes a large change, as many moving scatterers contribute. As an example which will be discussed later, the motion of diffusing colloidal particles follow $\Delta r^2(t) = 6Dt$, where D is the self diffusion coefficient. In this case the change in phase would be written as,

$$\langle \Delta\Phi_p^2(t) \rangle = 4k_0^2 Dt \frac{s}{l^*} \qquad (3.12)$$

We will verify this later for colloidal particles, using the formula as a test of the experimental technique.

Sum over all paths and calculation of $P(s)$

We now insert our expression for $\langle \Delta \Phi_p^2(t) \rangle$ into Equation 3.4, and sum over path *lengths*. Rewriting Equation 3.4 in terms of $P(s)$, the fraction of scattered intensity in a path of length s, instead of $\langle I_p \rangle / \langle I \rangle$, we obtain,

$$g^{(1)}(t) = \sum_s P(s) \exp\left(-\frac{1}{3} k_0^2 \langle \Delta r(t)^2 \rangle \frac{s}{l^*}\right) \tag{3.13}$$

This is the main result of our calculation, and it relates the decay of $g^{(1)}$ to the motion of the scatterers. Thus, if this equation can be inverted, the mean square displacement of the particles as a function of time can be directly obtained. For experimental data, $g^{(1)}$ can be obtained from $g^{(2)}$ using Equation 3.6; numerical inversion of Equation 3.13 will give the desired $\langle \Delta r(t)^2 \rangle$. To proceed, however, we must have an expression for $P(s)$. The calculation of $P(s)$ is where the diffusion approximation is used. We assume that the light undergoes a large number of scattering events, and on length scales much larger than l^*, we write the diffusion equation for the energy density of light, U (number of photons per unit volume):

$$\frac{\partial U}{\partial t} = D_l \nabla^2 U, \tag{3.14}$$

where D_l is the diffusion coefficient for the photons. To obtain $P(s)$ from U, consider the following argument. If photons are sent into the sample at time $t = 0$, they will undergo random walks with step size l^*, scatter many times, and emerge from the sample sometime later. Those photons emerging at time t will have traveled a distance $s = vt$ where v is the average speed of light in the medium [183]. Therefore, the emerging flux of photons, J, will be proportional to the number of photons which traveled the path of length s. But this is equivalent to the probability for a photon to travel a path of length s, $P(s)$. Thus, to find $P(s)$, we must compute J, and this is done using Fick's law, $J = D_l \nabla U$. U is obtained by a solution of Equation 3.14 with the appropriate boundary conditions.

It is clear that a solution to Equation 3.14, and thus $P(s)$, will depend on the geometry of the scattering situation. In this way, the geometry of the sample affects the *qualitative* behavior of the autocorrelation function. For example, consider transmission through a very thick sample with $L \gg l^*$. If the sample is thick enough, all of the

detected photons will have scattered roughly the same number of times[2], and $P(s)$ can be approximated by a delta function. In this case, assuming diffusive particle motion, the autocorrelation function would decay exponentially. If scattered light is collected in the backscattering geometry [192], some paths can be short and others long and the decay function would be complicated mixture of the multiple path lengths. As we will only consider the transmission case through relatively thick samples, our correlation functions will be almost exponential. We now calculate the exact form to get the corrections.
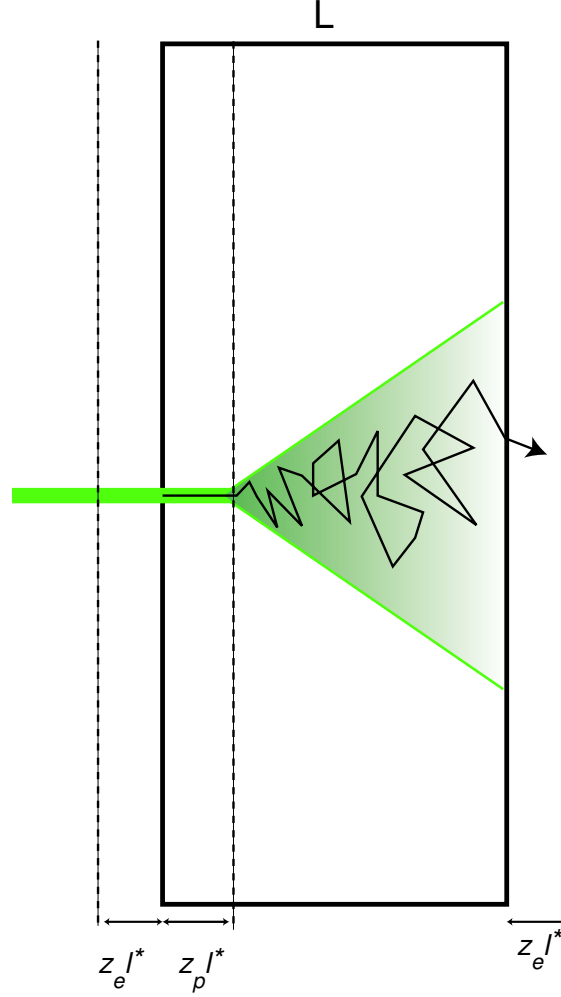
Figure 3.15: The different length scales involved in the boundary conditions for DWS.

The solution to Equation 3.14, is obtained by assuming as an initial condition that

---

at $t = 0$ a pulse of light spread over a region of size d begins diffusing at distance z_p inside the cell. Here, $z_p \approx l^*$. Another boundary condition must be imposed, and this is often taken to be that $U = 0$ at a distance z_e outside the boundary; we will comment on this in a later section. For a schematic of the different length scales involved, see Figure 3.15. For simplicity, for now, we use the standard approximation that $z_e = 2l^*/2$ [192]. For solutions to Equation 3.14, we refer the reader to [192] where the diffusion equation is solved for a variety of incident light configurations. For the case in which the illumination is taken to be constant over the incident face (a plane wave, $d \to \infty$), the autocorrelation function takes the following form,

$$g^{(1)}(t) = \frac{\frac{L/l^*+4/3}{z_p/l^*+2/3}\{\sinh\left[\frac{z_p}{l^*}\sqrt{\frac{6t}{\tau}}\right] + \frac{2}{3}\sqrt{\frac{6t}{\tau}}\cosh\left[\frac{z_p}{l^*}\sqrt{\frac{6t}{\tau}}\right]\}}{(1 + \frac{8t}{3\tau})\sinh\left[\frac{L}{l^*}\sqrt{\frac{6t}{\tau}}\right] + \frac{4}{3}\sqrt{\frac{6t}{\tau}}\cosh\left[\frac{L}{l^*}\right]}, \tag{3.15}$$

In this equation and the following expressions, $\frac{t}{\tau} = k_0{}^2\langle\Delta r(t)^2\rangle/6$. For a point source $(d \to 0)$, it can be shown that,

$$g^{(1)}(t) = C\int_Q^\infty J_0(\frac{R}{L}\sqrt{\xi^2 - Q^2})D(\xi, \epsilon, \zeta)\xi e^{-(1-\zeta)\xi}d\xi, \tag{3.16}$$

where $Q \equiv (L/l^*)\sqrt{6t/\tau}$, $\epsilon \equiv 2l^*/(3L)$, $\zeta \equiv z_p/L$, and C is a normalization constant such that $g^{(1)}(t = 0) = 1$. The function $D(\xi, \epsilon, \zeta)$ is given by,

$$D(\xi, \epsilon, \zeta) = \frac{2\epsilon[(1 + \epsilon\xi) - (1 - \epsilon\xi)e^{-2\zeta\ xi}]}{(1 + \epsilon\xi)^2 - (1 - \epsilon\xi)^2 e^{-2\xi}}. \tag{3.17}$$

For the realistic case of an incident Gaussian beam of beam diameter d, a different form is obtained,

$$g^{(1)}(t) = C\int_Q^\infty e^{-(\xi^2 - Q^2)(d/4L)^2}D(\xi, \epsilon, \zeta)\xi e^{-(1-\zeta)\xi}d\xi. \tag{3.18}$$

This formula reduces to the forms of Equations 3.15 and 3.16 in the appropriate limits. In the experiment, the point source distributes more photons into the bed than an expanded source, and thus produces smoother correlation curves. However, the narrow beam can cause local heating effects. Thus, we find it useful to vary the beam size with a lens to optimize between heating effects and signal-to-noise considerations. We use Equation 3.18 to calculate $\langle\Delta r(t)^2\rangle$ for this case.

3.5.3 DWS on colloidal suspensions

To gain proficiency with the many complicated expressions in DWS, we have repeated the results of [192] using colloidal suspensions. This allows us to study DWS in a well understood situation.

Measurement of parameters

In practice, extraction of meaningful quantities using DWS can be tricky. Once $g^{(2)}(\tau)$ is obtained, Equation 3.15 must be inverted to find $\langle \Delta r(\tau)^2 \rangle$. The inversion is accomplished using a root finding technique using Matlab.

There are several fitting parameters which cannot be calculated from first principles and must be measured. Theses are the scattering length l^* and z_e, the extrapolation length[3]. Durian [52] has proposed techniques to measure l^* based on a formula which says that for multiply scattering media, the transmission coefficient T is inversely proportional to the sample thickness,

$$T = \frac{1 + z_e}{(L/l^*) + 2z_e},\tag{3.19}$$

It can be shown that z_e can be found from the angular distribution of light emitted from the sample,

$$P(\mu) = \frac{z_e \mu + \mu^2}{z_e/2 + 1/3},\tag{3.20}$$

where $\mu = \cos \theta$.

To compare with experiments, the intensity must be calculated and it can be shown that the detected intensity as a function of θ goes like,

$$I = [\frac{I_t D^2}{2\pi R_D^2}]P(\mu)\tag{3.21}$$

where I_T is the total transmitted intensity. Thus by angular detection of the light we can fit z_e, and from a measurement of the transmission coefficient, we can calculate l^*.

We measure the transmitted intensity through a 1% by mass colloidal suspension using a Coherent Fieldmaster head which has a 10 degree opening angle and we also measure the intensity with 10 degree integration using this head. Figure 3.16 shows the

---

[3]The penetration length is to a good approximation always taken to be $z_p \approx l^*$. I will assume this in the measurements on the colloids.
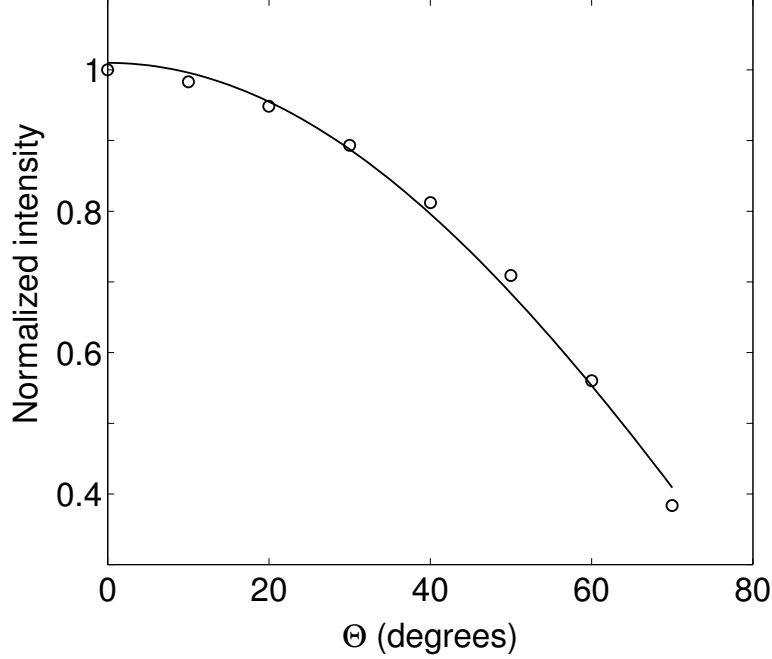
Figure 3.16: The intensity of light scattered from a colloidal suspension as a function of angle. The fit to Equation 3.21 gives the value of $z_e \approx 0.89$.

angular distribution and the fit to Equation 3.21. From this fit we find that $z_e \approx 0.89$, in reasonable accord with other measurements and the theoretical prediction of 2/3 [192].

Colloid diffusion

We present data in which we measure the motion of 0.596μm polystyrene spheres suspended in water. Since the colloidal suspensions have been well studied using the DWS [192], they provide a useful test of our setup. We use two different geometries: a "slab" in which the cell is much larger than it's thickness (10x8x0.5 cm^2, aspect ratio 20) and a square tube with dimensions like those of the bed (2.54 x 2.54 x 15 cm^3, aspect ratio 1). The slab geometry is used to test DWS in the limit where Equations 3.16-3.15 are valid. The tube geometry is used to confirm that for large enough L/l^*, the small aspect ratio does not lead to significant corrections. In fact, we find no significant difference between measurements in the two geometries, indicating that we are in the multiple scattering limit for the colloids.

In Figure 3.17, we present $g^{(2)}(\tau)$ for 0.596 μm polystyrene spheres (Duke Scientific, 5060A) with volume fraction 0.01 at room temperature. The laser was expanded to a beam 1 cm in diameter onto the incident face of the slab. Since we want to maximize counts, we do not use a polarizer between the sample and the detector. Thus, the
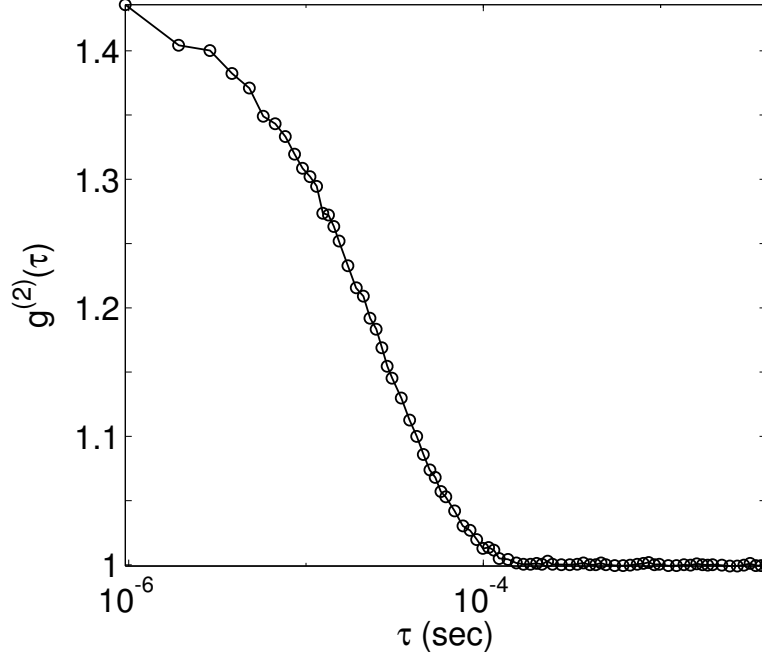
Figure 3.17: The autocorrelation function for the colloidal suspension described in the text, slab geometry

intercept $g^{(2)}(0)$ is approximately 1.5, in accord with theory [119]. The value of 1.45 indicates that we have detected only about one coherence area and that we have sampled a sufficient number of decorrelation times[4].

Using Equations 3.19- 3.21 and the measured angular intensity data, we find $z_e = 0.89$. Taking reflections into account from all surfaces, we measure $T = 0.1$ over the integrated area of the power meter head (1 cm in diameter). This yields a value of $L/l^* \approx 20$, indicating that we are in the limit in which DWS will apply. Inverting $g^{(2)}$ using Equation 3.15, we find that $\langle \Delta r(t)^2 \rangle = Dt^\alpha$, and this is plotted on log-log axes in Figure 3.18. α is very close to 1, indicating diffusive motion. Our best fit measures 1.05 and we believe that the deviation is due to flow induced by thermal heating from the laser; measurements at lower laser power have exponents closer to 1. Measurements in which the fluid was agitated using a magnetic stir bar show exponents that deviate further from 1 as the stir rate increased. The intercept gives the value for D, and we find that it is 0.7 $\mu\,m^2$/sec. This is in good agreement with $D = 0.73\ \mu\,m^2$/sec calculated from the Stokes-Einstein relation, $D = kT/6\pi a\mu$, where a is the particle radius. However, for

---

[4]For the colloids, the decorrelation occurs within roughly 100 μ seconds, much shorter than the sampling times. For slowly moving granular materials, the decorrelation times can approach the sampling times. In this limit, the intercept deviates from the ideal value [186].
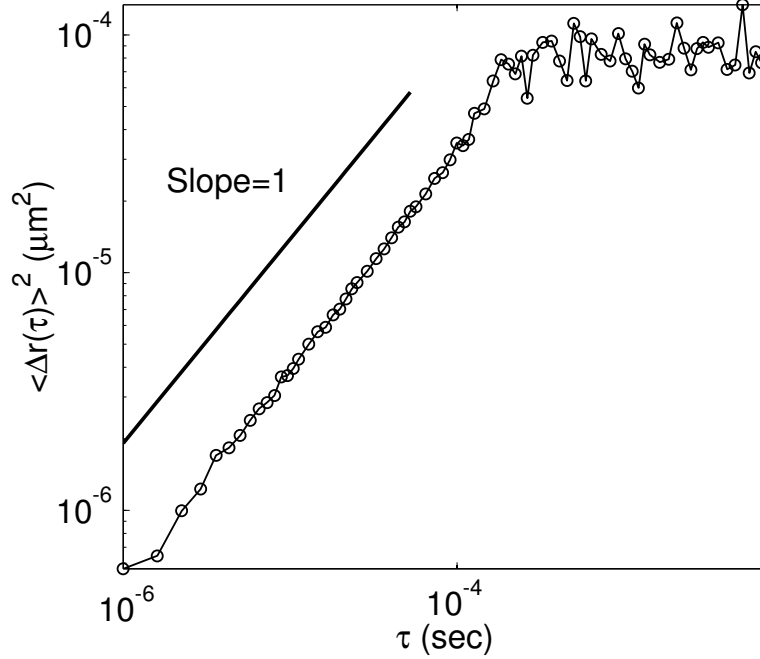
Figure 3.18: The MSD for colloids, showing diffusive behavior, slab geometry.

our purposes, the value of the intercept is unimportant: inaccuracy in a measurement of the value l^* scales all MSD curves (changes the intercept, the value of D), but does not significantly effect the scaling exponents (the values of α). We will examine the behavior of α during fluidization in Chapter 8.

Practical considerations and limitations

As shown, DWS allows measurement of diffusion coefficients of colloidal particles. These particle are typically sub-micron, with sizes comparable to $2\pi/k_0$. However, we would also like to use DWS to measure properties of large particles which may not move diffusively. Note that the curves $g^{(2)}$ bend over after some time–this is the time it takes for light paths to change by a wavelength λ due to particle motion. This time sets the limitation on maximum particle displacements that can be resolved. We can estimate the time and distance for which measurement of particles in the following way: For thick samples in which every photon path undergoes many scattering events, the average photon will undergo $\approx (L/l^*)^2$ scattering steps of length l^* so the light is scattered many times on average $\langle s \rangle \approx (L/l^*)^2 l^*$ by the time it emerges. Thus as a sample becomes very thick, the spread of path lengths relative to the longest path length goes to zero and $P(s)$ can be approximated by a delta function, $P(s) \approx \delta(\langle s \rangle)$. Substituting into Equation 3.13 the integral disappears and the correlation takes takes a purely exponential form,

$$g^{(1)} = \exp(-\frac{1}{3}k_0^2 \langle \Delta r(t)^2 \rangle \frac{L}{l^*}) \qquad (3.22)$$

For diffusing colloidal particles, $\langle \Delta r(t)^2 \rangle / = 6Dt$ where D is the diffusion co-efficient. Thus, $g^{(1)}$ will be approximately exponential and decay in a time $t_{\text{dec}} = 1/k_0^2 D(l^*/L)^2$. For the diffusing particles measured in our experiment, this works out to be 70μsec, in agreement with our data. The particles will have moved $\sqrt{6Dt_{\text{dec}}} \approx (l^*/L)^2\lambda$, roughly the wavelength of light. This makes sense, as the correlation functions decay over the time it takes for a path to change length by λ or equivalently, the time the phase changes by π. For our 0.596 μm colloidal particles, the distance traveled in a decay time is 0.013 μm, much less than a particle diameter. Thus we are visualizing short time and length scale diffusion.

Now we would like to make a similar estimate for glass spheres which are moving (as will be shown in Chapter 8) ballistically, such that $\langle \Delta r(t)^2 \rangle / = v^2 t^2$, where v is a typical particle velocity. Inserting this into Equation 3.13, we find that $g^{(1)}$ will decay like $\exp -\frac{1}{3}k_0^2 v^2 t^2$; we determine that a characteristic decay time (e-folding time) goes like $t_{\text{dec}} = \sqrt{3/v^2 k_0^2}(l^*/L)^2$. For particles moving ballistically at 1 mm/sec, this is roughly 10 μsec in accord with our measurements in Chapter 8. In this time, a 335 μm particle will move $vt_{\text{dec}} \approx 13$ nm, a factor of 20000 of its diameter[5]. Thus, we will only resolve the short time and length scale motion, even with several decay times because of experimental limitations of noise. This is obviously a huge limitation for examining long time dynamics. This timescale can be increased by increasing l^* but there is a fundamental limitation on the size of l^* before the diffusion approximation becomes invalid. However, the technique becomes very useful if short time behavior is desired. The technique is *extremely* sensitive to small scale motion–since we would like to understand the motion of grains which are trapped at long times but can rattle in local cages, DWS is ideal. In fact, as will be seen in Chapter 8 we are able to resolve the short time ballistic motion associated with fluidization. The multispeckle DWS is sensitive to similar length scales, but increases the timescale over which decorrelation can be accurately measured. In addition, the measurement of transient events due to minute grain rearrangements is possible using the multispeckle technique. Data will be presented in Chapter 8.

To resolve larger scale motion, the wavelength of the scattering field must be increased and techniques involving ultrasound have been used to do this, for example the tools of Diffusing Acoustic Wave spectroscopy [34].

---

[5] We have used a Vision Research Phantom 4 camera with a 5 kHz frame rate to confirm the collisional velocity measurement.

Chapter 4

Emergence of order in an oscillated granular layer

The contents of this chapter have been published in [73]

4.1 Introduction

Our experiments on a vertically oscillated granular layer reveal that spatial patterns emerge in two stages following a change of parameter into the pattern-forming regime: an initial, domain-forming stage and a later stage in which domains coarsen to form ultimately an extended regular pattern. We characterize the evolution of the pattern using a "disorder function" $\bar{\delta}(\beta)$, where β is a moment of the disorder operator [Gunaratne et al., Phys. Rev. E **57**, 5146 (1998)]. The disorder in the initial stage is found to be consistent with a decay given by $\bar{\delta}(\beta) \sim t^{-\beta/2}$, in accord with theory that predicts that behavior in this stage should be universal for pattern forming systems. The final stage is non-universal.

Nonequilibrium spatial patterns have been extensively studied in laboratory experiments and model systems, but most studies have focused on the dynamics of small deviations from asymptotic well-ordered states described by amplitude equations [35]. The dynamics of such perturbations exhibit universal (system-independent) properties. Much less is understood about the development of a pattern from an arbitrary initial condition and the extent to which this dynamics is universal. We present experimental measurements of the time evolution (ordering) of a pattern from an initial noisy, featureless state and compare our observations to theory [37, 58, 82, 94, 161].

We characterize the development and ordering of a pattern using a recently introduced measure, the disorder function, $\bar{\delta}(\beta)$, which vanishes for any completely ordered pattern, and has a nonzero positive value that increases as the amount of disorder in the pattern increases. A further description of $\bar{\delta}(\beta)$ will be given in Section 4.4 Before presenting our main results, we describe our experimental apparatus in Section 4.2, present results for a typical experimental realization in Section 4.3, and review previous theoretical work on the development of nonequilibrium patterns in Section 4.4.

4.2 The Experiment

Our experiments generate patterns in a layer of 0.165 mm bronze spheres contained in a vertically oscillated circular container with a diameter of 140 mm [129]. The layer is four particle diameters deep, and the cell is evacuated to 4 Pa so that hydrodynamic interaction between the grains and surrounding gas is negligible. The control parameters are the frequency f of the sinusoidal oscillations and the peak acceleration of the container relative to gravity, $\Gamma = (2\pi f)^2 A^2/g$, where A is the amplitude of the oscillation and g is the gravitational acceleration. As f and Γ are changed, a variety of temporally subharmonic patterns including locally square, striped, or hexagonal patterns are observed [129]. In this paper we consider the development of the square patterns.

To visualize patterns, the granular surface is illuminated with a ring of LEDs surrounding the cell and is strobed at the drive frequency of the container. The light is incident at low angles and the scattering intensity is a nonlinear function of the height of the layer; scattering from peaks (valleys) creates bright (dark) regions. The circular container allows relaxation to an almost perfect square array through wavelength adjustment of the pattern at the container wall over a distance of less than one wavelength [1]. In the region of the $\Gamma - f_d$ phase diagram studied, square patterns appear for increasing control parameter at $\Gamma \approx 2.75$; the bifurcation is subcritical. In our experiments, Γ is suddenly increased at a specific phase in the vibration cycle from an initial value of 2.2, where no discernible structure is observed. The grains are not in contact with the plate when the acceleration is changed, and we assume that the initiation of the quench (the time origin for our experiments) occurs at the last layer takeoff time before Γ is changed (the point where the acceleration of the plate is equal to $-g$); this is the lower bound of possible quench initiation times, and is physically reasonable, as it is the last time that the layer "knows" about the initial $\Gamma = 2.2$. The uncertainty in the time origin is the dominant source of systematic error in the interpretation of our observations. This is illustrated in Figure 4.1.

For a typical quench experiment, we take 10 sets of data at the same Γ and f, and record images of the pattern at a fixed phase in the oscillation cycle. Since the images' absolute phase in the oscillation cycle relative to the last layer takeoff time is arbitrary (chosen for highest contrast in the images), the time between the last layer takeoff time and the first image will not in general be an integer period of oscillation and may be different for different sets of runs, although this time is fixed within a set of 10 runs. Thus in our analysis of the image data, the values for the number of container oscillations may be fractional, but in each case there is one container oscillation between

---

[1]Experiments done in square containers also exhibit our main results. However, the formation of a single domain takes a much longer time, as the final pattern orientation is strongly influenced by the boundaries.
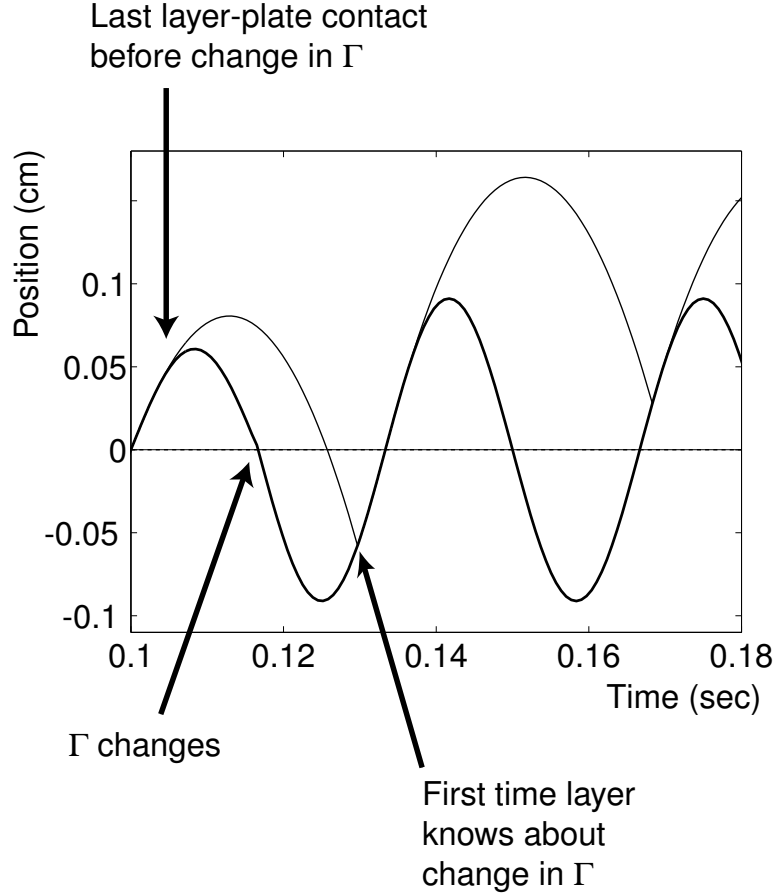
Figure 4.1: The trajectory of a single inelastic ball during a jump from $\Gamma = 2.2$ to $\Gamma = 3.0$. The single inelastic ball described the motion of the center of mass of the layer. Γ changes while the layer is in the air, resulting in uncertainty in the initial quench time. We take $t = 0$ to be the last time the layer was on the plate before the change in Γ. Trajectory calculated with the code in Appendix D.

successive images (see the abscissas of Figure 4.3 and Figure 4.5; the number of periods has been rounded in Figure 4.2).

4.3 Observations of the development of order

The emergence of local square domains and their coarsening to a final, almost perfect square array is shown in Figure 4.2 The first three frames of the top row show that the system quickly (within six oscillations) creates a pattern with a range of orientational order the size of a wavelength. The last three frames show slow growth of domains of
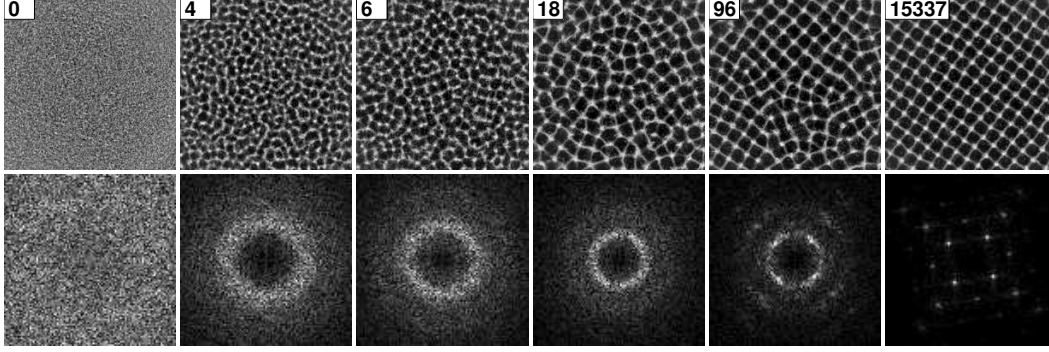
Figure 4.2: Snapshots showing the emergence of a square spatial pattern in a granular layer at $f_d = 27$ Hz and $\Gamma = 3.3$; the times given in the upper left corner of each image are in units of container oscillation periods. Each image in the top row is of the central 8 cm of the 14 cm diameter circular container. Each image in the bottom row is the Fourier transform of the image above it. The first three frames of the top row show the emergence of local domains from a uniform background, and the last three show the slower coarsening of these domains to an almost perfect square array.

pattern with different orientations. These domains grow and compete, and the final state of the system is a single domain of pattern. This process can be viewed in Fourier space as well, as shown in the bottom row of Figure 4.2. The early stage narrows the range of wavevectors in k-space, while the later stage selects a discrete set of wavevectors. We study aspects of this relaxation that are invariant under repetition of the experiment and analyze the dependence on the control parameters f_d and Γ. Our goal is to gain a quantitative understanding of the process of pattern evolution. Before we present our analysis of the observations, we review theoretical work on the evolution of patterns after a quench from an initial noisy and spatially featureless state and the methods that have been used to characterize this evolution.

4.4   Theory

Most analyses of the development of patterns have focused on solutions $u(\mathbf{x}, t)$ to the Swift-Hohenberg equation [35],

$$\frac{\partial u}{\partial t} = \left(\epsilon - (\triangle + q_0^2)^2\right)u - u^3 - \nu(\nabla u)^2 + \eta(\mathbf{x}, at), \tag{4.1}$$

where $u(\mathbf{x}, t)$ is a two-dimensional scalar field, ϵ is the distance from pattern onset, ν is the strength of a non-variational term [82], and η a random forcing term such that $\langle \eta(\mathbf{x}, t)\eta(\mathbf{x}', t') \rangle = 2F\delta(\mathbf{x} - \mathbf{x}')\delta(t - t')$, where F denotes the strength of the noise. For

suitable control parameters, random initial states evolve to patterns under spatiotemporal dynamics given by (4.1).

The most common measure used to characterize patterns generated by (4.1) is the width of the structure factor $S(t)$ [28, 37, 58, 161] (i.e., the width of the peak in the azimuthal average of $\langle \tilde{u}(\mathbf{k}, t)\tilde{u}(-\mathbf{k}, t)\rangle$), which decays in two distinct stages [161]: $S(t) \sim t^{-\frac{1}{2}}$ is obeyed until the peak amplitude of the field $u(\mathbf{x}, t)$ saturates, beyond which time the pattern coarsens and the decay becomes slower. For $\epsilon = 0.25$ and $\nu = 0$, Elder et al. [58], Cross and Meiron [37], and Hou et al. [94] found that in this second region $S(t)$ decreased as $t^{-\frac{1}{5}}$ when $F = 0$, and as $t^{-\frac{1}{4}}$ when $F \neq 0$. Schober et al. [161] found that for $F = 0$ and $\nu = 0$, $S(t) \sim t^{-\frac{1}{4}}$; the discrepancy with earlier results could be due to the one-dimensionality of their model [2].

The structure factor provides a single characterization of a pattern while the disorder function $\bar{\delta}(\beta)$ provides families of characterizations of a pattern, just as the generalized dimensions d_q [87] and singularity spectra $f(\alpha)$ [174] provide a family of characterizations of strange attractors. The details of a pattern depend on the initial state, but different patterns generated under fixed control parameters have the same $\bar{\delta}(\beta)$ [80]. For a pattern at fixed time represented by a scalar field $v(\mathbf{x})$ (e.g., $v(\mathbf{x}) = u(\mathbf{x}, t_0)$ at time t_0) the disorder function is defined as

$$\bar{\delta}(\beta) = \frac{(2 - \beta)}{(\int d^2x)} \frac{\int d^2x |(\triangle + q_0^2)v(\mathbf{x})|^\beta}{q_0^{2\beta}\langle |v(\mathbf{x})|\rangle^\beta}, \tag{4.2}$$

where q_0 is the typical wavevector associated with the pattern, $\langle |v(\mathbf{x})|\rangle$ denotes the mean of $|v(\mathbf{x})|$, $\bar{\delta}(\beta)$ ($0 \leq \beta < 2$) has been normalized to be scale invariant, and $\int d^2x$ is the area of the system. The ingredients used to deduce the form of the disorder function are its invariance under arbitrary rigid motions of the pattern and the fact that the pattern locally consists of a small number of plane waves. Modulation of squares due to curvature of the contour lines contributes to $\bar{\delta}(\beta)$ through the Laplacian, while variations of the size of squares contribute via the choice of a "global" q_0 [82]. Unlike the information contained in the structure factor, $|(\triangle + q_0^2)v(\mathbf{x})|$ is a measure of local irregularity in the pattern, and hence distinct "moments" β can be used to quantify multiple aspects of the disorder in patterns. For example, $\lim_{\beta \to 2} \bar{\delta}(\beta)$ is proportional to the density of defects [81].

Calculating $\bar{\delta}(\beta)$ for experimental data requires some care. Images shown in Fig 4.2 have sharp changes at the edges which lead to high frequency contributions

---

[2]Additional quantities have been measured in the second relaxation region. Hou et al. measured total domain wall length as a function of time. For $F = 0$, it was shown to decay as $t^{-\frac{1}{4}}$, while for $F \neq 0$ the decay was proportional to $t^{-0.3}$. Cross et al. showed that a stripe orientation correlation field decayed as $t^{-0.24}$. The interpretation of these results is that different measures probe different features of the pattern, and these features relax at different rates.

in their Fourier spectra. Consequently, their removal through simple filtering causes contamination of the pattern near the edges and leads to error in calculating the disorder function. We use a method of noise filtering that involves extending the image to a periodic one [90] using "Distributed Approximating Functionals" (DAFs) [91]. A method for calculating $\bar{\delta}(\beta)$ from filtered data has been presented in Ref. [80].

The disorder function analysis of the evolution of patterns generated by (4.1) from an initial noisy state reveals two stages: the emergence of domains characterized by $\bar{\delta}(\beta) \sim t^{-\sigma_E(\beta)}$, where $\sigma_E = \frac{1}{2}\beta$ is an exponent that characterizes this early stage, and a later slower domain-coarsening behavior characterized by $\bar{\delta}(\beta) \sim t^{-\sigma_L(\beta)}$ [82]. Unlike $\sigma_E(\beta)$, $\sigma_L(\beta)$ depends on the value of ν in (4.1), and is thus expected to be system and model dependent. Since (4.1) contains the general features of a nonequilibrium pattern-forming system, we will compare the results obtained for $\bar{\delta}(\beta)$ from our experiments with the results from numerical simulations of (4.1) [82].

4.5 Analysis of the observations

4.5.1 Evolution of the disorder function for fixed Γ

The behavior of $\bar{\delta}(1)$ for the relaxation of Figure 4.2 is shown in Figure 4.3. In repetitions of the experiment for identical control parameters, the details of the patterns differ for each run, but $\bar{\delta}(1)$ behaves the same. The initial formation of domains and the final coarsening exhibit different decay rates. The transition in behavior coincides with the saturation of the peak amplitude (cf. Figure 4.3). This transition is consistent with that exhibited by the structure factor for the spatio-temporal dynamics of (4.1) [161].

During the initial stage of pattern formation the data are described by $\bar{\delta}(1) \sim t^{-0.5\pm0.1}$. The domain formation stage is short, lasting only through the first six periods of oscillation of the container; hence the observation of power law behavior in the initial stage is suggestive rather than conclusive. The uncertainty in the exponent is a result of two main sources of error. First, the short time range of the data makes the contribution of the beginning and end points of the initial region very important. The uncertainty in the time of the initiation of the quench contributes to a systematic shift in the value of the exponent; the value of -0.5 is found if we assume that the quench begins at the time of the last layer takeoff before Γ is changed (see discussion in Section 2). In addition, the end point of the initial region is known only to within one period of oscillation. Variation between runs also contributes to uncertainty in the exponent, but the error bars in Figure 4.3 show that it is small relative to the above uncertainties.

Since nonlinear effects are negligible during the initial stage, the evolution can be modeled by (4.1) without nonlinear and stochastic terms. Numerical integration of noisy
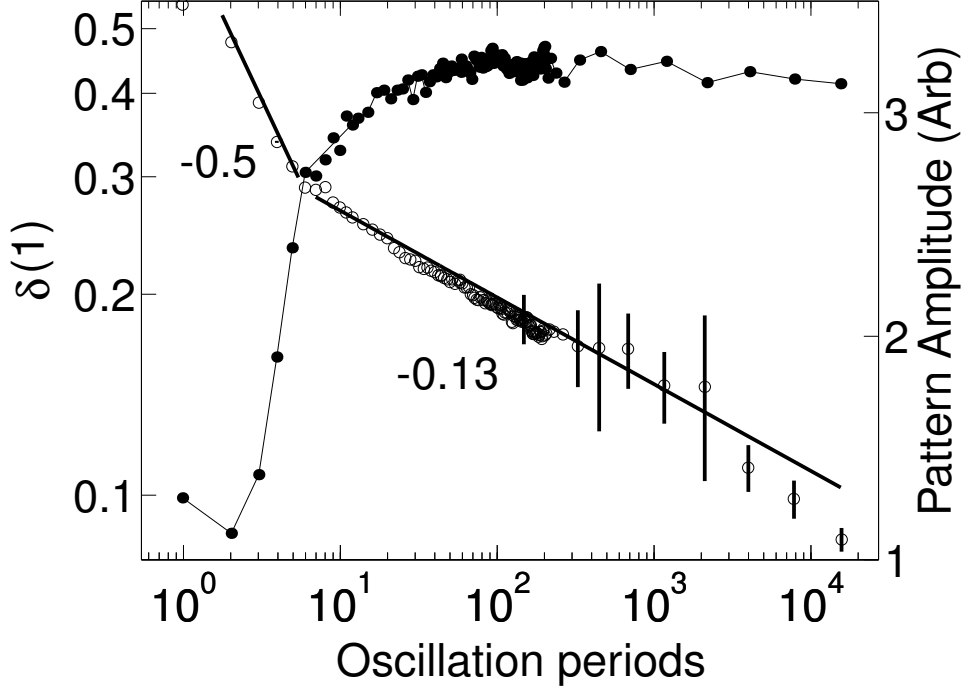
Figure 4.3: The time evolution of the disorder function $\bar{\delta}(1)$ for square patterns at $\Gamma = 3.3$ ($\circ$), showing the domain forming stage with slope of -0.5 and the coarsening stage with slope of -0.13. Also shown is growth of the pattern amplitude ($\bullet$), which grows rapidly in the domain-forming phase and saturates in the later coarsening phase. Each curve is an average of 10 runs at the same control parameters. The error bars at late times show typical variation between runs. The error bars at early times are the size of the symbols. The abscissa is in units of number of container oscillations from the last layer takeoff time before the container acceleration was changed.

initial states shows that $\int d^2x|u(\mathbf{x},t)| \sim e^{\epsilon t}t^{-\frac{1}{4}}$ and $\int d^2x|(\triangle + q_0^2)u(\mathbf{x},t)| \sim e^{\epsilon t}t^{-\frac{3}{4}}$ [3]; consequently $\bar{\delta}(1) \sim t^{-\frac{1}{2}}$. The same behavior has been found in the initial decay of the structure factor [161] and in the rate of domain growth. More generally, for $0 < \beta < 2$, we find that in our data the moments of the disorder function decay as $\bar{\delta}(\beta) \sim t^{-\sigma_E(\beta)}$, where $\sigma_E(\beta) \approx \frac{1}{2}\beta$; see Figure 4.4. This is also seen in numerical integration of the linearization of (4.1).

The latter stages of pattern formation correspond to nonlinear spatiotemporal dynamics of the field [161]. For the evolution shown in Figure 4.3 at $\Gamma = 3.3$, the decay of disorder at long times is described by $\bar{\delta}(1) \sim t^{-0.13}$. This decay exponent is

---

[3]In the absence of diffusion, $u(\mathbf{x},t) \sim e^{\epsilon t}$. The effects of the diffusive terms are thus studied through the behavior of $e^{-\epsilon t}\int d^2x|u(\mathbf{x},t)|$, which is numerically observed to decay as $t^{-\frac{1}{4}}$.

72
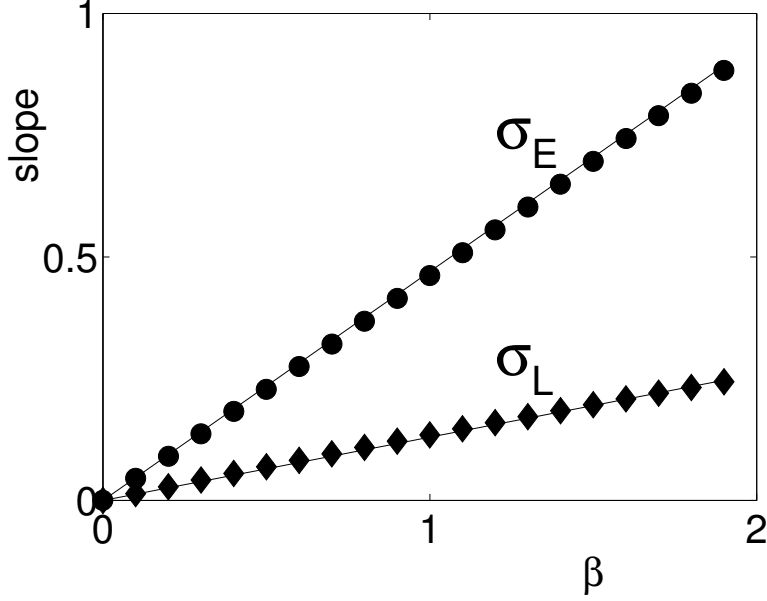
Figure 4.4: The slopes of log-log plots of $\bar{\delta}(\beta)$ vs. β during domain formation ($\bullet$) and domain coarsening ($\blacklozenge$). The results are for a single run at $f = 27$ Hz and $\Gamma = 3.3$. There is no scatter in the curves because the calculation for $\bar{\delta}(\beta)$ is done for multiple values of β on the same data set. Since we assume that the quench initiation time is the time of last layer takeoff before the acceleration is changed, the uncertainty in the initial time does not enter the error calculation and the error estimates on the slopes of the lines, 0.47 ± 0.05 and 0.13 ± 0.02, are obtained by comparing different data sets within a 10 set run and different choices for the region over which a power law is fit. While statistical variation between runs is a source of error for both σ_E and σ_L, the narrow range of time in the first region is the dominant source of error for σ_E.

not expected to be universal [82]. The magnitude of the exponent is smaller than that for the relaxation rate of the structure factor upon integration of (4.1) with $F \neq 0$, -0.25 [58, 94], and also with $F = 0$, -0.20 [37, 58, 94]. We find that $\sigma_L(\beta)$ is linear with $\sigma_L(\beta) \approx 0.13\beta$ (Figure 4.4). In contrast, (4.1) yields [82] a nonlinear concave-down function for $\sigma_L(\beta)$. We speculate that the linearity found in our study implies that the spatiotemporal dynamics is governed by relaxation with a single length scale, and is thus a consequence of finite cell size. If we calculate $\sigma_L(\beta)$ for intermediate times (10-1000 oscillation periods), where domain sizes are small compared to the system size and boundary effects should be negligible, a nonlinear concave-down relationship is obtained. This nonlinearity implies that during intermediate times relaxation of the pattern occurs over multiple length scales, and work is in progress to test this hypothesis using (4.1).

4.5.2 Evolution of the disorder function for increasing Γ

Next, we consider changes in the behavior of the disorder function as Γ is increased from 2.8, driving the system further away from the onset of patterns (Figure 4.5). We find that in the domain formation stage the exponent $\sigma_E(\beta)$ is independent of Γ; identical behavior is observed on integration of (4.1) [82]. Although the form of the curves in the second region deviates from power law decay, the mean decay rate (measured by $\sigma_L(1)$ for a given Γ) decreases from 0.18 to 0.12 as Γ increases from 2.8 to 3.2; similar behavior is seen with decreasing ν in (4.1) [82]. The long time behavior of the curves is not shown because for Γ < 3.3 a secondary oscillatory motion dominates the dynamics of the pattern after about 100 oscillations; work is in progress to understand these oscillatory dynamics.
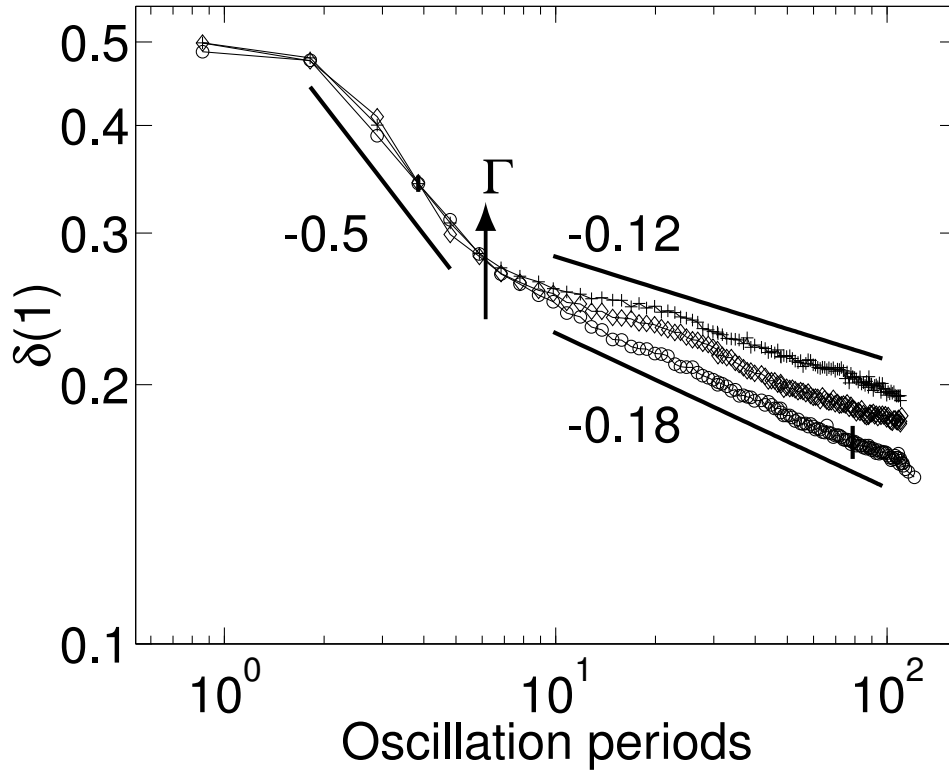
Figure 4.5: The time evolution of $\bar{\delta}(1)$ for square patterns at three different final container accelerations, Γ = 2.8 (∘), Γ = 3.0 (⋄), and Γ = 3.2 (+). The decay during the initial domain forming stage is independent of Γ while the magnitude of the slope in the later stage decreases as Γ increases. The abscissa is in units of number of container oscillations from the last layer takeoff time before the container acceleration was changed.

4.6   Conclusions

We have shown that the formation of a pattern in a vertically oscillated granular layer occurs in two distinct stages. During the early stage the spatiotemporal dynamics is essentially linear and the decay of the disorder function determined in our experiment is consistent with the power law found in pattern formation for the Swift-Hohenberg equation: $\bar{\delta}(\beta) \sim t^{-\sigma_E(\beta)}$, with $\sigma_E(\beta) \simeq \frac{1}{2}\beta$. During the later domain coarsening stage the emergence of order is described by $\bar{\delta}(\beta) \sim t^{-\sigma_L(\beta)}$, where $\sigma_L(\beta)$ is a nonlinear function at intermediate times and becomes linear at long times, when the finite system size dominates the decay. This relaxation is not universal, since the decay rate (and thus $\sigma_L(1)$) decreases with increasing Γ. Such behavior is also seen in model systems, in which $\sigma_L(\beta)$ is a model and parameter dependent nonlinear function of β [82]. Such characterizations of pattern formation can be used to determine the validity and limitations of model systems [189], and can be used to study patterns and their evolution in other laboratory experiments.

Chapter 5

Lattice vibrations and melting of square patterns

5.1 Introduction

Previous studies of the square patterns in shallow vibrated granular layers studied average properties of the pattern like wavelength and angular correlation [181]. In this chapter, we present studies of the dynamical behavior of the square patterns. For certain control parameters Γ and f_d, the patterns can have time independent long-range order the size of the system, as seen in Fig 5.1. In this chapter, we will discuss dynamics of the patterns which disrupt the perfect long-range order. To summarize our main findings, we have observed that the square patterns exhibit dynamics like those of a two-dimensional crystal lattice with elements coupled by Hookian springs. Different transverse normal modes of the granular lattice are resonantly excited for different container frequencies and accelerations. If the container frequency is modulated at a particular normal mode frequency, that normal mode amplitude increases until the lattice melts (becomes disordered). Molecular dynamics simulations conducted for decreasing friction between the particle and vibrating plate also show melting, and this occurs in accord with the Lindemann criterion for 2D melting.

Although the dynamics that will be described will be in the $f_d/2$ strobed reference frame, for completeness, we briefly discuss the sloshing motion of the grains that forms the peaks and valleys of standing wave square pattern. A three dimensional view in Fig 5.2 reveals that the peaks in shallow layers are formed of several hundred particles connected by thin lines containing many fewer grains. The four peaks surround a valley in which there are almost no particles. After a single plate oscillation, the peaks become valleys and the valleys become peaks. A schematic of this process is shown in Figure 5.3. Every plate oscillation, the peaks collide with the plate and spread radially. A cycle later, a new peak is created in the intersection of the collision of grains from neighboring peaks, forming in the place where there was a valley. The lines are formed by the intersection of flows along the lattice directions and also contribute to the formation of peaks–upon plate collision, grains spread perpendicular to the lines and contribute to the formation of the peak.

There is some indication that the dynamics of the peak to valley motion is neces-
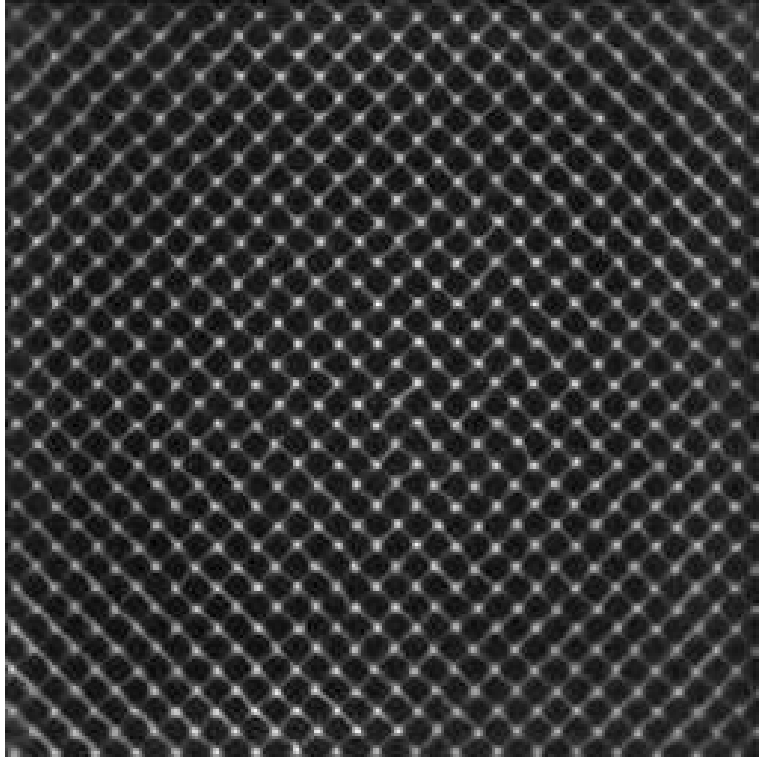
Figure 5.1: A square pattern formed in a square container with four layers of 165 μm bronze for $\Gamma = 3.0$ and $f_d = 27$ Hz. The pattern is oriented at $\pi/4$ to the container walls. The region shown is 16x16 cm^2.
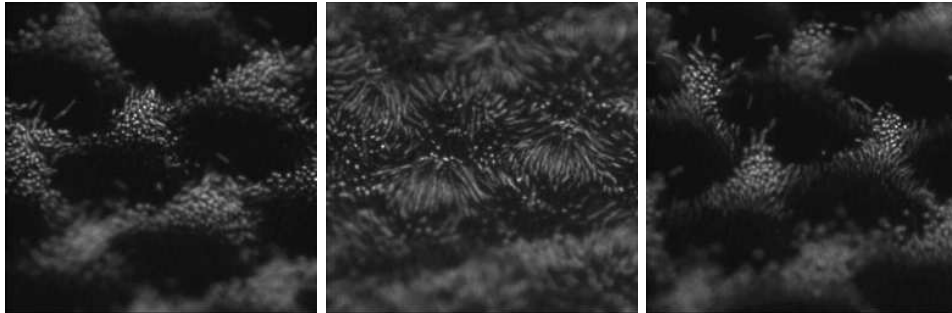
Figure 5.2: A time sequence of images taken at an oblique angle to the container: during one plate oscillation, peaks containing several hundred grains become valleys which contain very few grains.

sary to develop the theory of the lattice dynamics that will be presented in this chapter[1].

---

[1]Private communication from Chris Bizon
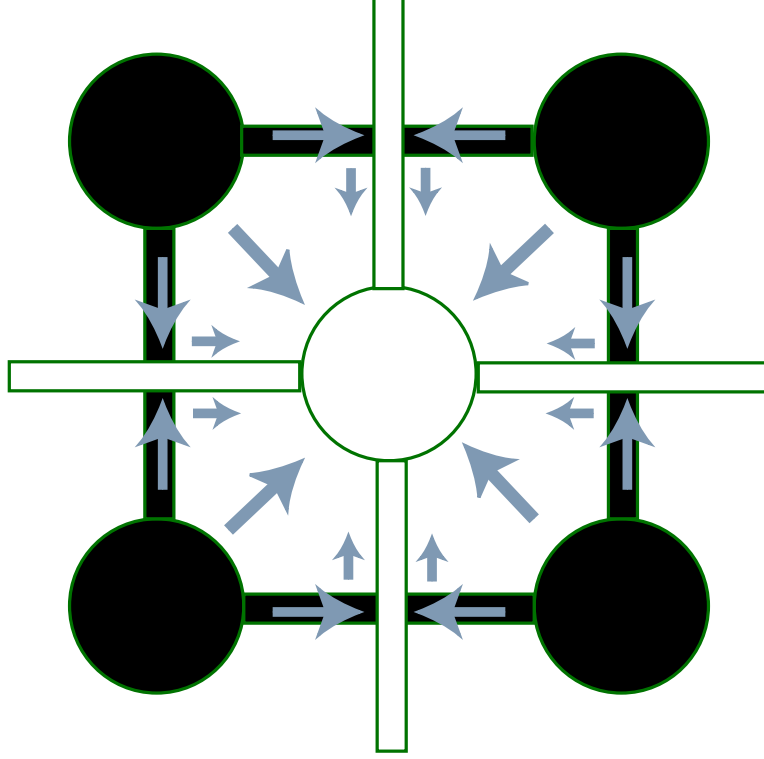
Figure 5.3: A schematic showing the flow of grains from peaks and lines into valleys after a plate oscillation cycle. The black and white indicate the positions of the peaks and the lines after one plate oscillation. The gray arrows indicate the direction of the flow of the grains. In the schematic diagram, the grains return to the original peaks after another oscillation cycle.

However, for simplicity, we will only consider motions of the pattern in the strobed $f_d/2$ frame.

Section 5.2 of this chapter is a preprint of a paper describing the dynamics of square patterns [72]. Following this section is a discussion of the frequency modulation technique that were briefly described in the paper. We present details of the dispersion relation calculation in Appendix C.

As the dynamics of the patterns are characterized by many different spatial and temporal frequencies, Table 5.1 presents the symbols used in this section.

Symbol	Description	Range
Γ	Peak plate acceleration	$0 - 4g$
f_d	Container drive frequency	$17 - 34$ Hz
f_L	Pattern normal mode frequency	$0 - 2.5$ Hz
f_{mr}	FM rate frequency	$0 - 5$ Hz
f_{ms}	FM span frequency	$0 - 5$ Hz
f_{BZ}	First Brillouin zone edge frequency	$1.5 - 2.5$ Hz

Table 5.1: The symbols used in this section
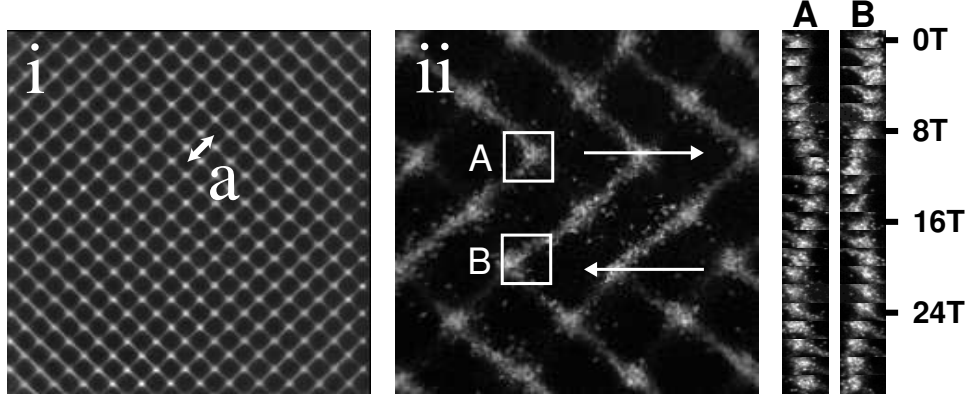
Figure 5.4: Square patterns form in a vibrated layer for a range of Γ and f_d and resemble two dimensional crystal lattices. (i) A lattice pattern at $\Gamma = 2.90$ and $f_d = 30$ Hz averaged over 10 plate oscillations. (ii) Relative motion of two peaks of the lattice (with lattice constant a) for $\Gamma = 2.90$, and $f_d = 30$ Hz. The lattice is oscillating in a fixed mode such that peaks separated by $\sqrt{2}a$ oscillate exactly out of phase at roughly 1 Hz.

5.2 Resonantly Excited Normal Modes and Shear Melting

5.2.1 Introduction

Systems driven away from thermodynamic equilibrium often form patterns when forced beyond a critical threshold. Close to the bifurcation, the dynamics of large length scale perturbations to the local wavelength of the pattern are well described by partial differential equations (PDE) called amplitude equations, whose form is universal [35]. Our study of square lattice-like patterns formed in a vertically vibrated granular layer finds that instead of diffusive relaxation of perturbations, which are often described by the amplitude equations, perturbations to these patterns relax in an oscillatory manner, and the individual peaks of the pattern behave as if they are interacting elements in a lattice. We propose that the behavior of this nonequilibrium pattern is governed by the coupled set of ordinary differential equations (ODE) that models the dynamics of the interacting lattice elements.

This ODE approach differs from the traditional description of patterns by the PDE amplitude equations. The inspiration for such an approach comes from the work of Umbanhowar *et al.* who postulated that nonequilibrium pattern dynamics could be described using a collection of interacting localized excitations called oscillons as the basic pattern elements [179]. Although the lattice elements in the square patterns are not oscillons, we will give evidence to show that the general approach of localized interacting elements is useful as a description of patterns found in a laboratory experiment.

80

5.2.2　Experimental details

As in [129], we oscillate a thin layer of bronze spheres[2] at a drive frequency of vibration, f_d, ranging from 17 to 34 Hz and the non-dimensional peak plate acceleration Γ ranges from 2.35 to 4.0. For these parameters, square patterns develop as shown in Fig 5.4. The granular surface is imaged by a 256x256 CCD camera using low angle illumination which creates bright regions at the peaks [14].

For the layer depth studied, square patterns exist in a region of parameter space for $2.5 < \Gamma < 4.0$, and $f_d < 34$ Hz. To verify that boundary conditions did not influence our main results, the experiments were checked in two different containers, a circular cell with diameter 7 cm and a square cell 18 cm on a side. The container shape only selects the direction of the pattern: a circular cell allows the pattern to form with any orientation, whereas in a square container, patterns form preferentially at $\pi/4$ to the direction of the container. None of the results reported depended upon the shape of the boundaries of the container[3], indicating that the lateral boundary conditions are unimportant for the phenomena described.

5.2.3　Oscillating peaks

An overhead snapshot of a typical square pattern seen in the experiment is shown in Figure 5.4i. At the phase in the plate oscillation cycle where the pattern amplitude is maximum, the pattern is composed of an array of peaks of grains arranged in a square lattice connected by a network of thin lines of sand[4]. The plate oscillates with a frequency f_d and the pattern oscillates subharmonically at $f_d/2$; after each plate oscillation, a peak becomes a valley. At maximum height, each peak typically contains on the order of 100 particles, and we collect images at this phase in the cycle. Between the peaks, in the dark regions, there is almost no sand. Thus, when strobed at $f_d/2$, the pattern resembles a two dimensional crystal lattice made of discrete elements separated by lattice constant a. In this paper, we will only consider the strobed motion of the pattern.

Even in the strobed frame, this pattern is not stationary — the center of mass of each peak of the pattern oscillates around its time averaged position (averaged over several hundred plate oscillations) which defines its lattice site. This motion occurs in the plane of the pattern, and may either appear as random, aperiodic oscillation (as would be seen in a lattice in contact with a thermal bath) or take the form of a collection of peaks oscillating around their respective lattice positions with fixed relative phases (coherent

---

[2]The phenomena was also observed in 165 μm diameter lead particles.

[3]Square boxes and circular cells of different sizes produced the same results.

[4]Connecting the peaks are thin lines of sand which could play an important role in the mechanism responsible for the dynamics of the patterns.

motion, the details of which will be discussed below). As an example of a type of motion that is seen, in Figure 5.4ii, a time series of snapshots of two peaks (in boxes A and B) is shown. In this case, the peaks oscillate exactly out of phase with each other, and the peaks within a particular row (shown in the box at $\pi/4$ to the natural lattice direction) maintain a constant separation of $\sqrt{2}a$ as they move; this is an example of a transverse mode in the $(1,1)$ lattice direction. In general, a series of frames will not always show such perfectly coordinated behavior, but will exhibit complicated motion around the mean lattice positions. We analyze this motion by decomposing it into Fourier modes.

5.2.4 Dispersion relation

To enumerate these modes we take a time series of 256x256 pixels images strobed at $f_d/2$ and perform the three dimensional discrete Fourier transform on this series, giving $\tilde{I}(k_x, k_y, f_L)$, and for each f_L, we determine the (k_x, k_y) at which the most power is present. To avoid confusion, we denote frequencies of motion of the peaks by f_L. Spatial modes, phase modulations of the square lattice, are represented as sidebands (at $f_L \neq 0$) of the the reciprocal lattice wavevectors (at $f_L = 0$). Although sidebands can in principle be found in any direction, we find them only in a direction $\pi/4$ (or the degenerate $3\pi/4$) relative to the lattice basis extending to distances of $1/(\sqrt{2}a)$, the maximum wavenumber modulation on the lattice. Examples of sidebands are shown by the dotted lines in Figure 5.5.

In the language of lattice dynamics, these are the $(1,1)$ modes of the lattice and we find that only the transverse $(1,1)$ modes are excited. Examples of modes in Fourier space are shown in Figure 5.5 in panels i and ii. The relationship between temporal and $(1,1)_T$ spatial modulations of the lattice is shown in Figure 5.5, plotted by finding the wavevector with maximum power for each f_L. This dispersion relation is fit well by the dispersion relation for modes produced by N harmonically coupled $(1,1)$ rows of peaks with free endpoint boundary conditions[5], $f_L = f_{BZ}|\sin(ka/(2\sqrt{2}))|$, where f_{BZ} is the frequency at the edge of the Brillouin zone, a the lattice spacing and $k = \frac{n\pi\sqrt{2}}{aN}$ is a wavevector in the $(1,1)$ direction [102]. Here N represents the number of $(1,1)$ rows of peaks in the lattice and $(0 \leq n \leq N)$ is the mode number. We emphasize that there are no fit parameters. N is determined by the number of $(1,1)$ rows and f_BZ is the frequency measured at the edge of the Brillouin zone. For the parameters in Fig. 5.5, $f_{BZ} \approx 2.5$ Hz. While f_{BZ} shows systematic variation with Γ and f_d, it is always approximately a factor of ten lower than f_d.

---

[5]We assume free boundary condition as the row of peaks near the wall is able to translate against the wall in a square cell. In addition, since in the square containers the patterns always form at $\pi/4$ relative to the container, there are always an integer number of $(1,1)$ rows in the container.
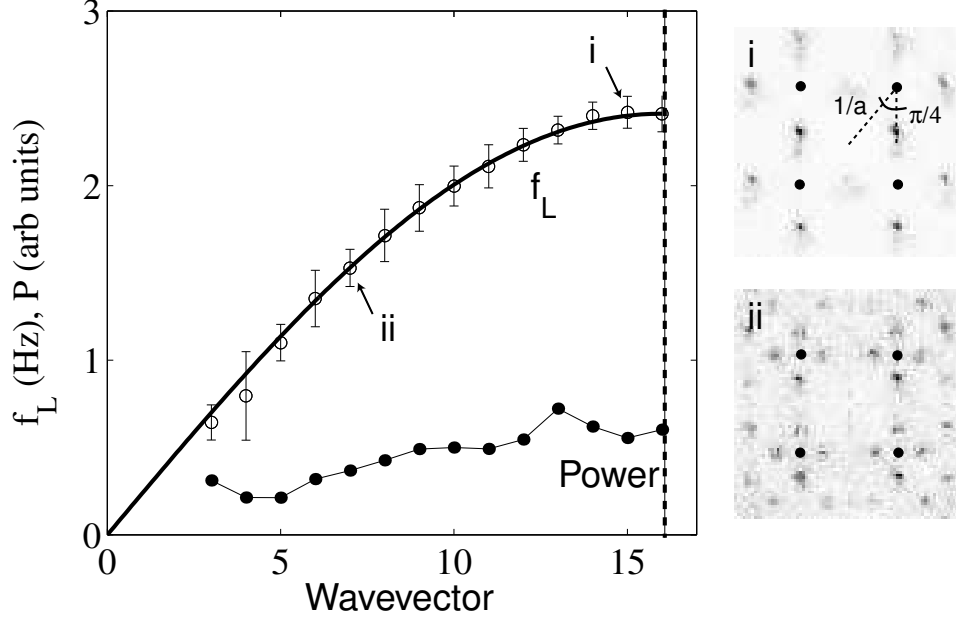
Figure 5.5: Comparison of the measured dispersion relation ($\circ$) for the $(1,1)_T$ normal modes of the lattice with a one dimensional lattice model (solid line) with harmonic coupling between $(1,1)$ rows. The wavevector, n is in units of $\frac{2\pi}{\sqrt{2}aN}$ where a is the lattice constant and N is the number of rows in the $(1,1)$ direction. The dashed line denotes the edge of the first Brillouin zone. The power in each mode ($\bullet$) is evenly distributed among all modes. The images in i and ii show spatial Fourier transforms, $\tilde{I}(k_x, k_y, f_L)$ at two temporal lattice oscillation frequencies, $f_L = 1.2$ Hz and $f_L = 2.3$ Hz, the mode at the edge of the Brillouin zone. For clarity, the location of the four peaks which form the basic square lattice (found at $f_L = 0$ Hz) are shown by $\bullet$ symbols in the Fourier transform images. The grayscale is proportional to $|\tilde{I}|$. Here $f_d = 25$ Hz and $\Gamma = 2.75$.

The power in each mode is also plotted in Fig 5.5. It is roughly independent of the mode, indicating that the system is in contact with an effective constant temperature thermal bath. Note that we cannot observe modes $n = 1$ and $n = 2$. This is due to large scale lighting variation present in the images of the patterns.

5.2.5   Resonant modes

We find that different lattice normal modes are excited with different amplitudes as the basic system parameters, Γ and f_d, are varied. The response of the pattern is found by the same Fourier transform procedure described above. We integrate the power in the dominant sideband after subtracting off a background, which can be present from disorder in the pattern which changes on a time scale longer than the measurement time. The integrated area gives a measure of the total amount of power present in the lattice modes, and this power is plotted as a contour map of lines of constant power absorption in Figure 5.6(a). Two regions of dominant response are seen, and will be referred to as resonance peaks I and II. Sufficiently far from the resonance peaks, the lattice is nearly stationary, with small amplitude, incoherent oscillation of the lattice elements around the mean sites.

The lattice oscillates in different normal modes in the resonance peaks: in the bottom panel of Figure 5.6 we plot the $(1, 1)_T$ dispersion relations measured at four different points in the resonance diagram and the corresponding power in each mode. For points near resonance I, the power is dominant in the Brillouin zone mode ($k = k_{BZ} = 2\pi/(a/\sqrt{2})$) while near resonance II, the power is dominant in a mode near the middle of the Brillouin zone. The even distribution of power found in Fig 5.5 is because this point lies between the tongues, away from the resonances.

Dispersion relations which agree with the harmonically coupled lattice model exist throughout the parameter range of square stability, and the frequency of the edge of the Brillouin zone (the effective spring constant) changes systematically as Γ and f_d are changed. We presently have no explanation for the timescales of the modes, or the resonances which excite these modes.

5.2.6   Disorder and Melting

For Γ and f_d near the peak of resonance II, the amplitude of oscillation of the modes can be large and the patterns often contain dislocation defects. These defects are created by a process in which the amplitude of a mode becomes large enough to locally "break" the lattice. The lattice then re-heals, although imperfectly, leaving a defect which contributes to the disorder of the lattice. This competition between disordering and ordering depends on the amplitude of oscillation of the mode. The disordering can
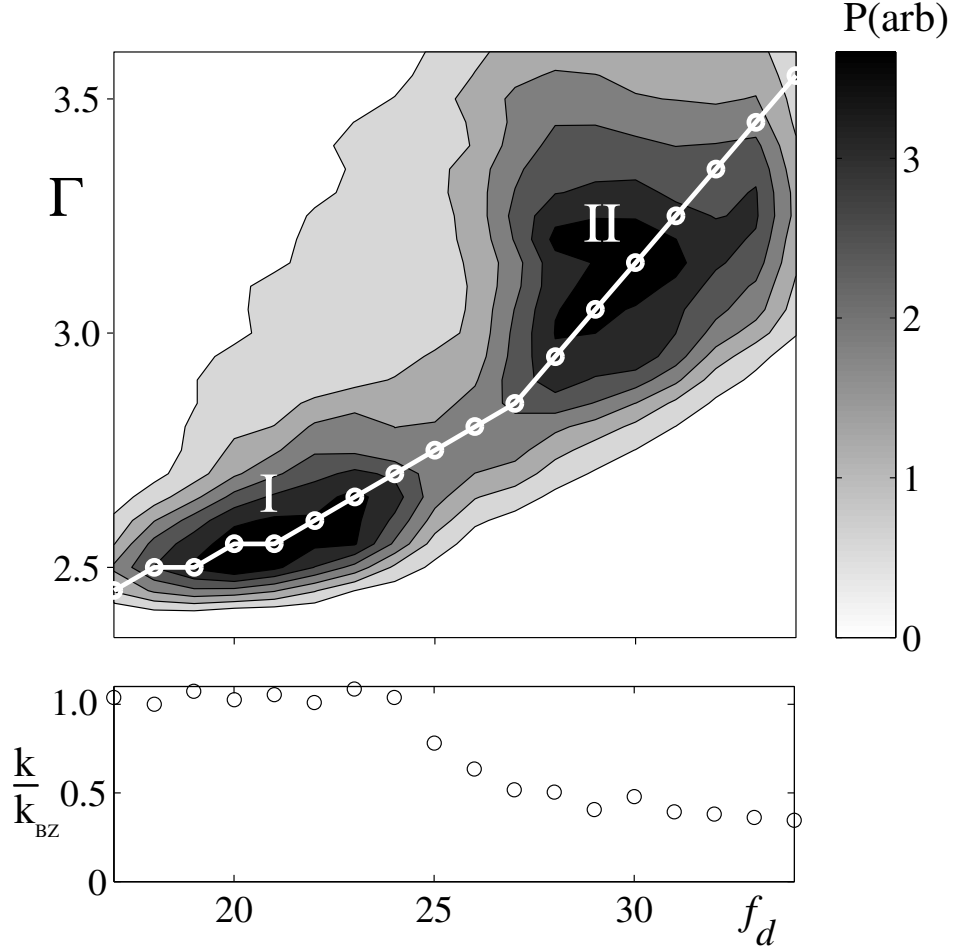
Figure 5.6: Excitation of different normal modes of oscillation for different values of Γ and f_d occurs in two resonance peaks, I and II. Top panel: Lines of constant power show the relative excitation of the lattice in the range of square pattern stability; the grayscale represents the power in the most dominant mode. Bottom panel: The wavevector normalized by the wavevector of the Brillouin zone traced by a path through both resonance peaks. When Γ and f_d are tuned to resonance I, modes at the edge of the Brillouin zone are excited; tuning to resonance II excites lower wavevector modes.
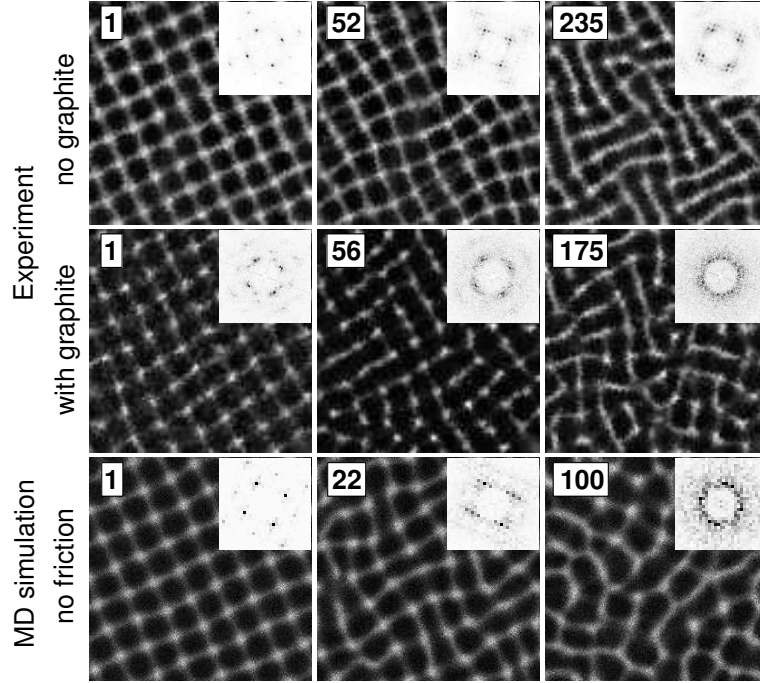
Figure 5.7: Defect creation and melting after a sudden change in system parameters at $t = 0$ for a weakly oscillating pattern at $\Gamma = 2.9$, $f_d = 32$ Hz. (a) At $t = 0$, frequency modulation with $f_{mr} = 2$ Hz and $f_{ms} = 5$ Hz is applied. (b) At $t = 0$ the same frequency modulation is applied for particles which have been cleaned and graphite has been added. (c) Molecular dynamics simulation by Sung Joon Moon: At $t = 0$, the friction coefficient μ between the grains and the plate is set to 0. The intensity is the local density of the grains. The insets in each panel shows the structure factor at the corresponding time.

be further enhanced by resonantly exciting modes using a modulation of f_d; the signal applied to the shaker has the form,

$$y = A \sin(2\pi f_d t + \frac{f_{ms}}{f_{mr}} \sin 2\pi f_{mr} t), \qquad (5.1)$$

where $0 < f_{mr} < 5$ denotes the rate of modulation and $0 < f_{ms} < 5$ denotes the depth of modulation (the span). The lattice responds to the frequency modulation (FM) at exactly $f_{mr}/2$. Details of the lattice response to FM are discussed in Section 5.4.

The top row of Figure 5.7 shows the use of FM to further excite the mode present near the peak of resonance II. Several hundred oscillations after the modulation is turned on, the amplitude of the excited mode is quite large and a few defects have been created.

We have found that the process of disordering can be enhanced by cleaning the bronze particles with acetone and methanol in an ultrasonic cleaner and adding of a small amount of fine graphite powder to the grains [6]. This creates much stronger resonances (the amplitude of oscillation at resonance peaks is much larger), and within several hundred oscillations after modulation is applied, the amplitude of the modes become large enough to completely disorder the lattice, creating a liquid-like time dependent pattern as shown in the middle row of Figure 5.7. We hypothesize that the addition of graphite changes the collisional friction properties between the grains (or between the container and the grains) and we now describe our study of the lattice resonances as a function of friction [7]. We point out that the implementation of friction in the kinetic and hydrodynamic description of granular materials is far from understood and an effect like we have described here can be useful in testing proposed theories. [98]

5.2.7 Friction and lattice melting

Since friction is difficult to change in a controlled way in the experiment, we used an inelastic hard sphere molecular dynamics (MD) code to study the effect of surface friction on the dynamics of the lattices. The simulations were performed by Sung Joon Moon. This code generates patterns which match patterns seen in the experiments for a wide range of Γ and f_d and the details have been reported elsewhere [14].

The effect of suddenly reducing the value of the sliding coefficient of friction μ between the grains and the vibrating plate in shown in Figure 5.7c at fixed $\Gamma = 3.0$ and

---

[6]Extra Fine Graphite powder manufactured by AGS Co, Muskegon, MI

[7]We note that the amplitude of the modes also depend on the bottom plate boundary condition; patterns created in containers with roughened bottoms (sandpaper grit 400 epoxied to the container bottom) show only weak modes and thus almost perfect defect free patterns, even at the peaks of the resonances.
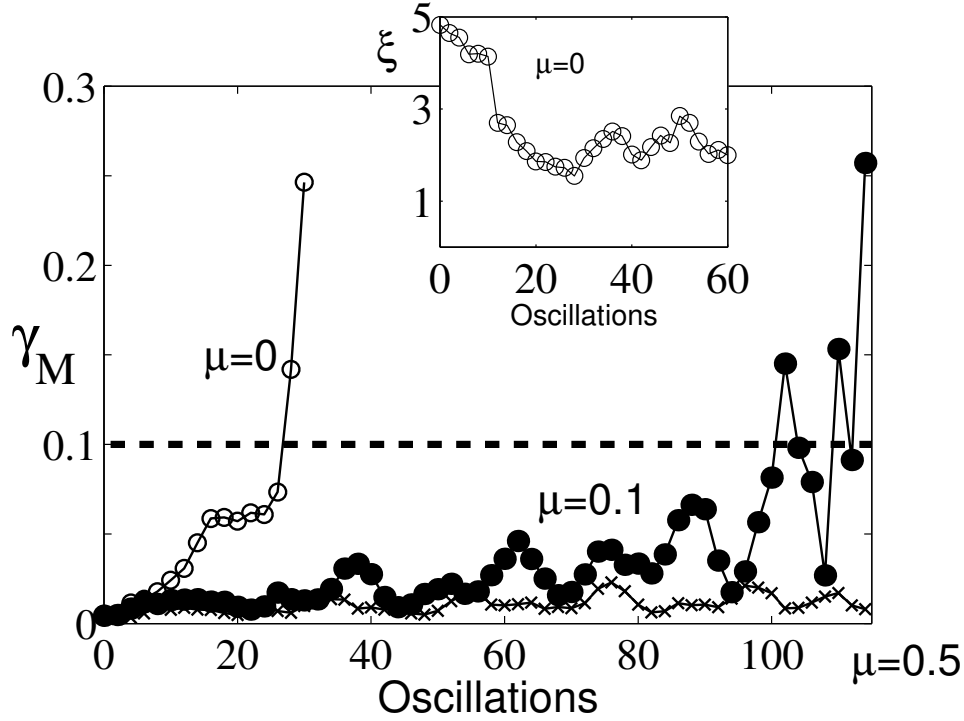
Figure 5.8: Melting occurs when the Lindemann ratio, $\gamma_M = \langle |u_m - u_n|^2 \rangle / a^2$, reaches approximately 0.1. Main figure: γ_M plotted versus time for different values of μ, the friction between the grains and the plate. Inset: The correlation length of the pattern ξ, ($\circ$) (normalized to 1 at $t = 0$) for $\mu = 0$ reaches the minimum value when $\gamma_M \approx 0.1$.

$f_d = 32$ Hz. The value of μ is a fitting parameter in the collision model and does not relate to physical values of the coefficient of friction. The time series is created by initially generating a prefect square pattern at $\mu = 0.5$ (the value chosen to match stable patterns between the MD simulation and the experiment) and suddenly changing the value of μ. At $\mu = 0.5$, the pattern weakly oscillates in a mode of roughly $k_{BZ}/2$ since Γ and f_d are close to resonance II. When μ is suddenly changed to $\mu = 0.0$, the amplitude of this mode begins to grow while the wavevector of the growing mode remains unchanged. As in the experiment, when the amplitude of this mode becomes large enough, the pattern ruptures. The motion is so vigorous that the lattice no longer is able to locally re-crystallize and instead forms a liquid-like state: individual lattice elements no longer maintain a fixed position in the lattice, but undergo large displacements away from their equilibrium sites and may even annihilate or spontaneously create new peaks. This leads to a small fluctuation in the number of lattice elements in the pattern, but we expect the fluctuations to become negligible as the system size increases.

To measure the spatial disorder expected in a transition from an ordered lattice to a disordered fluid, in Figure 5.8 we plot the correlation length of the pattern, ξ versus time (see inset). ξ is calculated by fitting an exponential to the envelope of the azimuthal average of the two-dimensional autocorrelation function and is written in units of a. For $\mu = 0$, ξ decreases monotonically in time from about $5a$ until the lattice disrupts after about 30 plate oscillations, after which it oscillates around $1.5a$ as the lattice continues to locally disrupt and re-heal. As shown in the main section of Figure 5.8, the loss of long range order coincides with the Lindemann ratio $\gamma_M = \langle |u_m - u_n|^2 \rangle / a^2 \approx 0.1$, where u_m and u_n are displacements from lattice positions of nearest neighbor pairs. γ_M is a commonly used criterion for predicting the melting temperatures of solids [172]. We compute γ_M by tracking the motion of peaks of the lattice using an algorithm which works well until the lattice becomes disordered. The value of γ is in agreement with literature values for two-dimensional melting [12] even though melting of the pattern in our experiments occurs in a non-thermal way, driven by a resonantly excited mode of the lattice.

The main figure indicates that a melted state is reached for $\mu = 0.0$ and not at all for $\mu = 0.5$ as $\gamma < 0.1$. For $\mu = 0.1$, the pattern oscillates with increasing amplitude until local melting events disrupt the perfect long-range order. However, this μ does not produce fully melted patterns; after a defect is created, the mode amplitude becomes small and the lattice can locally re-crystallize, as seen in the re-crossing of the $\gamma_M \approx 0.1$ line. This prevents a transition to a fully liquid state. We emphasize that the value of γ_M is somewhat arbitrary and further work is necessary to determine if there is an actual transition that occur at this value. However it does provide a condition for onset of defect creation or loss of long range order away from the primary bifurcation in a nonequilibrium pattern.

5.2.8 Conclusions

We have demonstrated that the square patterns in a vibrated layer behave like a two dimensional lattice and that conditions which govern the dynamics and steady states of real equilibrium lattices apply in this analogous nonequilibrium system. We have also shown a nontrivial effect of friction on the properties of patterns, and such an effect could be useful in judging friction collision models in granular kinetic theories. Whether such concepts and predictive criteria can be applied to other nonequilibrium systems is an interesting and open question.

We note that a study of melting in the lattice should include development of the FM techniques to create a more thermal type of heating of the lattice, such that power is distributed equally in every mode. It would be interesting to study the defect creation

under such forcing, looking for 2D melting transitions such as those predicted by the theory of Halperin and Nelson [85].

5.3   Temporal frequencies of the modes
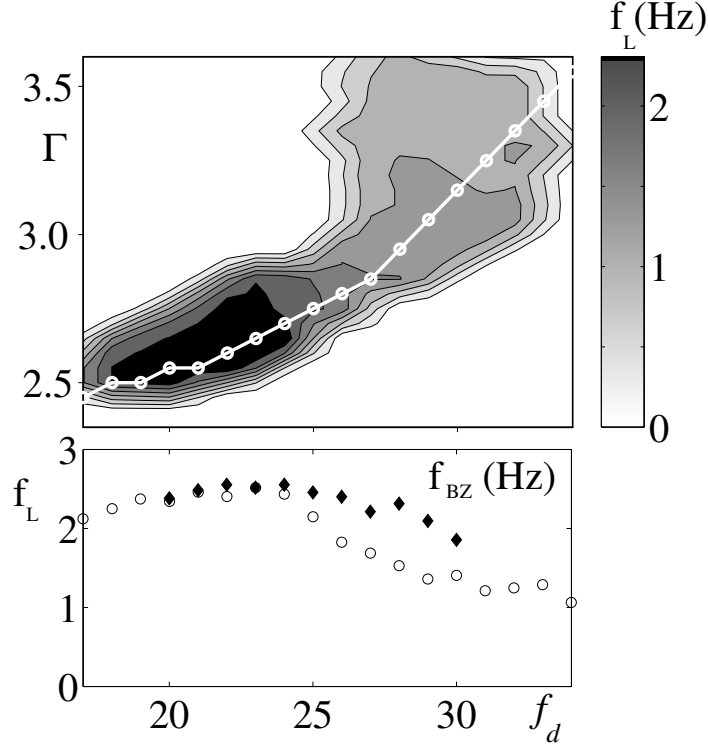
Figure 5.9: The temporal frequencies of the resonantly excited modes. In the top panel, the grayscale represents the frequency of the excited mode, f_L. The bottom panel plots the frequency of the resonantly excited mode along a cut through both resonance peaks, ∘. The frequency at the edge of the the Brillouin zone, f_{BZ} is also plotted, ♦ for a range of the data to show the dependence of f_{BZ} on system parameters.

The resonance diagram of Fig 5.6 shows that the lattice is excited in two main resonance peaks. In peak I, the short wavelength Brillouin zone mode is excited and in peak II, a longer wavelength mode is dominant. In Figure 5.9 we plot the corresponding temporal frequencies of the modes excited throughout the parameter space. The grayscale indicates the frequency of the most dominantly excited mode and shows that the Brillouin zone modes of peak I have frequencies of about 2.5 Hz, while the longer wavelength modes in peak II have frequencies of about 1.5 Hz. The white line is a cut which passes through resonance peaks I and II and the values of the frequency along the cut are plotted in the

lower panel, shown by the ○ symbol.

For data in the middle range of the cut, we were able to find the frequency at the edge of the Brillouin zone, f_{BZ}, and this is also plotted in the lower panel (♦). As expected, in peak I, the most dominant excited mode has the frequency of the Brillouin zone mode. However, as in the wavevector plot in Fig 5.6, near 26 Hz the dominant mode is no longer at the edge of the Brillouin zone and as shown in Fig 5.9 begins to deviate from f_{BZ}. We emphasize that the important feature of the curve is the maximum value of f_{BZ} at around 26 Hz. This indicates that the spring constant of the lattice elements reaches a maximum, and a theory of the normal modes should predict the shape of this curve.

5.4   Frequency modulation and parametric resonance

In this section we present more results from the frequency modulation experiments.

We frequency modulate the container drive frequency by applying a signal to our shaker of the form in Eq 5.1. Shaking at a particular f_d and Γ, we apply the modulation at a specific rate frequency, f_{mr} (rate) and span frequency, f_{ms} (span) and wait a number of cycles (≈ 1000) for transients to decay away. We then take a time series of images and apply the techniques described in the previous section to extract the dominant spatial and temporal modes of the pattern. To summarize our results, we find that a signal with a fixed f_{mr} excites a normal mode with temporal frequency of $f_{mr}/2$ independent of f_{ms}. The normal mode excited has a wavevector determined from the dispersion relation of the crystal at the particular f_d and Γ. We find the the response occurs in a tongue centered on approximately $f_{BZ}/2$ whose width increases as f_{mr} increases.

5.4.1   Temporal response

Figure 5.10 shows the temporal response of the lattice for a fixed f_{mr}, found by Fourier transforming in both space and time and integrating over (k_x, k_y). A forcing frequency of f_{mr} excites oscillation with dominant response at exactly $f_{mr}/2$.

Subharmonic response is found in a a tongue centered approximately around $f_{BZ}/2$ shown in Figure 5.11(a). Figure 5.11(b) shows the measured response near the bottom the tongue, with the integrated power in the $f_{mr}/2$ peak after background subtraction plotted as grayscale pixel for a given f_{mr} and f_{ms}. For $f_{ms} < 0.1$ Hz, there is no subharmonic lattice response; as f_{ms} is increased, a threshold is crossed, and the lattice oscillates in a mode with temporal frequency $f_{mr}/2$, independent of f_{ms}. This threshold is a function of f_{mr}, and the width of the tongue in f_{mr} is an increasing function of f_{ms}.

91
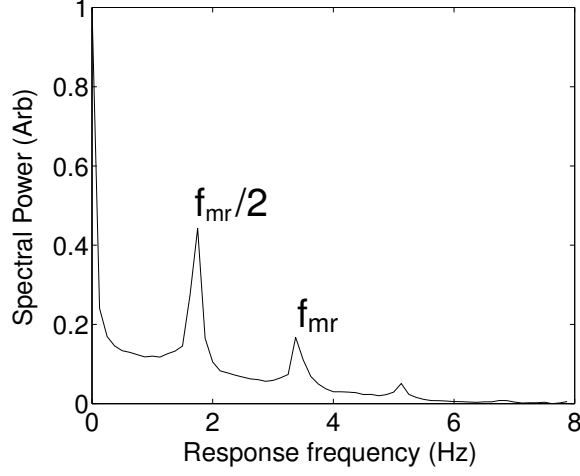
Figure 5.10: The temporal response of the lattice under frequency modulation at $f_d = 32$ Hz and $\Gamma = 2.90$. The imposed rate frequency is $f_{mr} = 3.70$. The strongest response occurs at one half of the imposed rate frequency. The other peaks shown are the harmonics of the $f_{mr}/2$ response.
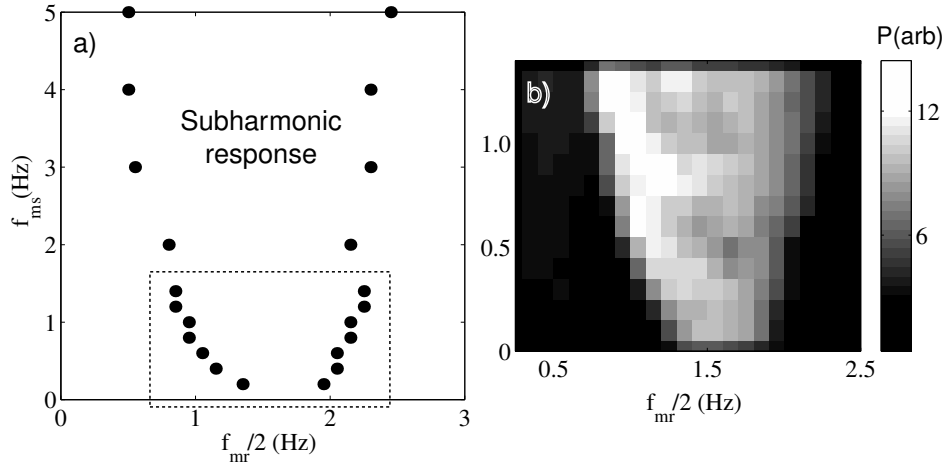
Figure 5.11: (a) The resonance tongue for f_d=32 Hz, $\Gamma = 2.90$. Subharmonic response is found inside the tongue and the width of the tongue increases with increasing f_{ms}. For $f_{mr} \approx 3.0$ above $f_{ms} \approx 4.0$ the crystal order is destroyed. (b) Detail of the lower section of the tongue. The grayscale intensity for each pixel represents the integrated power in the response at a given f_{mr} and f_{ms} after background subtraction.

When f_{ms} is large enough, the amplitude of oscillation of the mode becomes large and the underlying lattice may be destroyed. As shown in the grayscale of the figure, within the tongue, the power absorbed by the lattice decreases with increasing f_{mr} for a fixed

f_{ms}, and is an increasing function of f_{ms} for fixed f_{mr}.

5.4.2 Spatial response

We now examine the spatial response to the imposed modulation–the real space representation of the modes found in Section 2. A few modes are shown in Figure 5.12. As expected, for a fixed f_{ms}, as f_{mr} is increased, the wavenumber of the excited mode increases. Also shown is a schematic which demonstrates the relative motion found in different modes. As before, the modes are excited at wavevectors at $\pi/4$ to the lattice direction, the $[11]_T$ modes.
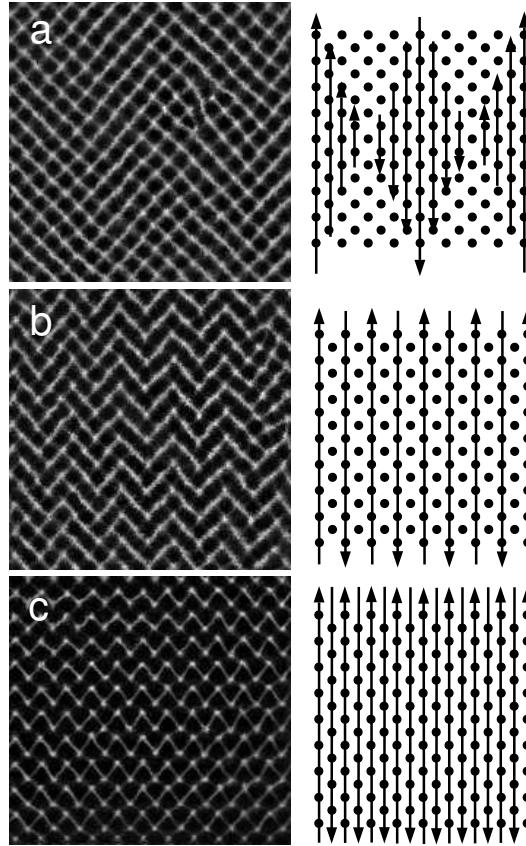
Figure 5.12: (a) and (b) are images taken at f_d=32 Hz and $\Gamma = 2.9$ under frequency modulation for constant $f_{ms} = 4.0$ Hz and increasing f_{mr}, where (a) $f_{mr} = 1$ Hz, (b) $f_{mr} = 2.25$ Hz. The wavenumber of the mode increases with increasing f_{mr}. To the right of each picture, a schematic shows the relative motion of the rows of the crystal in the given mode. The mode shown in (c) is never excited over the range of f_{ms} and is an image of the lattice in resonance peak I, with $\Gamma = 2.65$ and $f_d = 21$ Hz.

In Figure 5.13, we plot the measured wavevectors vs. $f_{mr}/2$ to compare to the form of the dispersion relation found in Figure 5.13. However, from Figure 5.11, we see that the number of modes capable of being excited is a function of f_{ms}. Thus, the range in wavevectors which can be probed (the extent of the dispersion curve) is a function of f_{ms}. This is a limitation of the excitation technique as we discuss below. The dispersion curves found for two different f_{ms} are shown in Figure 5.13. For low f_{ms}, all of the points fit a dispersion relation which is in good agreement with that by natural forcing (see Section 5), but that at larger f_{ms} there is significant deviation for f_{ms} near the center of the resonance band for a fit to the same dispersion relation. We propose that this is because at these f_{mr}, (inset in Figure 5.13), the amplitude of the amplitude of oscillation is large compared to the lattice spacing and may distort the perfect crystal lattice; at such large amplitudes, it is unclear whether the response of the lattice is linear.
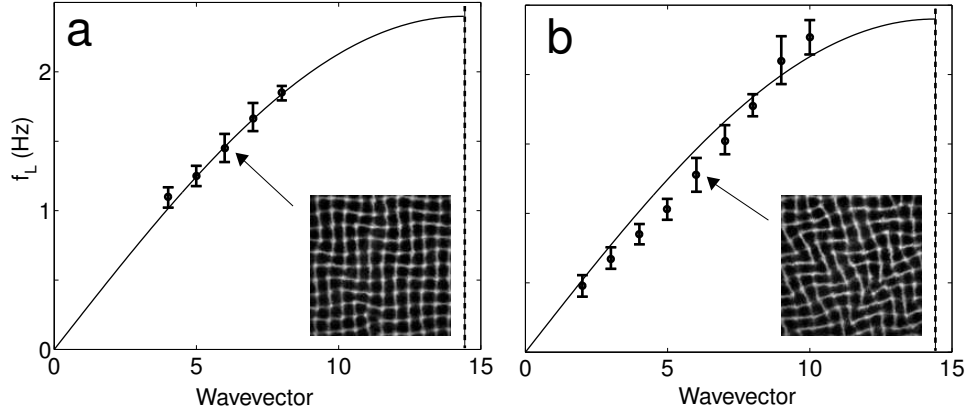
Figure 5.13: Dispersion relations produced by excitation at (a) $f_{ms} = 1.0$ Hz and (b) $f_{ms} = 4.0$ Hz for $f_d = 32$ Hz and $\Gamma = 2.90$. The range of modes excited is a function of f_{ms} and is seen to increase with increasing f_{ms}. The insets show a snapshot of the lattice. Note that the largest deviation from the harmonic fit occurs at the point of large distortions of the lattice.

5.4.3 Discussion of parametric resonance

The presence of a resonant tongue and subharmonic response is typical of systems that are parametrically forced, and the excitation of the lattice by frequency modulation may have features in common with a Mathieu equation modified to include spatial dynamics that has been studied by Rand [149]. We propose that the parametric forcing results from changes in the effective spring constant (f_{BZ}) due to changes in f_d.

Using the frequency modulation technique, we have been unable to excite the highest mode of the lattice. We believe that this is a combination of two factors: Since

the sides of the resonance tongue are very steep, we must apply large f_{ms} in order to excite the modes near the edge of the Brillouin zone. However, if f_{ms} is large enough, the exciting waveform becomes significantly different from sinusoidal and can no longer produce the underlying square pattern.

For a given f_{mr}, the lattice always oscillates at exactly $f_{mr}/2$; this locking is responsible for the spread in the points in Figure 5.13–the same spatial mode can be excited in a range of temporal frequencies. We hypothesize that dissipation is large for each mode: if dissipation were low, at low forcing amplitude (where nonlinear detuning effects are small) each mode would have a sharply defined resonant frequency. Dissipation tends to broaden such response and thus allow locking at exactly $f_{mr}/2$ for any f_{mr}.

5.5 Oscillatory behavior in deep layers

5.5.1 Lattice oscillation in deep layers

The oscillations of the lattice are not specific to shallow layers, but manifest in deeper layers as well. We have observed that for square patterns, at a given Γ and f_d, the Brillouin zone frequencies, f_{BZ} decrease as layer depth increases although no systematic study has been undertaken.

As the depth increases, the number of grains that form each peak increases, and effects of the height of the peak can become important. For thin layers, the peaks move as a single unit and the lattice element approximation is quite good. However, for deep layers, the peaks can become so large that the tips execute significant motion. A snapshot of a peak in a deep layer with a moving tip is shown in Figure 5.14.
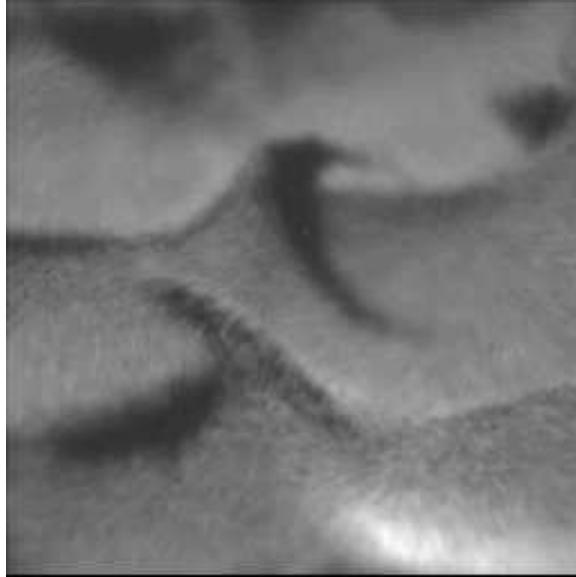
Figure 5.14: A zoom showing that the peaks bend quite dramatically at the maximum lattice oscillation amplitude. $\Gamma = 3.0$, $f_d =$??, N=15.

We observe that the lateral motions of the tips of the peaks are induced by the lateral normal mode motion of the base of the peak. Shown in Figure 5.15 are two images taken in 15 layer bronze particles, taken one lattice mode oscillation apart. The dashed arrow indicates the transverse lattice motion of a particular $(1,1)$ row. Clearly visible are the tips of the peaks–when the lattice mode is at a maximum in amplitude, the tips point in the opposite direction. Thus the tips execute a flopping motion that is exactly out of phase with the normal mode oscillation of the base of the peak. We note that the elements near the boundary are pinned and do not execute transverse oscillation.
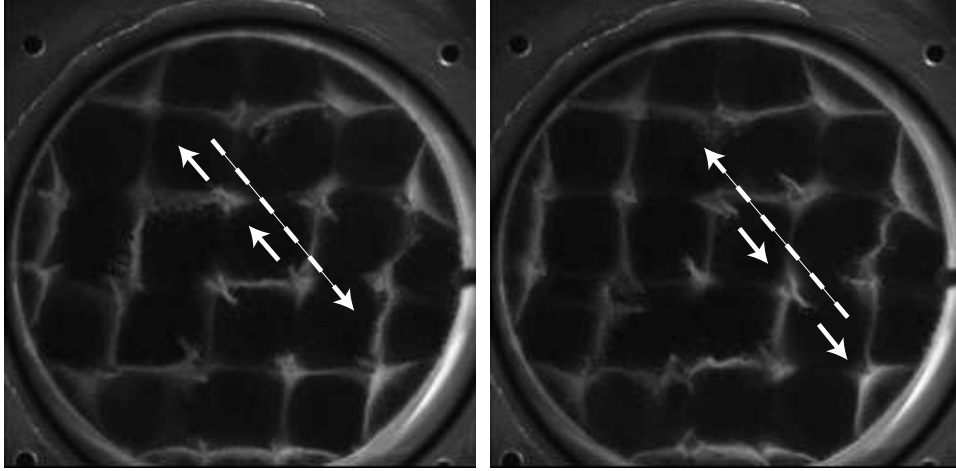
Figure 5.15: A time sequence of images spanning one normal mode lattice oscillation, showing the motion of the top of the peak tied to the pattern oscillation, $\Gamma = 3.0$, $f_d = ??$, layer depth=15. The large dashed arrow indicates the motion of the $(1, 1)$ row while the smaller arrows indicate the motion of the tips of the peaks.

Figure 5.16 further demonstrates that the tip flapping is slaved to the normal mode oscillations of the square patterns. In (a), the system is detuned from the resonance and the positions of the tips of the peaks do not deviate significantly from the position of the base. However, when the system is tuned to a normal mode resonance, the peaks of the peaks execute a strong flapping motion.

5.5.2 Oscillation of 1-d stripe patterns in deep layers

Briefly, I describe a rather surprising pattern which seems to act like a one-dimensional lattice. This was observed in 25 layer 165 μm bronze spheres.

As shown in Figure 5.17, the stripe pattern oscillates in an optical mode like that seen in the experiment on falling liquid columns. This oscillation occurs at $f_d/4$. This is an example of a $(1, 0)$ mode and is surprising, as this compressional mode is never seen in the two-dimensional lattice patterns. It may be due to the softening of the effective compressional springs between row elements. When Γ is increased slightly, the roll acts like a set of coupled strings. The observation of the optical mode indicates that a Coullet type argument might be useful in describing the dynamics of these stripe patterns [33][8]

---

[8]Oscillatory behavior of the string-type has been observed in roll patterns in Rayleigh-Bénard convection in CO_2 by Karen Daniels – private communication.
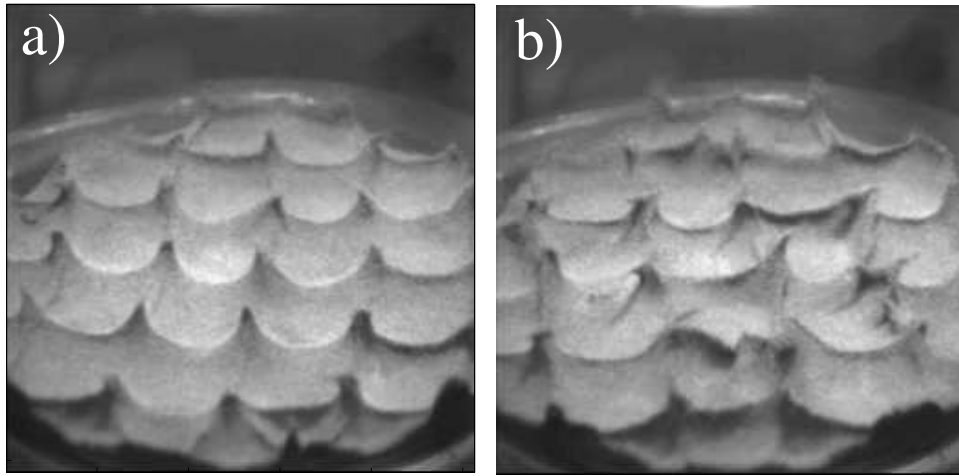
Figure 5.16: The tops of the peaks do not oscillate coherently when the system is detuned from a resonance. (a) The system is detuned from a normal mode resonance, $\Gamma =$??, $f_d =$??. (b) Tuning to the resonance excites the motion of the tips of the peaks. $\Gamma =$??, $f_d =$??, layer depth 15.
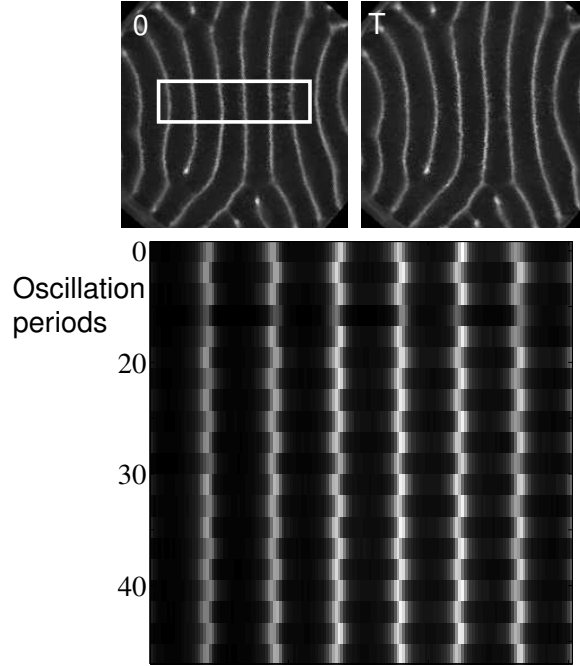
Figure 5.17: Top panel: Stripe patterns taken two plate oscillations apart. Bottom panel: A time sequence of stripe patterns in 25 layers, $\Gamma = 3.65$, f_d=27 Hz. The entire length of the stripes vibrates in an optical mode. The space-time diagram is calculated by plotting a row of pixels (in the middle of the box, perpendicular to the roll) as a function of time and shows the $f_d/4$ optical mode oscillation. The time series was taken at $f_d/2$.
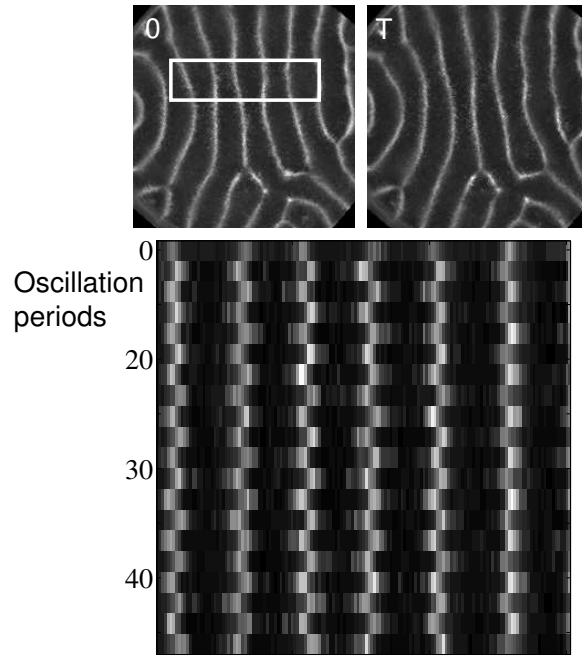
Figure 5.18: Top panel: Same as the previous Figure, but Γ is slightly higher. The amplitude of oscillation is larger and the mode develops a transverse structure: Different points on the roll expand and contract out of phase and this repeats every four oscillation periods. Bottom panel: Space-time diagram for a row of pixels perpendicular to the roll

5.6 Comparison with previous Work

5.6.1 Square patterns

The most detailed work on nonequilibrium square patterns has been done in a vertically oscillated container of liquid — the Faraday instability. Lattice dynamics of the type described above is not seen in this system. As the container acceleration is increased, the square patterns become time dependent due to defect creation; for large enough forcing amplitude, a large amount of defects are created and the pattern becomes spatio-temporally chaotic as shown in Figure 5.19. Several groups have studied these transitions and found that the defects are created due to a transverse amplitude modulation instability [29, 40, 59, 178, 199]. It was found that the disordering of the pattern does not occur through a two-dimensional melting scenario like that described by Halperin and Nelson [85]. Could the Lindemann criterion describe this melting? Although the "peaks" in the Faraday pattern are not as localized as the peaks in the granular square pattern, it would be an interesting to determine if the elements of the Faraday pattern interact similarly to the waves described in this chapter.

5.6.2 Secondary instabilities of one-dimensional patterns

We have shown that phase disturbances of square patterns in a shaken granular layer propagate in an oscillatory fashion. However, most patterns studied in nonequilibrium systems show diffusive behavior [35]–perturbations to the local phase of the pattern relax according to phase diffusion equations. We now discuss other systems in which propagating phase dynamics have been seen. We emphasize that the dynamics seen in our square patterns are unique: while other groups have reported bifurcations to secondary oscillatory instabilities with a specific wavevector modulation of a one-dimensional pattern, the lattice patterns act like a coupled array whose dynamics is governed by a dispersion relation that contains all possible lattice modulations.

Most of the systems for which oscillatory behavior has been observed are one-dimensional: these systems form patterns in which the "elements" collectively oscillate in a mode or many modes. A good example of a nonequilibrium system that displays oscillatory dynamics is the Taylor-Couette system studied by Wu et al. When a sudden perturbation was applied to one end of the container, propagating phase perturbations to the Taylor rolls were seen [197]. Analysis revealed a coupled set of phase equations which had damped oscillatory solutions [21].

In an experiment on falling liquid columns, Wesfried [64–66] found that the columns would spontaneously begin to oscillate in a particular mode (the so-called optical mode) as the distance between the columns was changed beyond a critical value, as shown in Figure 5.20
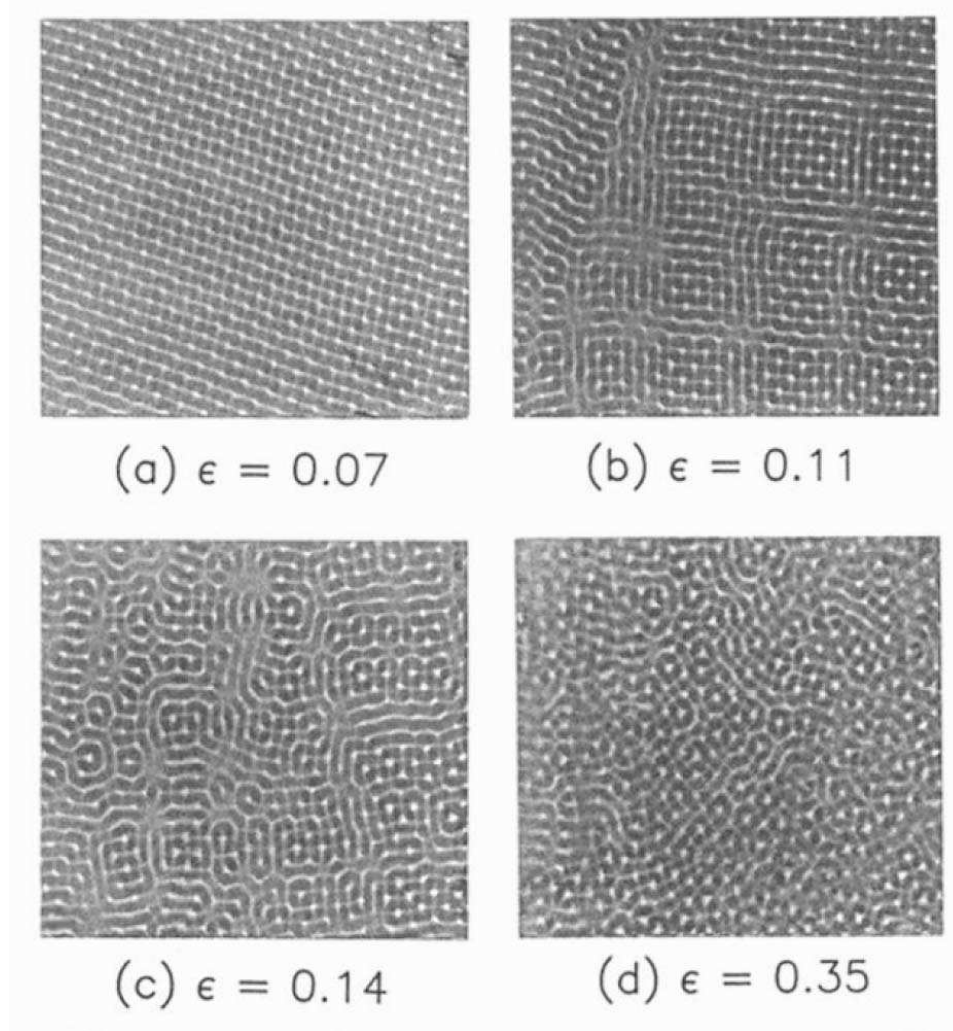
Figure 5.19: Images of capillary wave patterns in n-butyl alcohol for four driving amplitudes $\epsilon = (A - A_c)/A_c$, where A_c is the threshold for waves. The region shown, about 20% of the cell is 3.5x3.5 cm². From [178].

Such spontaneous oscillation in a particular mode has also been seen in an annular Faraday system [48], in a narrow Rayleigh-Benard system [50], and in viscous fingering experiments [131].

A theory which classifies the types of secondary instabilities of one-dimensional patterns has been advanced by Coullet and Iooss. It is based on symmetry arguments and predicts ten possible types of secondary instabilities [33]. They find that the oscillatory modes can either have a wavelength twice the roll space, or a period irrationally related to the base wavelength. It would be interesting to determine whether this theory can
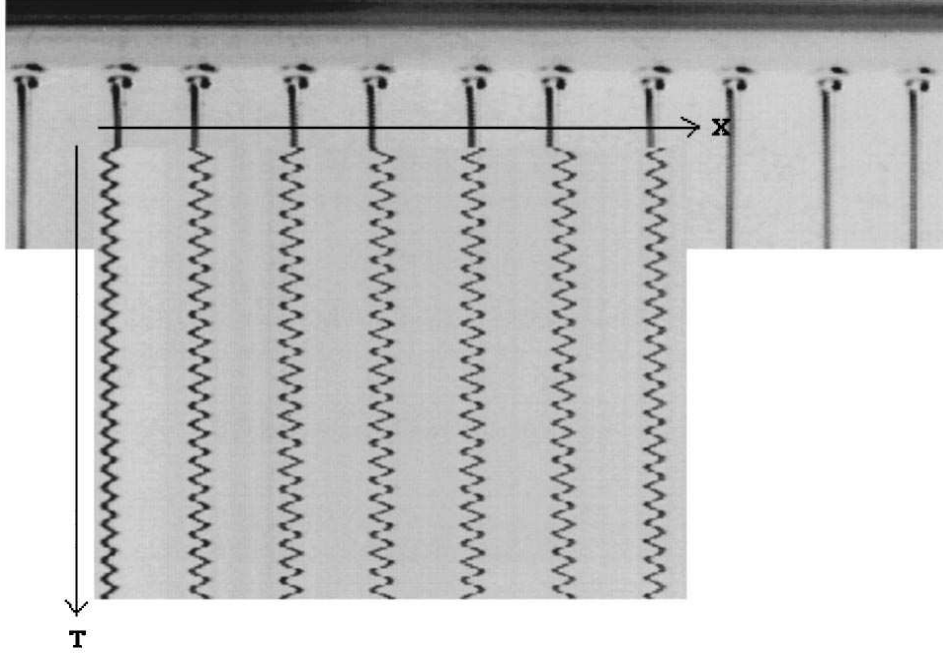
Figure 5.20: Array of liquid columns observed below a horizontal cylinder along which a liquid is flowing from top to bottom at a constant rate. Inset: space-time diagram of the array of liquid columns for fixed boundary conditions (optical mode). From [66].

be extended to two-dimensional patterns as work has been done to classify the possible secondary bifurcations of square patterns [96].

However, we find that our experiment does not fall into this classification scheme, as we can excite all modes of the square lattice. Furthermore, the modes of the lattice are excited resonantly, thus a theory of bifurcation is probably irrelevant. However, the "optic mode" oscillations of the stripe pattern are effectively one dimensional and may fall into the classification scheme.

5.7 Open questions

We have shown that a pattern generated in a layer of vibrated granular material displays behavior associated with a collection of localized interacting elements (lattice elements). There are many open questions in this study, and here we address some of them.

1. What mechanism is responsible for an effective potential between the lattice elements? Any proposed mechanism should address these two other questions: Why are the modes seen only in the $\pi/4$ direction? What sets the frequency at the edge of the

103

Brillouin zone, and why is it so much smaller than the natural drive frequency of the container? The dependence of mode frequencies on layer depth should also be addressed.

2. Where do the resonances in the natural response come from and by what resonance mechanism can a system which is vibrating at f_d excite a mode which oscillates with a frequency which is an order of magnitude smaller? A satisfactory explanation of the resonance should explain the excitation of the k_{BZ} mode in resonance one, and the sudden jump to a mode of roughly twice the wavelength.

We note that the mode seen in resonance I is very difficult to excite using the FM due to the steepness of the tongue as a function of f_{ms}, but is easily excited when Γ and f_d are tuned to the parameters near resonance I. This implies that the mechanism of excitation in the resonance is different than a frequency modulation.

3. Is an approach which treats a pattern as a collection of elements (lattice elements) useful, and can it address questions which an amplitude equation formalism cannot? Can it be treated in an amplitude equation formalism? There is a general theory of secondary instability on cellular patterns due to Iooss and Coullet [33] which uses symmetry arguments to predict bifurcations to instabilities at twice the wavelength of the underlying pattern. The fact that we see such a mode may be coincidence, and this mechanism seems unlikely, as it predicts a bifurcation, and we see a resonance. Is there a feature of the pattern we can explain with a lattice dynamics model which could not have been explained using amplitude equations? The fact that we can make a prediction about the stability of a nonequilibrium pattern using a melting criterion from lattice dynamics is a sign that this approach could have merit.

4. Effectively, the lattice patterns produce a reduction of the partial differential equation describing a hydrodynamic field (the waves) to a coupled set of ordinary differential equations describing concentrated regions of the field (the lattice elements). Can such a property be derived for wave phenomena in general, or does it rely on the fact that the density field of the square pattern has steep gradients?

Chapter 6

Wavelength evolution, noise induced patterns, phase discontinuities, and segregation in vibrated granular layers

The chapter deals with several different phenomena in vibrated granular layers. The first section studies the evolution of the wavelength of a pattern following a sudden change in Γ from below to above onset. The second section examines fluctuations in the layer below the onset of patterns. The third section describes phenomena associated with phase discontinuities present at higher Γ.

6.1 Wavevector selection and evolution after a quench

6.1.1 Introduction

Building on our studies of the time evolution of disorder in patterns in Chapter 4, in this section we investigate the behavior of the average wavelength of the pattern after a sudden change in Γ. Γ is changed from below a flat state below the onset of patterns to above onset at constant f_d. Examples of the type of sequences we will analyze are shown in Figure 6.1. We will show that evolution of the wavevector following a quench in Γ is a consequence of a fluidization of the layer.

The question of asymptotic wavevector selection is an important one in pattern formation in nonequilibrium systems and no clear cut criterion works for all cases. The most linearly unstable mode controls the wavevector very close to onset, but further from the bifurcation, no theory has been developed [35].

6.1.2 Evolution of the wavevector–observations

All of the experiments we will present monitor the average wavevector q_0 as a function of time following a jump from $\Gamma = 2.2$ to a final value of Γ. The jumps are done at constant f_d and images are recorded at either f_d or $f_d/2$. We also verified that the phenomena described did not depend on the initial state. The acceleration of the plate is also monitored during the experiment and this allows precise determination of the initial quench time. Also, perturbations of the acceleration due to the impact of the layer with
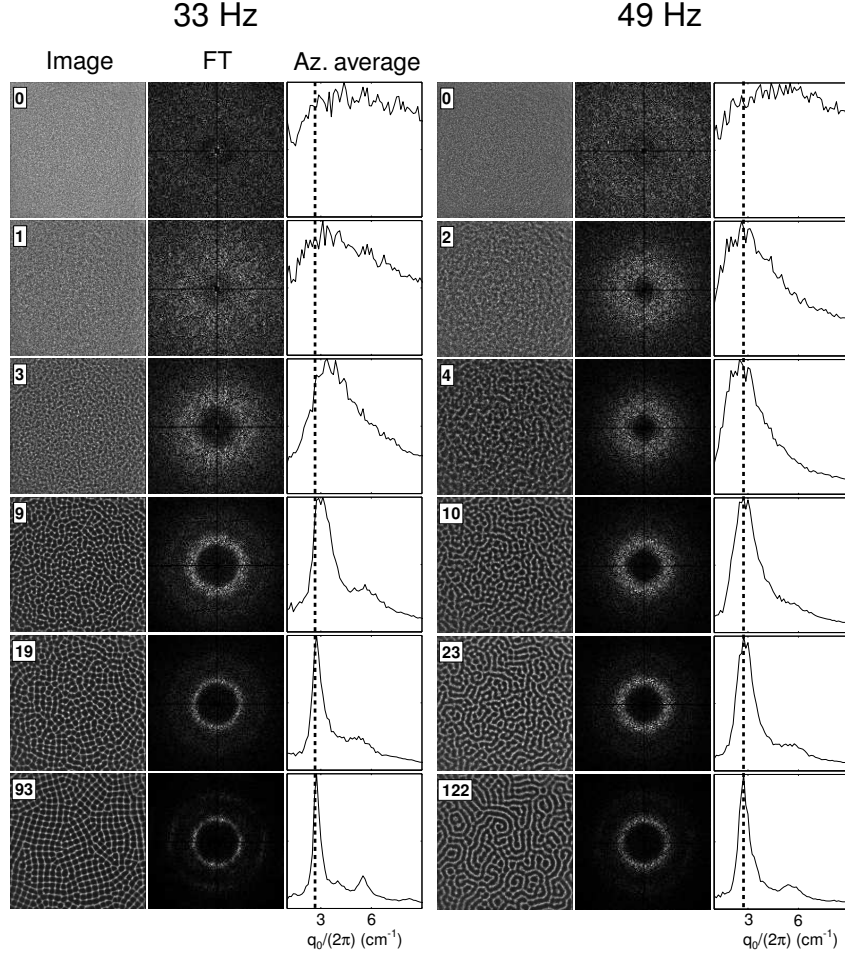
Figure 6.1: The time evolution of pattern after sudden change in control parameters for two different frequencies. For a given frequency, the columns correspond to an image of the granular layer, the modulus of the Fourier transform of the image, and the azimuthal average of the Fourier transform. For (a) 4 layer, $f_d = 33$ Hz, $\Gamma = 2.2 \rightarrow \Gamma = 3.0$, q_0 decreases with time, while in (b) 7 layers, $f_d = 49$ Hz, $\Gamma = 2.2 \rightarrow \Gamma = 3.0$, q_0 increases with time. The dashed vertical lines are to guide the eye and represent the asymptotic value of q_0. The time units are in plate oscillations.

the plate are used to characterize the average dilation of the layer as function of time. We will discuss acceleration data later in this section.

To determine q_0 of the pattern, each image is Fourier transformed and the azimuthal average is computed. The region above the half maximum of intensity in the main peak in the azimuthal average is fit to a Gaussian and we define q_0 as the mean of the Gaussian. Fourier transforms and azimuthal averages for two time sequences are

106

shown in Figure 6.1 [1].
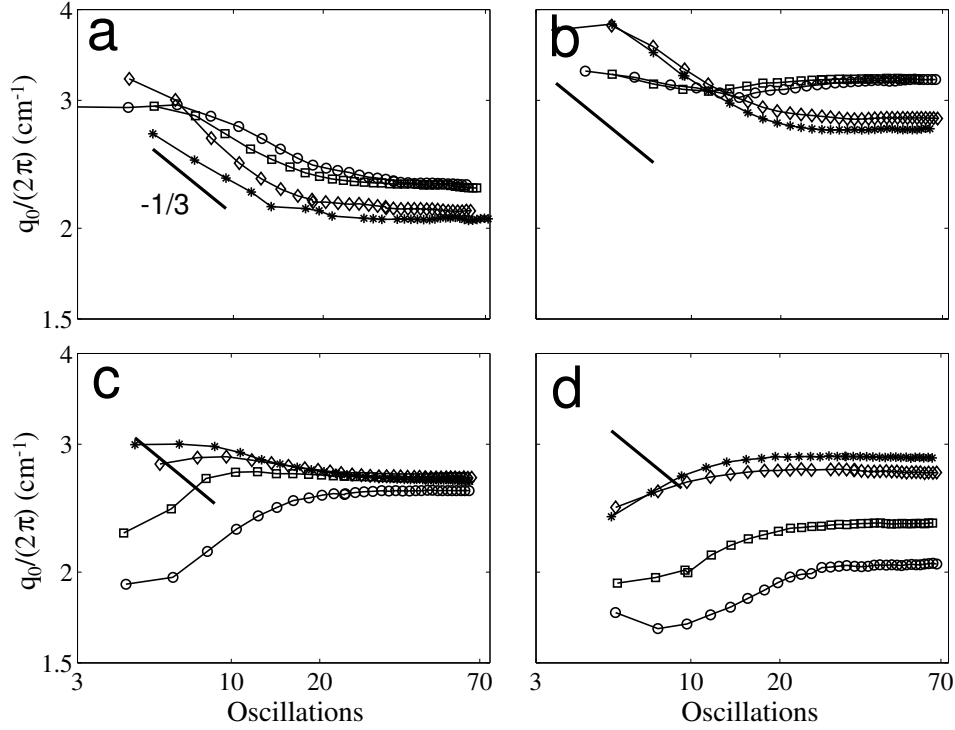
Figure 6.2: The time evolution of q_0 after a rapid jump from initial $\Gamma = 2.2$ to final Γ for constant f_d. In each panel the f_d, N, and initial $\tilde{v}$ of the jumps are (a) 27 Hz, N=4, $\tilde{v} = 3.16$ (b) 33 Hz, N=4, $\tilde{v} = 2.59$ (c) 40 Hz, N=7, $\tilde{v} = 2.13$ (d) 49 Hz, N=7, $\tilde{v} = 1.74$. Each panel shows jumps to increasing final Γ and final $\tilde{v}$ denoted by symbols $\circ$, $\square$, $\diamond$, $*$, with the final Γ: (a) $(2.65, 2.70, 2.95, 3.18)$, (b) $(2.55, 2.58, 3.10, 3.40)$, (c) $(2.75, 3.20, 3.35, 3.8)$, (d) $(2.48, 2.60, 2.85, 2.98)$ and the final $\tilde{v}$: (a) $(3.81, 3.88, 4.24, 4.56)$, (b) $(3.0, 3.03, 3.64, 3.99)$, (c) $(2.67, 2.68, 3.10, 3.24)$, (d) $(1.96, 2.06, 2.26, 2.36)$.

Figure 6.2 shows the time evolution of q_0 for different values of f_d and Γ plotted on log-log scales. We observe that for low f_d (Figure 6.2a), q_0 is monotonically decreasing during the first 10-20 oscillations. For large f_d (Figure 6.2d), q_0 typically increases. We will argue that this difference in behavior is due to the fluidization of the initially flat layer.

For intermediate values of f_d, we find that for low Γ, q_0 increases with time. As Γ is increased, q_0 begins to decrease as a function of time, and the rate of decrease of q_0 with time increases for increasing Γ. However, the Γ at which this crossover occurs is a

---

[1]We note that a broad peak in the power spectrum is visible even below onset and we will discuss the significance of the peak in Section 6.3
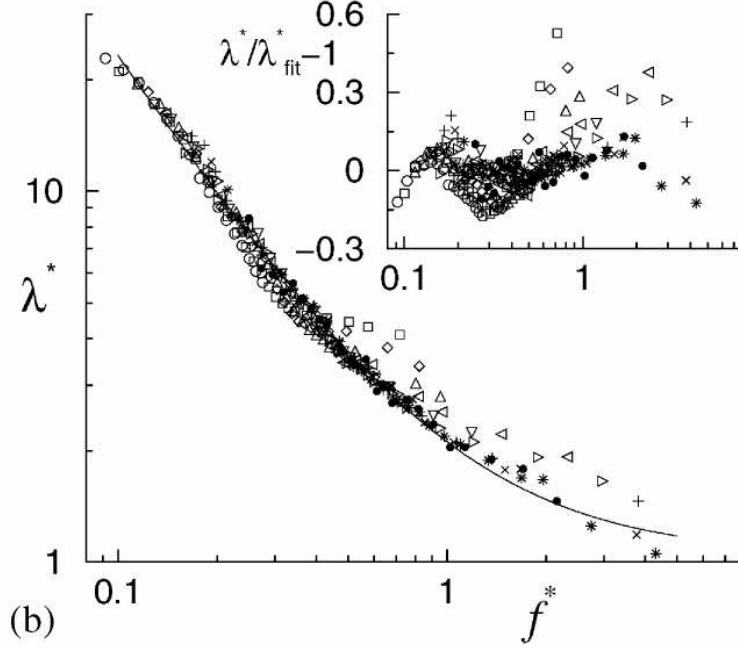
Figure 6.3: Dispersion relation taken for fixed Γ at constant particle size and varying particle depth obtained in [181]. The different symbols represent different dimensionless layer depths, $N = h/D$, where h is the layer depth and D is the grain diameter. The fit is to $\lambda^* \equiv \lambda/h = 1.0 + 1.1(f_d/\sqrt{h/g})^{-1.32}$. Thus, $q_0 = 2\pi/\lambda \sim f_d^{4/3}$. The inset show the deviation of the data from the fit.

function of f_d. For example, at $f_d = 33$ Hz (Figure 6.2b), we find that q_0 increases for $\Gamma < 3.0$ and decreases for $\Gamma > 3.0$. A similar behavior is seen Figure 6.2c for $f_d = 40$ Hz, but there the crossover occurs at $\Gamma \approx 3.3$.

We have observed that both crossover points occur when the normalized collision velocity between the plate and the grains at the final Γ, $\tilde{v} = (2\pi A f_d)/\sqrt{Dg}$ reaches a value of $\tilde{v} \approx 3.0$. Here A is the amplitude of oscillation of the plate, D is the grain diameter and g the acceleration of gravity. The values of $\tilde{v}$ for a given jump are given in the caption of Figure 6.2. $\tilde{v}$ is a parameter which has been shown to correspond to a transition in grain mobility within the layer [181]. For $\tilde{v} > 3.0$, the collision velocity between the layer and the plate is large enough to dilate the layer enough to allow grains to slip past each other in the horizontal direction during some portion the oscillation cycle. Thus the layer is fluidized for some fraction of the cycle and the waves are hydrodynamic-like. These are typically low frequency waves and follow the dispersion relation shown in Figure 6.3, with $q_0 \sim f_d^{4/3}$.

For $\tilde{v} < 3$, plate does not impact the layer with a large enough collision velocity to dilate the layer significantly and the grains are unable to move past each other in the

108

horizontal direction. The layer does not fluidize and instead acts like a weak solid—the excited waves are bending motions of the solid. These are non-hydrodynamic excitations of the layer and the dispersion relation for q_0 deviates from the $f_d^{4/3}$ scaling. This is seen in the residual plot in the inset. As the frequency is increased, $\tilde{v}$ decreases and the fit no longer represents the data.

To investigate the role of $\tilde{v}$ after the jump on the evolution of the wavevector, in Figure 6.4 we plot the average slope in the initial scaling region as a function of $\tilde{v}$ for all data sets . As $\tilde{v}$ increases, the value of the average slope decreases until it reaches 0 at approximately $\tilde{v} = 3$. For large $\tilde{v}$, the average slope has a value of roughly -0.3. We hypothesize that the crossover in the slope of the evolution of q_0 shown in Figure 6.4 occurs at $\tilde{v} = 3.0$ due to changes in nature of the supported waves: for jumps such that the final $\tilde{v} > 3.0$, the layer undergoes a fluidization process, becoming dilated enough to support sloshing hydrodynamic waves. For a final value of $\tilde{v} < 3.0$, the layer does not dilate enough to fluidize. Therefore, we propose that the evolution of q_0 should be strongly influenced by the time-fluidization of the layer and we now use the accelerometer data to study the transient fluidization.

6.1.3   Fast fluidization of the layer after a jump

In figure 6.5, we present the accelerometer signal of an accelerometer attached to the plate recording during the jump for $f_d = 33Hz$ for a jump from $\tilde{v} = 2.6$ to $\tilde{v} = 3.5$. The accelerometer signal is almost sinusoidal but because of the finite mass of plate, perturbations are present. When the layer impacts the plate, the collision creates a spike in acceleration. We find that the spike can excite the high frequency modes oscillatory "ringing" modes of the container. We discuss our interpretation of the ringing below.

In Figure 6.6, we plot the accelerometer signal for single cycles 100 cycles before and 500 cycles after the jump in acceleration. The left column shows a jump from below $\tilde{v} = 3.0$ to *above* $\tilde{v} = 3.0$, while the right column shows a jump from below $\tilde{v} = 3.0$ to *below* $\tilde{v} = 3.0$. The patterns that form from the jumps are shown in Figure 6.1.

We examine the structure of the perturbation: For both cases, below the onset of waves the perturbation signal consists of a large spike followed by a high frequency ringing of the plate. Above onset, there is a difference. For the case where the final $\tilde{v} > 3$, the ringing is not present. When the jump is made so that the final $\tilde{v} < 3$, the ringing persists asymptotically. This is revealed in the Fourier spectra of the subtracted signal shown in Figure 6.7. The ringing mode of the plate has frequency of roughly 1 kHz.

We propose that the compact unfluidized layer below $\tilde{v} < 3$ hits in a sudden impact, with a short collision duration. The impact is sharp enough to cause the plate
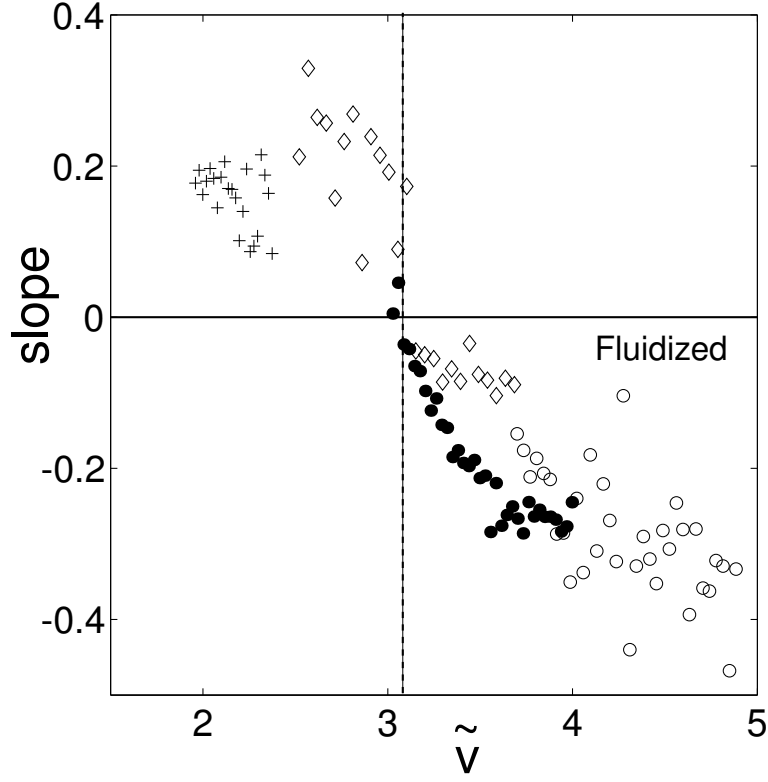
Figure 6.4: The slope in the transient region plotted as a function of $\tilde{v}$ for ($\circ$) $N = 4$, 27 Hz, ($\bullet$) $N = 4$, 33 Hz, ($\diamond$) $N = 7$, 40 Hz, ($+$), $N = 7$, 49 Hz
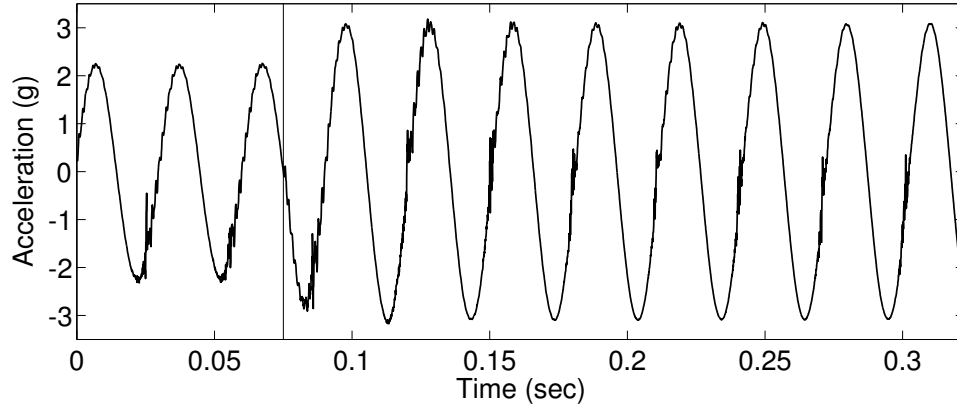
Figure 6.5: The acceleration of the container during a jump in acceleration. $f_d = 33$ Hz, Initial $\Gamma = 2.2$, final $\Gamma = 3.0$
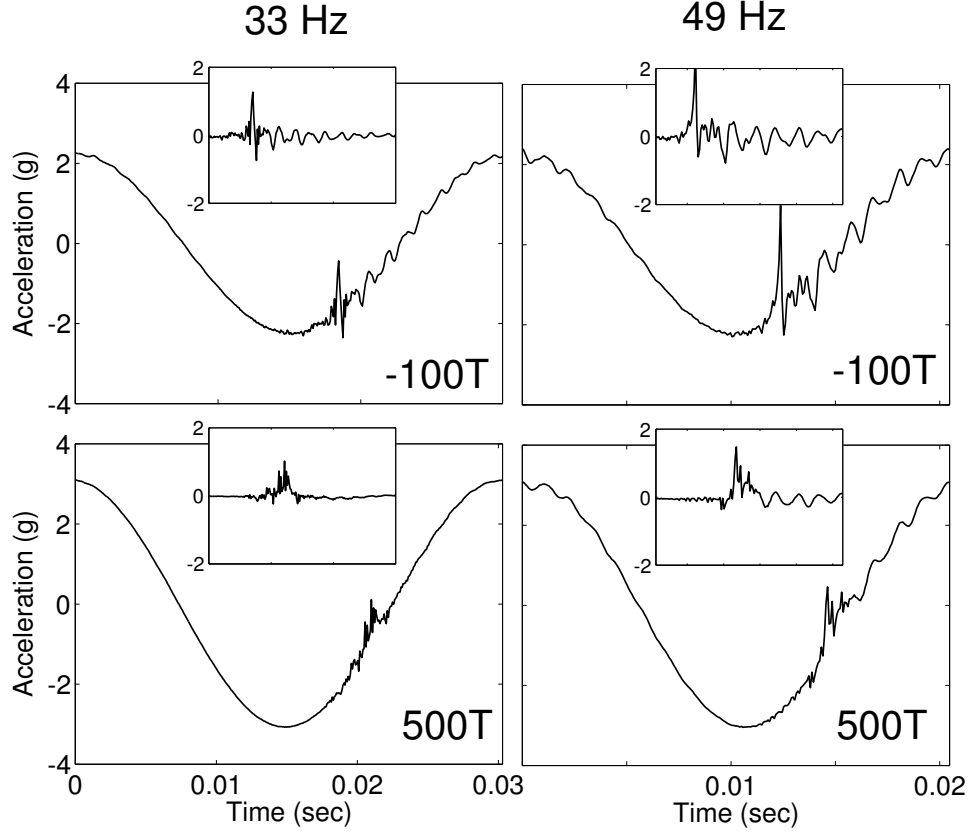
Figure 6.6: The accelerometer signal for a cycle at two different frequencies taken 100 oscillations before the jump and 500 oscillations after. Left column: $f_d = 33$ Hz, $\Gamma = 2.2 \rightarrow \Gamma = 3.0$, $\tilde{v} = 2.6 \rightarrow \tilde{v} = 3.5$ (fluidized layer), Right column: $f_d = 49$ Hz, $\Gamma = 2.2 \rightarrow \Gamma = 3.0$, $\tilde{v} = 1.74 \rightarrow \tilde{v} = 2.4$ (layer not fluidized)

to ring at its natural frequency. The impact of the more dilated fluidized layer for $\tilde{v} > 3$ occurs over a longer time and may also damp the oscillations of the plate. The result is that the fluidized layer impact does not cause the plate to ring.

Since the ringing of the plate characterizes the fluidized state of the layer, we will use this signal to study the evolution of fluidization of the layer during the quench.

Evolution of fluidization

To make correspondence between the evolution of the wavevector and the rapid fluidization of the layer, we plot a time series of the impact event in Figure 6.8 for jumps above and below $\tilde{v} = 3.0$. There is a marked difference in the evolution of the perturbation. Above $\tilde{v} = 3.0$, the spike quickly spreads out, and the ringing stops within
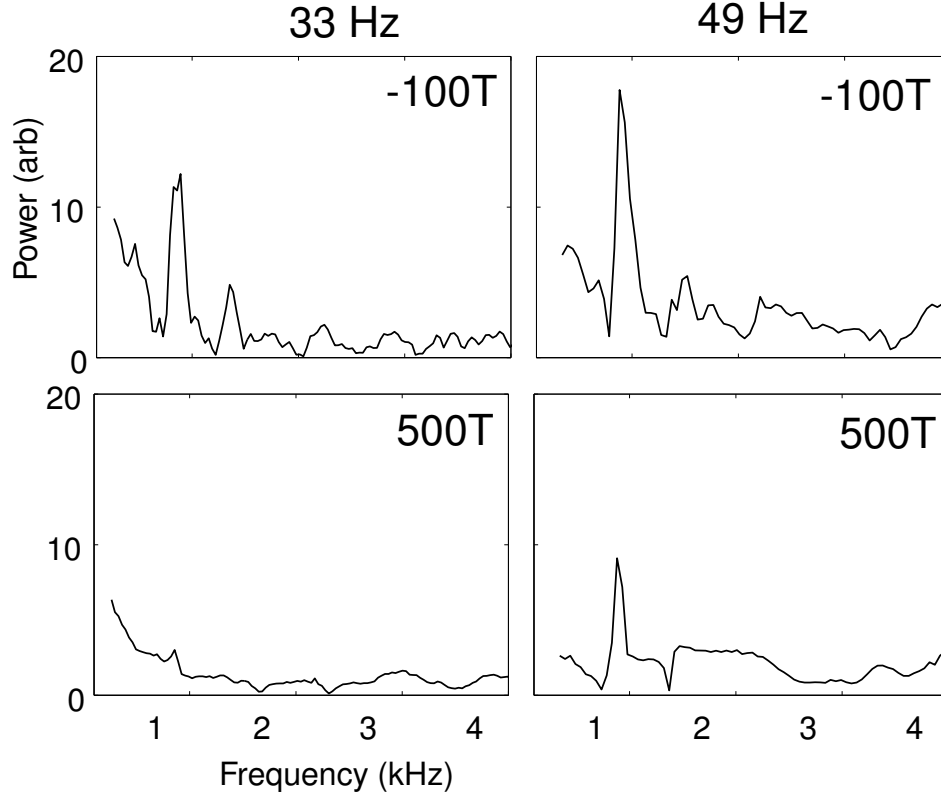
Figure 6.7: The Fourier spectra of the insets of Figure 6.6.

a few cycles indicating that it rapidly becomes fluidized. Below $\tilde{v} = 3$ the ringing never decays. We emphasize that patterns like those in Figure 6.1 form in both experiments.

We propose to characterize the fluidization process by measuring the integrated area under the 1 kHz peak. The evolution of the fluidization process is plotted in Figure 6.9. For the jump with $\tilde{v} > 3$, the power in the 860 Hz mode quickly decays away, reaching the noise floor. In the jump with $\tilde{v} < 3$, the power decays initially and then remains a constant value.

We have demonstrated that the layer fluidizes during the jump and we use this idea to propose a mechanism for change in q_0 as a function of time.

6.1.4   Proposed mechanisms for wavevector evolution

Here we discuss two possible explanations for the time evolution of q_0 and give a possible argument for the scaling of the wavevector as a function of time for $\tilde{v} > 3$.

112
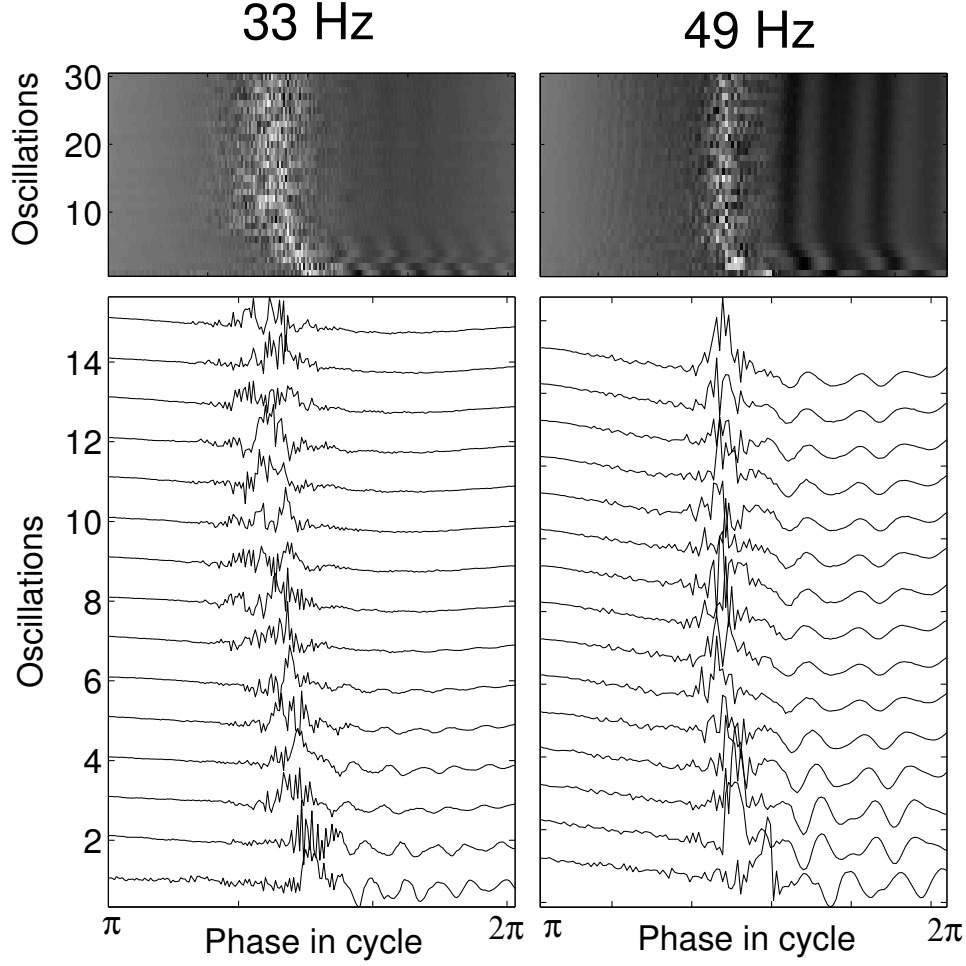
Figure 6.8: Time sequences of the perturbation signal. Top panels: Space-time diagram for 30 oscillations after the change in Γ. The amplitude of the acceleration is represented by the grayscale, black to white. Bottom panels: Time traces of the first 15 oscillations after the jump. The parameters of the jumps are the same as those in Figure 6.6.

Fluidization changes wavevector

We propose that the evolution of the wavevector is governed by the how the material properties of the layer change with time. Since the properties are strongly dependent on the state of fluidization of the layer, there should be a dramatic difference for the evolution of q_0 between jumps to $\tilde{v} > 3$ and jumps to $\tilde{v} < 3$ and this difference is clear from the scaling exponent shown in Figure 6.4.

Jumps to $\tilde{v} > 3$

Figure 6.10 shows a jump for $\tilde{v} > 3$. The wavevector stops decreasing after the
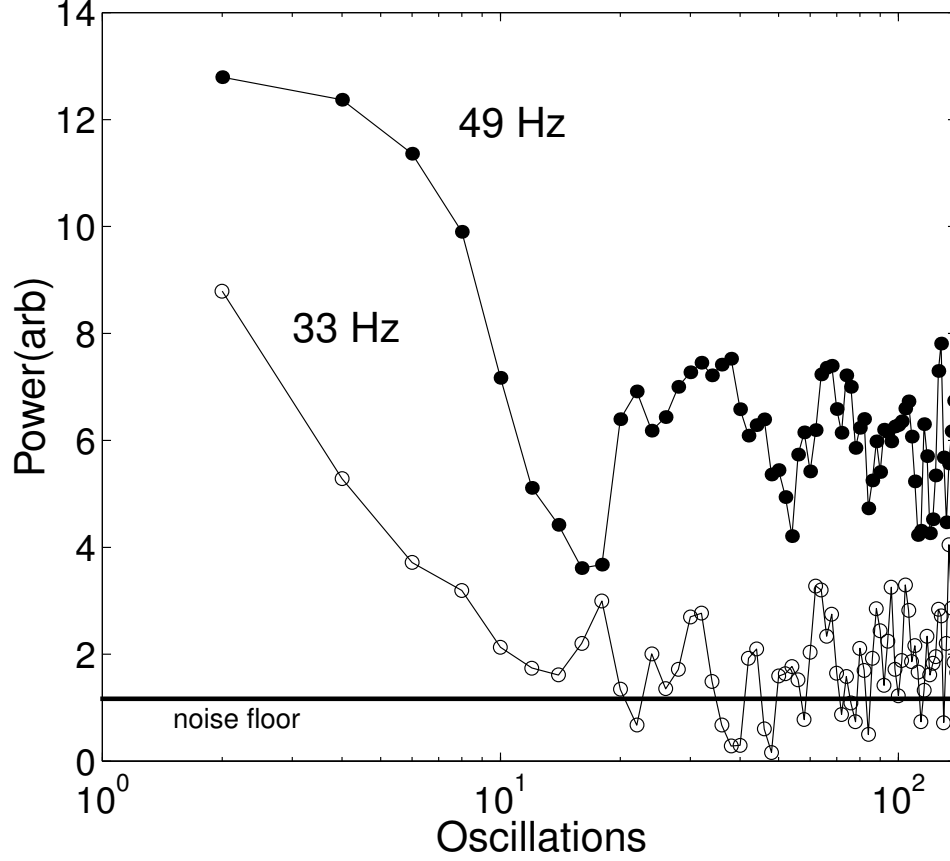
Figure 6.9: The integrated power in the 1 kHz ringing mode for a jump to $\tilde{v} = 3.5$, ○, and to $\tilde{v} = 2.4$ ●. The parameters of the jumps are the same as those in Figure 6.6.

layer is fluidized.

Figure 6.11 shows the picture we get from the previous section. We propose that the transient fluidization process studied in the previous section for $\tilde{v} > 3$ sets the effective hydrodynamic fluid depth as a function of time: as the amplitude of the pattern increases, it fluidizes the rest of the layer.

Since the wavevector of the pattern is a function of the depth of the layer, $h = ND$ (Figure 6.3), as the depth changes, so should the wavevector. Below onset $\Gamma = 2.5$, only the surface layer of the grains is fluidized for all $\tilde{v}$ and this should set the highest wavevector in the problem. In fact, we have determined that there is a length scale for the fluctuations in the surface layer. We return to this phenomenon when we study noise below onset, section 6.3.

Qualitatively this argument makes sense: from the dispersion relation in Figure 6.3, for $\tilde{v} > 3$, as h increases, the wavevector should decrease, in accord with data
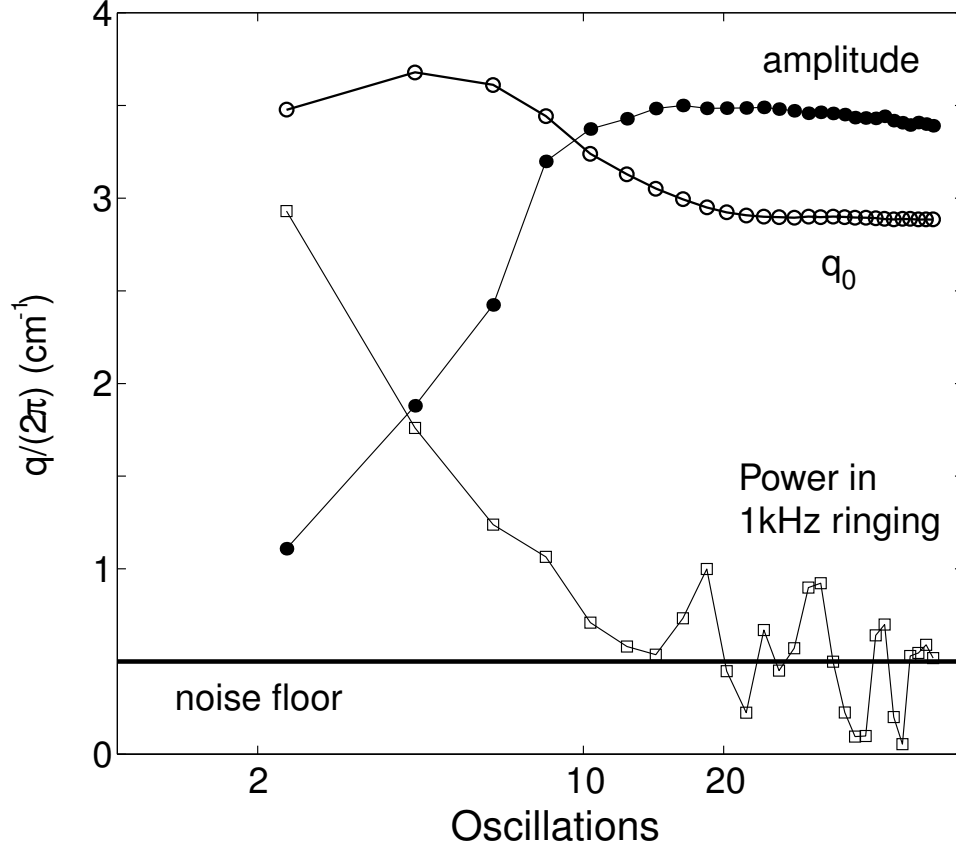
Figure 6.10: The changes in different layer characteristics during the jump to $\tilde{v} = 3.5$ at 33 Hz. q_0 ($\circ$) decreases until the layer is fully fluidized as measured by the integrated power in the 1 kHz ringing mode ($\square$). A measure of the amplitude ($\bullet$) of the pattern increases and reaches a peak before the layer is fully fluidized.

for jumps where $\tilde{v} > 3$.

A tentative argument for the scaling exponent in the decrease of q_0, $q_0 \sim t^{-.33}$ for large $\tilde{v}$ (see Figure 6.4) can be made if we assume that the effective depth scales linearly in time, $h_{eff} \propto t$. From the dispersion relation in Figure 6.3, above $\tilde{v} > 3$, the wavevector of the patterns scale like $h^{1/3}$, where h is the depth of the layer. If we assume, $h = h_{eff}$, during the fast growth stage then $q_0 \propto t^{-1/3}$. Figures 6.2 and 6.4 show that for large enough $\tilde{v}$, the data is consistent with this scaling. In fact, we see from Figure 6.10, that the amplitude of the pattern has reached its maximum before the entire layer has fluidized. Thus, subtle changes must occur in the fluid properties of the layer in the final few oscillations of wavevector change.

Jumps with $\tilde{v} \approx 3$
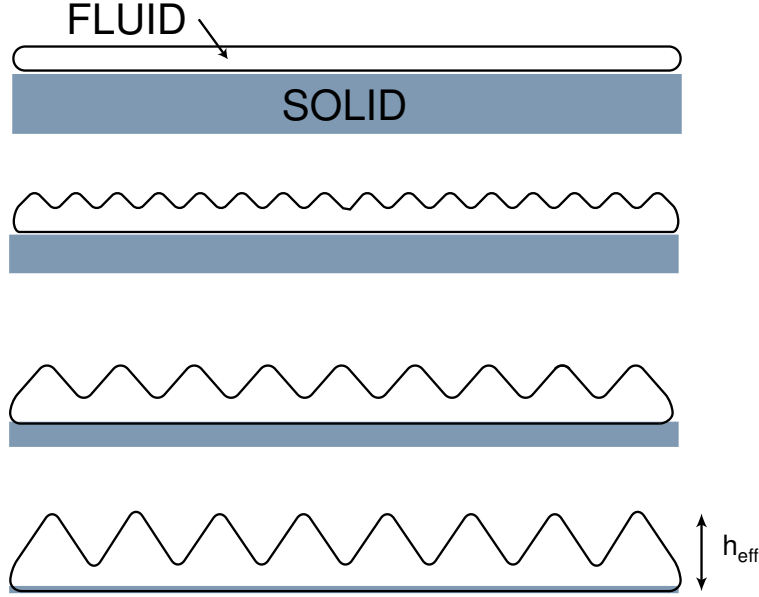
Figure 6.11: A schematic of the process of a jump with $\tilde{v} > 3$, showing how the effective fluid depth grows in time as the amplitude of the pattern increases. The wavevector decreases with increasing fluid depth.

Jumps close to $\tilde{v} = 3$, see Figure 6.2b, are more complicated and may evolve non-monotonically. We do not comment on them here.

Jumps with $\tilde{v} < 3$

Jumps sufficiently below $\tilde{v} = 3$, show a monotonic increase in q_0, and we propose the following argument to account for this behavior. When $\tilde{v}$ is increased to a value below 3, although the entire layer does not fluidize, there is more free volume per grain and the layer is more compressible. This change in compressibility happens rapidly during the initial growth stage and a more compressible layer should be able to bend on a shorter length scale. Thus the wavevector should increase. This is not an explanation, but we feel that viewing this phenomenon as a rapid fluidization process could lead to interesting ideas about the nature of granular flow in the non-hydrodynamic, but agitated region—frustrated waves.

6.1.5 Comparison with Swift-Hohenberg model

The Swift-Hohenberg model (Chapter 4, Equation 4.1) is often used to gain understanding of pattern formation. In Chapter 4, it was used to study the behavior of the evolution of order in a pattern. The scaling observed in the experiment was in good accord with the scaling predicted by SH equation in the linear regime. However, the be-

havior of the changing wavevector described in this section is in contrast to the behavior of the SH model. In this model, the wavevector selected by the pattern remains constant in time and has a value of the wavevector with maximum growth rate (very close to q_0 in Equation 4.1), see Figure 6.12, as expected for a supercritical bifurcation.

Mean flows in amplitude equations

However Cross and Meiron have shown that the behavior of q_0 can be modified by the addition of coupling between the rolls and a mean flow [37]. A different (not SH equation–for the explicit form see [37]) model of pattern formation was developed to include this coupling. It was found that for no coupling, the final wavevector had the same value as wavevector of the most linearly unstable mode. Coupling produced final wavevectors that deviated from the most linearly unstable mode; as the coupling increased, the average wavevector deviated further.
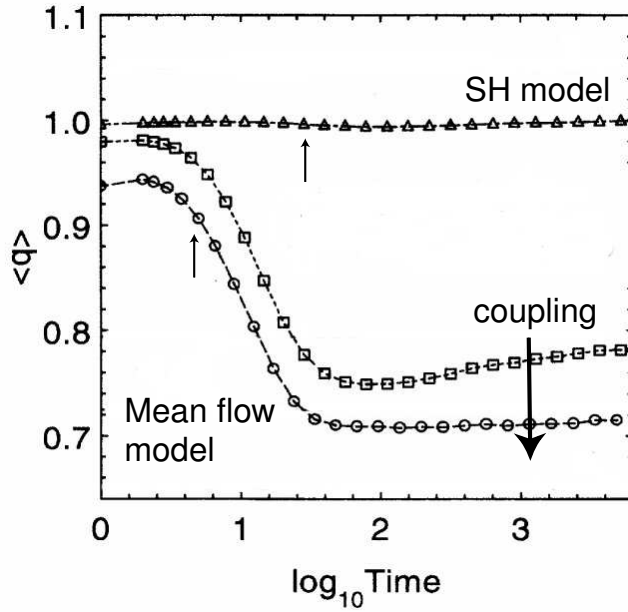
Figure 6.12: The behavior of the wavevector for a numerically integrated Swift-Hohenberg model ($\triangle$). $\square$ and $\circ$ are for a pattern formation model which couples the rolls to a mean flow. The evolution changes as the coupling changes. Taken from [37].

In fact, this model seems to capture well the behavior of the data presented for $\tilde{v} > 3$. The bulk of the wavevector change comes *after* the fast initial growth of the amplitude of the pattern both in the model and in the data. It also comes after the rapid fluidization transition (see Figure 6.10). Perhaps the fluidization transition of the layer

117

creates a mean flow, while a jump below $\tilde{v} = 3$ does not fluidize and thus cannot create a mean flow. Since the molecular dynamics simulation can easily visualize flow in the bulk, it should be able to determine is such a flow is present.

6.2   Nucleation in the subcritical region
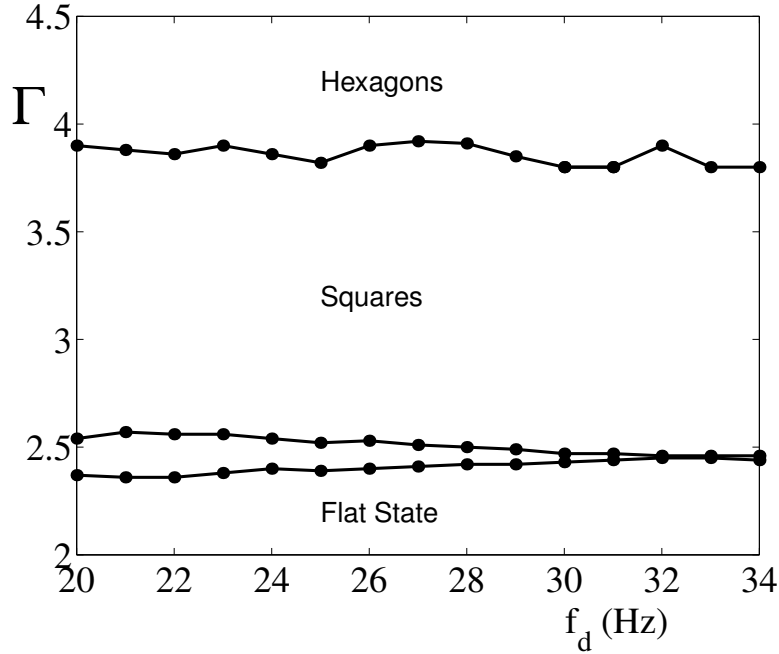
Figure 6.13: Phase diagram for 4 layers showing subcritical behavior at low frequencies. The bifurcation to hexagons for increasing Γ is drawn for reference

Pattern formation is quite different when a jump is made into the hysteretic region for square patterns(see the phase diagram, Figure 6.13). Instead of uniform amplitude growth throughout the entire container, the pattern forms from the growth of nucleation events: locally, small circular regions quickly (within 2-4 cycles) nucleate and then propagate, invading the rest of the flat layer, see Figure 6.14. Asymptotically, the pattern reaches a perfect array of squares.

We have observed similar pattern formation by local nucleation in a Swift-Hohenberg equation modified by the addition of a quintic term,

$$\frac{\partial W}{\partial t} = [\epsilon - (q_0^2 + \nabla^2)^2]W + aW^3 - bW^5 \tag{6.1}$$

The addition of the term modifies the amplitude diagram, as shown in Figure 6.15.
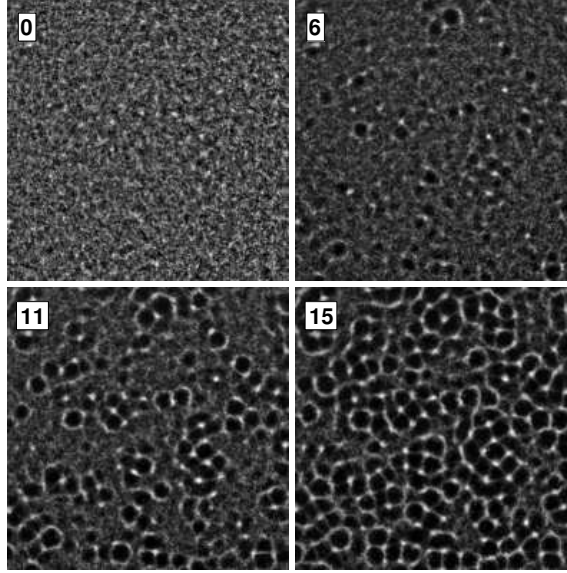
Figure 6.14: Nucleation of pattern after a jump into the subcritical region, 27 Hz and Γ from 2.2 to 2.52. The units are in plate oscillations after the jump. 0.165μm bronze particles with $N = 4$.

The bifurcation to the pattern state of rolls is now subcritical, displaying the hysteresis seen in the shaken layer experiment for square patterns.
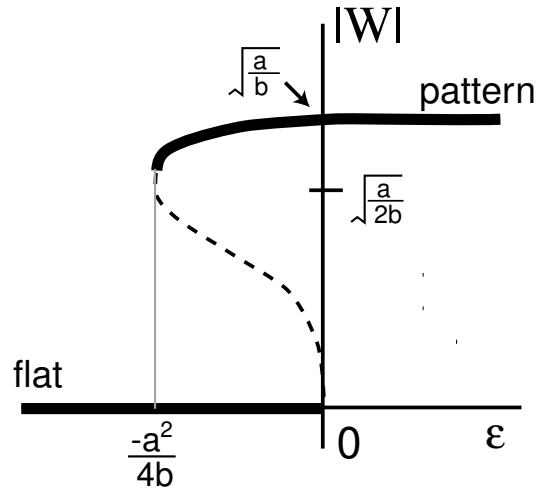
Figure 6.15: The subcritical bifurcation for Equation 6.1. The solid lines indicate the linearly stable attractors and the dashed line indicates the unstable state.

Figure 6.16 shows the integration the modified SH equation (Details of the SH

simulation are given in Appendix A) with initial condition of spatially random noise with amplitudes uniformly distributed over a range $(-n, n)$. n controls the strength of the noise. At $t = 0$, ϵ is changed to a value in the hysteretic region. As in the experiment, the pattern nucleates local circular regions which spread to fill the entire integration domain. In this case, the final state is a pattern of rolls.
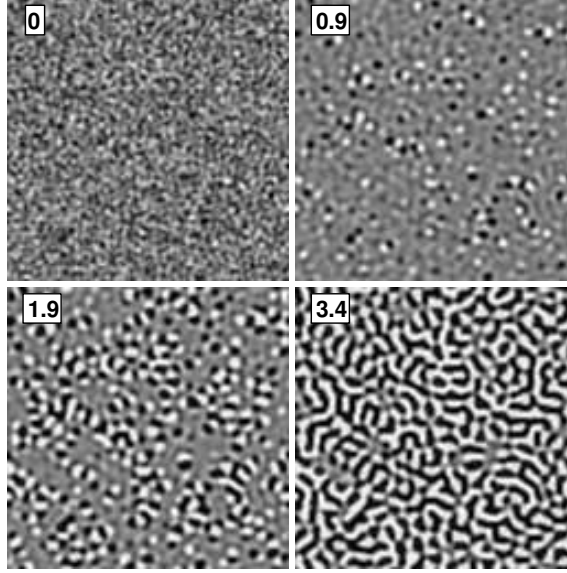
Figure 6.16: Nucleation of pattern after a jump into the subcritical region in a Swift-Hohenberg model. At $t = 0$, integration is started from a state with initial noise strength, $n = 2.0$ (see text for details). Parameters for Equation 6.1: $\epsilon = -.05$, $b = 3.0$, $c = 1.0$, $q_0 = 1$

6.2.1 Discussion

The hysteresis in a subcritical bifurcation can modify pattern formation in a non-trivial way. Pattern formation in the hysteretic region requires finite amplitude perturbation. Thus, unlike a supercritical bifurcation or a jump into the non-hysteretic region which proceeds by the growth of the linearly most-unstable mode, the system must have a noisy initial condition to provide local regions with amplitude greater than the unstable attractor: these regions will rapidly amplify and reach the stable pattern branch, while regions of with amplitude too small do not grow in time. Once the region nucleates, the pattern grows in a front propagation like that studied in a one-dimensional Swift-Hohenberg equation. [9]. The rate of nucleation and thus the rate at which the pattern forms increases as the amplitude of the noise, n is increased.

As seen from these results, in the flat, featureless region of the experiment, we

120

have a noisy initial condition. In the next section we examine this noisy state more closely.

6.3   Noise below onset

6.3.1   Introduction

Patterns form above $\Gamma \approx 2.5$, and for $\tilde{v} > 3$ some portion of the layer is fully fluidized throughout the cycle. It has been shown by measuring the reflectivity of light of the granular surface that in fact the layer undergoes a fluidization transition at $\Gamma = 2.0$. The vibrated layer is in a fluidized state, but no patterns are visible for $2.0 < \Gamma < 2.5$ [137]. We have explored the region $2.0 < \Gamma < 2.5$ and find that there are strong spatially inhomogeneous fluctuations at the surface of the layer. These fluctuations appear random in individual images, but show a well-defined ring in Fourier space, indicating a length scale in the noise. We now describe our measurements and comment on the relevance to hydrodynamic theories of granular materials.

6.3.2   Measurements of noise below onset

The top four panels of Figure 6.17 show images of the granular layer for increasing values of Γ. Individual grains are clearly visible and fluctuations in the density are seen which are roughly 10 grain diameters in size. The bottom four panels of Figure 6.17 show the corresponding structure factors for the images, computed by time-averaging the Fourier transforms of a sequence of 100 images taken at $f_d/2$. A ring in Fourier space is clearly visible and grows in intensity as Γ approaches the up-onset value of 2.58.

Figure 6.18 shows the azimuthal average of the structure factors and in Figure 6.18b we plot the integrated power in the main peak as a function of Γ. The intensity of the ring increases as Γ is increased in accord with the reflectivity measurements measurements of [137] which showed that the intensity of the fluidized fluctuations increased with Γ.

Thus, we also find that even below onset of patterns, modes of the top fluid layer are excited by fluctuations in the local density of the patterns and we now comment on previous studies in other fluids.

6.3.3   Comparison to convection in CO_2

Convection and noise

Our study is analogous to that performed in a Rayleigh-Bénard convection experiment [196], see Figure 6.19. In Rayleigh-Bénard convection where non-Boussinesq effects are important, the primary bifurcation is subcritical and forms hexagonal patterns [17]. Swift and Hohenberg [173] showed that that the effect of thermal noise could be seen below the bifurcation, essentially imaging the slowest decaying mode, but the effect was
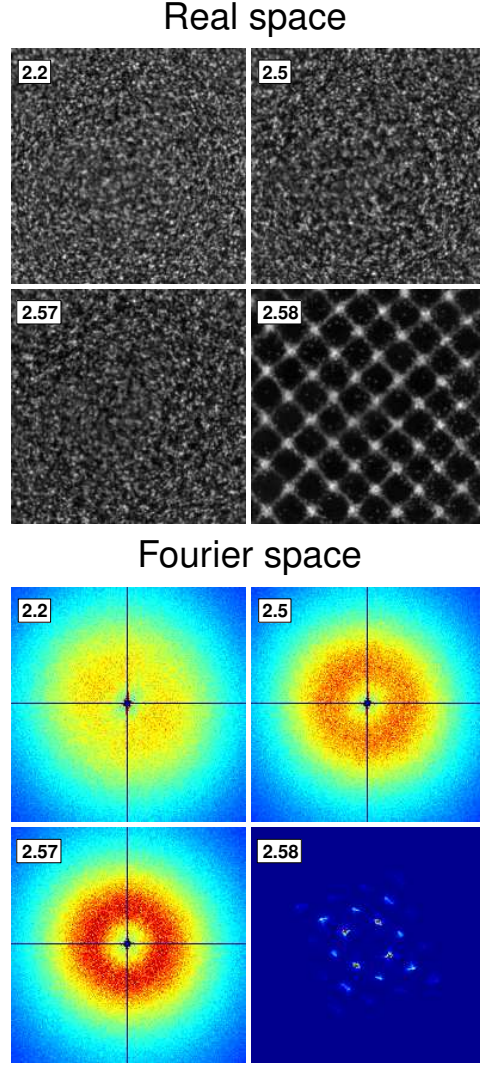
Figure 6.17: (a) Snapshots of the vibrated granular layer below onset of patterns for increasing values of Γ at $f_d = 29$ Hz. Each image is The layer depth $N = 4$ of 0.165 mm bronze spheres. (b) The modulus of the Fourier transform averaged in Fourier space over 100 plate oscillations. Blue to red indicates increasing intensity. The image at $\Gamma = 2.58$ has been scaled in intensity by a factor of 10. The length scale is the same as that in Figure 6.18.

predicted to be unobservable due to the small size of $k_B T$ relative to the kinetic energy in a roll, a factor of roughly 10^{-9}.
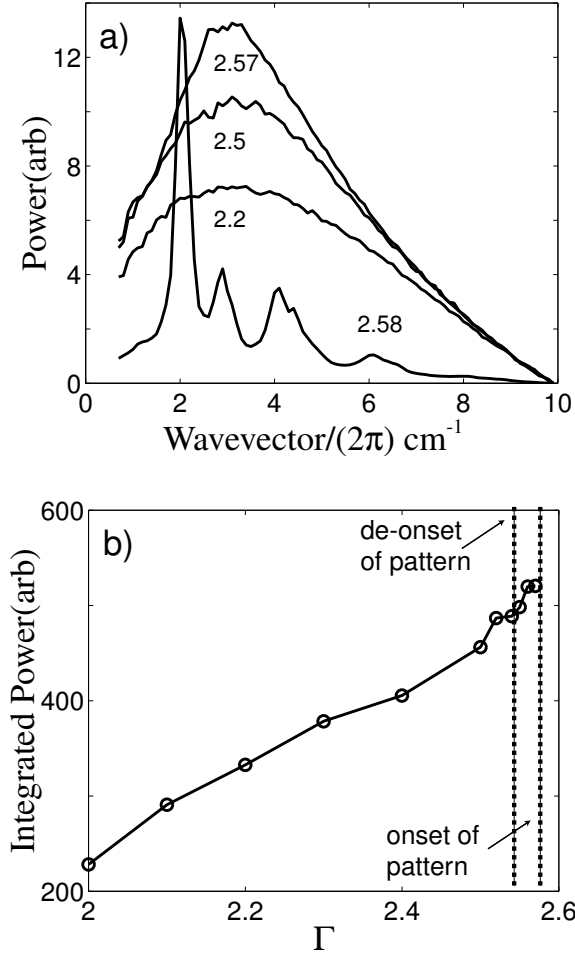
Figure 6.18: (a) The azimuthally averaged structure factor for the same values of Γ in Figure 6.17. For comparison, the curve for $\Gamma = 2.58$ has been scaled by 0.1. (b) The integrated power in the azimuthally averaged structure power as Γ is increased to the onset value of $\Gamma \approx 2.58$. The value for the power at $\Gamma = 2.58$ is not shown and is 5000.

Noise size and control

The experiments on gaseous convection were a tour-de-force. Since the noise power was so small compared to the average energy in a roll structure, to observe the predicted effect of pattern below onset of waves, the control parameter $\epsilon = (\mathrm{Ra} - \mathrm{Ra}_c)/\mathrm{Ra}_c$ had to be controlled to a precision of -10^{-4} below the bifurcation. In our experiments, the fluctuation induced pattern can be seen at control parameters $(\Gamma - \Gamma_c)/\Gamma_c \approx -10^{-1}$ below the onset of patterns. This indicates that the size of the noise compared to a typical energy scale in the problem, mgh, is quite large. In fact, it is very clear from the images in Figure 6.17 that individual grains can be seen, and thus can produce fluctuations in
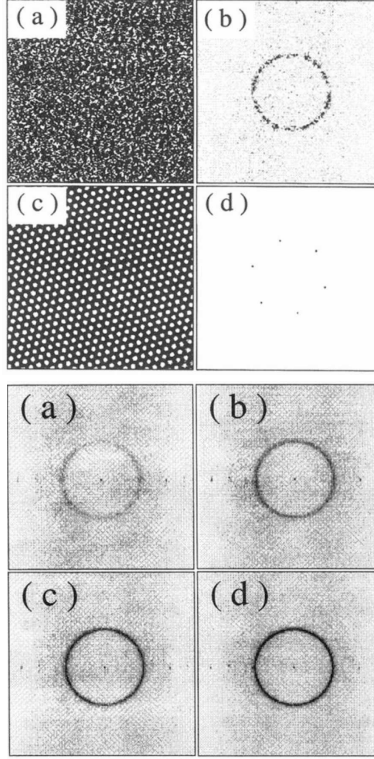
Figure 6.19: Shadowgraph images of gas convection in CO_2. Top 4 panels: (a) Fluctuating rolls, for $\epsilon = -3.0 \times 10^{-4}$, (b) Square of the modulus of the Fourier transform of the image in (a). (c) Shadowgraph image of a hexagonal pattern, for $\epsilon \simeq 0$. (d) Square of the modulus of the Fourier transform of the image in (c). Bottom 4 panels: Structure factors for increasing $-\epsilon$ (a) $\epsilon = -4.2 \times 10^{-3}$, (b) $\epsilon = -1.6 \times 10^{-3}$, (c) $\epsilon = -7.1 \times 10^{-4}$, (d) $\epsilon = -3.0 \times 10^{-4}$. Images taken from [196].

the height of the layer which are comparable to the depth of the layer.

Subcritical vs. supercritical

Without non-Boussinesq effects, the bifurcation in Rayleigh-Benard is supercritical, and the wavelength of the pattern slightly below onset should be the same as that slightly above onset. In the Ahlers experiments, the primary bifurcation is subcritical due to unavoidable non-Boussinesq effects which manifest very close to the bifurcation[2]. Because the bifurcation is subcritical, there is no *a priori* reason that the wavevectors below and above onset should match. In the granular layer, as seen in Figure 6.20, the

---

[2]Further above the onset where the Boussinesq approximation is valid, the hexagons lose stability to straight rolls.

wavelength above and below are quite different. However, this is not unexpected as the bifurcation is subcritical, see Figure 6.13. A full understanding of the subcritical behavior is not yet known, but should involve fluidization of the entire layer. As before, below onset, the effective depth is smaller, thus the wavelength should be smaller. Above onset, the depth is the full depth. As f_d increases, the hysteresis in the bifurcation becomes smaller and the ratio of the wavevector above onset to that below increases (Figures 6.20 and 6.21). However, there is the competing non-hydrodynamic effect of the fluidization of the layer above $\tilde{v}$. As f_d increases at constant Γ, eventually $\tilde{v}_c < \tilde{v}$ and at this point there should no relation between the wavelengths above and below onset. Below would be a small top fluidized layer, outside the $\tilde{v}$ theory while above onset the wavelength would follow the non-hydrodynamic region of the dispersion relation. For 0.165 μm particles and assuming onset around $\Gamma \approx 2.5$, this sets the maximum f_d for hydrodynamic waves as roughly $f_d = 32$ Hz. From Figure 6.21, the ratio of the pattern to noise wavevectors is about 0.7, and from Figure 6.13, we see that the hysteresis is on the order of 1%. These are much larger than the corresponding quantities in the convection experiment. Since the hysteresis, and presumably the difference in wavevector, is related to the effective fluid depth, it would be interesting to study the effect in a "pre-fluidized" vibrating layer. This could be accomplished by the addition of a high frequency forcing or by using air to fluidize the layer.

Fluctuations and noise strength–fluctuating hydrodynamics

We speculate that these fluctuations are the analogue of thermal fluctuation present in fluids. These fluctuations occur on timescales comparable to mean free and length scales comparable to the mean free time, and consequently do not appear in hydrodynamic equations, equations for the evolution of quantities which change slowly compared to the mean free time and over length scales much longer than the mean free path. They manifest by creating spontaneous local stresses and heat gradients in the fluid. To study their effects, the fluctuations must be re-incorporated into Navier-Stokes equations, and this is typically accomplished by the addition of a stochastic forcing term to the Navier-Stokes equations [110]. Using such equations, Rayleigh-Bĕnard convection can be analyzed around the bifurcation point and analysis shows that the effect of noise was 10^{-9} and thus ϵ should be very small to see the effect of the noise.

It is a fascinating question how (or whether) such terms should appear in the Jenkins-Richman equations (Equations B.2 - B.4 in Appendix B) modified with stochastic forcing terms like in **??**. Since the averaging done to derive these equations occurs on length scales which are not much larger than the particle size and/or mean free path, are the fluctuating terms already present? If not, how should they be put in? The type of experiment described could provide a resolution to the question of appropriate
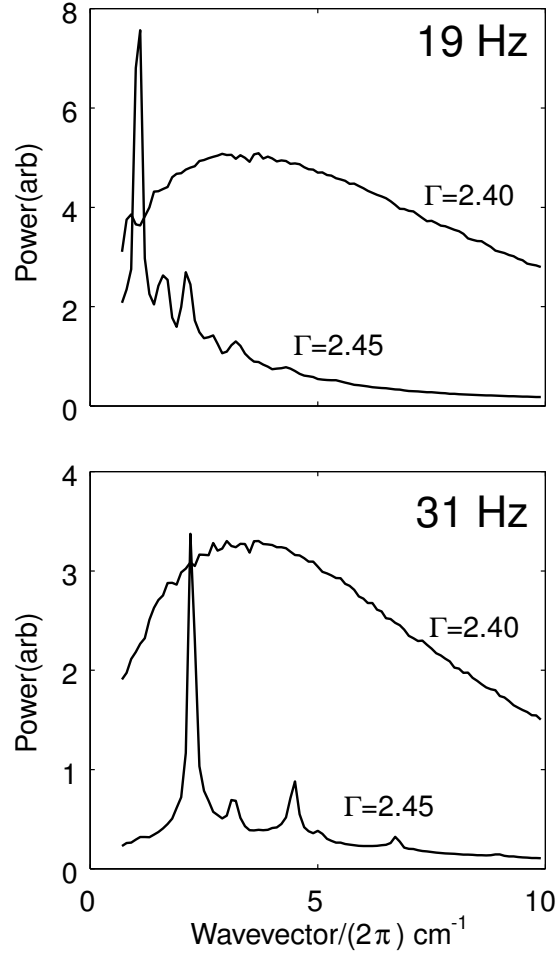
Figure 6.20: The azimuthally averaged Fourier spectra for images at different f_d, above and below onset of patterns, $\Gamma = 2.40$ and $\Gamma = 2.45$. q_0 of the noisy state below onset does not vary significantly with f_d, while q_0 of the pattern above onset changes by almost a factor of 2. The difference in vertical scales is a result of the enhanced reflectivity at lower frequencies due to higher amplitude patterns.

averaging and separation of scales which plagues the hydrodynamic theories of granular materials [51, 175].
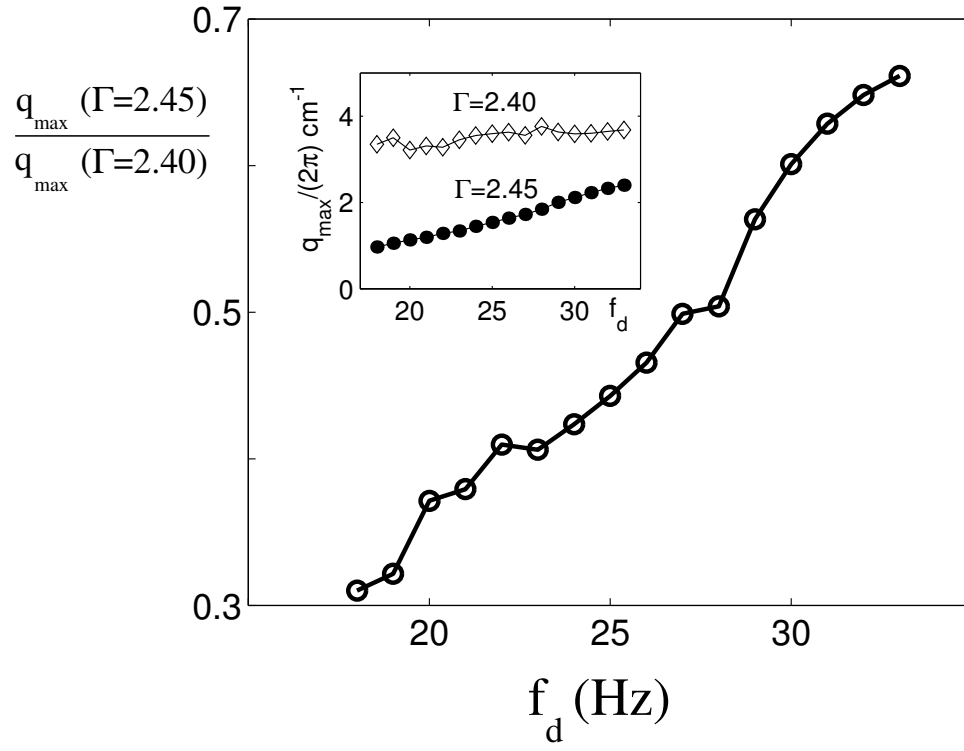
Figure 6.21: The scaling of the noise wavevector with container frequency (Inset) and the ratio of the wavevector of the noise and the wavevector of the pattern slightly above onset.

6.4 Phase discontinuities and segregation

6.4.1 Introduction

The experiments in this section are mainly experimental verification and realization of effects predicted in the hard sphere event driven molecular dynamics (MD) simulations of Sung Joon Moon [135]. In the experiment, we examine the dynamics of phase discontinuities (regions of the layer which oscillate out of phase with each other) in vertically vibrated layers. For $\Gamma < 7.5$, the phase discontinuities are asymptotically stable and form a time-independent feature of the vibrating layer called a kinks. For $\Gamma > 7.5$ localized regions of the layer can spontaneously change phase. These regions are called phase bubbles and for sufficiently high Γ they strongly disrupt the layer and create spatio-temporally chaotic patterns. We will study the stability of patterns disrupted by the chaotic phase bubble state. In addition, Moon has shown that a pair of counter-rotating convection rolls exist near the kinks [134]. We have demonstrated that this convection produces spontaneous segregation of a vibrating layer composed of different-sized particles.

6.4.2 Kinks

Above $\Gamma \approx 4.5$, the vibrated granular layer develops phase discontinuities in which different portions of the layer oscillate π out of phase. These portions of the layer are separated by an interface called a kink, examples of which are shown in Figure 6.22.
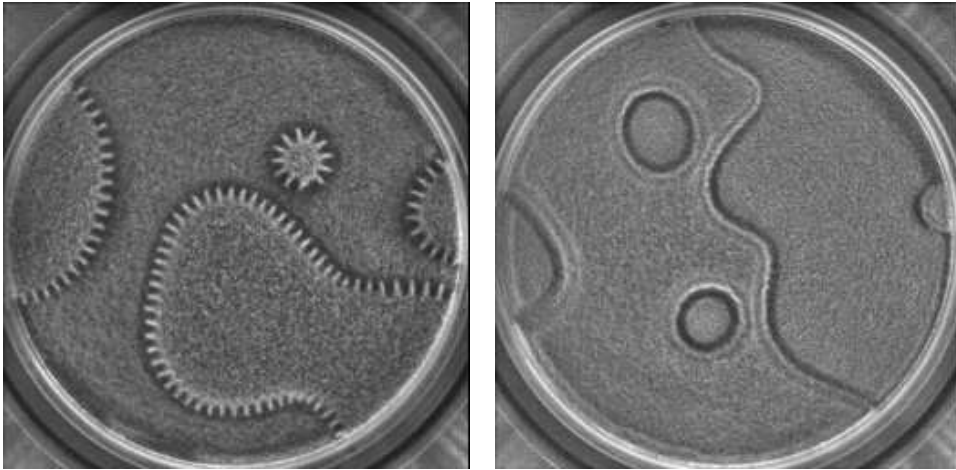
Figure 6.22: The degeneracy leads to kinks, $\Gamma = 5.2$, f_d=40,57 Hz. Layer depth, N=15

The temporal dynamics of the layer can be well described by a single inelastic-ball model [129]. This model predicts that kinks can occur when the Γ is large enough so

that the layer collides with the plate every *two* oscillations as shown in Figure 6.23 for $\Gamma = 4.5^3$. This allows some portions of the layer to collide with the plate while other regions are off the plate. In small enough container, the entire layer oscillates at $f/2$, but as soon as there is some imperfection in the driving, the layer will spontaneously break into two equal mass portions and this is typically driven by the sidewalls. In fact, the location of the interface can be controlled by additional subharmonic driving, details have been studied in [8].

As shown in Figure 6.23, for $\Gamma > 4.5$, the layer always skips an oscillation and thus the degeneracy necessary for kink formation is always present. In fact, most observed patterns have phase discontinuities present in the form of stationary kinks, with patterns of different phase occupying the continuous regions between kinks, see Figure 6.24.

Transient kink dynamics

The kinks are asymptotically stable and for a well-balanced experiment the interface forms a straight line dividing equal mass sections of the layer [8]. This is due to an effective surface tension of the interface and has been shown to be a consequence of mass flux across the kink [135]. We can see the effects of surface tension at work in Figure 6.25. Here the system is initially prepared in a disordered state and rapidly jumped in the kink region. High amplitude regions are out of phase with low amplitude regions and become kinks. The kinks straighten and merge to form a single kink after roughly 10^3 oscillations.

Generally, small enclosed regions of different phase (phase bubbles) disappear over several hundred oscillations. However they can merge if they are close, forming kinks, and this is shown in Figure 6.26. It is important to note that these phase bubbles are created by the initial condition. We now describe bubbles that spontaneously appear and slowly shrink–this process plays an important role in the order of patterns at higher Γ.

6.4.3   Phase bubbles

Kinks form due to perturbations of the collision of the layer and the plate. These perturbations often due to poor leveling of the system and the kinks usually are initiated at the sidewalls. We have found that kinks can be suppressed in small containers in which the mass of the layer is much smaller than the mass of the plate. However, above a critical $\Gamma \approx 7.5$ the layer becomes unstable to formation of localized phase discontinuities (phase

---

[3]Trajectories calculated from the program that solves the motion of a inelastic particle falling under gravity and colliding with an infinitely massive oscillating plate. Source code is given in Appendix D
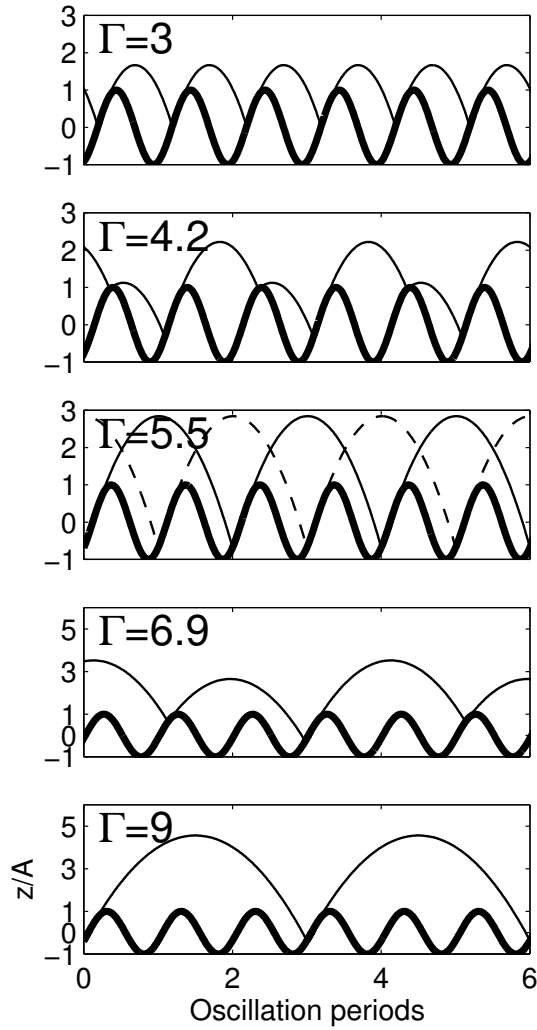
Figure 6.23: The calculated trajectories of a single completely inelastic ball for increasing Γ at fixed f_d. Trajectories calculated using the code in Appendix D.

bubbles) in the *bulk* of the layer. Phase bubbles differ from normal kinks in that they are not only created by the boundaries or imperfections in levelling. Moon has shown that a phase bubble forms because for large enough Γ, the layer bottom develops large length scale undulations. The amplitude of the undulation can grow during flight of the layer and when a portion of the layer hits the plate before another portion, a phase bubble is nucleated. He has shown that phase bubbles are more numerous as Γ is increased and experiments confirm this as seen in Figure 6.27. The phase bubbles nucleate with a finite
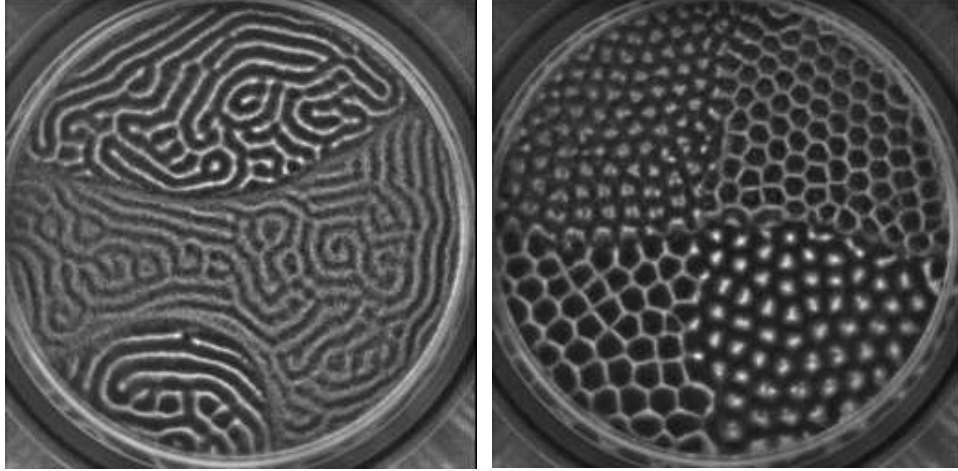
Figure 6.24: The degeneracy leads to patterns with multiple phases, in stripes with $f_d = 60$ Hz, $\Gamma = 6.2$ and hexagons with $f_d = 67$ Hz, $\Gamma = 6.8$. $N = 15$ in both cases.

size and as in the above section, they shrink over several oscillations [135]. However, as Γ is increased, the rate of nucleation becomes quite large and the phase bubbles form complicated time dependent labyrinth pattern.

Spontaneous phase changes are seen in the inelastic ball model (IEB), Figure 6.28, in a narrow region where the temporal dynamics are chaotic. It may be coincidence that the phase bubbles seen in the experiment begin at roughly the point where chaos begins, around $\Gamma \approx 7.5$. However, phase bubbles are seen well above this region, where the model predicts non-chaotic dynamics.

In fact, in the experiment, stable patterns are never seen above the phase bubble onset. Instead, as Γ is increased, the rate of phase bubble nucleation increases. At some point a time-dependent, disordered state of connected kinks and phase bubbles forms, shown in Figure 6.29. It is not yet known if there is a bifurcation between the phase bubble states and this strongly disordered state. Either way, such complicated time-dynamics of the layer is not present in the IEB model. Above $\Gamma \approx 8.0$, the IEB model predicts that the layer should oscillate at $f_d/3$, see Figure 6.23 and Figure 6.28. If we use lower Γ behavior as a guide, we would expect to see flat or pattern states oscillating at $f_d/3$. It has been proposed [135] that the disruptive spontaneous formation of phase bubbles prevents formation of $f/6$ patterns $\Gamma > 8.0$: the random appearance of phase bubbles disrupts the coherent oscillation necessary for formation of the pattern. It was proposed that the inelastic ball model fails because it does not take into account the dynamics of the layer due to its thickness. The IEB models the center of mass motion of the layer and cannot account for large spatial deviations which are present at the higher Γ [135].
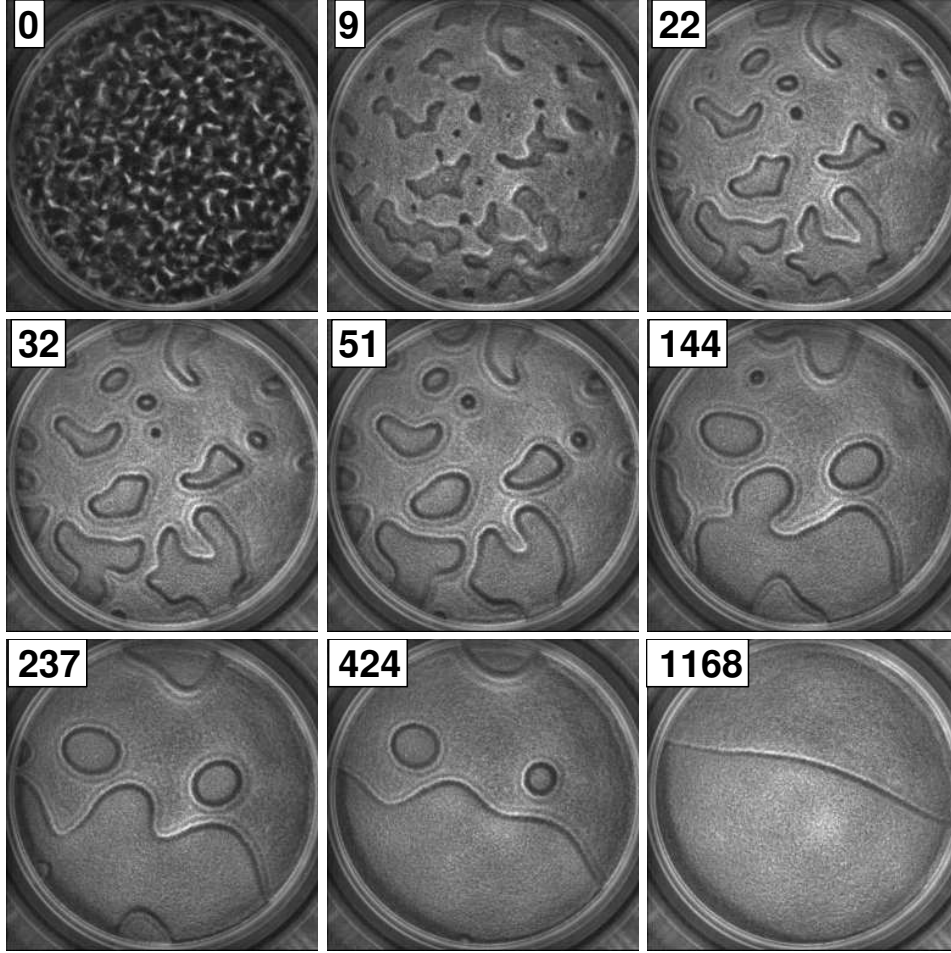
Figure 6.25: The kinks straighten and bubbles shrink. A jump from a disordered state at $\Gamma = 9.2$ to $\Gamma = 5.2$ at $f_d = 57$ Hz, $N = 15$. The numbers in each image are in units of plate oscillations.

6.4.4 Transient $f_d/6$ patterns

We emphasize that in the experiment in large aspect ratio containers, there is no bistability between ordered $f_d/6$ patterns and the chaotic phase bubble/connected kink state. This is in contrast to the bistability between the straight roll and spatio-temporally chaotic spiral defect chaos (SDC) states seen in Rayleigh-Benard [23]. The phase bubbles are always seen in the granular system at sufficiently high Γ. However, we have found that $f_d/6$ patterns can exist as *transients*, which are soon destroyed by phase bubbles. We now describe these experiments.

The following prediction was made and verified in the experiment: The $f_d/6$ patterns are never seen due to the disruptive phase bubbles. The instability of the layer
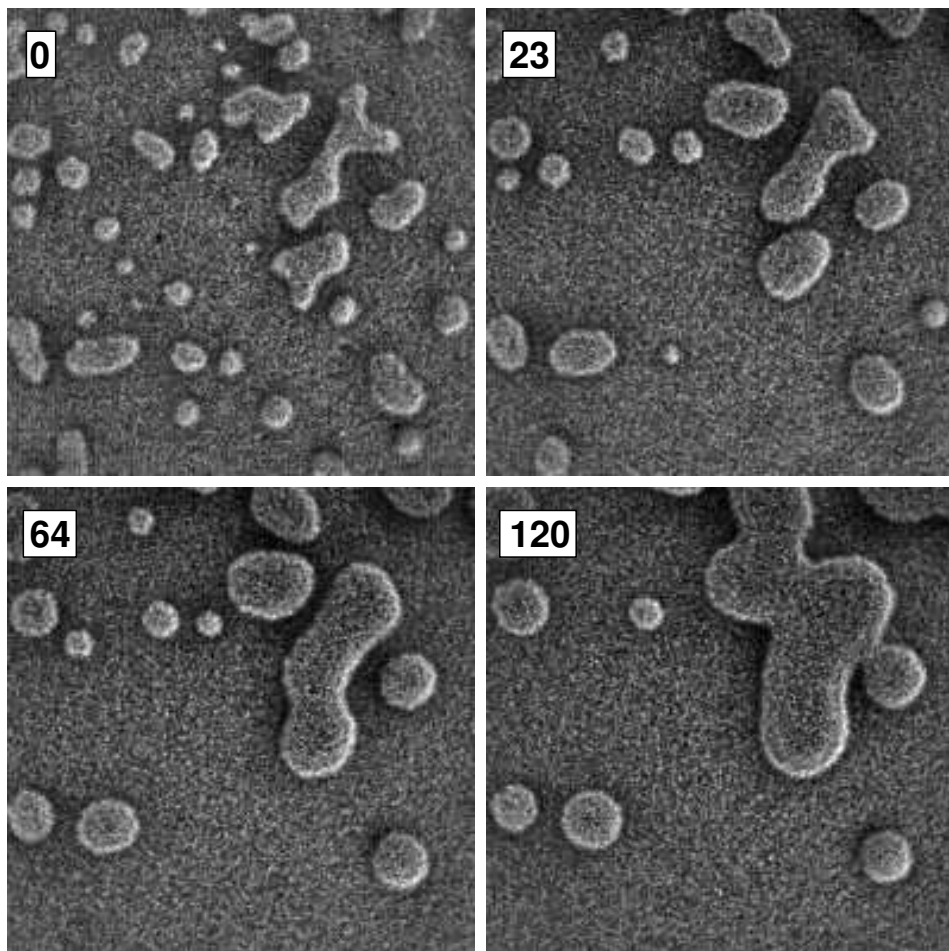
Figure 6.26: Phase bubbles always shrink, but if they get close enough they merge. A jump from $\Gamma = 9$ to $\Gamma = 4.5$ at $f_d = 118$ Hz, $N = 15$. The numbers in each image are in units of plate oscillations.

which creates phase bubbles is due to the growth of local height inhomogeneities at the bottom of the dilated layer. Thus, if these inhomogeneities can be suppressed, no spontaneous phase jumps will occur. It was predicted that an $f_d/6$ pattern could be seen by the following method. Prepare the layer in a compact initial state with a very flat bottom interface and then suddenly jump into the region where the layer should oscillate $f/6$. The $f/6$ oscillation will occur until the undulation of the bottom of the layer has time to grow and create phase bubbles. Thus, $f_d/3$ pattern should persist until the pattern is overwhelmed by phase bubbles.

This process was observed in the experiment, as seen in Figure 6.30. The layer was prepared below the onset of patterns at $f_d = 83 Hz$ and $\Gamma = 2.2$ and Γ was suddenly
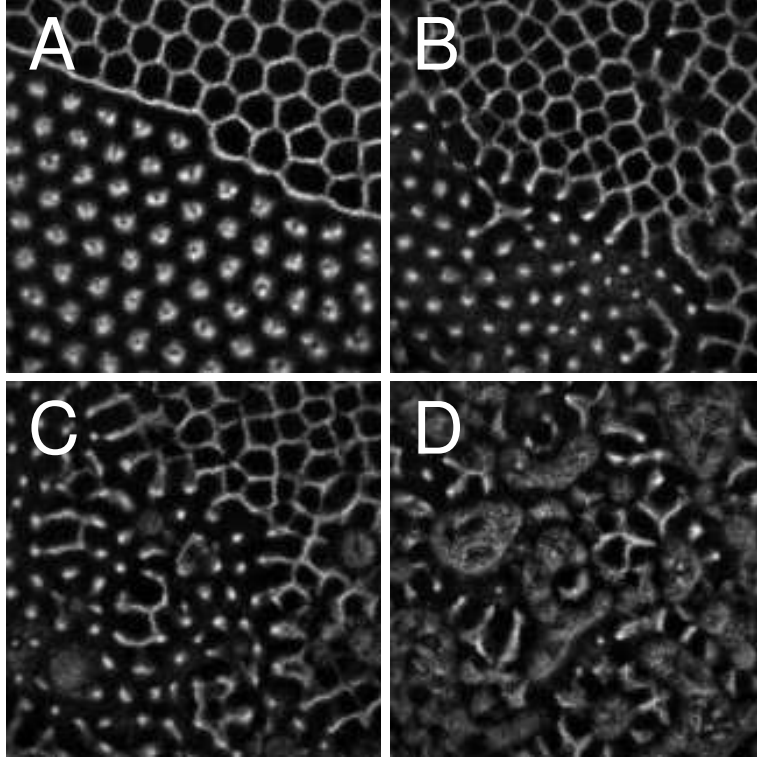
Figure 6.27: Phase bubbles destroying $f/4$ hexagons as Γ is increased. $\Gamma = 6.9, 7.27, 7.29, 7.56$, $f = 78$ Hz, $N = 10$ layers

increased to $\Gamma = 9.2$ keeping f_d constant. An initial square pattern vibrating at $f/6$ grows in amplitude from a flat layer vibrating at $f/3$. The pattern begins to coarsen to create a more ordered pattern, but after several hundred oscillations, local phase disturbances have destroyed the pattern, leaving a state of labyrinthian phase bubbles [4]. A close-up of the decay of the $f_d/6$ pattern is shown in Figure 6.32. We note that for $f_d = 83$, a transient square pattern is seen. [5] To verify that the oscillation occurs at $f_d/3$, in Figure 6.31 we plot the variance of the image as a function of time. The variance is large when a pattern is present and small for a flat layer. The inset shows the Fourier spectrum of the variance, with a peak at exactly $f_d/6$. Thus, we conclude that the predictions of the inelastic ball model are still good, but the model fails to capture the extra dynamics of the layer associated with dilation and thickness variations. The source of the local long wavelength inhomogeneity which presumably triggers phase bubble formation is still

---

[4]In addition, a kink from the boundary helps to destroy the pattern

[5]At higher f_d, we have observed the formation of transient stripe patterns analogous to the behavior of $f_d/2$ and $f_d/4$ patterns.
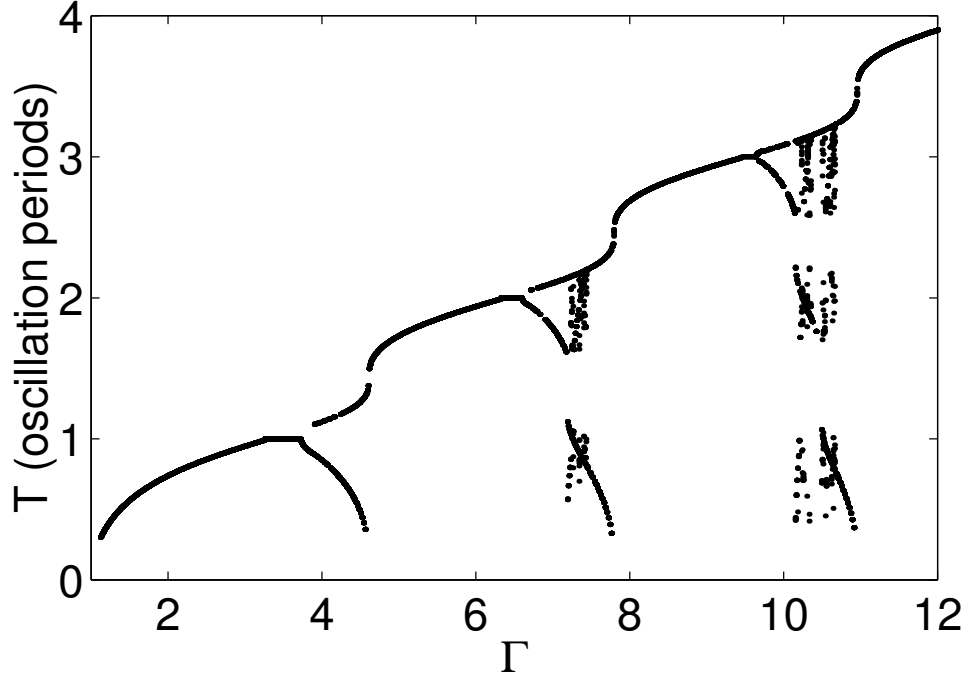
Figure 6.28: Time between collisions for the single inelastic ball model, calculated using the code in Appendix D.

unknown [135].

6.4.5 Segregation in the presence of kinks

A detailed study of the dynamics of grains near an $f_d/4$ kink has been made. This study found that the kink interface is bounded by a pair of counter-rotating convection rolls [134], see Figure 6.33. This convection is due to a combination of shearing of the layer and an avalanching of particles and is described in [134].

We now demonstrate that if different size particles are added to the oscillating layer, they are drawn into the kink by the convection roll and remain trapped along the kink interface. Thus, the kink acts to segregate different sized particles. Other experiments in granular materials have observed that convection can lead to segregation of different size particles. However, the convection in each of these experiments was either driven by frictional contact [30, 103, 105] with a boundary or due to interaction with surrounding fluid [142] [6]. In contrast, the convection in the kinks is due to the intrinsic dynamics of the layer and can be precisely controlled by changes in Γ and f_d.

---

[6]We note that segregation phenomena are fairly common in granular flows in excited granular materi-
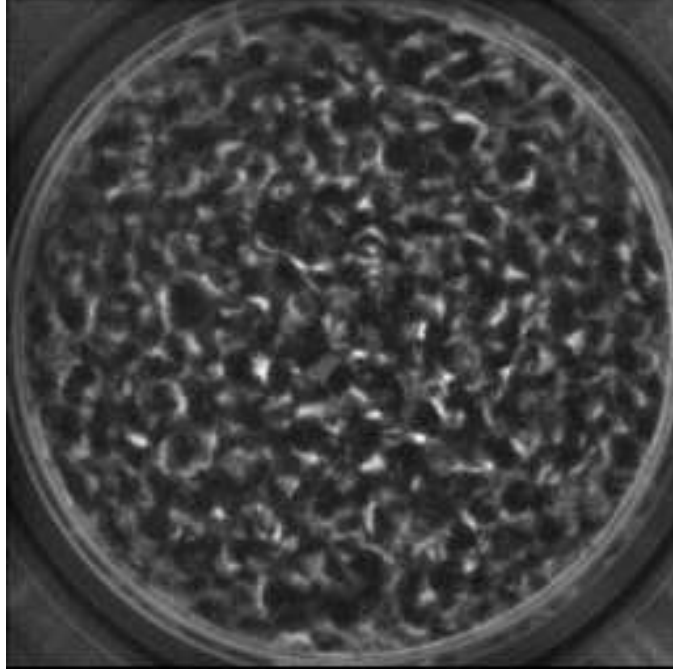
Figure 6.29: A snapshot of a disordered pattern at $\Gamma = 9.2$ and $f_d = 90$ Hz, $N = 15$.

Consequently, the rate of segregation and the number of particles that can remained trapped can be easily varied. We now describe our experiments.

The experimental confirmation of this prediction is shown in Figure 6.34. A container with 10 layers of 165 μm bronze spheres is evacuated to avoid hydrodynamic convection effects and shaken vertically with $\Gamma \approx 4.5$, and $f_d = 90$ Hz. We add a small number of larger, 650 μm glass particles which have had their surfaces blackened with a coating of graphite powder.

Initially, all particles are on one side of the kink. As the kink moves due to a slight tilt of the cell (because the container is out of level), the large particles are attracted and stick in the kink–they never cross the kink "barrier". For this high frequency the particles remain at the top of the layer in the middle of the kink. This happens by a similar effect observed in experiments of wall driven convection [103, 105]. The large particle is convected into the kink but is unable to squeeze through the middle due to dense packing of the bronze spheres at high frequency.

As the frequency is decreased, the density of bronze spheres in the kink decreases and the large particle can follow the convection roll. At this point it circulates in the

---

als and are not always linked to convection, for example radial and axial banding in a rotating drum [88] and segregation into bands by pouring two-sized particles into a narrow cell [106]
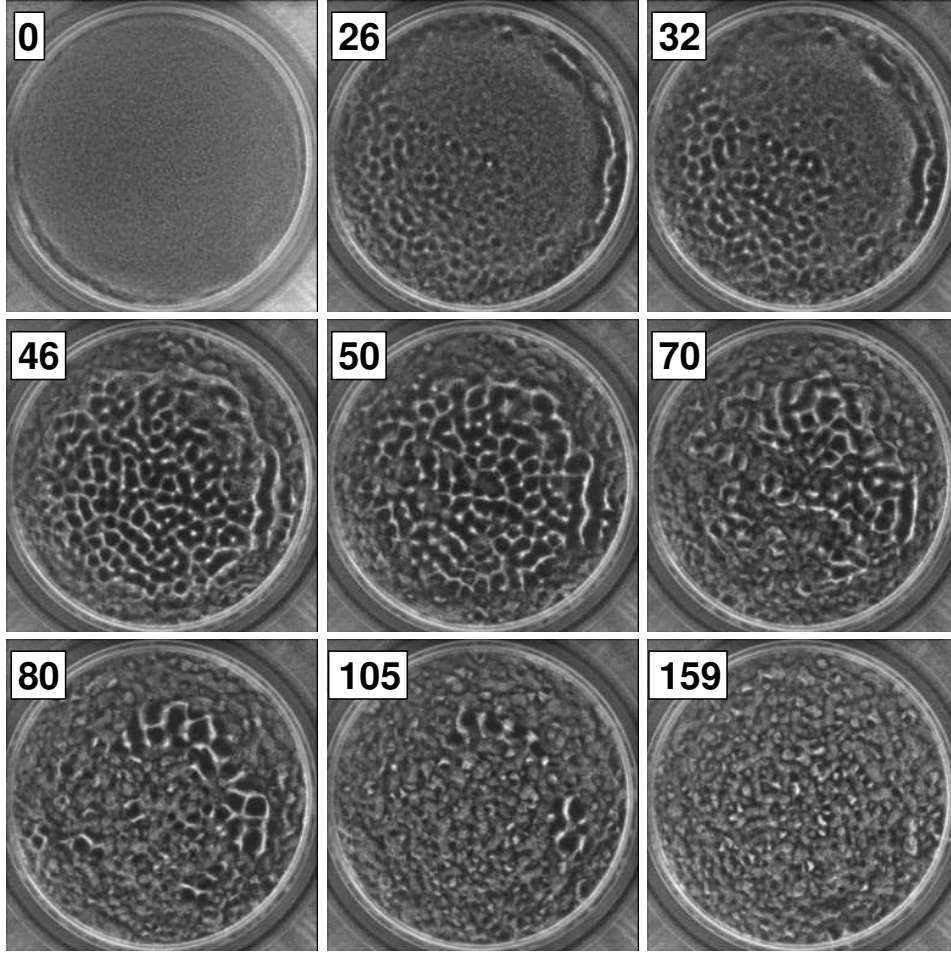
Figure 6.30: Transient growth and decay of square patterns oscillating at $f/6$. At $t = 0$, Γ is increased from 2.2 to 9.2 at $f_d = 83Hz$, $N = 15$.

kink, disappearing in the middle and popping up on the side. Thus, the dynamics of the trapped particles can be very complicated, and depends strongly upon the mobility of the small particles in the vibrating layer and the size ratio between the two species; this is schematically illustrated in Figure 6.35. Once a particle is trapped in the kink, it remains. However, there is a limit on the number of particles that can be trapped; at some point the large particles will not all fit in the trapping zone. When this occurs, particles leak out of the kink region.

When the frequency is decreased below a certain transition at roughly $f_d = 45$ Hz, the kinks develop a decoration. The trapping also works in the decorated kink state, but here the dynamics of the large grains is much more complicated. They seem to circulate between the the stripes in the decoration occasionally jumping from one roll to another,
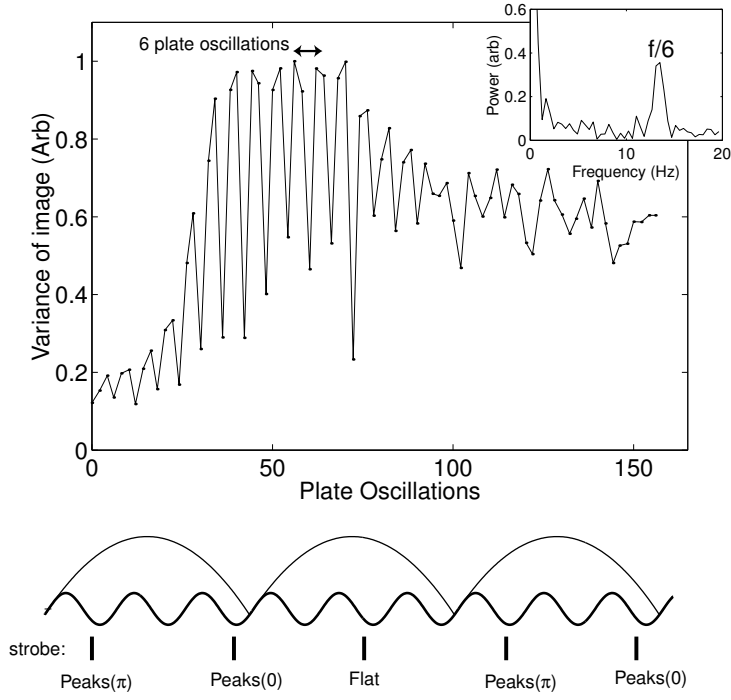
Figure 6.31: Main Figure: The variance of each images in the time series in Figure 6.30 plotted as a function of plate oscillations. Since the images were collected at $f_d/2$, the variance reaches a local maximum every 4 frames. As the schematic shows, this indicates that a complete pattern oscillation occurs every 6 plate oscillations, at $f_d/6$. The inset is the power spectrum of the variance.

see the time trace in Figure 6.36. This motion has the effect to transport the particles along the kink. This is in contrast to the high frequency kinks in which the particles execute no motion along the kink. The motion of large particles in the decorated kink occurs by long excursions and trapping events. It would be interesting to study the diffusion of the grains in this direction.
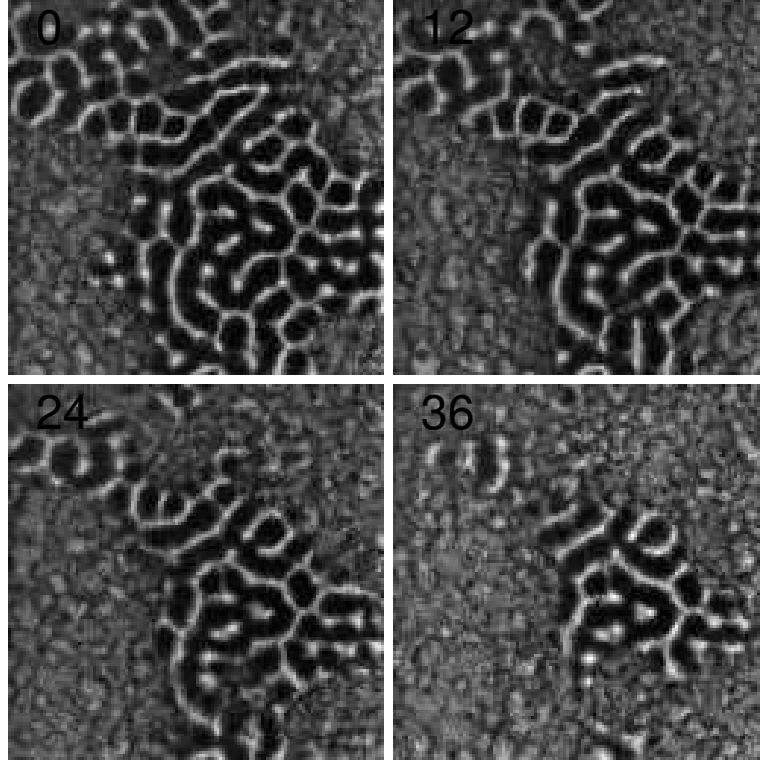
Figure 6.32: Close-up of the decay of a transient $f/3$ pattern shown. The parameter values are the same as those in Figure 6.30. The image area is 2x2 cm^2
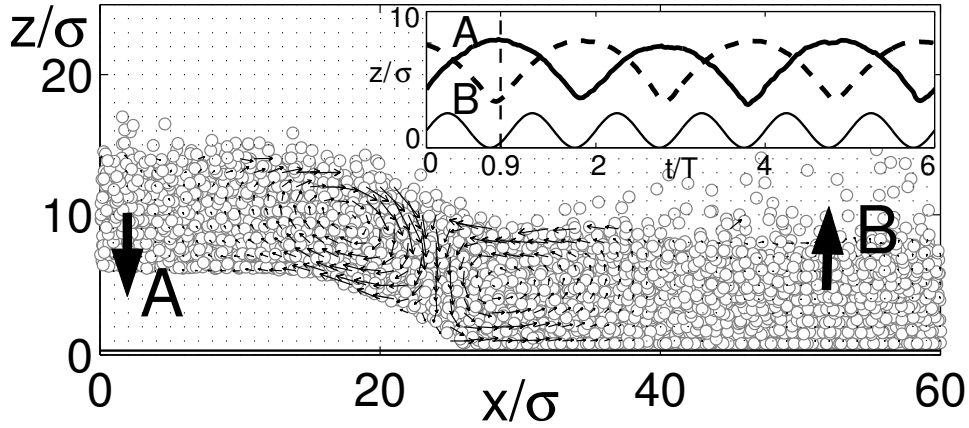
Figure 6.33: A projected side view of a kink created in a molecular dynamics simulation. A pair of convection rolls is associated with the kink and the small arrows represent displacement vectors over two plate oscillations. The inset shows the trajectory of the local center of mass of the layer at points A and B. Courtesy S. J. Moon.
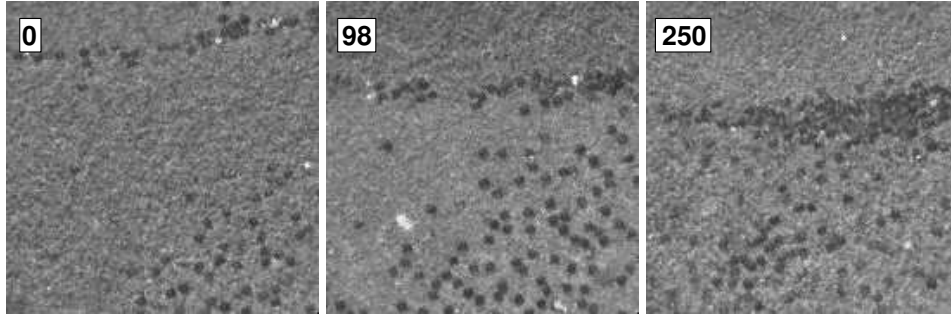
Figure 6.34: Transport and segregation of 650 μm glass spheres into a $f_d/2$ kink formed in 10 layers of 165 μm bronze spheres shaken at $f_d = 90$ Hz and $\Gamma \approx 4.5$. Both particles have a thin layer of graphite on their surfaces and the glass spheres appear black under overhead illumination.
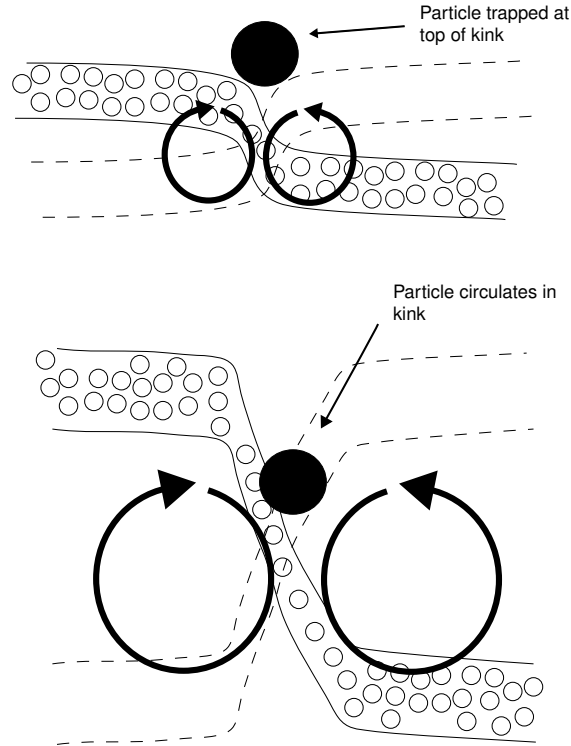
Figure 6.35: A schematic side-view of the behavior of large particles trapped in a kink formed in an oscillating layer of smaller particles. The top panel shows a high frequency kink in which the large particle remains trapped at the surface of the layer. The bottom panel shows a low frequency kink in which the local solid density of small particles is low, and the large particle can freely circulate within the convection roll.
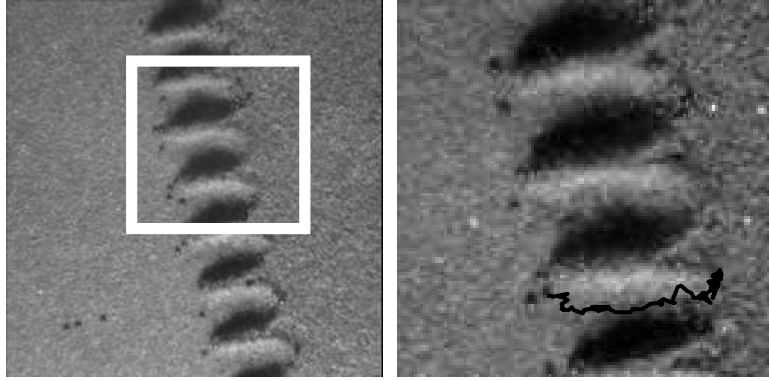
Figure 6.36: Segregation effects in decorated kinks for 650 μm glass spheres into a $f_d/2$ kink formed in 10 layers of 165 μm bronze spheres shaken at $f_d = 40$ Hz and $\Gamma \approx 4.5$. The large particle remains trapped in the kink but executes a complicated motion along the decoration which leads to transport along the kink.

6.5　Particle surface contaminants

The role of surface contamination was mentioned in Chapter 5 and will be briefly discussed here. It has a strong effect on pattern formation and also plays a role in the strength of the modes discussed in that chapter. In fact, the effect described could be a useful check on the form of friction proposed theories of granular materials.

We found that cleaning the particle in an ultrasonic cleaner for several hours in alternating baths of methanol-water and acetone water modify the particles so that when shaken, patterns which look like those in Figure 6.37a are seen. The patterns develop a haze above them. The addition of a small amount of contaminant (graphite powder, Moly-powder) restores the patterns as seen in Figure 6.37b. The haze decreases with increasing layer depth.
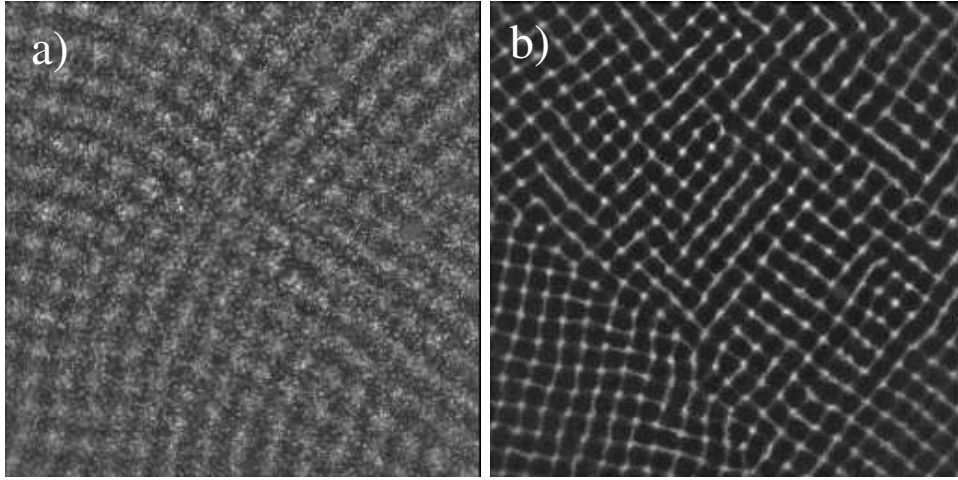
Figure 6.37: The surface properties of the particles influence pattern formation a) Four layers of 165 μm bronze spheres after after being cleaned in acetone and methanol. b) The same spheres after the addition of a small amount of graphite powder and the spheres have been shaken for 10^5 oscillations. In both panels, $\Gamma = 3.0$ and $f_d = 30$ Hz.

In fact, the restoration of the patterns also seems to trigger the normal modes. This is seen dramatically in Figure 6.38. A small amount of graphite was added to the layer and shaking began. The graphite slowly diffuses throughout the layer, and where it reaches, after only a few plate oscillations, the patterns crispen and modes grown in amplitude. In fact, if FM is applied, the section with graphite wiggles wildly while the pattern in the region without graphite do not display any normal mode oscillation.

Also, we find that particles direct from the factory (manufactured by Acupowder International, Union, NJ) do not display modes and have very hazy patterns. A magnified image reveals only that the factory particles are shiny and the graphite particles have a
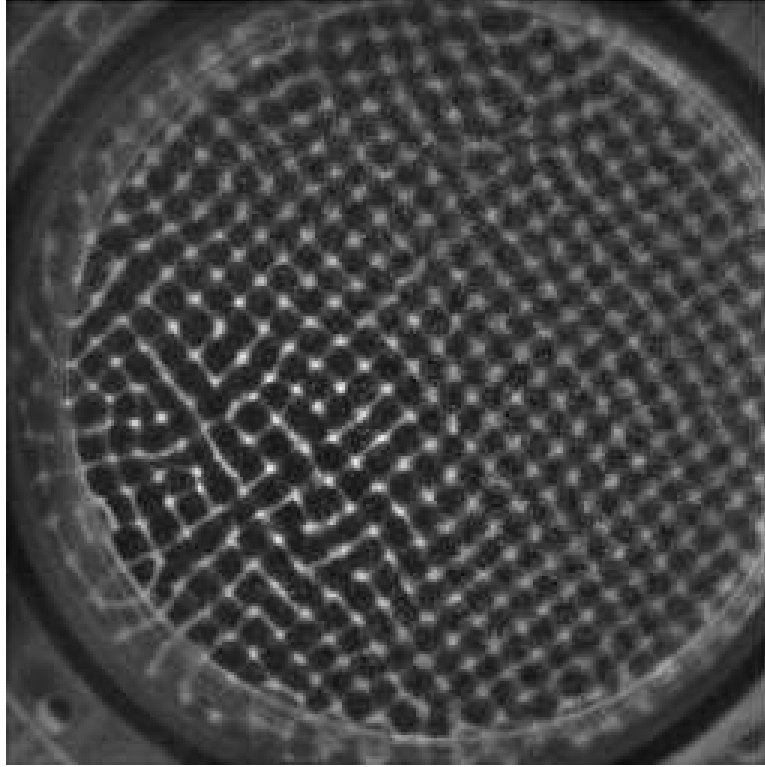
Figure 6.38: The addition of graphite reduces the haze around the particles and modes of the lattice appear. Here, $\Gamma = 3.0$, $f_d = 29$ Hz, at the top of resonance peak II. The clean particles show no modes, but immediately after addition of graphite, the modes appear.

dull surface. We speculate that the addition of the graphite does two things. It decreases the coefficient of restitution and decreases the friction by adding a low-friction layer to the particles. It would be interesting to fully characterize this as it is an experimental way to modify friction in granular flows. Acupowder makes different types of bronze with different materials alloyed. Since we have found that lead powder also makes crisp patterns, it would be interesting to try other alloys.
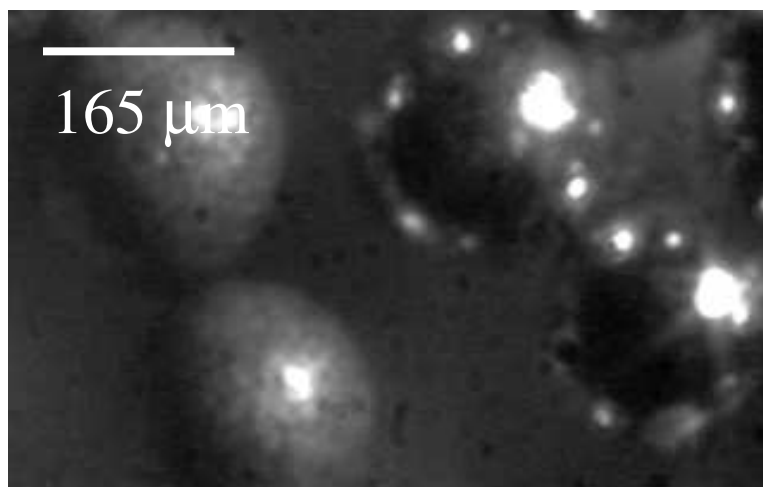
Figure 6.39: The two shiny particles on the right are fresh from the Acupowder factory and the two dull particles on the left have been shaking in graphite. The dull particles form crisp patterns with large amplitude normal modes.

Chapter 7

Absence of inelastic collapse in a realistic three-ball model

The contents of this chapter have been published in [71]

In this chapter, inelastic collapse, the process in which a number of partially inelastic balls dissipate their energy through an infinite number of collisions in a finite amount of time, is studied for three balls on an infinite line and on a ring (*i.e.*, a line segment with periodic boundary conditions). Inelastic collapse has been shown to exist for systems in which collisions occur with a coefficient of restitution r independent of the relative velocities of the colliding particles. In the present study, a more realistic model is assumed for r: $r = 1$ for relative velocity equal to zero, and r decreases monotonically for increasing relative velocity. With this model, inelastic collapse does not occur for three balls on a line or a ring.

7.1   Introduction

Energy loss during collisions of macroscopic particles is often described by a coefficient of restitution r, the ratio of the relative normal velocity of the particles after the collision to the relative normal velocity before the collision. Analyses of particle dynamics with constant r have shown that for r below a critical value r_c, many initial particle velocities and configurations lead to an infinite number of collisions in a finite time [13, 31, 77, 126, 127, 200]; both the relative spacings and velocities of the balls go to zero. Such a process is called inelastic collapse. In addition to the collapse analyses, simulations [120, 121, 123] and hydrodynamic analyses [13, 26, 49, 70, 78, 79, 165, 187, 194] of granular media have usually assumed r to be constant, *independent* of the relative collision velocity u. For real materials, however, r is not constant; rather, it increases monotonically with decreasing u and approaches unity in the limit that $u \to 0$ [5, 75, 108, 147].

To illustrate the problem with the usual assumption of constant r, we examine the two simplest models in which inelastic collapse has been shown to occur for constant r: three balls confined to an infinite line[31, 126, 200] and three balls confined to a periodic line segment (ring) [77]. For both of these models we find that if r is a physically reasonable function of the relative collision velocity, there is no collapse state. This
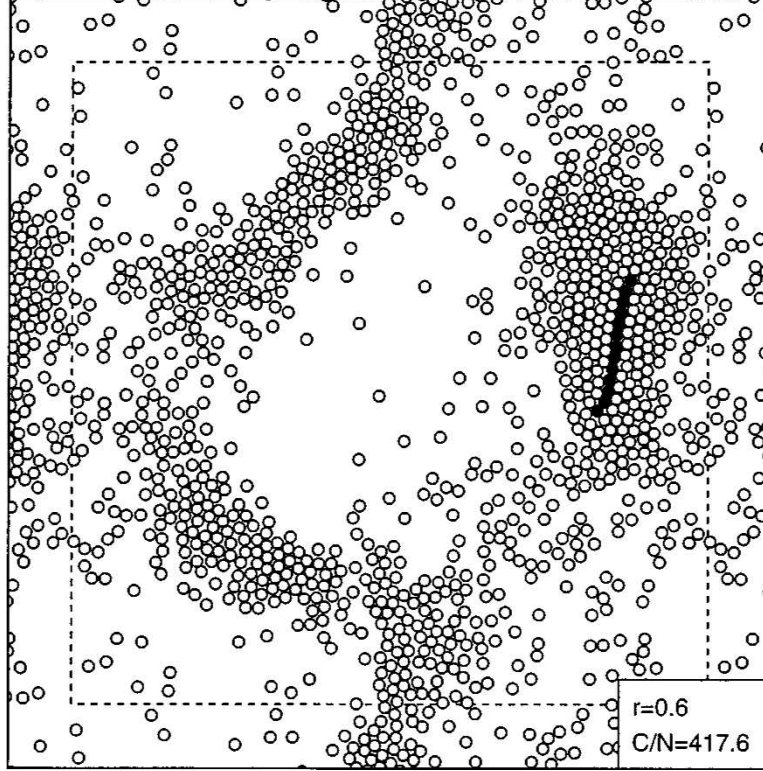
Figure 7.1: A 2D event driven molecular dynamics simulation of inelastic disks with a constant coefficient of restitution, $r = 0.6$. After several hundred collisions, large clusters have formed. The simulation was stopped when inelastic collapse was detected; C/N is the total number of collisions per particle at the time collapse occurred. The particles involved in the last 200 collisions are shaded black; these create the collapse state. Figure reproduced from [128].

result builds on a conjecture of McNamara and Young that collapse is an artifact of the idealized constant r model, and that a velocity-dependent r might eliminate this artifact [126].

The reason for the absence of inelastic collapse with a physical model for r is straightforward. If collapse is to occur, the relative velocities of all particles must go to zero. If $r \to 1$ as the relative velocity $u \to 0$, then for u small enough, a collision will occur for which $r > r_c$. From the previous work, this insures that collapse cannot occur. Thus, collapse in the line and ring geometries happens only for nonphysical coefficients of restitution. Therefore, the results obtained in recent analyses of inelastic collapse [13, 31, 77, 126, 127, 200], as well as work on the hydrodynamics of granular materials [13, 26, 49, 70, 78, 79, 165, 187, 194], should be re-examined using a more physically accurate form of r.

7.2 Three balls on an infinite line

Consider three balls of unit mass and labels L, M, and R (left, middle, and right). The balls' velocities are v^L, v^M, v^R, and their relative velocities are $u^L = v^L - v^M$, $u^R = v^M - v^R$. Assume that the balls undergo instantaneous binary collisions and that the relative velocities of two particles before and after their i^{th} collision, u_i and u_{i+1}, are related by a velocity-dependent coefficient of restitution, $r(u_i)$:

$$u_{i+1} = -r(u_i)u_i. \tag{7.1}$$

Without loss of generality, we assume that the system is prepared such that the velocities of the left and right balls are directed in towards the middle ball, and that the velocities of the balls are such that the left and middle balls undergo the first collision (*i.e.*, $u_0^L > u_0^R > 0$). After the collision between the left and middle ball, the relative velocities are (using the conservation of momentum and the definition of r):

$$u_1^L = -r(u_0^L)u_0^L, \tag{7.2}$$

$$u_1^R = u_0^R + \frac{1 + r(u_0^L)}{2}u_0^L, \tag{7.3}$$

The middle and right balls collide next. After the collision, the final relative velocities can be written

$$u_2^L = u_1^L + \frac{1 + r(u_1^R)}{2}u_1^R, \tag{7.4}$$

$$u_2^R = -r(u_1^R)u_1^R. \tag{7.5}$$

After this collision, the system will be in a state such that the only possible collision is between balls L and M. If these collide, then the next possible collision will be between R and M. Thus, we can generate a map which returns the system to a potential collision between L and M after every two collisions. This is done by substituting (7.2) and (7.3) into (7.4) and (7.5) and generalizing to obtain

$$u_{n+2}^L = -r(u_n^L)u_n^L + \frac{1}{2}(1 + r(u_n^R + \frac{1 + r(u_n^L)}{2}u_n^L))(u_n^R + \frac{1 + r(u_n^L)}{2}u_n^L), \tag{7.6}$$

$$u_{n+2}^R = -r(u_n^R + \frac{1 + r(u_n^L)}{2}u_n^L)(u_n^R + \frac{1 + r(u_n^L)}{2}u_n^L). \tag{7.7}$$

The iteration must stop if both $u_n^L < 0$ and $u_n^R < 0$ because then both L and R are moving away from M, and there can be no more collisions (*i.e.*, the range of the map contains points that do not lie within its domain). We now investigate the properties of this map.

The only fixed point of the map is $(u^L, u^R) = (0,0)$, for which the three balls move together with both relative velocities equal to zero. To show this, set $u_{n+2}^L = u_n^L \equiv u^L$

148

and $u_{n+2}^R = u_n^R \equiv u^R$. Substituting into the above equations, rearranging (7.6), and denoting $b = (1 + r(u^L))/2$ gives

$$3bu^L = u^R + r(u^R + bu^L)(u^R + bu^L), \qquad (7.8)$$

$$u^R = -r(u^R + bu^L)(u^R + bu^L). \qquad (7.9)$$

These yield $bu^L = 0$, so that either $u^L = 0$ or $b = 0$. If $b = 0$, the definition of b implies that $r(u^L) = -1$, which is unphysical. Substituting $u^L = 0$ into (7.9) leads to the condition $u^R(1 + r(u^R)) = 0$, giving either $u^R = 0$ or $r(u^R) = -1$. Again, the only physical result is $u^R = 0$.

To explore the long time behavior of the system, we calculate the stability of the fixed point. Writing the map in matrix form for small relative velocities du^L and du^R near the fixed point $(u^L, u^R) = (0, 0)$ gives [1]:

$$\begin{pmatrix} du^L \\ du^R \end{pmatrix}_{n+2} = \begin{pmatrix} \frac{(1+r(0))^2}{4} - r(0) & \frac{1+r(0)}{2} \\ -r(0)\frac{1+r(0)}{2} & -r(0) \end{pmatrix} \begin{pmatrix} du^L \\ du^R \end{pmatrix}_n. \qquad (7.10)$$

The eigenvalues of the matrix are:

$$\lambda_\pm = \frac{1 - 6r(0) + r^2(0) \pm \sqrt{(-1 + 6r(0) - r^2(0))^2 - 64r^2(0)}}{8}. \qquad (7.11)$$

The linearization of our map recovers the previous result of the existence of a critical r [31, 126, 200], and shows that for velocity dependent coefficients of restitution, the only value which determines whether a system will collapse is $r(0)$, the value of r at the fixed point. Substituting $r(0) = 1$ into (7.11) gives the complex eigenvalues $\lambda_\pm = (-1 \pm i\sqrt{3})/2$. The complex eigenvalues have magnitude unity, which implies neutral stability; hence we must argue further to determine the long time behavior of the linearized map around the fixed point.

Since $r(0) = 1$, the analysis reduces to that for perfectly elastic collisions. If collisions are elastic, a collision between two identical balls acts as if the balls pass through each other. Therefore, a maximum of three collisions may occur before the balls move away from the fixed point. As the relative velocities approach zero, the balls act elastically, and the dynamics must result in a state where all relative velocities are negative. Since the linearization of the map is valid for small u, inelastic collapse cannot occur – the balls will never reach a state where all relative velocities and separations are

---

[1]Since $r(u)$ might not be Taylor expandable near the fixed point, we linearize the map by writing it in terms of the difference $du_n^L = u_n^L - 0$ from the fixed point. We then drop terms of order $(r(du^L) - r(0))du^L$. Such a procedure allows $r(u)$ to be any continuous monotonic decreasing function with finite r(0)

zero. This is because the ranges of both the full and linearized maps contain points that do not lie within their domains.

If $r(0)$ is not unity, but $r_c \leq r(0) < 1$, where $r_c \equiv 7 - 4\sqrt{3} \approx 0.0718$, previous analysis has shown that the fixed point is unstable, and collapse cannot occur. Collapse can only occur if $r(0) \leq r_c[31, 126, 200]$. In experiments, such a situation can never be observed, since for real materials, $r(u) \rightarrow 1$ as $u \rightarrow 0$.

7.3 Three balls on a ring

The result for balls on an infinite line says nothing about what might happen if the balls were not allowed to go to infinity as soon as both relative velocities were negative. Therefore, we examine a model which allows continued interaction with neighboring balls, specifically, three balls of equal mass on a ring, *i.e.*, confined to a line segment of unit length with periodic boundary conditions. This geometry does not allow the balls to escape collisions. Note that there is no radial acceleration in this model; the ring merely imposes periodic boundary conditions. Grossman and Mungan [77] have shown that collapse occurs in such a configuration for $r < r_c$.

However, if collapse is to occur on a ring, the distances between the balls and their relative velocities must go to zero, so that one of the particles collides alternately with the other two particles, which do not collide with one another. This situation is indistinguishable from three particles collapsing on an infinite line. Since we have already shown that collapse does not occur on the line, collapse does not occur on the ring.

7.4 Discussion

We have shown that inelastic collapse, which was found in previous analyses with a constant restitution coefficient, does not occur with a realistic model for the restitution coefficient. While we have considered only three particle systems, we argue that collapse will not occur in a N particle system. Such systems have been studied [126] for constant coefficient of restitution with N particles on a line, and it was found that when r is near 1, the minimum number of particles necessary to create collapse varies as $-[\log(1 - r)]/(1 - r)$. Thus, as $r \rightarrow 1$, $N \rightarrow \infty$.

Studies predicting inelastic collapse have assumed instantaneous collisions. More realistic models of binary particle collisions would have to account for the duration of collisions (particle contact time), which diverges as $u^{-1/5}$ as $u \rightarrow 0$ [75]. Since inelastic collapse requires that the particles undergo an infinite number of collisions in a finite time, collapse cannot occur if the collisions are not instantaneous. For small relative velocities, the duration of the collision significantly affects the particle dynamics. The

incorporation of the finite contact time into the analysis complicates the problem because particles are no longer limited to binary collisions. The combined effects of a velocity dependent coefficient of restitution and finite duration collisions make inelastic collapse in the laboratory unlikely. We note that simulations with a velocity dependent r [169] and experiments [107] do not produce collapse, but show particle clustering, a situation in which variations in particle density spontaneously occur. It is possible that clustering in granular media proceeds through frustrated collapses, situations in which the collision frequency increases rapidly until the relative normal velocities are such that collapse ceases. However, clustering may also be due to finite duration collisions, or the inelasticity of particles may cause clustering through a scenario less catastrophic than inelastic collapse.

Chapter 8

Dynamics of particles at the onset of fluidization

8.1 Introduction

In this chapter we present a detailed study of the dynamics of glass spheres in a water fluidized bed near the onset of fluidization. As discussed in Chapter 2, the response of material properties (like strain, strength of material, yield vs. consolidation) of a collection of grains to a stress are strongly dependent on the packing density. We will study the dynamics of grains during fluidization, the application of a stress by a fluid flow, for different initial packings[1]. We find that corresponding to dramatic differences in material behavior for different packings under stress, there are dramatic differences in the *dynamics* of the grains under fluidization (stress from the fluid). Therefore, before we discuss the main results on the fluidization process, we will describe the procedure by which the volume fraction of the grains can be set to a repeatable value. We will then return to the subject of fluidization. Before we begin, we list the relevant parameters associated with the experiments described in this chapter.

Experimental parameters

We will describe the bed in terms of the voidage $1 - \Phi$, the average fluid volume fraction measured from the average height of the bed. The voidages will range $0.39 < 1 - \Phi < 0.5$. We will study the fluidization of 335 μm glass spheres, $\rho_p = 2.56$ g/cm^3 in water. The bed has a cross section 2.54x2.54 cm^2, which for Random Loose Packed (RLP), $1 - \Phi \approx 0.45$, gives roughly 80x80 particles across. We typically use 60 g of particles which for RLP pack the bed approximately 7 cm high. Typical flow rates at the onset of fluidization are between 30-45 mL/min, depending on the initial packing fraction. This gives typical fluidization velocities, v_f, at onset between $0.08 - 0.1$ cm/sec. For the 335 μm spheres, the single particle sedimentation velocity, v_s was measured as $v_s = 4.5$ cm/sec. This is in accord with the Richardson-Zaki law which predicts $v_f/v_s \approx 0.02$ for the RLP state. The Reynolds number for the flow, using the particle as the length scale and v_f as the velocity scale gives $Re \approx 0.3$. $Re \approx 15$ when the v_s is used. We measure

---

[1]The basic process of fluidization was discussed in Chapter 1, and the experimental apparatus was described in Chapter 3.

the relative collision velocity, $v_{\rm rel}$ using Diffusing Wave Spectroscopy techniques and confirming the measurement with a high speed camera. From this, we compute the Stokes number, a measure of the importance of hydrodynamic effects during collisions, $St = \rho_p a v_{\rm rel}/\mu \approx 0.6$, where ρ_p is the particle density, a is the particle diameter, and μ is the fluid viscosity. $St \approx 0.8$ when v_f is used. The size of the Froude number, $Fr = v_f^2/ga$ has been shown to correspond to bubbling vs. non-bubbling behavior at the onset of fluidization [193]. $Fr \ll 1$ corresponds to a fluidization with a smooth initial expansion while fluidization in which $Fr \gg 1$ demonstrates bubbles of fluid rising through the bed. In our experiments, $Fr \approx 3 \times 10^{-4}$, well below the bubbling transition. $Fr \approx 0.6$ when v_s is used.

8.2 Flow pulse experiments

Everyday experience shows that tapping a pile of grains results in a decreased voidage–shaking the cereal box is a good example. Extensive work has been done to study the voidage of a container of dry grains as a function of tapping rate and amplitude [104]. We study the fluid-dynamical analogy to the tapping experiment, in which short fluid pulses act like taps.
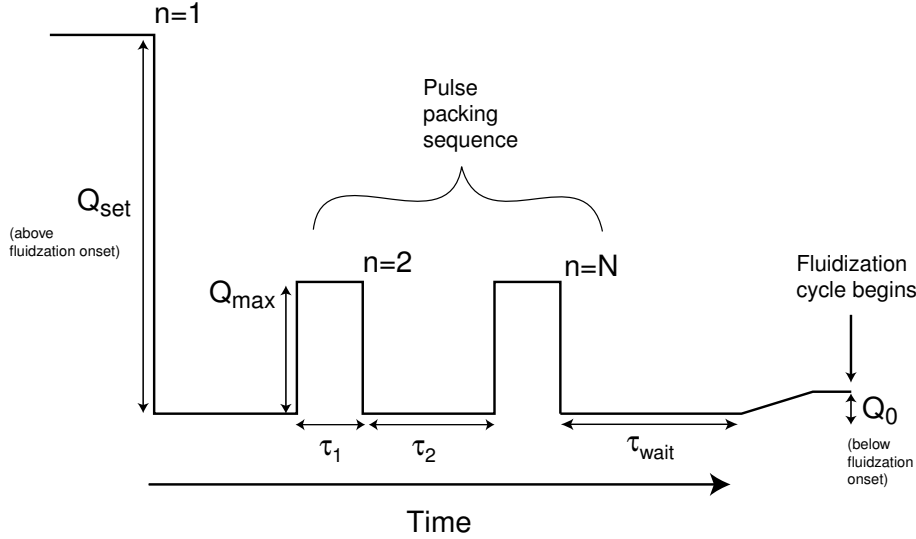
Figure 8.1: Flow pulses of amplitude $Q_{\rm max}$ and duration τ_1 can be applied to the bed after initial fluidization at $Q_{\rm set}$. N total pulses are applied after which the flow is set to a value Q_0 below the onset of fluidization.

To set $1 - \Phi$, we apply a series of flow pulses to the grains. This is schematically shown in Figure 8.1. The maximum amplitude of the pulse, $Q_{\rm max}$ and duty cycle can be

easily controlled by means of a three way valve (See schematic in Figure 3.4 in Chapter 3). The procedure is as follows: The flow rate is set to a value Q_{set} (Q_{set} is always greater than Q_{max}) well beyond the point of fluidization and controlled at this point until the system equilibrates, typically 30 seconds, reaching a steady voidage. At this point, the sequence of flow pulses is applied with maximum pulse amplitude Q_{max} and duty cycle defined by $\tau_1/(\tau_1 + \tau_2)$. For increasing total number of pulses, N, the voidage of the bed decreases—the bed packs as shown in Figure 8.2. When the target voidage is achieved, the flow is set to $Q = 0$ for a time τ_{wait} to allow the system to settle. Flow is then slowly increased to value Q_0 well below fluidization. This small flow does not alter the voidage and in fact it stabilizes the packing by jamming the grains against the sidewalls. We will discuss this point further in the section on jamming, Section 8.4. A fluidization cycle begins at the flow rate Q_0. We note that the loosest packing is obtained by stopping the pulse sequence after the $N = 1$ toggle, allowing the bed to sediment for τ_{wait} with $Q = 0$ and then slowly increasing the flow to Q_0.
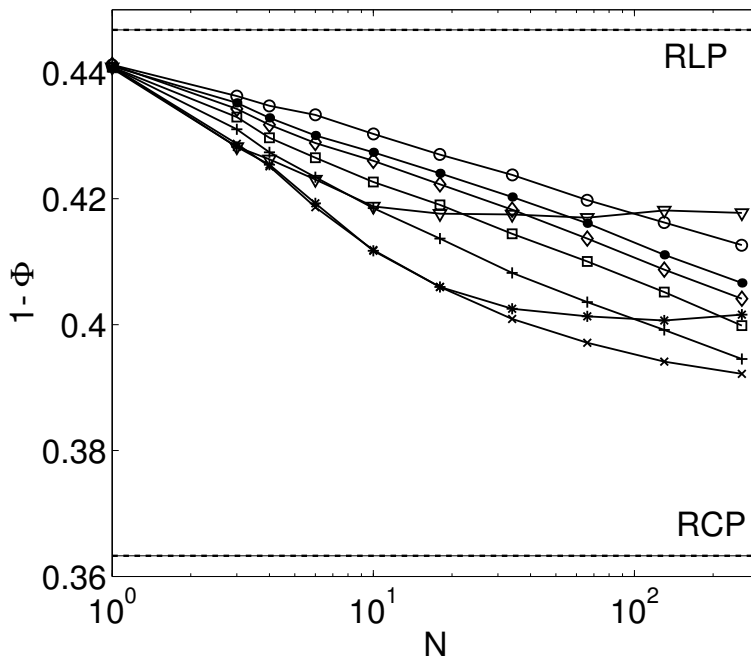
Figure 8.2: The voidage of the bed decreases as the number of toggles increases. Here duty cycle is fixed to 1/3 on 2/3 off and the entire cycle lasts 2 seconds. Q_{max} has values of $(\circ, \bullet, \diamond, \square, +, \times, *, \triangledown)$, $(0, 17.3, 27.2, 48.6, 71.3, 94.1, 116.2, 136.5)$ mL/min.

There are several points to notice about Figure 8.2. The first is that the rate of decrease of $1-\Phi$ with N is a function of Q_{max} for fixed duty cycle. For a range of Q_{max} the average rate of decrease in voidage increases as Q_{max} increases. We interpret this as stronger rearrangement pulses allow the bed to explore local crevices more efficiently.

154

However, for large enough Q_{max} the voidage behaves non-monotonically for increasing N. We can explain the non-monotonicity by the following argument. In a fluidized bed, the pressure drop across the bed (which determines the fluidization) increases as voidage decreases. Since a pulse is essentially a short fluidization event, there exists a voidage at which Q_{max} becomes large enough to fully fluidize to a voidage greater than the voidage before the pulse in the time during which the flow is on. For a given Q_{max}, for further N, the voidage increases as a function of N. The value of N at which the voidage should increase decreases as Q_{max} increases. A plot of the voidage of the bed for $N = 256$ reveals that there is an optimal Q_{max} for the particular duty cycle chosen, see Figure 8.3. The effects of changing duty cycle have not been investigated but are expected to play a role as they influence the time during which the system can reach a new height or relax. The question of packing optimization, by which the voidage could be decreased to its smallest value in the most efficient way, has not been addressed. We speculate that some recent models of energy landscapes of glasses could shed light on the packing problem [45]. In addition, packing experiments could be useful tests of different landscape theories.
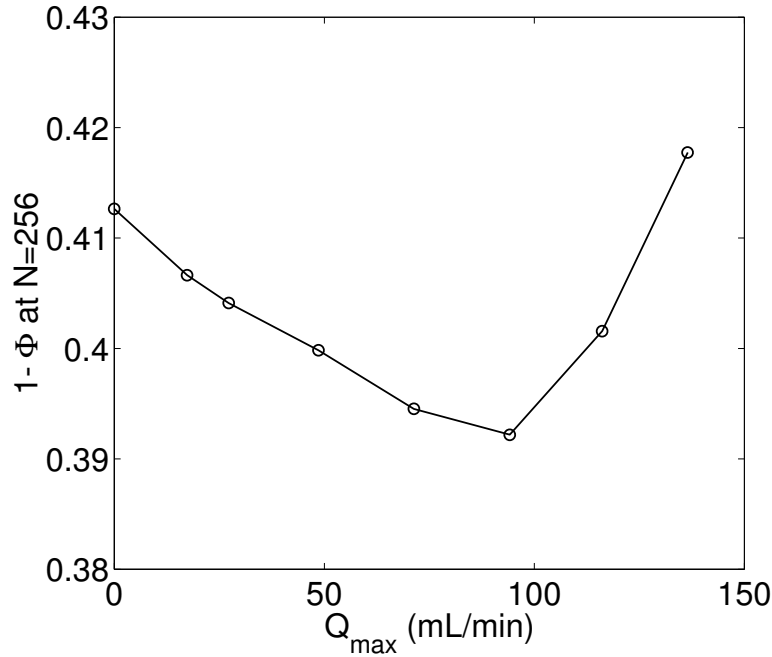
Figure 8.3: The voidage of the bed for a fixed number of pulses, $N = 256$ as a function of Q_{max}.

8.2.1 Sedimentation

The maximum voidage state is always obtained by simply allowing the particles to sediment freely from a very high voidage state. This is achieved by fluidizing at $Q_s et$ and stopping the pulse sequence after $N = 1$. When the flow is removed, the voidage decreases from $(1-\Phi)_{\text{initial}}$ and after sedimentation, reaches a stationary loosely packed state, $(1 - \Phi)_{\text{final}}$. This final voidage depends upon the initial voidage as shown in Figure 8.4. The curve appears to asymptote to a value of $1 - \Phi \approx 0.445$. This value is in good agreement with the results of Onoda and Liniger [139] who measured the volume fraction of grains sedimenting in fluids of varying particle-fluid density difference. As the density difference approached 0, the sedimentation rate approached 0 and they found that the volume fraction reached the limiting value of $1 - \Phi = 0.445$ They identify this as the Random Loose Packed (RLP) state and define it as the highest voidage state which is mechanically stable in the limit that $g \rightarrow 0$. This state will play a very important role in the dynamics of fluidization and we will refer to it again later. In practice, we find that it is almost impossible to maintain a bed in the true RLP state, due to its fragile nature.
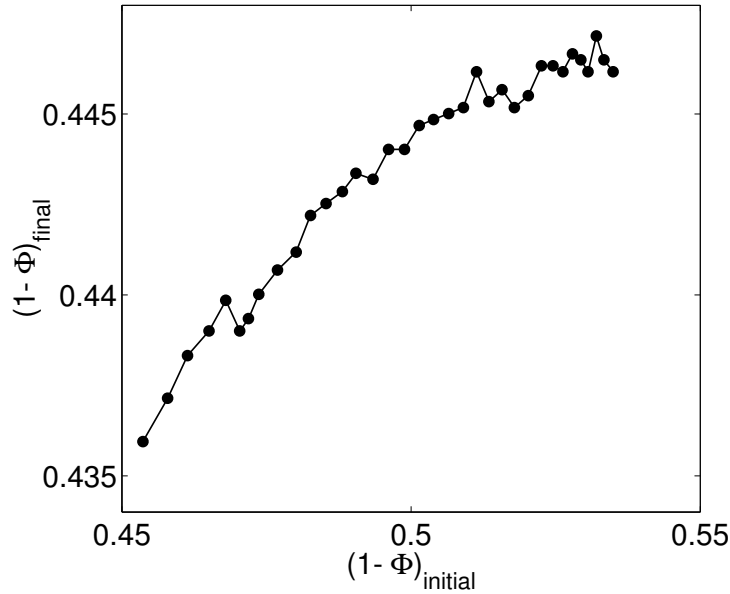
Figure 8.4: The final voidage of the bed after flow is suddenly turned off as a function of initial voidage of the bed. The initial voidage increases with increasing Q_{set}

Our sedimentation experiment differs from that of Onoda and Liniger as the density difference is kept fixed while the initial packing is varied. Thus, our experiment is

analogous to the sedimentation experiments performed on much smaller colloidal parti-
cles [1]. As the particles sediment, the voidage decreases. The net result is that the final
volume fraction approaches RLP as the initial voidage increases. We note that the sedi-
mentation behavior in water is much different from that of grains sedimenting (falling) in
air. We when pour grains into the system without water present, we observe that grains
almost immediately pack into a state near a voidage of $1 - \Phi \approx 0.37$, the Random Close
Packed (RCP) state.

8.3 Fluidization

We now discuss the fluidization process and the dynamics of the grains at fluidiza-
tion. We will refer to an experiment in which the flow is increased and then decreased to
the initial point as a fluidization cycle. The goal of this section will be to investigate the
behavior of a bed during a fluidization cycle as a function of the initial condition. The
initial condition will be set by the pulsing procedure described above. All experiments
used the mesh flow distributor arrangement shown in Figure 3.5 in Chapter 3.

8.3.1 Fluidization and initial conditions

In this section we describe the dynamics of the glass spheres upon increase of
flow rate from an initial packing of the 335 μm particles. Other particle sizes showed
similar qualitative behavior. The techniques we will use to characterize the average
properties of the bed have been discussed in Chapter 3. Two complete fluidization
cycles for different initial conditions are shown in Figure 8.5. The plot shows both
fluidization and defluidization, but in this section, we will only discuss the fluidization
branch. We postpone the discussion of the defluidization branch until the next section,
subsection 8.3.2.

To take these curves, we use the following protocol: starting from $Q_0 = 0$ mL/min,
we slowly increase the flow for 30 seconds until a particular Q is reached. At Q, the flow is
controlled while the system equilibrates, typically 30 seconds. After equilibration, various
measurements are made. These include voidage, pressure drop, and light scattering
measurements. When the measurements are complete, we ramp slowly to the next Q and
repeat. The increment in Q between measurement points is fixed during an experiment.

For a given path, as Q is increased, ΔP, the pressure drop across the bed normal-
ized by the buoyant weight of the grains per unit area increases. ΔP increases past the
point of force balance for the weight of the grains, $\Delta P = 1$, until it reaches a maximum
value. At this point, it begins to decrease. At the point where ΔP begins to decrease,
the voidage of the bed begins to increase—the system becomes fluidized. The tightly
packed state displays complicated paths during which ΔP begins to increase again as Q
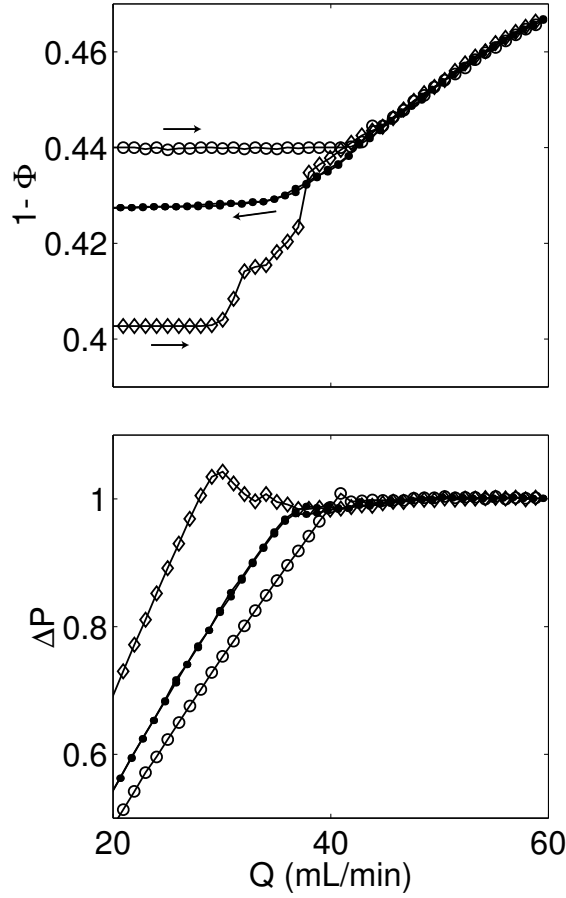
Figure 8.5: Fluidization cycles for increasing flow for two different initial voidages 0.440 (∘), 0.403 (◇) (a) Voidage vs. flow rate (b) Pressure drop vs. flow rate. Particles are 335 μm glass spheres with total mass 60 g. The curve with • symbol is for defluidization and is independent of the initial voidage. Protocol: 30 sec ramp between each point with 30 second equilibration time.

increases. During this range of Q, the voidage remains roughly constant. We believe this behavior is a consequence of poor flow distribution and will be discussed later. The different packings fluidize at different values of Q. This is a consequence of Darcy's law–the tighter packed bed has a lower permeability and thus develops a larger ΔP for the same Q. The fluidization curves intersect at a certain value of Q, close to the value of RLP, $1 - \Phi \approx 0.44$. From this point, the voidage continues to increase while ΔP remains at a value of unity.

We now examine the dynamics of the grains during these two fluidization cycles

by measuring the autocorrelation of multiply scattered light, $g^{(2)}(\tau)$ (see Chapter 3 for details). Examples of $g^{(2)}(\tau)$ at different Q along the loosely packed fluidization branch are shown in Figure 8.6. For each Q, 10 correlation curves, each sampled for 30 seconds, were taken at 1 second intervals. This is done so that we can study repeatability of the measurements. In addition, it allows us to capture changes which might occur on a timescale longer than 30 seconds. To achieve 10% accuracy in the curves, it is necessary to sample on a timescale roughly 10^2 longer than any timescale of interest. Thus, we expect that decays of $g^{(2)}$ as long 0.3 seconds should be measurable with some reliability. Later in the chapter, we will use the multispeckle techniques described in Chapter 3 to extend the range of accessible timescales by another factor of 10. We note that even for completely motionless particles, measurements of correlation curves over long times decay with a characteristic time of roughly 3 seconds. We believe that this is due to either slow movements in the apparatus or heating from the laser. This sets the fundamental decay time limit for the correlation measurements.
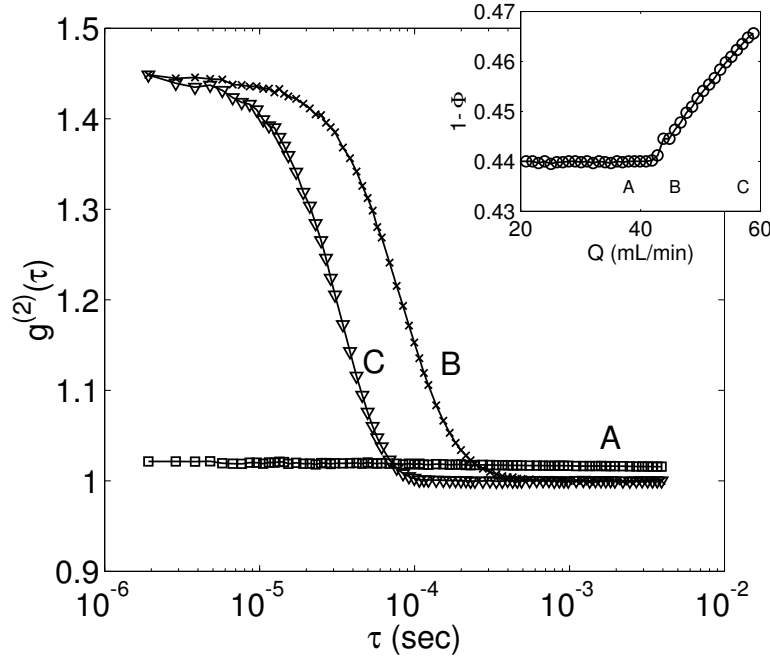
Figure 8.6: Correlation curves, $g^{(2)}(\tau)$ along the loosely packed fluidization branch, showing no decay below onset and a rapid decay above onset. Flow rates A-C, 37 mL/min ($\square$), 45 mL/min ($\times$), 56 mL/min ($\triangledown$)

For the point A below fluidization, $g^{(2)}(\tau)$ does not decay significantly. This indicates that the particles remain motionless below fluidization. Above fluidization (points B and C), $g^{(2)}(\tau)$ decays with a timescale which decreases as the system becomes

more fluidized. We will denote this decay time as τ_d, defined as the time at which $g^{(2)}(\tau) - 1$ reaches the $1/e$ point. The intercepts of the $g^{(2)}(\tau)$ for the fluidized states are close to 1.5, the expected value for depolarized light [119]. This value indicates that we are imaging one coherence area and that enough decorrelation cycles have been taken to ensure good statistics. The intercept for the motionless particles is close to 1, the value predicted for a signal of constant intensity [119]. Using the theory of DWS from Chapter 3, we can extract the ensemble averaged mean square displacement, $\langle \Delta r(\tau)^2 \rangle$, of the particles from these curves. However, to gain understanding, we first use the inverse time-scale of decay of $g^{(2)}(\tau)$, $1/\tau_d$, to analyze the motion of the grains at onset.

Figure 8.7 shows a comparison of the inverse decay time $1/\tau_d$ as a function of flow rate for the two fluidization cases discussed. For each curve in (a), the mean value of 10 correlation curves taken after equilibration is shown and the error bars indicate the spread in the decay times. For the two different initial packings, we see a remarkable difference in the dynamics of the grains at the point at which the voidage of the bed begins to increase. In both cases, well below fluidization, $1/\tau_d$ is close to zero, indicating a motionless state. For the loosely packed state, at the point where the bed height begins to increase, $g^{(2)}(\tau)$ immediately decays with a timescale of about 1 msec. The transition point is marked by the dashed line. This indicates that the grains begin to move immediately at the onset of fluidization, as might be expected. However, the behavior of the grains on the tightly packed state is quite different. Here the system reaches a point where the voidage begins to increase, near 30 mL/min but $g^{(2)}(\tau)$ does not decay. In fact, no decay of the correlation occurs until a higher flow rate, around 33 mL/min. At this flow rate, $g^{(2)}(\tau)$ decays in a finite time, but there is a large variation in $1/\tau_d$ for the different measurements. This indicates that the system is experiencing transient behavior. As flow is increased, $1/\tau_d$ continues to increase until the curves for the loosely and tightly packed states intersect.

It is instructive to examine the pressure drop across the grains during these changes in grain dynamics. As discussed above, the voidage begins to increase when ΔP reaches a maximum above 1. For the tightly packed case, once ΔP reaches the maximum pressure, further increases in Q result in a decrease of ΔP. When ΔP reaches a value close to 1, the grains begin to move[2]. Thus, there exists a range of Q for which the bed temporarily fluidizes and the voidage increases, but after some time, the bed settles into a motionless state. Such behavior has also been observed in air-fluidized beds [130]. In the loosely packed state, the overshoot in ΔP is much smaller. For this case, the step size in Q is presumably too small to resolve the motionless regime. In both cases, when

---

[2]We note that the behavior of ΔP once the grains have begun to move is complicated. For increasing Q, ΔP increases until it reaches a maximum, after which it begins to decrease. We will discuss this behavior later in the chapter.
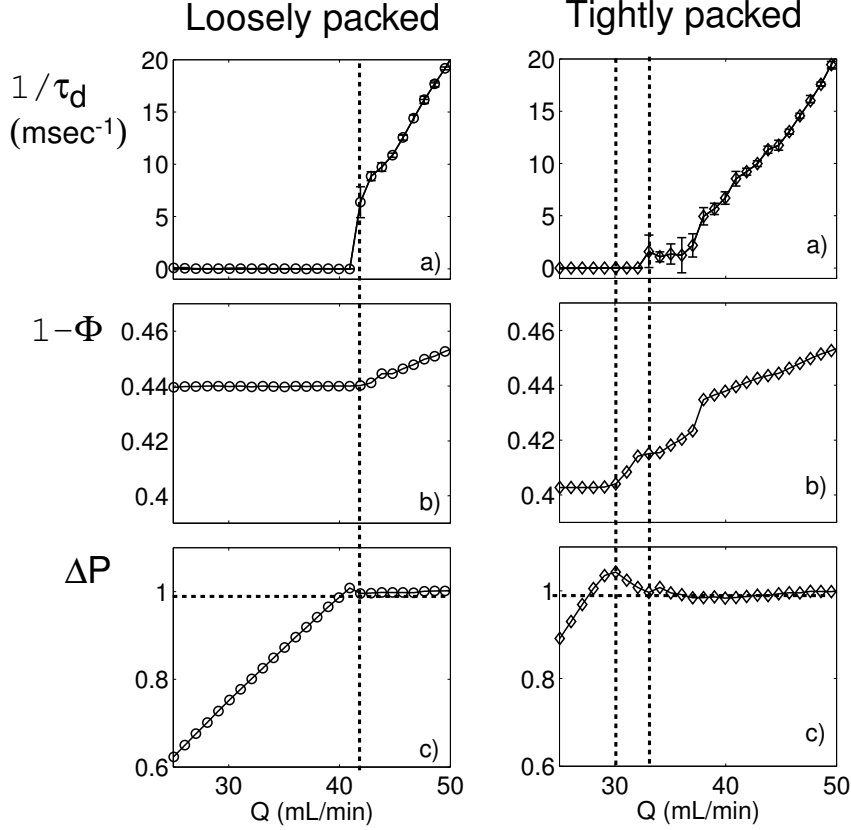
Figure 8.7: Top panels: The decay times of the correlation function, $1/\tau_d$, for fluidization from loosely ($\circ$) and tightly ($\diamond$) packed initial conditions. The corresponding pressure and voidage curves are included for reference. Loosely packed: the dashed line denotes where motion begins as indicated by a finite value of $1/\tau_d$. The point where the material yields and the point where motion begin are separated by a single flow increment in this experiment. Tightly packed: the leftmost dashed line denotes the value of Q where ΔP reaches a maximum and $1 - \Phi$ begins to increase. The dashed line to the right denotes the Q on the tightly packed branch where particle motion begins. Protocol: 30 second ramp with 30 second equilibration time.

Q is large enough all curves intersect, and $\Delta P = 1$. At high enough Q, the system can be considered truly fluidized. At this point all grains are continuously in motion and in contact only during very short collision times[3]

We interpret these experiments using the results of Onoda and Liniger [139] and the theories of Jackson discussed in Chapter 2 as guides. According to the theory of

---

[3]As will be discussed, for $St \ll 1$, lubrication layers may prevent true particle contact during collisions.

dilation [151], any applied stress (like the pressure drop due to the flowing fluid) causes a granular material to dilate. If there are confining sidewalls, the dilation is frustrated, and a pressure against the sidewalls develops. This is the source of the yield stress in tightly packed granular materials (see Chapter 2 for details). As the shear stress increases, the force from the boundary will increase until the material yields. We see this behavior for the tightly packed bed. ΔP increases to a maximum almost 5% past the force balance necessary to move the grains. Once the material has yielded, ΔP displays non-Darcian behavior, decreasing for increasing Q. In addition, since ΔP is smaller than the maximum overshoot value, the bed has becomes weaker and a smaller amount of stress is needed to continue the yield process and further increase the bed height[4]. While the material is yielding, the $1/\tau_d$ data show that the grains are motionless. Eventually, the system reaches a state where there is no more extra stress to overcome. Now, the force balance can now move the grains.

We contrast this to the behavior in the loosely packed state. As shown by Onoda and Liniger, in the RLP state, $1 - \Phi \approx 0.45$, in stress does not promote dilation. Roughly put, at this voidage, the grains do not need to expand an extra amount in order to shear, slipping past each other. Thus, in fluidization of such a state, a shear will not have to overcome any extra contact forces, and the grains will move as soon as there is a force balance. The loosely packed data is in accord with picture—the overshoot is much less and the grains begin to move at onset[5].

The results described deviate slightly from the schematic of fluidization sketched in Chapter 1 due to the presence of extra contact forces. In summary, due to pressure drop developed across the resistive medium, a stress is created on a collection of grains. This stress seeks to dilate the grains, but the walls and frictional contacts prevent this dilation. Thus, an extra stress is developed, and this must be overcome before true fluidization can occur; the stress overshoot is larger for the tighter packing. In Figure 8.8 we plot the % overshoot of the pressure for fluidization from different initial packings. In the limit of RLP, the overshoot approaches zero, indicating that the stress required to yield this material approaches zero.

Short-time dynamics

We now examine the short-time dynamics of the grains during these processes. The ensemble mean square displacement, $\langle \Delta r(\tau)^2 \rangle$ of the grains at short times is measured using the multiple scattering Diffusing Wave Spectroscopy described in Chapter 3.

---

[4]Equivalently, the material has a lower strength, as predicted in Chapter 2. Thus, further stress will cause the material to yield more easily.

[5]However, we never fluidize from the RLP state, as it is unstable to infinitesimal perturbation. There would be no overshoot at such a state.
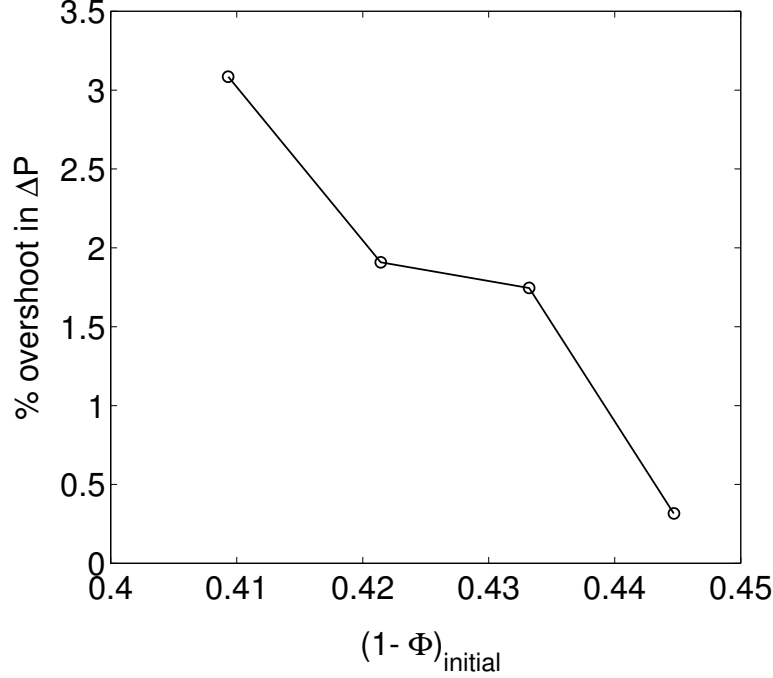
Figure 8.8: The % overshoot over $\Delta P = 1$ in the fluidization pressure curves as a function of initial packing for the fluidization cycle.

Figure 8.9 plots $\langle \Delta r(\tau)^2 \rangle$ for the correlation curves shown in Figure 8.6. These curves are found by the inversion techniques described in Chapter 3. Below onset the grains do not move, but far enough above onset, $\langle \Delta r(\tau)^2 \rangle \sim \tau^\alpha$, with $\alpha \approx 2.0$. This indicates the the motion of the grains is ballistic at short times. Note, however, the scale over which the grains execute the ballistic motion. $g^{(2)}(\tau)$ decays to close to 1 at roughly 0.1 msec. At this time, the particles have displaced roughly 10^{-2} μm, a factor of roughly 30000 times smaller than their diameters. Thus, for short times, the grains are free to undergo small displacements in the fluid.

Figure 8.10 plots the average exponent, α of the short time behavior during fluidization for the two packing cases. In both cases, below onset $\alpha \approx 0.2$. This is a consequence of the slow decay of $g^{(2)}$. At onset in the loosely packed state, as was shown in Figure 8.7, motion is detected immediately. Figure 8.10 reveals that α quickly rises to $\alpha \approx 2$. Thus, in the loosely packed state, there is enough free volume for *all* particles to immediately establish collisional dynamics. The tightly packed case displays complicated dynamics after the material has initially yielded. In this case, α slowly (compared to the increase in α for the loosely packed state) increases until sufficiently far above onset, it reaches a value of 2.

We propose that $\alpha < 2$ indicates that the behavior of the grains is not homo-

163
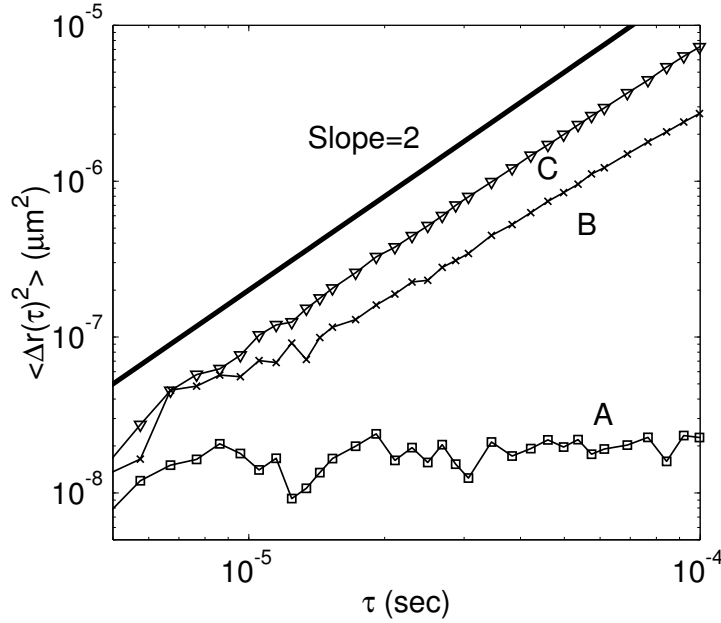
Figure 8.9: $\langle \Delta r(\tau)^2 \rangle$ shows that when the system is fluidized, the particles move ballistically during short times. These curves correspond to the curves in Figure 8.6: A-C, 37 mL/min ($\square$), 45 mL/min ($\times$), 56 mL/min ($\triangledown$). The intercepts have been normalized to the minimum detectable displacement, roughly 1 $\AA$.

geneous throughout the bed. Recall that we are visualizing extremely small trajectory times and displacements. Since the multiply scattered signal for DWS samples all particles in the bed, $\langle \Delta r(\tau)^2 \rangle$ will contain contributions from motion averaged over many regions. This is shown schematically in Figure 8.11. In some regions, the grains are executing ballistic trajectories between collisions, and $\alpha \approx 2$. In other regions of the bed, the particles are in contact for times long compared to a mean free time between collisions. Thus, $\alpha \approx 0$ in these regions[6]. Presumably, these regions are not static, but change on timescales much shorter than the sampling time (we will further examine this assumption when we discuss multispeckle techniques). Thus, we propose that the value of α is directly related to the average fraction of completely mobile grains. Below onset, all grains are immobile and α stays at the baseline noise value of $\alpha \approx 0.2$. As Q is increased above fluidization, the fraction of mobile grains increases until all grains are mobile and $\alpha \approx 2$.

The results above demonstrate that the contact forces between particles can play

---

[6]Recall that due to the slow decay of $g^{(2)}$ presumably due to heating effects, α is never identically zero. We will assume that the baseline of $\alpha \approx 0.2$ indicates the lack of motion at short times.
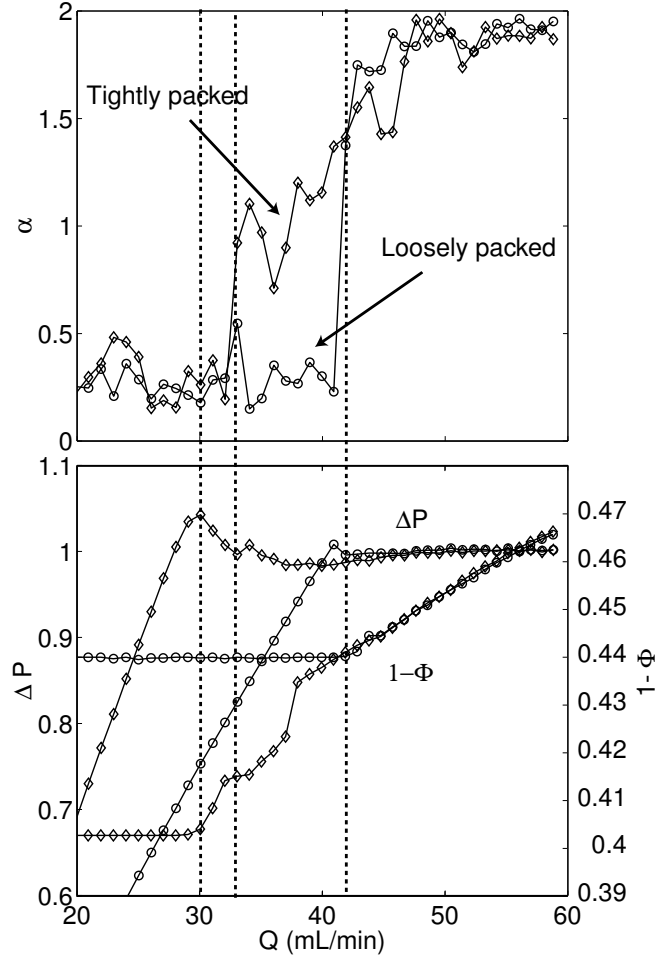
Figure 8.10: Top panel: α as a function of flow rate for fluidization from two different initial packings, tightly packed ($\diamond$) and loosely packed $\circ$. Note the baseline value of $\alpha \approx 0.2$ below fluidization. This is due to a slow drift in the system and is discussed in the text. The voidage and pressure data is included for reference in the bottom panel. The dashed lines indicating transitions in bed behavior and protocol for fluidization are the same as those in Figure 8.7.

a major role in the motion of particles at onset. We now study a case in which contact forces do not play a role, defluidization from a fluidized state.
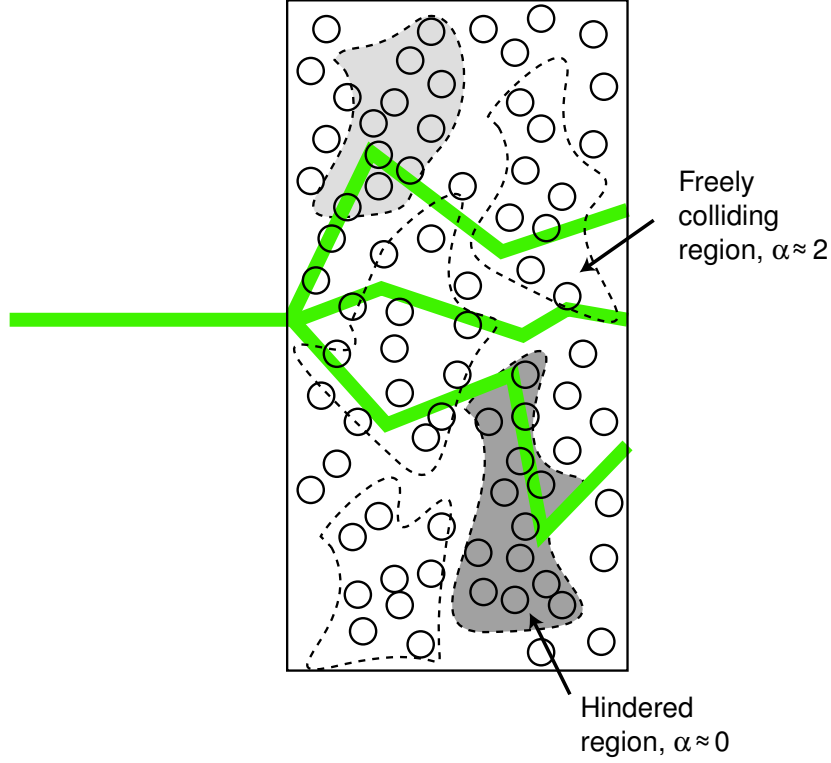
Figure 8.11: A schematic of the different regions of particle dynamics. The multiply scattered light follows paths which sample all regions. Note that this diagram is not to scale, nor is it intended to represent the actual size or shape of the regions.

8.3.2 Defluidization

Hindered motion

When the system is in a fluidized state, well above RLP, the contact network is not established. Consequently, defluidization from such a state will not be subject to sustained contact forces. We then expect that the behavior of the bed should be different. This is seen in Figure 8.12. The defluidization branch follows the fluidization branch until it reaches a point near RLP. From this point $1 - \Phi$ continues to decrease as Q is decreased. As some point, the condition for force balance, $\Delta P = 1$ is no longer satisfied. As Q is decreased from this point, the voidage continues to decreases, but at much slower rate. Note that this path is independent of the initial state, provided that the initial state is sufficiently fluidized. We will return to this point in the section on jamming.

Figure 8.12 shows the behavior of α during defluidization. For Q such that $1 - \Phi > 0.45$, $\alpha \approx 2$. Thus, the particles undergo ballistic collisional dynamics when the voidage
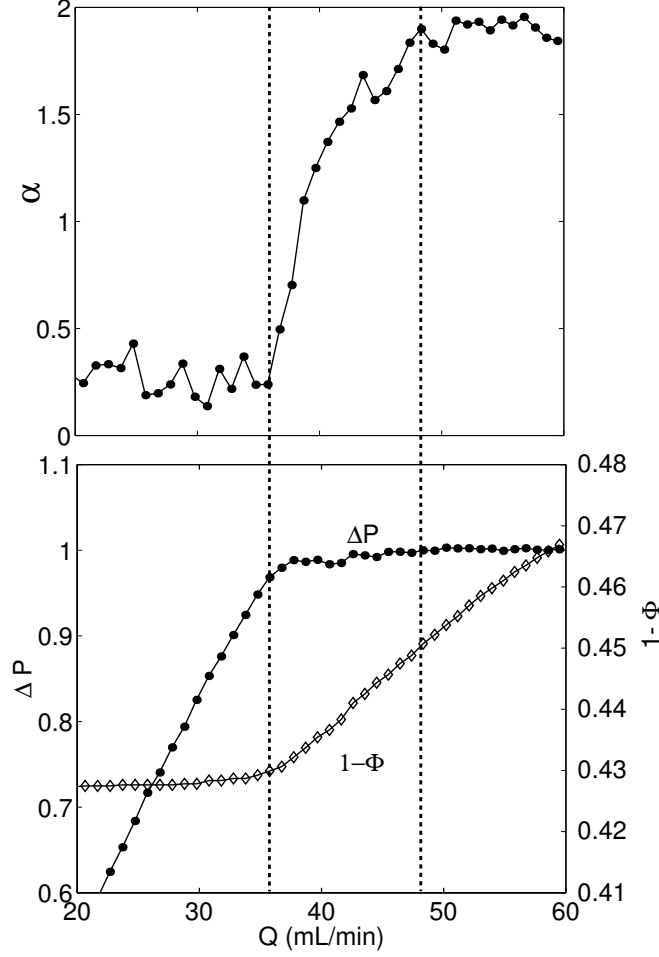
Figure 8.12: Top panel: α as a function of Q for defluidization. Bottom panel: The pressure and voidage are given for reference. The dashed lines indicate the hindered region in which $\alpha \neq 2$, but $\Delta P \approx 1$.

is greater than RLP. For values of Q such that $1 - \Phi < 0.45$, α decreases with decreasing Q. As argued above, this is due to particle contact. Although the force balance, $\Delta P = 1$ is still maintained, the system does not have enough free volume to maintain a state in which all particles undergo ballistic trajectories. As Q decreases, the fraction of immobile particles increases; motion has become hindered. At some point lower than RLP, both α and τ_d begin to change rapidly. We believe that the bed is now approaching a glass transition, and this will be discussed in Chapter 9.

Volcanos in the hindered region

At flow rates in the hindered region, the side of the bed reveals small transient worm-like jets; they occur for increasing and decreasing Q. These reach the surface and break through, forming spouting volcanos. Locally, a volcano will spout for some time, then subside. This process repeats at different points over the surface. As Q is increased, they appear over larger areas until the entire surface is boiling. Images of the top of the bed showing the volcanos are shown in Figure 8.13. Such volcanos and worms have been observed slightly above onset, but not studied carefully. The observation of volcanos were reported in [177] and the existence of a worming region has been observed in [53] and [124]. In [124], they were called channels and described as "Channelling spots flitted from one point to another on the bed surface and at the lateral surface." We believe that these localized worms and volcanos are a consequence of the local mobile and immobile regions, and will be further discussed in Chapter 9. The local worm regions might be analogous to the "weak spots" discussed in molecular dynamics simulations of Lennard-Jones fluids [157]. These weak spots were proposed to play a role in bubbling or nucleation in true liquids.

$\Delta P < 1$: wiggling motions

For low enough Q, ΔP decreases sufficiently below 1 and the pressure can no longer drive bulk fluidized dynamics. However, we observe that the voidage continues to decrease, although much slower than in the $\Delta P = 1$ state. In this regime, due to the loss of the force balance, the system has lost the ability to translate the grains. However, locally, the particles are still acted on by a drag force. From the Richardson-Zaki relation, Equation 1.2, the drag force on a given particle near onset due to fluidization flow velocities is about 50-100 times smaller than the drag force due to sedimentation. We propose that if the grains are not locked into place by frictional contacts (jammed), these small forces can promote local re-organizations. If Q is decreased sufficiently slowly, these small changes in flow will cause a continued decrease in voidage.

In this region, rearrangements can occur on timescales which are on the order of or greater than to the DWS sampling time (30 seconds for the data discussed). This is shown in Figure 8.14. The top panel shows τ_d for decreasing Q. As the motion of the system becomes increasingly frustrated (see the plot of α in the bottom panel), the dynamics slow considerably. At some point they reach the limit of the time-resolution of the measurement that, roughly 0.3 seconds. Also plotted in the top panel is the intercept value of $g^{(2)}$ for the corresponding correlation measurements. When ΔP first decreases from $\Delta P = 1$ (denoted by the dashed line), $g^{(2)}(0)$ suddenly drops from the value of 1.5 to a value slightly greater than 1. As Q continues to decrease, $g^{(2)}(0)$ remain near 1. Recall that $g^{(2)}(0) = 1.5$ is obtained for a system which undergoes a sufficient number decay
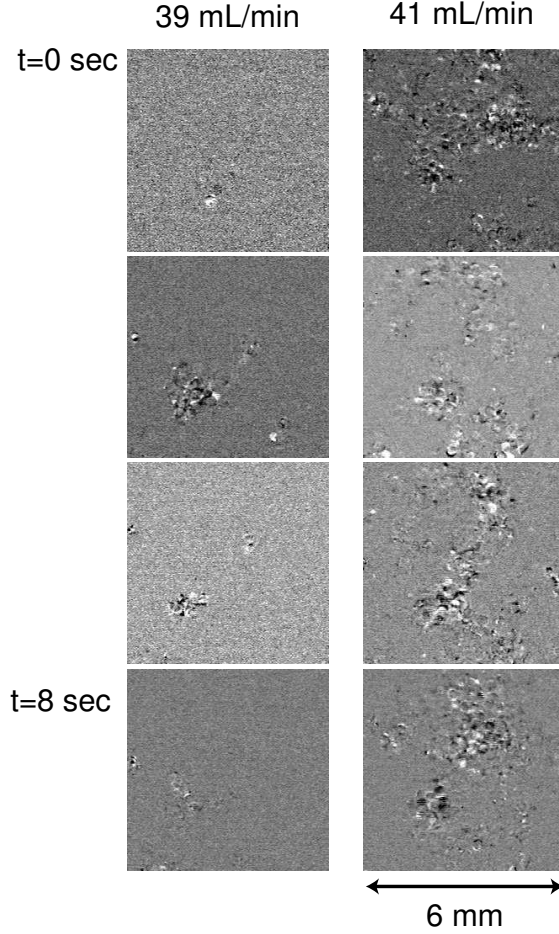
Figure 8.13: Top panel: Time sequences of the top of the bed for different flow rates in the hindered region. Each image is computed as the difference between two frames taken 200 msec apart. The surface of the bed shows small spouting events (volcanos) which increase in frequency and intensity as the flow rate increases. The images represent the central $1/4 \times 1/4$ of the bed surface.

periods during the sampling time. Also recall that if the scattering signal is constant, $g^{(2)}(0) = 1$. Intermediate cases will have $1 < g^{(2)}(0) < 1.5$. Thus, the sharp drop corresponds to the point at which the pressure driving has disappeared. In this regime, the dynamics of the grains drastically changes character. At this point, the baseline value of α (bottom panel of Figure 8.14) indicates that all particles are in contact. For decreasing flow rate, any further dynamics can only come from local rotational "wiggling" of the grains following the decrease in stress. A schematic of a possible packing by small constrained motion is shown in Figure 8.15. When the stress is reduced, there is less force on the particles, and they seek to move to the lower energy state in the gravitational
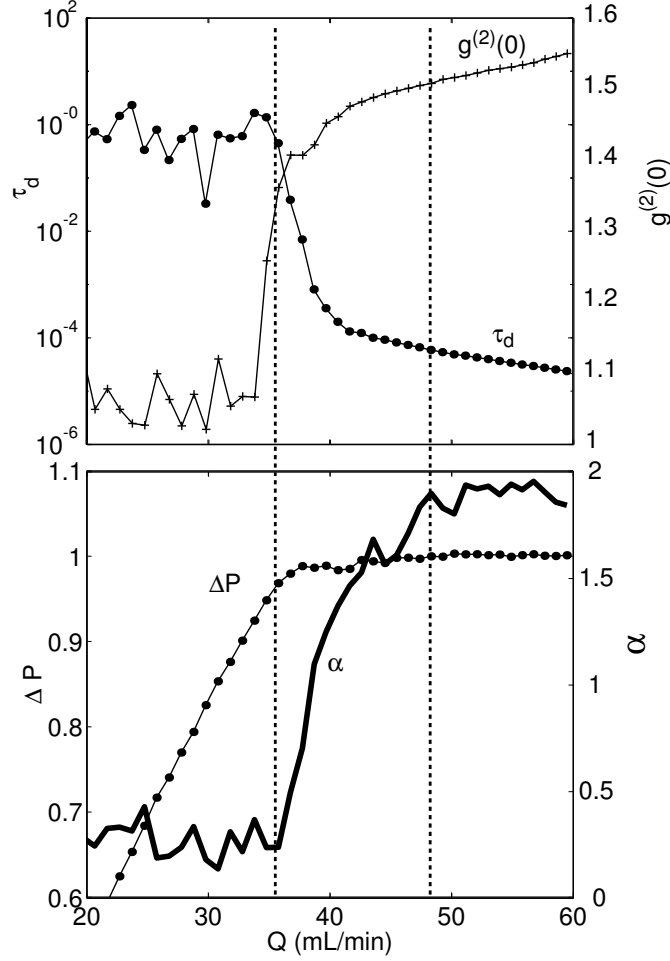
Figure 8.14: Top panel: The characteristic decay time of $g^{(2)}(\tau)$ ($\bullet$) for for 30 second DWS measurements. The intercept (x) $g^{(2)}(0)$ gives a measure of the ergodicity of the sample. It rapidly drops when the decay time becomes comparable to the sampling time; this is indicated by the leftmost dashed line. The dashed line to the right indicates the point at which α begins to deviate from $\alpha \approx 2$. Bottom panel: ΔP ($\bullet$), α ($-$)for defluidization are shown for reference.

field. Contrast this to the efficient packing by fluid pulses, discussed in Section 8.2. Flow pulses locally increase the free volume by quick fluidization events; the grains can then sediment to find a tighter packing.

Multispeckle correlation measurements

We have used multispeckle techniques to extend the time range of τ_d measurements by a factor of 10, see Figure 8.16. The multispeckle measurement of τ_d matches the τ_d

decreasing flow
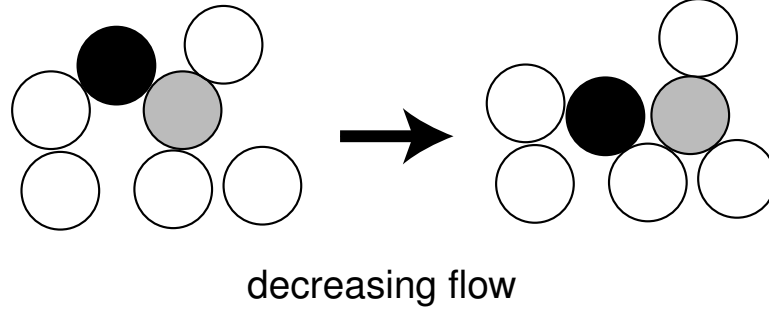
Figure 8.15: A schematic of the packing produced by local constrained motions. The grains are always in contact, but the system is not jammed. Thus, slight perturbations will induce small local rearrangements.

in the timescales over which they overlap. This gives us confidence that the technique is working. We find that τ_d actually reaches the 3 second limiting time-scale—thus the grains become almost completely motionless as $Q \to 0$.

8.4   Interpretation of results as jamming

We now use the concept of jamming to describe the dynamics of the bed below onset. Recall from Chapter 2, that a definition of a jammed state is a state that has developed a yield stress and in which all particle motion has stopped. As will we study slow transient processes, we will use the multispeckle techniques to image the motions of the bed. These spectroscopy techniques were described in Chapter 3. Recall that scattered laser light is imaged onto a CCD such that each CCD element (pixel) images a single coherence area. If the intensity in a pixel changes, this means that some motion occurred in the bed. Since each coherence area is statistically independent, this allows averaging over the image and the statistics improve. This technique allows detection of motions as small as 1 nm. Thus we have a very sensitive technique to determine if a state is motionless. We note that observing a motionless state doesn't necessarily mean that the state has developed a yield stress, and we will comment on this.

Above RLP, the system is un-jammable. This means that any applied stress can be accommodated by a dilation. For voidages greater than RLP, there is free volume enough for the dilation to occur. Below, RLP there is not enough free volume, and increased stress will cause an attempted dilation. This dilation will cause particles to push into each other and into the walls and can effectively jam the grains. This will occur as long as ΔP remains less than 1.

171
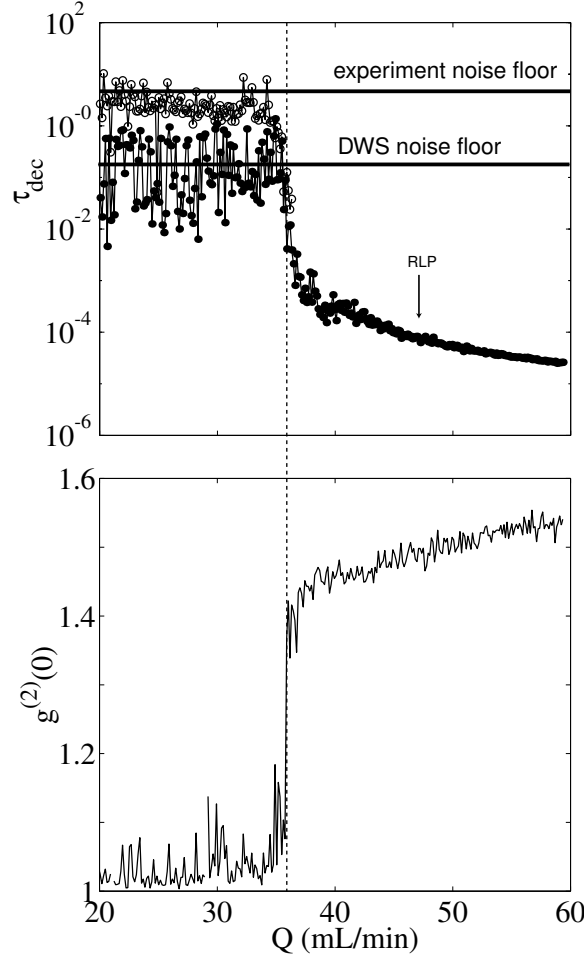
Figure 8.16: Top panel: The characteristic decay time of $g^{(2)}(\tau)$. $\bullet$ is for 2 second DWS measurements and $\circ$ is for 30 second 128 pixel multispeckle measurements. Bottom panel: The intercept $g^{(2)}(0)$ gives a measure of the ergodicity of the sample. It rapidly drops when the decay time becomes comparable to the sampling time. This is where the multispeckle is useful.

8.4.1 Jamming as a function of the sign of $\frac{dQ}{dt}$

We now present the fundamental observation of jamming in our system—the wiggling motion of the grains depends strongly on the sign of $\frac{dQ}{dt}$. We have observed that after a decrease in Q to below onset, the speckle in the images takes a long time to become motionless. However, a small increase in flow will quickly cause the motion of the speckle to arrest. This is illustrated in Figure 8.17. The top panels in Figure 8.17 show a time trace of a row of pixels in the CCD for two different flow protocols. The bottom panels show a measure of decoherence of speckles. This measure allows us to

172

study the transient speckle motion: after normalization and subtraction of a background due to camera noise, each time-trace of a pixel is differentiated with respect to time, and the absolute value of this quantity is averaged over all pixels. This is denoted $\langle \frac{dI}{dt} \rangle$, where I is the intensity of a single pixel. If there is no intensity change in a coherence area, this quantity would be zero for all time. Recall that any motion of the grains changes path lengths and this contributes to a change in phase of the scattered light and thus a change in intensity of photons at each pixel.

In the first column, the flow is slowly increased from below onset, 6 mL/min, to a larger flow rate still below onset, 17 mL/min. $t = 0$ is when the flow has reached the target flow rate. The speckle rearranges during a short (30-60 seconds) transient period and then becomes motionless. This indicates that the system is locked into place. This is in accord with our observation that below onset, motionless speckle can be created by slight increases in flow rate. Contrast this to the second column. Here we show a sequence in which the flow is slowly decreased from above fluidization to below onset, 17 mL/min. In this case, the speckle continues to move for several hundred seconds after the target flow rate has been reached, despite no obvious change in bed height after the initial defluidization. This asymmetry is remarkable, and we propose that it is due to jamming of the system.

We propose that the increasing flow jams the system, creating a yield stress which then must be overcome to change the voidage. The decreasing flow does not jam the system, and since the material started with no yield stress, none is created. This explains how the voidage can decrease for decreasing Q during defluidization: when Q is increased during fluidization, the increased stress dilates the grains. Thus, they are forced against each other and the walls. In this case, the stress network is immediately created, locking the grains into place. In the case for slowly decreasing flow, no stress network was present in the initial fluidized state. Upon defluidization, the stress on each grain becomes smaller and the effective weight of the grain becomes larger. At some point, the grains press against each other under the force of gravity. To jam, the weight will have to balance the force due to hydrodynamic drag on each particle. It is not clear whether just the weight can develop a yield stress. This reorganization can only take place by the minute wiggling motions that can be excited by the small flows. Our data shows that this can take a long time; we have observed speckle motion in a defluidized state after one hour. It is an interesting question whether after the speckle has completely stopped, the system has jammed. We observe that when the flow is slowly ramped down to $Q = 0$, speckle motion persists for even longer times. This effect is greater for smaller sized particles. In fact, $100 \mu m$ sphere always show residual motion, even after many hours. This indicates that the absence of a counterflow, the minute wiggling persists due to local, thermally induced flow fluctuations. Since the system is not jammed, these can induce small wiggling motions. Presumably the lubrication layer surrounding each

173
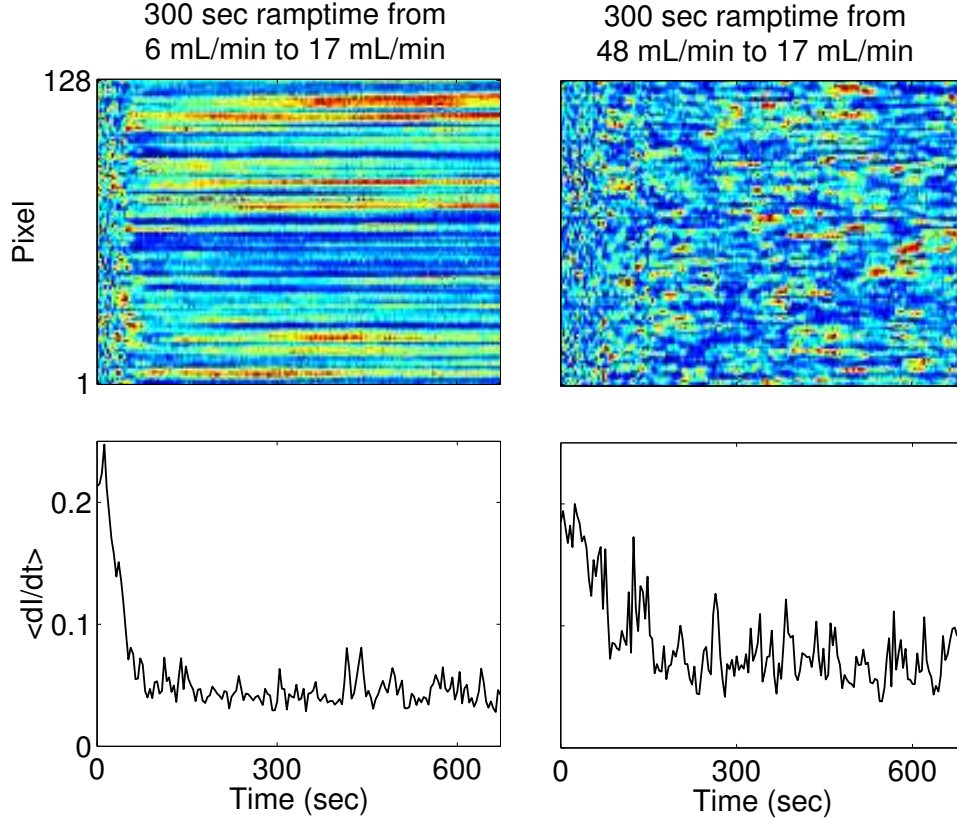
Figure 8.17: Speckle pattern movement for two different approaches to $Q = 17$ mL/min, which is below the onset of fluidization. The top panels show a row of pixels in the CCD as a function of time. The colormap is low intensity (blue) to high intensity (red). The bottom panels measure $\langle \frac{dI}{dt} \rangle$ of the corresponding image. The protocols are given above the images. $t = 0$ refers to the time at which the target flow is achieved.

particle plays a role in this process [24]. It would be an interesting experiment to measure the typical decay time of $\langle \frac{dI}{dt} \rangle$ after defluidization for different final Q.

8.4.2 Jamming and fluidization cycles

The behavior of $1 - \Phi$ and ΔP during fluidization cycles can be understood from the jamming picture. Figure 8.18 studies the effect on $1 - \Phi$ and ΔP of varying the point at which the flow reaches a maximum and begins to decrease, the turnaround point. Two cases are shown: the top two rows show $1 - \Phi$ and ΔP for fluidization cycles starting from a loosely packed state. The bottom two rows show the corresponding plots for a tightly packed initial condition. In fluidization cycles that do not pass the yield point of the material, the voidage for the defluidization branch re-traces the fluidization branch. This
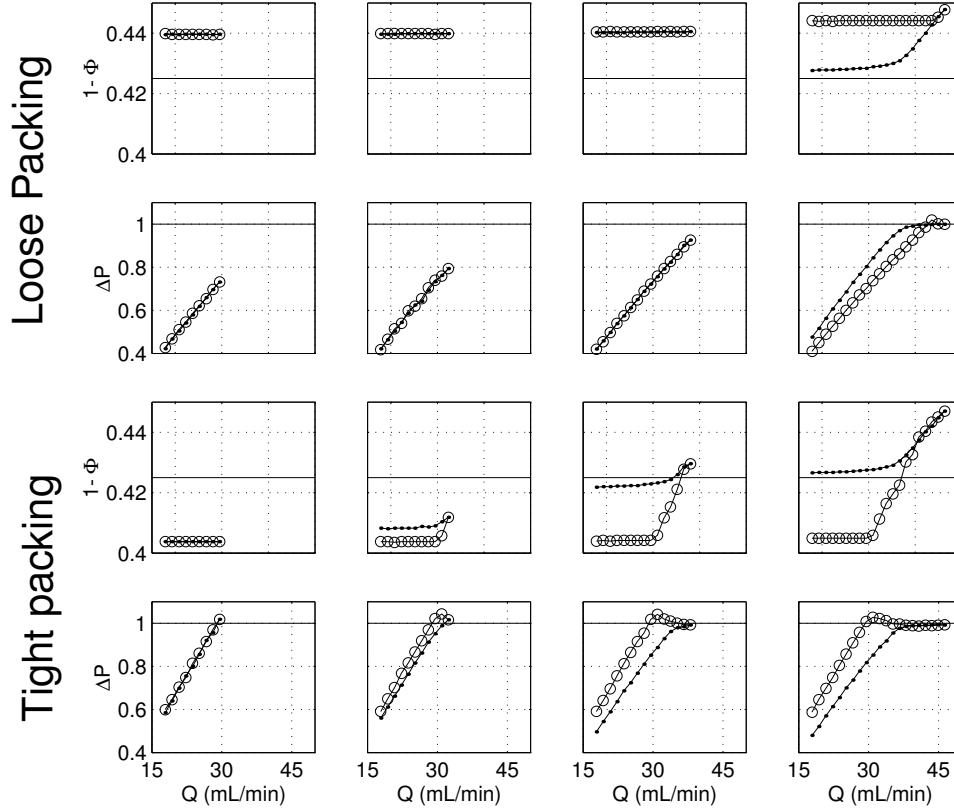
Figure 8.18: Top two rows: voidage and pressure data for fluidization cycles with approximately the same loosely packed initial condition. The panels from left to right show fluidization cycles for increasing turnaround points. Bottom two rows: same as the top two rows, but for a tightly packed initial condition. Increasing flow denoted as ○, while decreasing flow as ●. If the yield stress is not broken, the paths are reversible for slow changes in Q. Once the material has yielded, defluidization follows a different path. The solid black lines in the voidage plots indicate the voidage obtained for slow defluidization from above RLP. The solid black line in the pressure plot denotes $\Delta P = 1$.

indicates that we have not un-jammed the system, and the force chains can accommodate the small changes in stress. On the branches where the voidage remains the same, the changes in the speckle look like Figure 8.19. These measurements are taken immediately after the ramps. However, even during the ramps, no motion occurs, indicating that once jammed, the system can accommodate small slow changes, independent of the sign of $\frac{dQ}{dt}$. This is because the yield stress is stronger than any counter stress induced by a small change in flow.

Contrast this to the case when the yield stress is broken. If the turnaround point reaches the value of Q where the material yields, $1 - \Phi$ decreases with decreasing Q
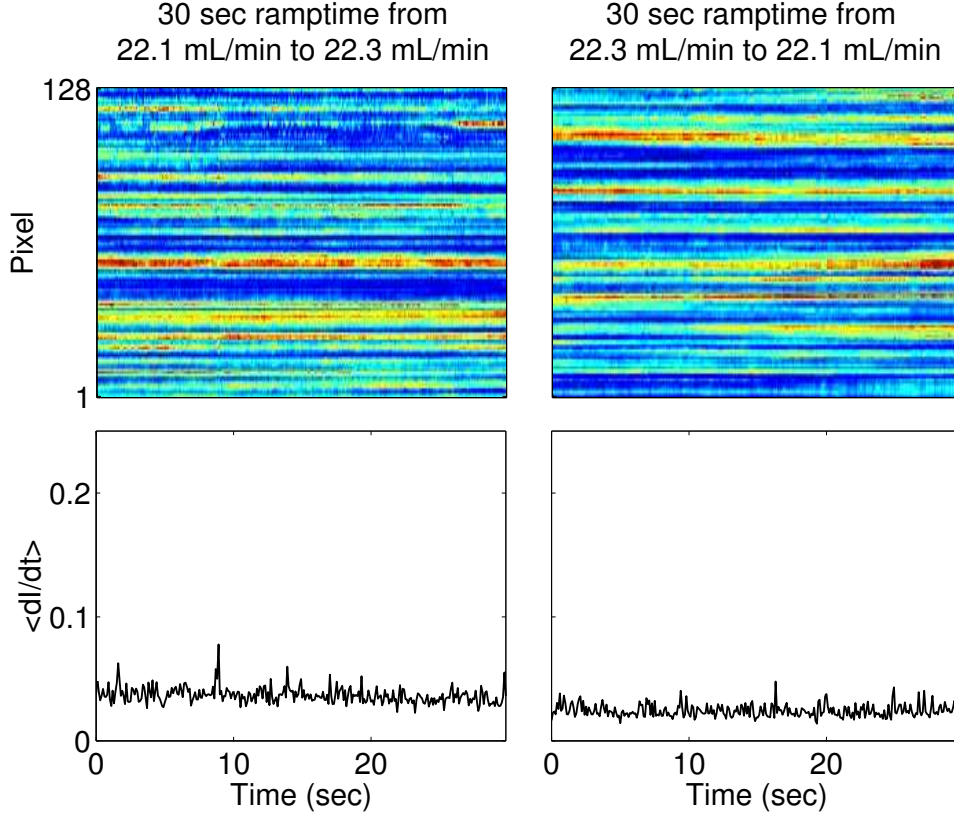
Figure 8.19: For small enough changes in Q below onset, regardless of the sign of $\frac{dQ}{dt}$ the speckle does not change when stress chains are not broken.

during defluidization. This indicates that the system has become un-jammed, and lost the stress chain backbone (a yield stress). Decreases in flow remove stresses from the particles, allowing them to wiggle into new more dense packings. Once the yield stress is relieved, the system is no longer jammed, and will wiggle to a new state for decreasing Q. It is important to note that the final defluidization state is not unique. The initial rapid decay of $1 - \Phi$ occurs in the regime of growing regions of motionless particles. This decay must depend on the average volume fraction at that flow. Like in Section 8.3.2, the very slow decrease in $1 - \Phi$ begins when ΔP is sufficiently below 1. Here only the local wiggling motions of the particles can cause rearrangement. However, as long as the system is not jammed, the wiggling motions will have the ability to pack the system.

Many factors influence the timescale of the rearrangement of the speckle during defluidization. For example, we find that that initial fluidized state (in a full cycle, the turnaround point) for the defluidization branch affects the duration of persistent speckle fluctuation. Figure 8.20 shows two defluidization events, each starting from a different initial condition. The ramp rate is kept constant for both experiments. The final voidage

for both cases is the same, but for the ramp from the more fluidized state, the speckle fluctuates for a longer time. At a given time after the target flow is achieved, the speckle fluctuation is smaller in the ramp from the less fluidized, more dense state.
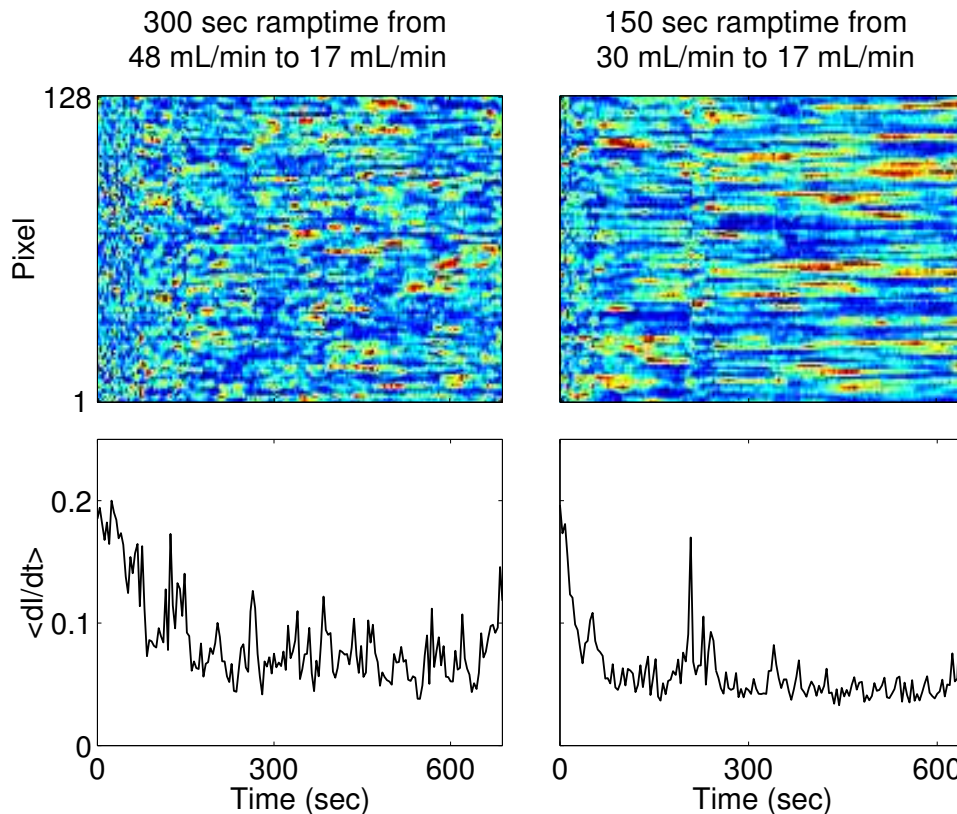
Figure 8.20: The speckle dynamics following defluidization sequences from different initial flow rates above fluidization. $t = 0$ indicates the time at which the target flow is achieved. The ramp rate is the same for the two runs.

As discussed in Chapter 2, it has been speculated that force chains play a large role in jammed systems [138]. In fact, Onoda and Liniger proposed that for packings with $1 - \Phi < .45$, the stress should be carried by a "rigid, continuous network" [139]. Thus, the chains should appear when a yield stress is developed. We briefly present evidence for the existence of force chains in the fluidized bed.

8.4.3   Probing force chains by local heat pulses

We have indirect evidence that force chains exist in the system. We perform experiments similar to those described in Chapter 2, in which a localized pulse of heat is applied to the grains. However, instead of monitoring the transmission of sound through
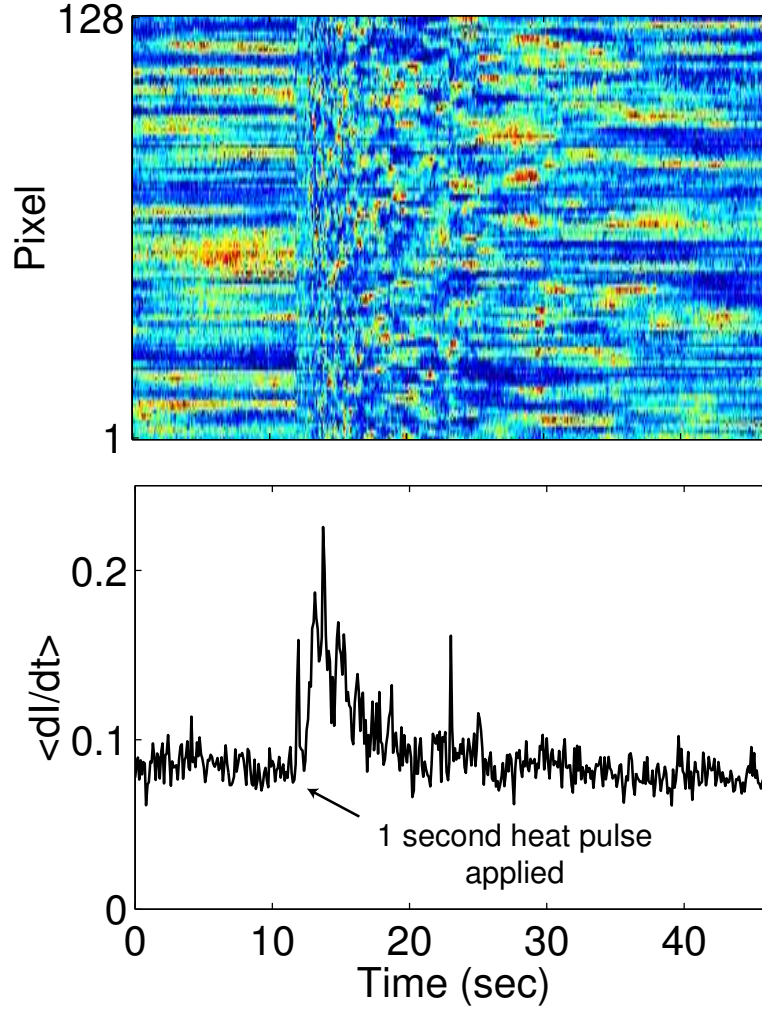
Figure 8.21: A heat pulse is applied at $t = 12$ seconds by applying current in a small (1 mm diameter x 2 mm length) 1/8 Watt, 16 Ohm resistor buried in the bed for 1 second with a 12 V pulse. Q is maintained constant at 17 mL/min for the duration of the experiment.

the medium, we study the time evolution of the speckle pattern. This process is shown in Figure 8.21 and should be compared to Figure 2.9 in Chapter 2. The heat pulse from a 12 V pulse to 1/8 Watt 16 Ohm resistor buried in th bed is applied for 1 second, and the effects are seen for over 30 seconds. Upon application of the pulse, the resistor expands and also locally heats the fluid and grains. The initial expansion of the resistor and the subsequent expansion of the grains due to thermal expansion (estimated for radial expansion as roughly 3 nm per degree C–easily detectable in speckle) disrupts the local force chains. The heat propagates throughout the network rearranging particles. We have

verified that convection of the water through heating is not important by performing the experiments without water.

In fact, if the current to the resistor is maintained, the speckle fluctuates initially but after roughly 100 seconds, it becomes stationary. The same effect is seen when the current is shut off. This indicates that the during the time it takes for the heater to establish a steady temperature profile, the changing temperature causes expansion of the beads. During this time, we see the effects of the heat modifying the force network by rearranging, wiggling and deforming beads. Once the temperature profile is established, the system is free establish a new stable network. Thus, it jams, and speckle fluctuation ceases. We have found that a similar effect can be induced by suddenly applying the 2 mm diameter laser beam to a face of the bed. After the beam is applied, the speckle fluctuates for roughly 30 seconds. If the power is reduced to less than 30 mWatt , no speckle motion occurs. Also, if we decrease the power density by expanding the beam spot to the size of the cell at constant power, a sudden application of the beam causes no speckle motion. We interpret this in the following way: As the power density is increased, the local heating becomes large enough to disrupt the chains. We believe that further experiments of local heating, combined with speckle imaging, should produce insights on the dynamics of force chains, and their sensitivity to perturbation.

8.4.4 Ramp rate effects

We now discuss the role of rate effects on the fluidization cycles. We will be interested in how the magnitude of $\frac{dQ}{dt}$ effects the fluidization process for increasing or decreasing Q. We first examine behavior for $\frac{dQ}{dt} > 0$.

Increasing flow rate

We have proposed a picture of a jammed system in which force chains dominate the static behavior of the grains. Presumably, there is a time-scale for the chains to set. Thus, fluidization at different rates should behave differently. In Figure 8.22, we present fluidization for tightly packed case taken with a much finer step size than the fluidization measurements taken in previous sections. Here, the ramptime is 30 seconds and the equilibration time is 30 seconds while the step size is almost a factor of 10 smaller than that in Figure 8.5. We see that under such slow fluidization, the behavior is very complicated. In the yield region, ΔP is no longer always decreasing, but occasionally increases. This is accompanied by no change in the voidage. Thus the system has re-jammed at a lower volume fraction and consequently must yield again. However, since it is at a lower voidage, it will yield at a lower stress. Eventually we reach RLP and no jamming can occur.
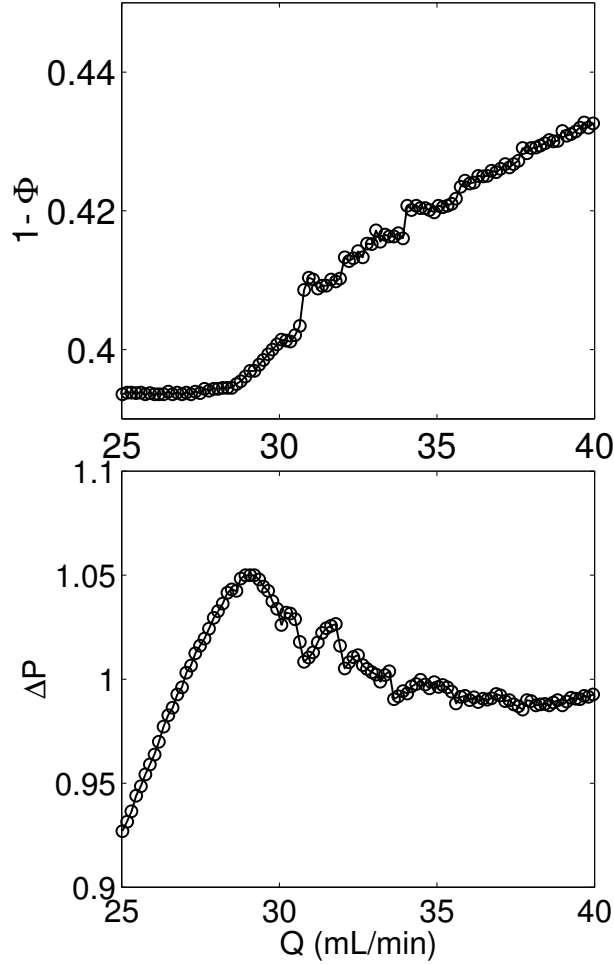
Figure 8.22: Fluidization of the bed at a different rate leads to different re-packing events. A slow enough rate allows for the system to re-pack at different points along the branch. Once re-packing occurs, the system must unlock, and thus the pressure will rise. The ramptime between measurements is 30 seconds and equilibration time is 30 seconds. The step size in flow rate is a factor of 10 smaller than in Figure 8.5

For increasing flow, below RLP, the system can always jam, as the increases in flow produce increases in stress which seek to dilate the system. The ramp rate should affect the fluidization, as it allows the chains to set, giving the material sufficient time to develop of a yield stress. As discussed, for a tightly packed state, once the material initially yields some particles are free to move and others are hindered. Since the voidage is lower than RLP, the system has the ability to jam if given sufficient time. All of this occurs when $\Delta P \geq 1$ where there is sufficient energy to translate grains. Thus, we can study jamming at an effective finite temperature. In fact, we speculate the the void cracks seen in Figure 8.13 are responsible for the jamming when the system is close to $\Delta P = 1$,

at the edge of fluidization. We have observed that in this region, the system can jam given sufficient time due to a dynamic process of spouts popping up and re-healing, with motion stopping in the healed region. At some point, the entire system may abruptly lock into place and all speckle motion can stop. At this point, the spouts have created a yield stress.

Defluidization

We now discuss the effect of decreasing the magnitude of $\frac{dQ}{dt}$ to defluidize a fully fluidized state. We find that the fully fluidized system responds differently as the magnitude of $\frac{dQ}{dt}$ is changed.

The history of the bed for different flow rate decrease rates $\frac{dQ}{dt}$ is shown in Figure 8.23. For a rapid shut off in the flow rate, the system gently sediments to a state close to RLP (the solid black line in Figure 8.23) as described in Section 8.2.1. We see that as the ramp time increases, the bed reaches a lower voidage state. We interpret this as the system is given more time to explore all configurations and does not get stuck in a high voidage state when ΔP becomes less than 1. Once $\Delta P < 1$, the voidage can only decrease through the wiggle packing described earlier.
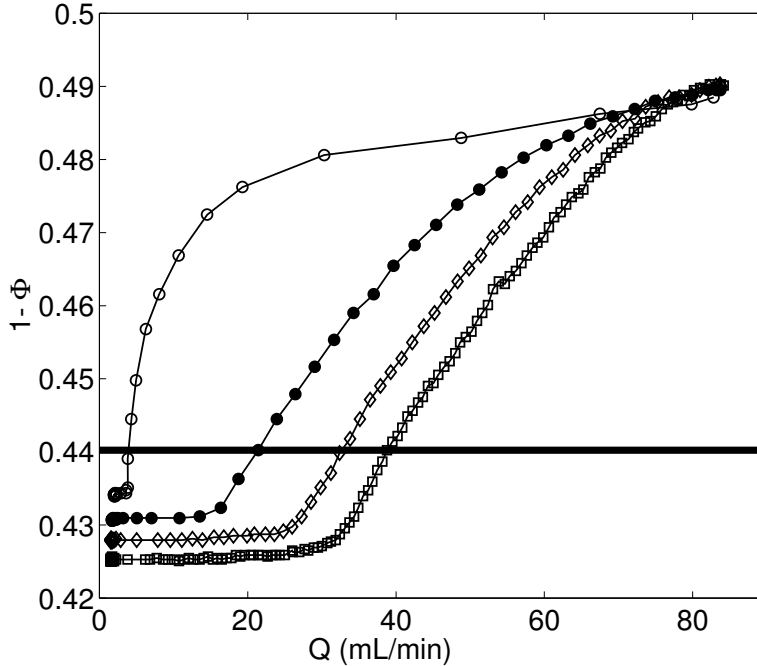
Figure 8.23: $1 - \Phi$ as a function of Q for different ramptimes, $(\circ, \bullet, \diamond, \square)$, $(11, 23, 35, 63)$ seconds. This gives the ramprate $-\frac{dQ}{dt}$ as $(0.12, 0.06, 0.04, 0.02)$ mL/sec/sec. The black line denotes the state reached when the flow is rapidly shut-off.

In fact, this has consequences in the dynamics of the grains. In Figure 8.24, we show two CCD speckle traces for defluidization from $Q = 48$ mL/min to $Q = 17$ mL/min for different ramp rates, 30 seconds and 300 seconds. The speckle moves much more in the slow ramp indicating that the system is dynamically finding the optimal locking, while the fast ramp has had time to find its place. We propose that the fast decrease in flow rate could even jam the system by the fast shock-like impulse. We note that the speckle can truly be locked by a slight increase in flow rate as this dilates the sample, jamming it, as seen from Figure 8.17. It is an interesting and unanswered question whether a system that has been very slowly defluidized will spontaneously develop a yield stress.
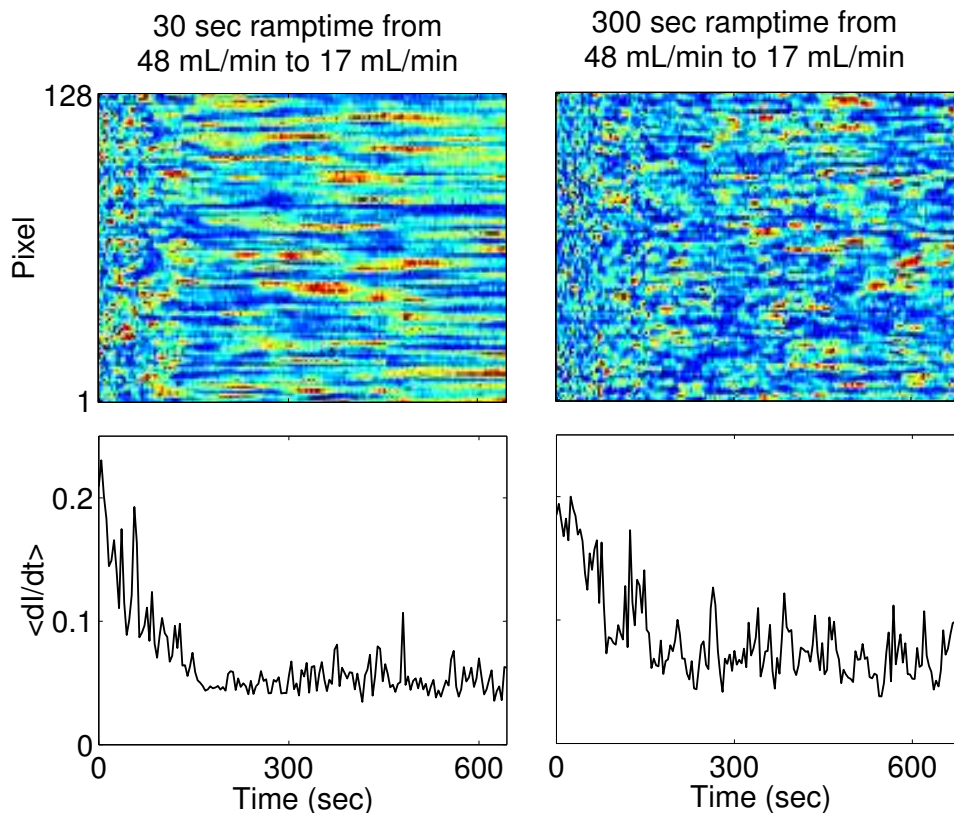
Figure 8.24: The speckle fluctuates for a longer time for the slower ramp time. 30 second ramp and 300 second ramp. $t = 0$ indicates the time at which the target flow rate is achieved.

In Figure 8.25, we plot the final voidage when Q reaches zero as a function of the inverse ramp rate. We see that it reaches a limiting value of roughly 0.42. Values close to this have been observed for different particle sizes and fluidization in air and the value may have something to do with the glass transition in hard spheres [145, 146], $1 - \Phi \approx 0.42$. However, since we have shown in Figure 8.18 that the defluidization branch

is not unique, and locks up when $\Delta P < 1$, this could be only coincidence. We will discuss this further in Chapter 9.
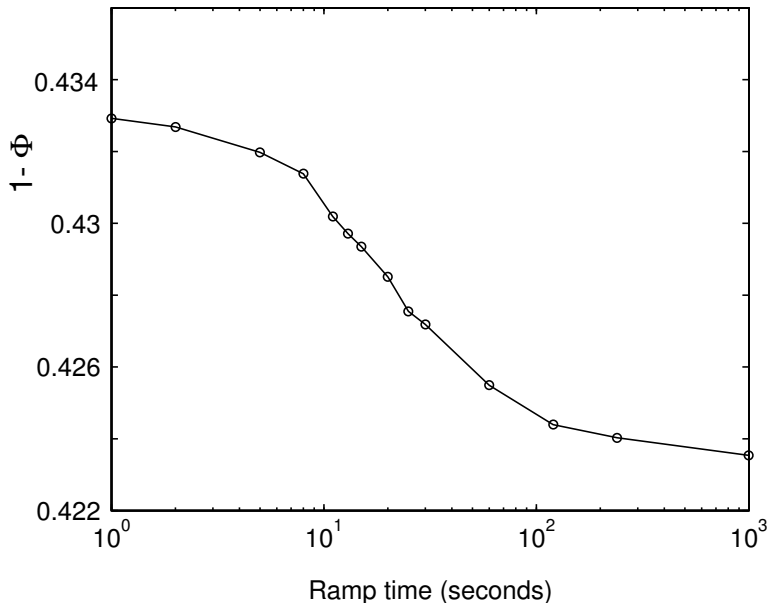
Figure 8.25: The voidage after defluidization to $Q = 0$ plotted as a function of the inverse ramp time for defluidization.

Now we begin to see supercooled liquid-like behavior, (eg dramatic change in timescale, rate dependent effects, jamming), and we postulate that this system can be used to study glasses. We will discuss this in the next chapter.

8.5   Conclusion and summary of results

In this section I summarize our proposed picture to account for the phenomena observed in fluidization cycles near onset. Consider a defluidization cycle. Above RLP, the system is fully fluidized and grains move for short times with ballistic trajectories. This is the freely colliding regime. When Q decreases such that the system becomes more packed than RLP, and the short time dynamics aren't ballistic. Our interpretation is that in this frustrated state, the bed has as a mixture of freely moving grains, while other regions contain grains which are packed together. This state can be jammed (CAN IT?) whereas states above RLP cannot. As Q decreases, eventually ΔP decreases enough and cannot translate grains through fluidization. When $\Delta P < 1$, only slight rotational modes (wiggling) are excited. Any forces due to flow can only effect the small rotations of grains (wiggling). If the flow is decreased slowly into this regime, the system is maintained away from a jammed state and small rotations still persist. These rotations can manage to

Fluidization

Defluidization
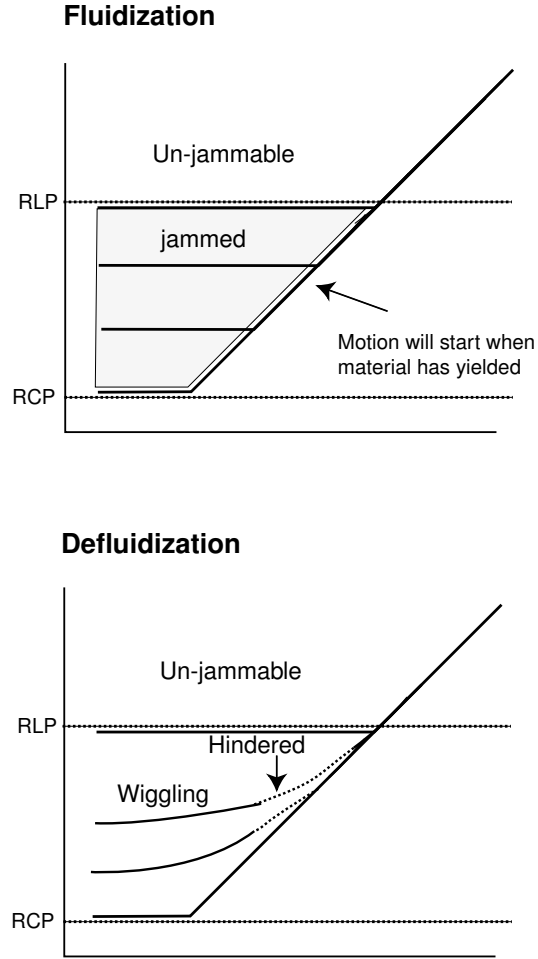
Figure 8.26: Schematics of the ideas discussed in this chapter.

wiggle the system into a new volume fraction–thus the voidage continues to decrease as the flow is decreased by the slight in-contact adjustments of the grains. We claim that unless the flow is increased slightly, the system will never jam in the wiggling region–no force chains will be established. Thus the system is *fragile*.

Contrast this to the case for increasing flow. Increasing flow jams the system, creating a yield stress. For particle motion, to occur, this yield stress must be broken. However, the material does not yield all at once. As Q is increased beyond the maximum yield stress, the voidage decreases and the yield stress decreases. However, since ΔP is still greater than unity, the system is still jammed, and no sustained grain motion occurs. Thus there will exist a range in Q where fluidization is not accompanied by grain motion. Only when the material has fully yielded and $\Delta P = 1$, will sustained particle motion begin. At this point the system cannot be fully jammed. The size of the range

of jammed fluidization will depend on the yield stress in the initial jammed state. For a loosely packed state, the yield stress is very small, and grains begin motion immediately at onset.

We also give some insight into the flow pulse experiments. This is a different way to pack the bed. Instead of in-contact wiggling adjustments which squeeze out free volume during defluidization, the pulses actually push the grains apart. This provides them with paths to squeeze out free volume. This is a much more efficient process, as the grains are not required to remain in contact. Thus we have pulse packing vs. wiggle packing.

In a sense, the continued decrease of the grains well below onset is the answer to how the grains can remain in contact and continue to decrease voidage–they wiggle into it. If the system is jammed, only the spectator particles will wiggle and these don't control the voidage–the stress chains do.

8.6   Comparison to previous work

Several studies have been made of Geldart A air fluidized beds which expand uniformly near onset (see [97] and references therein) These studies have revealed the existence of an apparently motionless state immediately after fluidization. Menon and Durian [130] used DWS techniques who found that the particles remained motionless until the onset of bubbling. Their work was done in air and for very tight packings and we show the comparison between our studies in water and their air fluidization studies in Figure 8.27. The results are in agreement in that we both see regions of increasing voidage without particle motion. However, they can observe a much longer transient regime, as their initial packing is close to RCP ($1 - \Phi \approx 0.37$), obtained by pouring grains into the container and lightly tapping). We are usually working at higher voidage where transient effects can dominate the path. Better tapping schemes should allow us to reach the voidage range in the air fluidized case.

However, there is a fundamental difference between the two experiments. This is the role of hydrodynamic interaction between the grains when they are close to contact. This effect is characterized by the size of the Stokes number, $St = \rho_p a v_{\rm rel}/\mu$, where ρ_p is the particle density, $v_{\rm rel}$ is the relative collision velocity, a is the particle diameter, and μ is the fluid viscosity [97, 99]. St measures the relative importance of particle inertia to viscous fluid forces. St can be thought of as roughly a measure of the distance in particle diameters it takes a particle moving with a velocity v to stop when an applied force is removed. For large collisions at St, $St \gg 1$, the lubrication layers near the particle break down, and the surfaces of the approaching grains contact during collision [97]. In
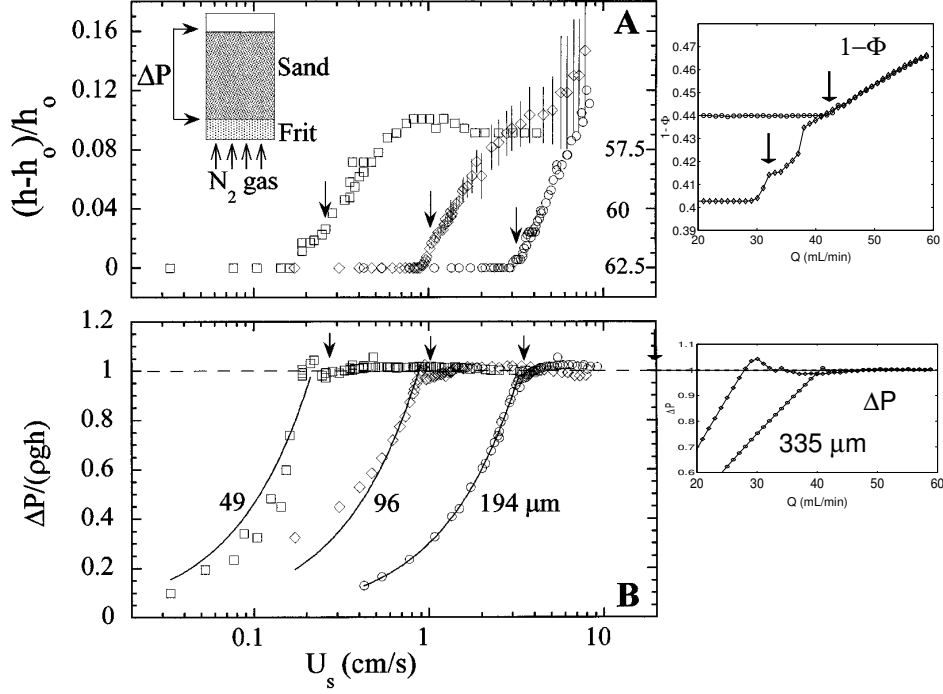
Figure 8.27: Comparison of our results with those in [130]. The two left panels are the results for air fluidization of spheres of different sizes at the same initial packing. The small arrows indicate where motion of the grains begins. The two right panels are our measurements in a water fluidized bed for different packings of 335 μm spheres. The arrows indicate where grain motions begin.

the small St limit, $St \ll 1$, the lubrication layer prevents surface contact[7]. For typical collisional velocities of 0.1 cm/sec found in both experiments, this yields $St \approx 0.6$ in water and $St \approx 50$ in air. Thus, the behavior of the contact network of the grains in water should be significantly different. In air fluidization the pressure overshoot almost immediately reaches the value of $\Delta P = 1$ once the material has yielded [177]. This is in contrast for the gradual decrease in pressure that we observe in water. Perhaps this is an effect of the extra lubrication for grains in water. This could be tested by varying particle density. We also observe that images of speckle always show fluctuation for the smallest particles ($100\mu m$), even after a jamming procedure. This is in accord with the idea of a permanent lubrication layer surrounding the particles and preventing the full frictional jamming forces. Further studies are necessary to distinguish all of these cases.

---

[7]For measurements of coefficient of restitution of particle-wall collisions and the role of St, see [76, 99]. For discussion of elastohydrodynamics of collisions of particles in fluids see [10, 167].

8.7 Higher flow rates
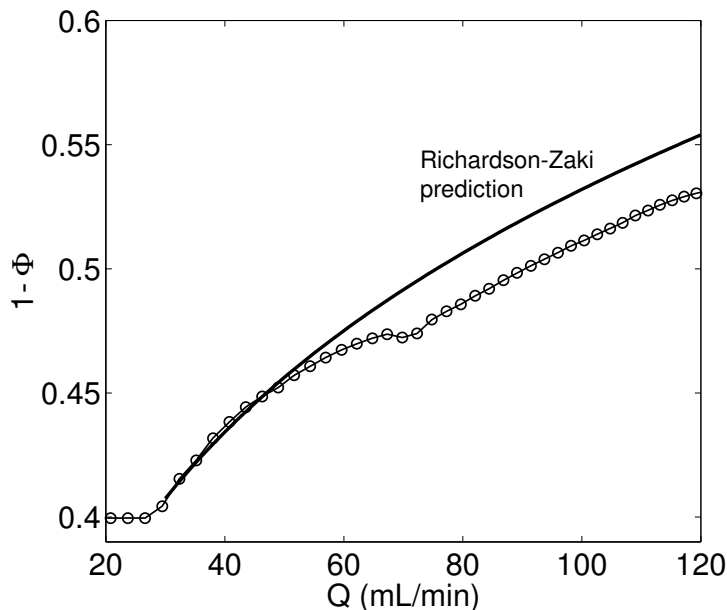
Figure 8.28: The fit to the Richardson-Zaki relation for 335 μm spheres for increasing flow rate. The data was taken for a tight initial packing and only the fluidization branch is shown.

We have briefly examined the behavior of the bed well above the fluidization onset. We attempt to fit to the Richardson-Zaki relation, Equation 1.2 for data at higher flow rates, see Figure 8.28. To measure the exponent n in the equation, we measured the single spheres sedimentation velocity, $v_t = 4.46$ cm/sec ($Re = 16$), giving $n = 4.5$. The fit works well in the hindered region and slightly above onset. However, far enough above onset, significant deviation is observed. We observe that the deviation from the fit occurs close to a point where the bed height has a small dip. A magnified view of the dip region for a *different* fluidization cycle from a loose initial packing is shown in Figure 8.29. The dip displays a complicated hysteresis for increasing and decreasing Q. A dip in the voidage-flow rate curve has been observed in gas fluidized beds, and has been shown to coincide with the onset of bubbling [156]. As Equation 1.2 only applies to non-bubbling beds, we expect deviation here [42]. Interestingly, above the dip in Figure 8.28, the data seems to have the same scaling exponent, but is slightly offset.
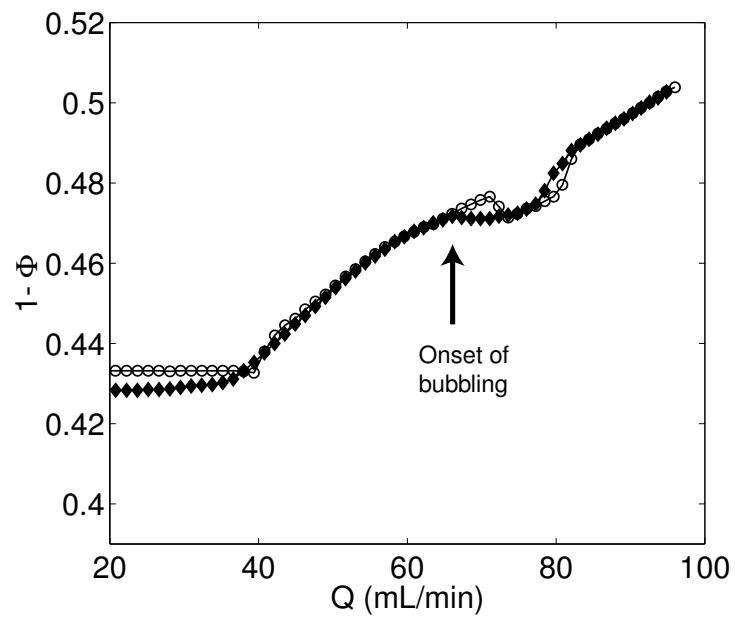
Figure 8.29: A close-in on the dip region for a full fluidization cycle from a loose initial packing. The dip region indicates that the bed is bubbling, and shows a complicated hysteresis. Note that this plot is not a magnification of Figure 8.28.

Chapter 9

Fluidized bed dynamics and supercooled liquids

Note to reader: This chapter deals with possible analogies between our experiments on fluidized beds and supercooled liquids and glasses. This is preliminary work, and the bulk of the chapter reviews the basic phenomena in this very complicated subject. Although the analogy between the systems is still quite tentative, we feel that the questions it raises can lead to fruitful directions in the study of fluidized beds. Therefore, we will try to point out possible common points between the systems and lay the groundwork for future studies.

9.1   Introduction

In Chapter 8, we studied fluidization cycles. In this chapter, we concentrate on the defluidization of the bed and the relation of this process to the supercooling of a liquid. In our studies of defluidization, we have found that when $\Delta P < 1$, the bed is defluidized. For further decreases in Q, motion proceeds through small wiggling rearrangements; however, if the system is jammed, it will be stable to small flow changes. When $\Delta P = 1$, and $1 - \Phi > 0.45$ (RLP), the bed is fully fluidized and all particles undergo ballistic trajectories between collisions. When $\Delta P = 1$ and $1 - \Phi < 0.45$, the bed is still fluidized but timescales for the decay of intensity correlation in the scattering experiments become very long. From light scattering data, we were able to measure the short-time exponent, α for the MSD of the particles. In this region we found $\alpha < 2$. Our interpretation was that the motion of the particles was becoming increasingly hindered in regions which grew in size Q decreased. We now discuss analogies between these observations and the canonical system which slows dramatically as a parameter is changed: a supercooled liquid cooled near its glass temperature. An analogy between a fluidized bed and a glass could result in increased understanding of a fluidized bed. In addition, we believe that since the fluidized bed can be well controlled and studied, the analogy could help to further understanding of glasses.

In this chapter, we begin with a short review of the salient features of a fluidized bed upon defluidization that have analogies to the characteristic behavior of supercooled liquids. We will then discuss the physics of supercooled liquids and glasses. Finally, we will provide a re-interpretation of the features of the bed in the supercooled liquid/glass

picture. The main sources for the review are [6, 7, 44, 45, 54, 55, 158, 170, 171, 191, 198]. I will reference specific results when appropriate.

9.2   Main features of defluidization

Listed below are the main features on which we will build the analogy to super-cooled liquids. The reference plots are found in Chapter 8.

● **Defluidization rate effects**

Figure 8.23-Figure 8.25

For defluidization, the final $1 - \Phi$ depends on the cooling rate, dQ/dt. A rapidly defluidized bed settles into a higher voidage state than that reached by a slowly defluidized bed. Furthermore, structural motion (wiggling) continues for a longer time in the slowly defluidized state.

● **Slow dynamics and hindered motion**

Figure 8.14, top panel, Figure 8.12

As measured by τ_d, the timescale of the decay of $g^{(2)}(\tau)$, when $1 - \Phi < 0.45$ (below RLP) and while $\Delta P = 1$, the dynamics of the bed slow dramatically. For example, τ_d changes by almost 10^4 for a 10% change in Q. Associated with the increase in τ_d is a corresponding rapid decrease in the exponent for the short time MSD, α. α decreases from $\alpha \approx 2$ as the bed goes below RLP. As argued in Chapter 8, our interpretation of $\alpha < 2$ is that system has become too crowded and the bed contains regions that execute free ballistic trajectories and regions in which the particles are in contact. We call this the *hindered* region of defluidization. Here we propose that the bed is spatially heterogeneous; different regions having different dynamics. We argue that these regions are not static, but the average fraction of mobile particles remains constant for a fixed Q. Note that α begins to deviate from the value of $\alpha = 2$ when the RLP voidage is crossed. Interestingly, the slope of τ_d vs. Q does not change at this point. As α decreases, the slope of τ_d remains constant until at a lower Q, α begins to drop rapidly; at this point τ_d changes by three orders of magnitude. At this point, ΔP displays a small glitch, but is still very close to $\Delta P = 1$. We currently have no explanation for this behavior. For slow defluidization, after $\Delta P < 1$, the dynamics essentially stop except for small wiggling motions of particles induced by further decreases in Q.

● **Worms and volcanos**

Figure 8.13

Visually, in the hindered region, the side of the bed is seen to contain worm-like structures. These are fast moving regions of flow which locally appear in the bed (we see

190

them at the side and the top, but presumably they exist in the interior), exist for some time, then disappear. The spouts then appear in another region. When the spouts reach the top, they eject particles and resemble small volcanos. Above RLP, all particles are moving and individual volcanos cannot be distinguished. As Q is decreased below RLP, they decrease in frequency and intensity until they disappear when $\Delta P < 1$. Thus, the spatiotemporal dynamics of the bed on longer timescales than those probed by DWS are visually seen to be heterogeneous in the hindered region.

These are the main features that characterize the bed upon defluidization. As will be seen, they are analogous to features of supercooled liquids. We now review the basic phenomena of supercooled liquids and glasses. We will return to the the fluidized bed after the review.

9.3 Glass basics

9.3.1 Metastable states and the glass temperature

Upon cooling, the molecular motion in a liquid slows down. If the liquid is cooled below its crystallization transition (freezing) at a rate which is faster than the crystal nucleation rate, it is called a supercooled liquid. As the temperature continues to cool, the timescale for molecular rearrangements will become longer than the timescale set by the cooling rate. At this temperature, T_g, the liquid appears frozen on laboratory timescales and is called a glass. The most striking feature associated with this change to a glass state is that near T_g, the tremendous slowdown occurs over a very small temperature change. Associated with the slowdown in molecular motion, is a corresponding dramatic increase in viscosity. In fact, T_g is often defined as the temperature at which the viscosity reaches 10^{13} poise. This change typically occurs as T changes by a few degrees C. However, T_g is not the temperature of a phase transition. Its value (and thus the temperature at which the viscosity reaches 10^{13} poise) depends weakly on the rate at which the liquid is cooled.

This behavior is illustrated in Figure 9.1. Typically, the volume of a liquid decreases as the temperature decreases. If the liquid is cooled sufficiently slowly in contact with a heat bath, the system will crystallize, condensing to its thermodynamically stable equilibrium state of lowest volume and minimum disorder. Further cooling will result in a continued change in volume with a much lower rate of change of volume with temperature, denoted $-\frac{dV}{dT}$. In the supercooled regime above T_g, $-\frac{dV}{dT}$ has the same value of the liquid state and the liquid has a greater volume than the crystalline state. At T_g, the dynamics become so slow that the system does not have time to rearrange to find its supercooled equilibrium volume for that temperature. At this point the system becomes a glass and $-\frac{dV}{dT}$ takes on a value close to the value in the crystal state. Note that we speak of supercooled equilibrium. Actually, the supercooled state is metastable and must
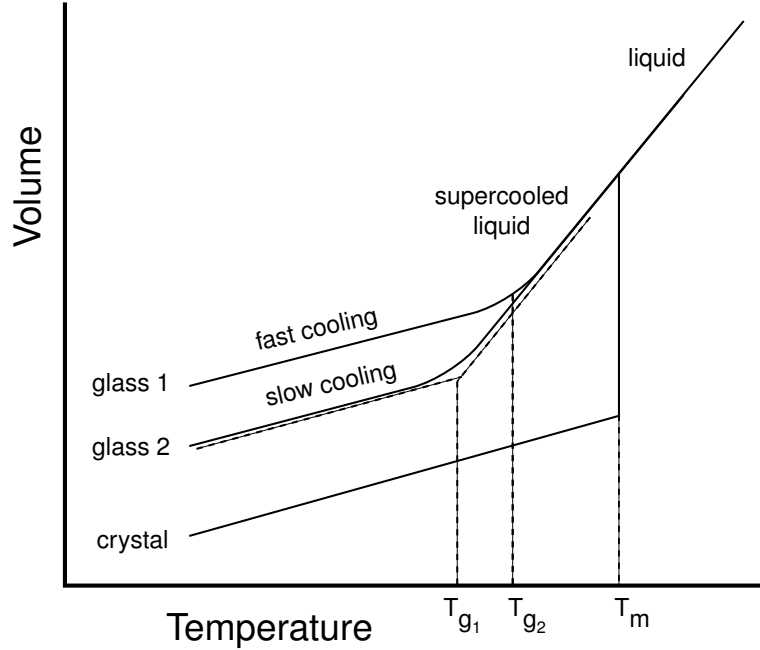
Figure 9.1: The specific volume (cm^3/g) of a liquid as a function of temperature for different cooling rates. The fast and slow cooling rates for the glasses are separated by a factor of 5000 (0.02 hours and 100 hours) and the T_g differ by about 8 degrees K. The values of T_g are obtained by the intersection of the extrapolation of the V vs. T branches above and below the transition. The supercooled regime extends from $T < T_m < T_g$. Crystallization is obtained for a very slow cooling rate. Adapted from [55, 198].

eventually relax to the lowest thermodynamically stable state, that of the lowest free energy. The supercooled liquid or glass may be mechanically stable on a long enough time so that the thermodynamic transition is not seen. This is what we mean by supercooled equilibrium.

Thus T_g can also be defined by the point at which $-\frac{dV}{dT}$ decreases suddenly (but continuously). From Figure 9.1, we see that T_g is dependent on the cooling rate. For a fast cooling rate, the system falls out of supercooled equilibrium at a higher volume than a system which is slowly cooled and given more time to find its lower volume, more "stable", supercooled equilibrium state. Note that a change in the cooling rate by a factor of 10^4 changes T_g by only a few percent. A very interesting point about glasses is that unlike crystallization, the slowdown is not accompanied by any obvious structural change above and below the glass transition: the molecular structure of a glass cannot be distinguished from that of its liquid above T_g.

9.3.2 Thermodynamics of the glass transition

Although not directly relevant to the experiments discussed below, the thermodynamics of this transition are very intriguing. We will discuss this subject briefly. Thermodynamics would argue that if the system is cooled infinitely slowly, the liquid must always freeze, forming the most stable-crystalline state. If crystallization is avoided, the liquid reaches a metastable state. At a given temperature and given enough time, the metastable state will eventually relax to the thermodynamically stable crystalline state. For a glass, since molecular motion is so slow, this may take the age of the universe. Suppose, however, that crystallization could be prevented for any T. Could a non-crystalline state remain at $T = 0$? This proposed state has been called the ideal glass state. The evidence for an ideal glass state is given by the entropy considerations from specific heat data, and was first discussed by Kauzmann.
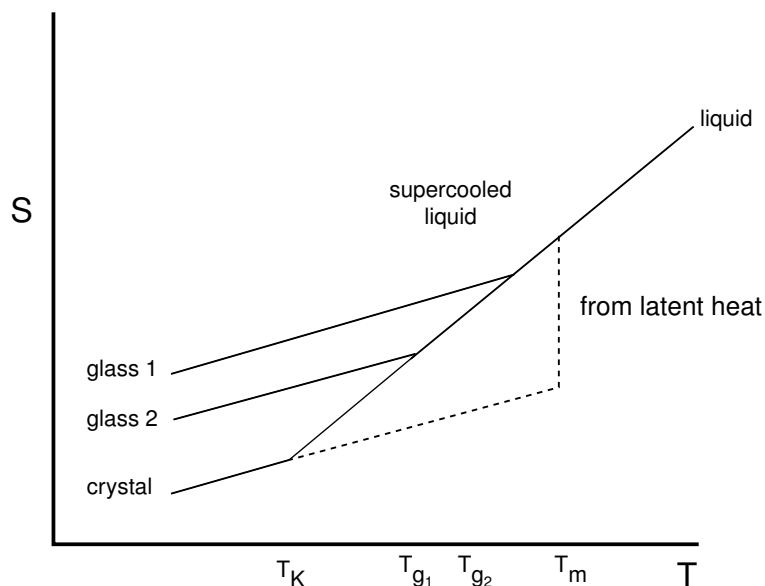
Figure 9.2: Entropy of a liquid as a function of temperature. Note that the entropy curves do not break sharply, but display a continuous change as T decreases. This is not shown on the schematic.

The behavior of the entropy is schematically represented in Figure 9.2. As T decreases, so does the entropy. If the system is cooled slowly enough, at the melting (freezing) point, T_m, the liquid undergoes a first order phase transition. Here, the volume of the crystal (see Figure 9.1) rapidly decreases, and the entropy will drop discontinuously to a lower value, with the size of the drop specified by the latent heat released. The entropy then continues to decrease as T is decreased until, by the third law of thermodynamics, $S = 0$ at $T = 0$. Now, suppose that the system does not crystallize at T_m because the

system is cooled too rapidly. Then, a glass transition will occur at a temperature T_g. Here, due to a change in the specific heat, the entropy begins to decrease more slowly, remaining above the value of S for the crystal. Since this is a metastable disordered state in contact with a heat bath, it will seek to find a lower entropy state. However the crystal is a lower entropy state with a lower free energy. Thermodynamics says system will eventually find the crystal, but it may take the age of the universe.

For a slower cooling rate, T_g is smaller and the entropy begins its slow change at a lower value of the entropy. Suppose that the liquid is cooled so slowly that the entropy of the amorphous liquid does not deviate from its curve. Eventually, it will intersect the crystal entropy branch. At this point, the amorphous liquid has the same entropy as the crystal. This temperature is called the Kauzmann temperature and it sets the lower bound on T_g. For a slightly lower temperature, the disordered state would have a lower entropy than the crystal state. This seems odd, but since the process is occurring at fixed T and pressure, it is the Helmholtz free energy for the liquid or solid phases that must be minimized; the entropy difference between the phases may be positive or negative. The main problem would occur if the slope of the liquid entropy curve did not deviate at the Kauzmann temperature. Eventually, S would reach zero at a finite temperature, in contradiction to the third law of thermodynamics. Thus, one argument that says the slope of the entropy vs temperature must deviate at T_k and this is called the ideal glass transition. The ideal glass state would have the same entropy as the crystalline state and the glass transition at this point would be a thermodynamic transition at a well defined temperature.

Another viewpoint says that given enough time at a fixed temperature below T_g, local nucleation of crystal will occur and system will crystallize. This would prevent the negative entropy state, as for a given temperature, the metastable state would always relax to the entropically favored crystalline state. However, estimates of nucleation rates vs. molecular motion timescales are not in favor of such a process [44]. Thus the fascinating thermodynamic issues of the glass transition raised by the Kauzmann argument are still not resolved.

9.3.3 Viscosity and time-scales of dynamics

The most noticeable effect that occurs for a glass is the tremendous change viscosity as T_g is approached. Angell has proposed a classification scheme based on the form of the viscosity vs T, and this is shown in Figure 9.3. Here T_g is defined as the point where the viscosity reaches 10^{13} poise. Liquids that show an almost linear dependence of the log of the viscosity on $1/T$ are called strong liquids, while fragile liquids show quite non-linear dependence. Fragile liquids have large thermal expansion coefficients at T_g. The viscosity of these liquids is *extremely* sensitive to T, as seen. As mentioned above, the
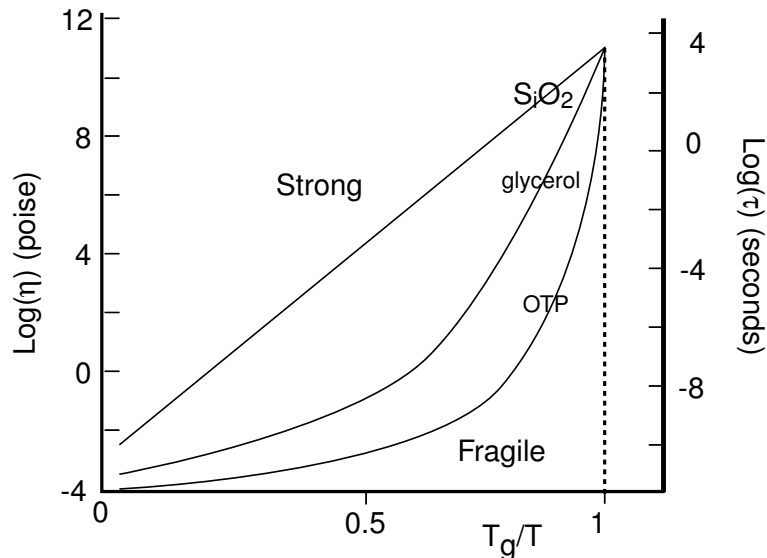
Figure 9.3: Left ordinate: Viscosity vs. temperature for different glass-forming materials. Right ordinate: corresponding molecular relaxation timescales for OTP.

viscosity increase is accompanied by a corresponding increase in characteristic relaxation times[1]. The right-side axis in Figure 9.3 shows the time-scale for molecular rotation of the *o*-terphenyl molecules (OTP). These display a tremendous change from the typical nanosecond relaxation timescales above T_m. The dependence of the relaxation time-scales (or equivalently viscosity) on the temperature can be fit to the Vogel-Fulcher-Tammann equation,

$$\tau = \tau_0 \exp\left(\frac{B}{T - T_0}\right) \tag{9.1}$$

When $T_0 = 0$, and $B = E_{\text{act}}/k_B$, the equation takes the Arrhenius form for kinetics determined by constant activation energy barriers of energy E_{act}. For $T_0 > 0$, the temperature dependence is non-Arrenhius, and the relaxation time becomes infinite at a finite T. The value of this equation is that changing B creates viscosity temperature curves that mimic the strong-fragile plot in Figure 9.3. Thus fragile liquids have small B values and strong liquids have large B values. The value of B is proportional to the ratio T_g/T_K, where T_K is the extrapolated Kauzmann temperature discussed in the section on

---

[1]Viscosity is the response of a liquid to shear and is related to the relaxation time the system needs to respond to the shear stress by the Maxwell equation, $\eta = G\tau$, where G is the high frequency shear modulus.

thermodynamics of the glass transition[2]

In fact, supercooled liquids usually display two typical time scales as T_g is approached. These are denoted the α and the β processes. In OTP, it is thought that α corresponds to full rotations of the polymer molecules and is the timescale which is seen in the response of the liquid to shear. β is related to the timescale for a sidegroup to rotate. Therefore, α can be thought of as a structural relaxation time and is thus related to the viscosity; this is plotted in Figure 9.3. β corresponds to small re-orientations. Above T_g, these timescales are the same, but below T_g in fragile liquids, the α timescale displays non-Arrhenius behavior while the β timescale continues to display Arrhenius behavior.

9.3.4 Nonexponential relaxation

A characteristic feature of supercooled liquids is that they generally do not relax exponentially is response to a perturbation. For example, if the temperature of a fragile supercooled liquid is dropped by a small amount, the volume will not approach the new equilibrium volume exponentially. Relaxation functions of a quantity $C(t)$ are often fit to the Kohlrausch-Williams-Watts (KWW), stretched exponential forms,

$$C(t) = \exp\left((-\frac{t}{\tau})^\beta\right) \tag{9.2}$$

There are two different explanations for how the dynamics could relax nonexponentially. The first is attributed to what is known as heterogeneous dynamics: different regions of the liquid can have dynamics with timescales that are orders of magnitude faster than other regions. Molecules in each region relax exponentially to a perturbation, but the regions have different relaxation timescales. Measurements of the dynamics of the entire sample in response to a perturbation would effectively average over the vastly different response timescales from different regions; this leads to a $\beta \neq 1$. The second explanation postulates that supercooled liquids are homogeneous and that each molecule relaxes in a nonexponential manner due to interaction effects with its neighbors. Here β would measure the degree of interaction. Much effort has been put into determining the correct mechanisms, and it now appears that the heterogeneous picture is the correct one [54]. Thus the picture that emerges is one that was postulated by Adam and Gibbs [2]. They postulated that the flow of the supercooled liquid proceeds though large regions moving cooperatively. As T_g is approached, the size of the regions diverges, and

---

[2]In some liquids, the VFT fits are usually very good below T_g but can show deviation close to T_g. In other liquids, VFT works well for the entire range up to T_g [44].

the dynamics must arrest, as it is increasingly difficult to move all of the particles in the regions as opposed to movement of single molecules.

Relaxation in the glass state is even more complicated. Here the system can display aging: relaxation to a different state after reaching the glass, by slow changes of material properties. We will not discuss this point here.

9.4   Hard spheres, colloidal glasses and MD simulations
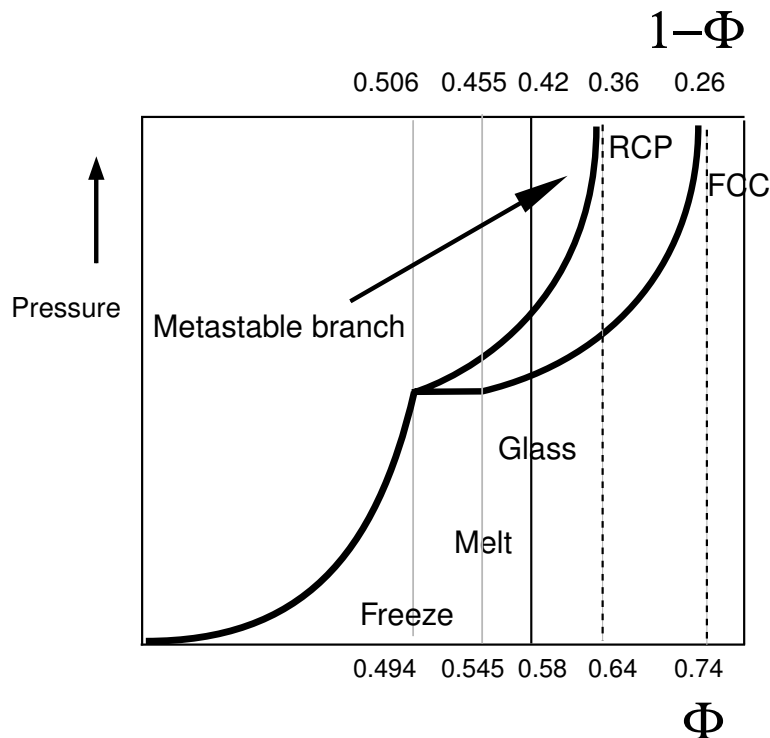
Figure 9.4: The hard sphere phase diagram in the pressure-volume fraction plane. Adapted from [153]

Hard sphere models, with particles that only interact repulsively at contact, have been used extensively to study the statistical mechanics and thermodynamics of simple liquids. Since there is no energy scale, temperature sets the timescale. The volume fraction Φ becomes the thermodynamic variable which is controlled. Hard sphere models were first studied by Alder and Wainwright [3], and there has been much simulation work to understand the phase diagram, equation of state and motion of particles. The phase

diagram in Figure 9.4 shows a phase transition as volume fraction is changed and has been used as a model to understand phase transitions in more complex fluids [3]. If Φ in a hard sphere system is increased sufficiently slowly, the system will crystallize and proceed along the FCC branch. If the volume is changed too rapidly, the system will fall along the amorphous branch. There is much debate whether a glass transition occurs in this system. Some results have shown that compression of the hard sphere fluid always yields an amorphous glass state with $\Phi_g \approx 0.64$[170]. Other results [153] have shown that if one waits long enough, crystallization always occurs.

Colloids at high densities have been shown to display the features of the hard sphere phase diagram [145]. Furthermore a glass transition at $\Phi \approx 0.58$ was observed by Pusey and van Megan [146]. This was observed by light scattering measurements which revealed a loss of ergodicity and decay of the correlation functions at the glass volume fraction. Since then, a large number of experiments have been done to characterize this transition and compare to Mode Coupling Theories [184, 185]. Specifically, the light scattering experiments have studied the relaxation of colloids near the glass transition and found that near Φ_g, the relaxation proceeds under two timescales, and these correspond to the α and β relaxation discussed earlier.

Recently confocal microscopy has been used to directly image glass forming colloids [62, 191]. This has shown the existence of growing cooperative regions [191] near $\Phi \approx 0.58$. These growing cooperative regions allow a nice interpretation of the α process in the hard sphere and colloidal system. The spheres are trapped in transient cages of their neighbors. β_F processes refer to motions of a sphere inside a cage and differ from the β processes described above. This is the fast process as it is just rattling around. The α process refers to structural rearrangements when the spheres break out of the cages. As things get more crowded, the size of the cooperatively rearranging region becomes larger, and it takes longer for a sphere to escape from a cage. As Φ_g is approached, this process requires the participation of more particles. It thus becomes slower and may eventually arrest at the glass volume fraction. The confocal experiments showed that the supercooled liquid was characterized by large regions of correlated fast moving particles surrounded by regions of slower particles, demonstrating the spatial heterogeneity discussed above. Thus, α relaxation occurs through cooperative particle motion; movement of a particle in a cluster results in movement of another particle in the cluster. Since all particles must move together in the cluster, relaxations require rearrangement of progressively larger groups of particles[3].

---

[3]The cooperatively arranging region is thought of as a subsystem of the sample that can rearrange into another configuration independently of its surrounding environment. In [2], the cooperatively rearranging region is defined as "the smallest region that can undergo a transition to a new configuration without a requisite simultaneous configurational change on or outside the boundary."

However, due to space shuttle experiments showing an eventual nucleation [201], the debate on the glass transition continues. However, colloids still are a nice way to study possible glass transitions in a simple controllable system.

In addition, recent studies of molecular dynamics of soft spheres, with Lennard-Jones potential have proven useful in visualizing some of the processes discussed above [46]. The simulations observe a similar slowdown and also reveal that the cooperative regions of fast-moving particles are linear string-like structures [46]. The particles in these string-like clusters are more mobile and are able to break out of their cages earlier. However, these studies are limited in the range of temperatures by the prohibitively long computation times required to observe effects near glass transitions.

9.5   Theories of glass transitions

9.5.1   Mode Coupling Theory

This theory has been successfully applied to colloidal glasses and could prove useful for granular matter. It has had some success explaining the two stage relaxation that occurs in glasses. However, as it deals the coupling of slow Fourier modes, it is very difficult to understand in a physical way. However, it does predict a power-law variation of the timescale for relaxation time (or viscosity) as a temperature T_c is approached, with $T_g < T_c < T_m$. Power law behavior for the viscosity of supercooled liquids has been observed in a wide variety of liquids. While mode coupling may be a good theory in the supercooled regime $T > T_c$, it does not do a good job at predicting the exponents of the power laws. Mode coupling also makes the prediction that the relaxation of perturbations should occur in a two step process close to T_c. These different time-scales for decay seem to correspond to the β_F and α processes. Extensive comparison between MCT and colloid light scattering experiments has been made [185].

9.5.2   Free volume theory

The free volume picture of supercooled liquids[4] postulates that the glass transition in a system will occur when "free volume is sufficiently squeezed out of the system" [198]. At this point, particles are confined to local cages; thus diffusion over length scales larger than a particle diameter becomes impossible. The theory proposes that clusters of particles in the fluid have different amounts of free volume. Clusters with sufficient free volume are termed liquid-like while clusters in which the free volume is below a critical value are called solid-like. As the system is supercooled, the solid-like clusters grow in

---

[4]For a non-mathematical discussion of this theory, see [198]

size until a percolation threshold is reached and the system becomes a glass. The notion of liquid-like and solid-like regions is appealing in light of our observation of ballistic and hindered regions in the fluidized bed.

9.5.3 Energy landscape picture
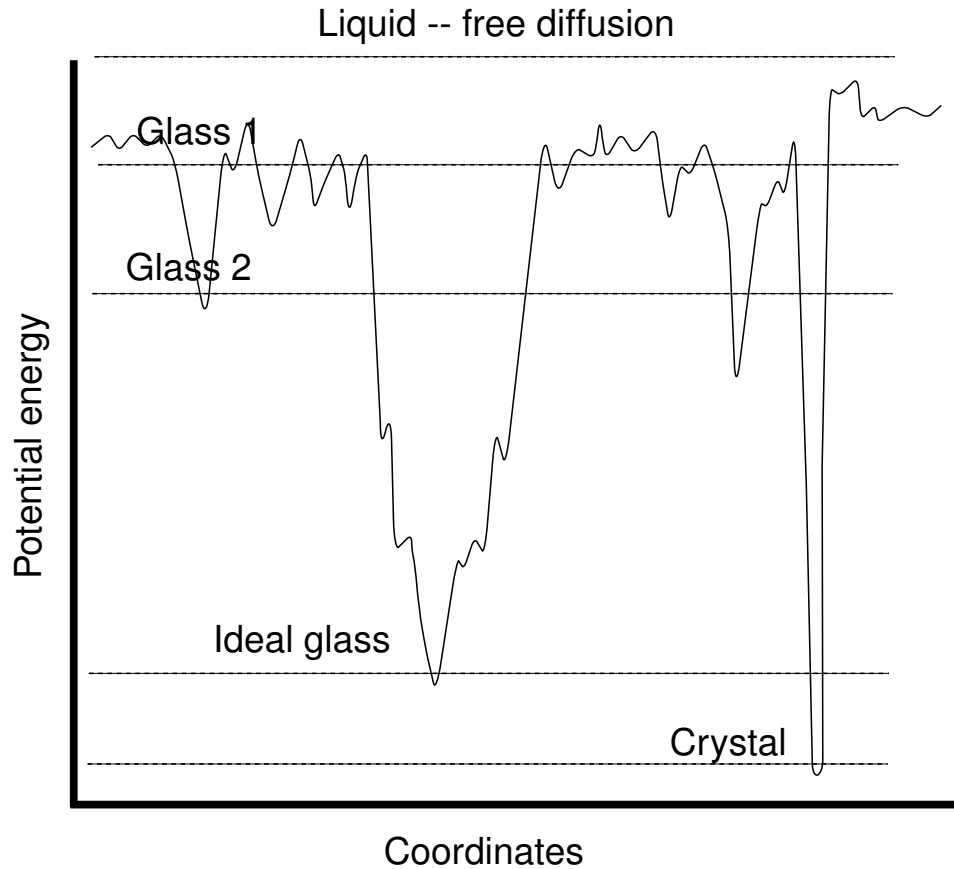
Figure 9.5: The energy landscape picture may be useful, adapted from [45]

A much more physical picture of glass formation is provided by the energy landscape picture. The energy landscape picture of glass transition was developed by Stillinger [171] and the essential diagram is illustrated in Figure 9.5. This is potential energy for every configuration of particles and only depends on the density of the molecules. At a given temperature, the system explores the local minima of the landscape for that temperature. The dynamics are governed by the number of minima of a given depth at the given temperature and the ability of the system to jump over landscape (or tunnel around, as this is many-dimensional). The dynamics of supercooled liquids can be interpreted in this picture. For high temperature, the most of the minima are very shallow

and the energy from the temperature is sufficient to allow the system to explore the minima and not get trapped. Here the system displays Arrhenius behavior. However, as the temperature is decreased, the system cannot surmount the larger barriers and has the ability to get trapped in local minima. These correspond to the non-thermodynamically stable states which may have long lifetimes. The system will thus show behavior that deviates from Arrhenius. There is one global minimum corresponding to the crystalline state. The lowest non-crystalline state is the ideal glass. In the energy landscape picture, the alpha process is associated with the exploration between different deep minima and the fast beta process is associated with the exploration of a single alpha minimum.

The landscape picture also helps to interpret the behavior of supercooled liquids as a function of cooling rates. If the system is cooled too rapidly, it may be stuck in a higher minimum. The faster it is cooled, the higher the volume. This is because if it starts from a high volume state, it will spend most time near high volume basins. If the temperature is quickly removed, it becomes stuck in these basins. Cooling slowly enough allows the system to always find the lowest minimum. The ideal glass state is the lowest non-crystalline minimum.

Workers have studied models of MD systems to determine whether this is a useful picture and we reproduce one particular plot in Figure 9.6. This is a MD Lennard-Jones simulation which was quenched at different rates and at each time step, the average potential energy of the atoms was measured. The free diffusion corresponds to a temperature high enough so that the system sees no energy barriers. This resembles the defluidization plot in Figure 8.23. The interpretation given is that the slower cooling rates allow the system to more efficiently explore the local minima, finding the correct set for each temperature. If the system is cooled too quickly, it becomes trapped in the minima is was exploring when the temperature was suddenly decreased. It is a glass at these low temperatures. In the intermediate region, below $T = 1$ and above $T_g \approx 0.45$, the time scale for relaxation no longer follows an extrapolated Arrhenius law and the relaxation functions describing the response to a perturbation become stretched exponentials. The authors in [158] call this the landscape influenced or dominated region.

9.6 Supercooled liquids, glasses, and fluidized beds

Below RLP, the defluidized state displays behavior and particle dynamics that are remarkably similar to those found in supercooled liquids and glasses. Here we discuss the main points in common. To make the analogy as suggestive as possible, we will refer to defluidization as cooling. We now provide a point-by-point comparison and then make some concluding remarks.

The bed has dynamics driven by effective temperature and volume fraction frus-
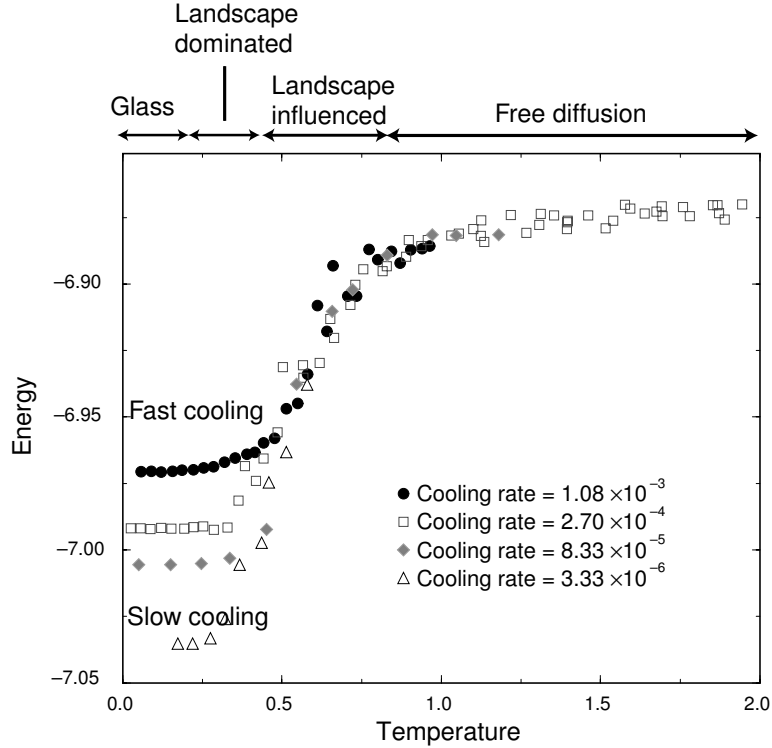
Figure 9.6: An MD simulation of Lennard-Jones molecules shows the exploration of lower parts of the energy landscape as a function of cooling rate as measured by the potential energy per atom after a quench. From [158].

tration dynamics. A liquid changes into a glass when the temperature decreases by a little bit. A fluidized bed effectively loses temperature when $\Delta P = 1$. Thus, a fluidized bed is like a supercooled liquid that reaches a temperature (or volume fraction) near but above T_g (or Φ_g) at which point the temperature is suddenly quenched near $T = 0$. At this point temperature can no longer drive the dynamics and any motion is due to the lack of jamming–the bed is still not at the lowest possible energy and will try to get there, but only through local wiggling motions. This is the deceptive glass analogy, as a glass below T_g is also frozen, but still has a finite temperature.

This said, there is still a regime in the bed where the dynamics rapidly slow, $\alpha < 2$, but $\Delta P = 1$. This is in the hindered regime, below RLP and here is where we believe the analogy to supercooled can be exploited. Here, it is our contention that the dynamics slow due to frustration effects–the system has run out of free volume and some particles are constrained to touch. This creates regions of immobile particles which grow in size as the flow is decreased. We should point out that this range of hindered motion can be seen even below the volume fraction reached upon very slow defluidization, as

seen in Figure 8.18. This indicates that the wiggle packing is effective until RCP.

This concludes our review on the basics of supercooled liquids and glasses. We now discuss the analogies from Section 9.2 with the previous ideas in mind.

9.6.1   List of analogies

• Dependence of state on cooling rate

We have shown that the rate at which a bed is cooled determines the final volume fraction and the dynamics of the wiggling motions. For example, Figure 8.23 resembles Figure 9.1 and Figure 9.6. The value for slow fluidization is $1 - \Phi \approx 0.425$, very close to $\Phi_g \approx 0.58$. However, this could be coincidence as we have argued that any true glass transition will be pre-empted by the loss of fluidization.

• Slow dynamics upon supercooling
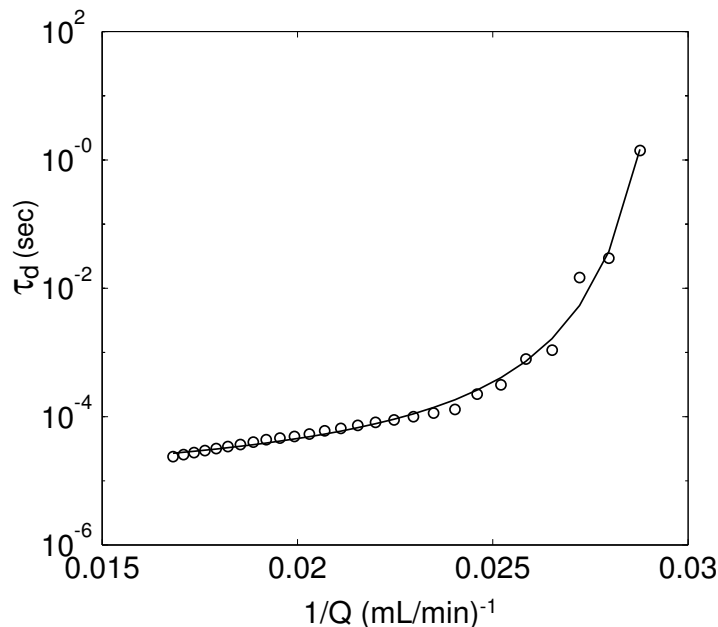
Figure 9.7: The fit for relaxation times from DWS to VFT form. We obtain $\tau_0 = 10 \ \mu$sec, $B = 26$, and $T_0 = 32$ ml/min. This plot resembles the fragile glass-former in Figure 9.3.

All timescales in the bed slow dramatically as a point in the the frustrated region is approached. Using Q for T, we have fit the τ_d data for which $\Delta P = 1$ and this is presented in Figure 9.7 and should be compared to Figure 9.3. We note that the fit does not do well in the high Q regime; in fact we have found that it can be better approximated with a power law fit in this region with an exponent around 2.5, close to MCT prediction.

Thus, before the fluidization is lost, the bed resembles a very fragile glass. We note that the point at which the dramatic slowdown begins is at a lower Q than the point at which α begins to slowly decrease from 2. It corresponds to the point at which α begins to decrease rapidly from 2. We currently have no explanation for this.

- **Cooperatively growing regions and spatial heterogeneity**

Our evidence for hindered dynamics is seen with $\alpha < 2$. We interpret this as immobile regions and the connection to cooperative heterogeneous regions could be very strong. As the system becomes more frustrated, the immobile regions grow in size. We must be seeing the short time picture of a cooperative region. In the supercooled state, some regions are moving rapidly while others are immobile. Thus we see the average. It would be useful to try to relate the stretching factor in Equation 9.2 to the value of α. We argued that $\alpha \neq 2$ results from the DWS sampling many regions of different dynamics. This is the same argument that accounts for the stretched exponential. Can they be related?

In addition, there is an intriguing correspondence between $\alpha < 2$ and the disappearance of the spouting volcanos, see Figure 8.13. Above RLP, the system is completely fluidized and the surface of the bed is quite agitated. Below RLP, in the hindered region, the surface of the bed is often broken by a local spout. Viewed from the side, these appear as small worm-like structure that are longer than they are wide. The frequency and spatial density of these spouts decreases as α decreases. Are these the manifestation of the string-like cooperative regions seen in [46, 47]? In this region, they appear and disappear all over the bed, locally spouting and then stopping. This needs to be studied carefully as it would provide an explanation of a fluidized bed using a feature of a supercooled liquid.

- **Nonexponential relaxation**

If the spatial heterogeneity in the bed corresponds to spatial heterogeneity in supercooled liquids, we should see nonexponential relaxation. This is something to study. For example, make a small change in Q and watch how various properties relax: volume, dynamics as measured by a series of short 1 second DWS measurements. There should be a difference in response for the fluidized and the hindered regions. We predict that the fluidized region should relax exponentially, while the hindered region should show nonexponential relaxation.

- **Aging**

In the wiggling regime, corresponding to a glass near $T = 0$, the non-jammed bed can display very slow changes in speckle motion for long times after a decrease in Q (see Figure 8.17). Is this an example of aging in the system?

- **Nonergodicity in light scattering measurements**

Our light scattering curves (see Figure 8.14, top panel) show a change in the intercept of $g^{(2)}$ just as seen in DLS measurements near glass transition.

● **Force chains**

Are force chains set up at glass transition upon defluidization, or is an extra jamming necessary? The existence of force chains also points favorably to the glass analogy. It has been proposed in the jamming picture that force chains form at a jamming transition [138]. If a glass can be thought of as a jammed state, this would be a useful concept.

9.7 Interpretation in energy landscape picture

We propose that the energy landscape picture is a useful way to interpret our results and a schematics are shown in Figure 9.8-9.10. The fundamental difference is that we postulate that the energy landscape is a function of Q. This is reasonable as the potential energy of the system must account for the presence of all forces, and Q creates a force through drag. We now separate the pressure in the bed into a pressure due to fluid flow ΔP_f and a pressure due to frictional contact forces ΔP_c. We also postulate the the temperature in the system is proportional to Q when $\Delta P_f = 1$ and effectively 0, when $\Delta P < 1$. The landscape must change as the voidage changes and should be taken into account. However, we will not speculate on its shape and distribution of local minima as a function of density here [45].
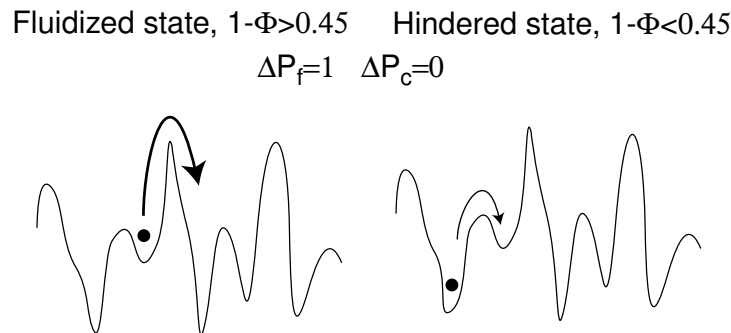
Figure 9.8: A proposed landscape picture for fluidized beds above onset in the completely fluidized and hindered regimes. ΔP_f is the pressure drop due to the fluid and ΔP_c is the pressure drop due to contact forces.

In the fluidized region, the system moves freely over low barriers, and the lowest point explored in the landscape is set by the balance of the fluid pressure (temperature).

The landscape is not changed with Q because $\Delta P_f = 1$ and there is no static component of ΔP. When Q is decreased, but still fluidized, the temperature decreases. However, there is still enough temperature to rearrange. When the system enters the frustrated regime, the landscape remains fixed, but the system is stuck in local barriers. The most probable state is always a balance between temperature and weight, but now there is considerable activation to overcome barriers.

Wiggle packing: $\Delta P_f<1$ $\Delta P_c=0$
static landscape
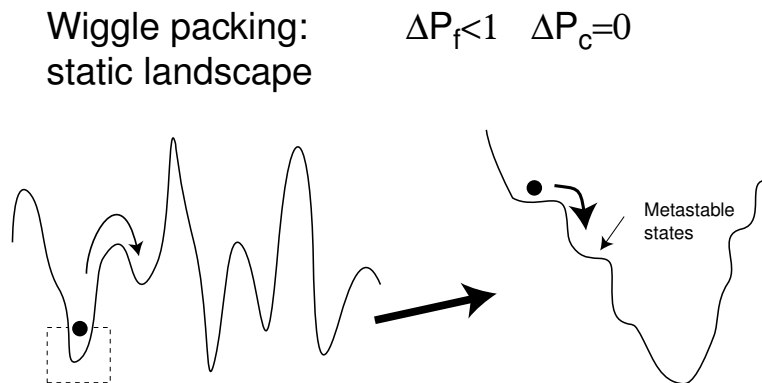
Metastable
states

Figure 9.9: In the wiggling regime, each local minimum must have a collection metastable states.

As Q is decreased, the system becomes localized in a local minimum which is lower as the ramp rate is made slower due to exploration of the landscape. When $\Delta P_f < 1$, whichever minimum the system is it stays and the system will now begin slow annealing. The local wiggle motions then pack it further by annealing. We present an energy-landscape pictures which could account for this. In this case the relaxation would be due to local metastable inflection points on which the system can remain until perturbed by a decrease in flow, or a slight tap. These are illustrated in Figure 9.9. [5]

We propose that jamming changes the landscape by creating sudden activation barriers. Jamming creates a $\Delta P_c > 1$ with only a small change in Q (ΔP_f). Thus, when jamming occurs, the walls of the potential well suddenly become very steep and the system is well-localized to the minimum. Before, the system could wiggle around in the bottom of the relatively wide well, moving between. Now, to move at all, the system must move over the high barriers, breaking the yield stress. These barriers are the force chains in the system. Thus, jamming freezes in the system–no longer can the fluid produce wiggle packing. Any decrease in flow in the jammed state must provide

---

[5]This is one explanation, but perhaps the landscape actually changes with changing flow rate for $\Delta P < 1$. A decrease in flow would make local minima deeper and the system would evolve by always staying at the changing minimum.

Jamming $\Delta P_f < 1$ $\Delta P_c > 0$

Q   Q+δQ
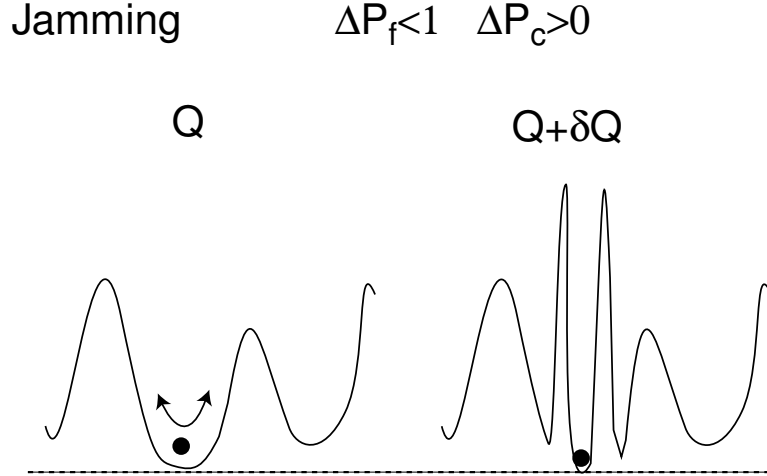
Figure 9.10: Jamming modifies the landscape by suddenly changing barrier heights, effectively locking the system into a narrow local minimum.

enough of a perturbation to unlock the system. This should be tested by examining the stability of jammed states to different size flow decreases. As the system is more jammed, the barriers are higher. When the grains yield, we have seen that the bed height increases to accommodate, but then the particles jam. This must occur in the following way. At yield, the high barriers are suddenly removed and the system can reach a higher local minimum. However, if the stress is applied slowly, the system will jam again, and the barriers will go back up. Presumably they won't be as high, as the system is now in a higher voidage. We have observed that if the stress is quickly applied by rapid increase in Q, the system will not have time to set up barriers (force chains), and the overshoot will be lower.

9.8   Conclusions

The fluidized bed displays many of the features associated with a supercooled liquid. The hydrodynamics drives the system as does loss of free volume. We believe that the bed is a supercooled liquid in the hindered regime and exhibits the familiar heterogeneous dynamics associated with such a liquid. However, this state becomes nearly frozen due to lack of driving when $\Delta P < 1$. At this point, it is stuck in whichever minimum it was in and the only dynamics are wiggling motions moving between inflection points. Thus, the true glass state is pre-empted by the rapid freeze due to loss of "thermal" driving. It is important to study things like relaxation in the frustrated region to understand supercooled fluidization and it is important to study wiggling in $\Delta P < 1$ to understand static jamming. Furthermore, can the worms and volcanos be explained by the same

mechanism of heterogeneity in supercooled liquids?

Chapter 10

Conclusions and future work

In this dissertation, we have described experiments on several different problems in granular materials. To gain understanding, we have used concepts from many branches of physics, including lattice dynamics and melting criteria, glasses and solid mechanics, fluctuating hydrodynamics, and local stress chains. This is the beauty of studying granular materials. In a small work area, and for little money, many different behaviors of matter can be interrogated in a precise way. Central to the work described, is the concept of fluidization in granular materials. As seen, fluidization, in both the fluidized bed and in the vibrated layer, strongly influences the grain dynamics. However, despite the fundamental role that fluidization transitions play in the flow of granular materials, there have been very few detailed experimental studies. Our initial detailed studies of fluidization transitions have raised as many questions as they have answered. We now discuss questions which are natural extensions to the work described in Chapters 1-9.

10.1   Vibrated layer

Due to its simplicity, the vertically vibrated system remains a very useful geometry to study granular flows. However, improvements can still be made to decrease lateral acceleration. Improved stability should prove useful for study of patterns at higher frequencies, or near the onset of waves. Using air-bearings with larger cross section, systems can be designed to significantly reduce the effects of lateral vibration[1]. In addition, with a more powerful shaker, the container mass could be increased, decreasing the effect of the layer collision. With sufficient improvements, it might be possible to study the vibrated layer with the same precision that has been developed for gas convection [196]. Even without this stability, there are many questions that can be addressed:

●**Fluidization transition in a vibrated layer**
The basic fluidization process in the vibrated layer is not fully understood. As we have

---

[1]Such a system has been designed and built by P. Umbanhowar, and suffers from no frequency dependent leveling effects.

shown, fluidization has consequences on the evolution of pattern, and determines the types of waves that are seen. Studying the grain dynamics near $\Gamma = 2$ with techniques like Diffusing Acoustic Wave Spectroscopy or Diffusing Wave Spectroscopy would yield important information about the grain dynamics.

Fluidization in dry grains raises important questions about the role of continuum modeling of granular materials. Hydrodynamic equations have been shown to well describe the flow of very fluidized grains [19, 150]. Can such equations equations capture the transition from solid to liquid behavior around the fluidization transition? Although hydrodynamic theory has been used to describe slowly deforming solids [89], this approach is in its infancy. In fact, there is no consensus on the correct equation of state to use at high volume fractions (see Appendix 2). Careful experiments in 3D would provide tests of such theories.

• Noise below onset and hydrodynamic theory

Our measurements on the noise induced patterns below the onset of patterns suggest the need for modification of the Jenkins-Richman equations. The noise induced patterns are produced by fluctuations which are of the order of energy scales in the pattern, but have been averaged over in the continuum limit. In thermal convection experiments, the effect has been studied for supercritical (or very slightly subcritical bifurcations). Thus, to make contact with theory, it would be interesting to study the noise below onset when the bifurcation in the vibrated layer is only slightly supercritical. This requires going to higher frequencies. However, $\tilde{v}$ decreases for increasing frequency. Thus, care must be taken, as the best place to study this effect should be in the fluidized case, $\tilde{v} > 3$. Perhaps it would be useful to pre-fluidize the grains, using a flow of gas or an additive high frequency excitation.

• 2D melting transitions

Melting in the square lattice should be studied in a more controlled way. We have reported on a type of shear melting, in which the lattice is heated by a single growing mode. To make contact with theories of 2D melting, it is necessary to create a more uniform type of heating. Preliminary attempts using a random frequency modulation have proven unsuccessful. Once developed, this technique would allow control of the temperature of the lattice. Perhaps the well-known Kosterlitz-Thouless-Halperin-Nelson-Young melting scenario [85] would be observed.

Additional work could be done to understand the motion of defects and grains boundaries in the lattice patterns. Can theories of defect dynamics [166] in equilibrium crystal lattices be used to predict the speed of propagation of point defects in a nonequilibrium pattern? Do line defects act like a collection of point defects? What types of

dynamics do they display? Results from such a study would be very useful for understanding ordering of patterns like those discussed in Chapter 4. Theories for ordering are based on amplitude equations, and do not yet predict the correct time dependence of the structure factor (the ordering of the pattern). Could a lattice dynamics approach predict the rate of ordering or "crystallization"?

It would be interesting to see if other patterns display coupled lattice type dynamics and thus be described by a set of ODEs. We have some indication that spring constants decrease with increasing layer depth. Thus, in sufficiently deep layers the presumably higher frequency compressional modes could become excited. We have indication that stripe patterns can display one dimensional dynamics. It would be interesting to study the behavior of more rigidly bound hexagonal patterns for which there is no "weak" direction.

•Segregation near phase discontinuities
Studies of segregation in vibrated layers due to effects other than boundaries or interstitial gas are just beginning. We have shown that segregation of different sized particles occurs near naturally occurring phase discontinuities. However, no systematic study of the dependence of the segregation rate and size of region of segregation on control parameters has been made. Perhaps a regime could be found in which the segregation process becomes useful in an industrial process? We envision a large scale sorting process in which grains of different size are placed in container vibrating in the kink regime. A kink would be then moved across the container by adding a slight subharmonic to the drive. The kink would act like a windshield wiper, removing large particles from the bulk as it swept through. The large particles could then be picked off the top, or the system could be slightly inclined to let them move along the kink into a reservoir.

10.2   Fluidized bed

The studies presented in Chapters 8 and 9 are a first step toward precision fluidized bed experiments. The fluidized bed geometry is an ideal way to study the dynamics of multiphase flows. However, precision experiments are hampered by lack of precision flow distribution elements for grains between $0.1 - 5$ mm. We believe that the design described in Chapter 3 should produce a distributor free from the extra channeling that complicates study of steady states. The proposed design in Figure 3.9 would maintain a stiff surface while allowing for different pressure drops through the distributor. The role of pressure drop has been studied theoretically, but quantitative experiments are lacking [97].

Once a good flow distributor is created, many interesting questions can be addressed. For example, how does the Geldart diagram change with changes in fluid parameters? It is not clear what appropriate nondimensional parameters characterize the transitions between stable and unstable fluidization, Geldart A and B. For that matter, it is not clear that there *are* clear transitions. The fluidized state is rarely dull–particles don't just bang around randomly. For example, as briefly discussed, in the frustrated regions, the side of the bed reveals small transient worm-like jets. If flow is increased enough, we observe a rapid drop in the bed height. This indicates that the system has begun to bubble as shown in Figure 8.29 in Chapter **??**. Is there a bifurcation to these states? transition between these states should be studied. What kind of bubbling is it? Qualitatively it looks like ill-defined voidage waves near 1Hz. Techniques like Diffusing Acoustic Wave Spectroscopy should prove useful in understanding the long time and long length scale behavior.

In addition, the analogy to supercooled liquids should be pursued. The many similarities between the two systems could yield insights into the behavior of both. For example, the role of spatial heterogeneity has only recently been studied in colloids and MD simulations. It is clear that the bed is spatially heterogeneous in the supercooled regime. Can the different systems be understood in the same way?

10.3   Conclusion

These projects have been fascinating and enjoyable to work on. The range in phenomena has kept it interesting and I look forward to hearing about (and possibly completing) some of the projects outlined above.

Appendices

Appendix A

Swift-Hohenberg equation solver

The code listing for the 2-d Swift-Hohenberg equation solver, written in Matlab, based on pseduo-spectral integration scheme taken from [36].

```
figure(1);clf;figure(3);clf;figure(2);clf;figure(4);clf
clear rato;
clear M;
clear raw;
clear stmat;
clear width;
clear max_k;
clear mm;

flag=1;
PLOTTIMES=1;

% Solves the 2-D Swift-Hohenberg equation %

N=128; %% number of NxN grid points
n=8;
xmax=N/2;
wind=15;  %% fitting window for Gaussians

%a=-1.505;b=3.0;c=1.0;d=16;q0=.5; % oscillons
%a=.1;b=-1.0;c=0.0;d=1;q0=1;
a=-.05;b=3;c=1;d=1;q0=1; % Subcritical
dx=2*xmax/N;
dq=2*pi/(2*xmax);
DT=.1
timesolve=0;

%setup grid in xy and q spaces
[x,y]=meshgrid(-xmax+dx:dx:xmax);
[qx qy]=meshgrid(-dq*N/2:dq:dq*N/2-dq);
```

```
% Initial condition stuff
%% fil matrix is initial condition

[th,r]=cart2pol(x,y);

%ffil=.05*randn(N,N).*(exp(-((r-20)/5).^2));
%ffil=ffil-mean(mean(ffil));
%fil=abs(ifftshift(fft2(ifftshift(ffil))))/N^2;
%fil=2*real(exp(i*th*n)).*(abs(r-20)<3); % central ring

%% This sets random noise with mean 0
fil= 2*rand(N,N);
fil=fil-mean(mean(fil));

W=fil;
W=W-mean(mean(W));

ffil=fft2(fil);

r=xy2rt(abs(fftshift(ffil)),N/2+1,N/2+1,0:N,2*pi*(0:255)/256);
st=sum(r')/100000;
stmat(1,:)=st/max(st);

figure(1)
colormap gray
simage(W);

% Set up linear stuff

lins=a-d*(q0^2-(qx.^2+qy.^2)).^2;
lins=fftshift(lins);

F=exp(DT*lins);
G=(F-1)./lins;
H=(F-(1+DT*lins))./(lins.^2);

k=0
ll=0;
Wf=fft2(W);

t0=clock;
```

```
while timesolve<20

W3=W.^3;
N0f=fft2(W3.*(b-c*W.^2));
N1f=0;
Wtmpf=F.*Wf+N0f.*G;  % first guess
Wtmp=real(ifft2(Wtmpf));
Wtmp3=Wtmp.^3;
Wtmp35f=fft2(Wtmp3.*(b-c*Wtmp.^2));
N1f=(Wtmp35f-N0f)/DT;
Wnf=Wtmpf+N1f.*H;

% back to real space
W=real(ifft2(Wnf));
WLin=real(ifft2(F.*Wf));
WNon=b*W.^3-c*W.^5;
dif=max(max(W-(WLin+WNon)))
Wf=Wnf;

timesolve=timesolve+DT

k=k+1;
if rem(k,PLOTTIMES)==0
disp(etime(clock,t0))
ll=ll+1;
figure(1)
simage(W);
colormap gray

%% Can store images here %%%

%raw(:,:,ll)=W;
%M(:,ll)=getframe;

mm(ll)=max(max(W));
%fwork=(abs(fftshift(Wnf))).^2;
rato(ll)=max(max(WLin))./max(max(WNon));

% Divide by initital pattern for good
% linear stage fitting %
if rato(ll)>100 & flag==1
fwork=(abs(fftshift(Wnf./ffil)));
```

216

```
%fwork=(abs(fftshift(Wnf)));

else
fwork=(abs(fftshift(Wnf)));
flag=0;
end
figure(4)
simage(fwork);drawnow;
colormap jet

%% Take azimuthal average and do fitting %%%
r=xy2rt(fwork.^2,N/2+1,N/2+1,0:N,2*pi*(0:255)/256);
st=sum(r')/100000;
%  stmat(ll+1,:)=st;
stmat(ll+1,:)=st/max(st);
[gg hh]=max(st)
hhmin=hh-wind;
if hhmin<=0
hhmin=10;
end
hhmax=hh+wind;
if hhmax>=max(size(st))
hhmax=max(size(st));
end
hhmin=1;
hhmax=N/2;

ttt=max(size(hhmin:hhmax));
stsm=st(hhmin:hhmax);
%p=[20 16 1 0]; lorentz fit
%p=[100/timesolve^.25 hh-hhmin gg 0]; %gauss
p=[100/timesolve^.25 hh-hhmin gg]; %gauss2
hold off;
q=1:ttt;
pout=fmins('fiterr',p,[],[],'gauss2',q,stsm);

width(ll)=4*pout(1); %gauss
%width(ll)=.3*pout(3)/sqrt(pout(2)); lorentz
max_k(ll)=pout(2)+hhmin-1;
pp=polyfit(log10(PLOTTIMES*DT*(7:ll)),
log10(width(7:ll)),1);
```

```
%%% Various useful quantities plotted here %%%

figure(2)

subplot(4,1,1);
plot(log10(PLOTTIMES*DT*(1:ll)),log10(width));
hold on;
plot(log10(PLOTTIMES*DT*(1:ll)),
polyval(pp,log10(PLOTTIMES*DT*(1:ll))),'r');drawnow
hold off
title('width');

subplot(4,1,2);
plot(log10(PLOTTIMES*DT*(1:ll)),mm);drawnow
title('max');

subplot(4,1,3);
plot(log10(PLOTTIMES*DT*(1:ll)),log10(rato));drawnow;
rato(ll)
title('ratio');

subplot(4,1,4);
plot(log10(PLOTTIMES*DT*(1:ll)),max_k);drawnow;
title('max k');

figure(3)
subplot(2,1,1);
plot(q,stsm,'go');
hold on
plot([1:.1:ttt],gauss2(pout,[1:.1:ttt]));
hold off;
subplot(2,1,2);
imagesc(stmat(:,1:end));drawnow

end
end
```

Appendix B

Hydrodynamic equations of granular materials

For reference, with permission from the authors, we have reproduced the Jenkins-Richman equations used in [19]. The granular temperature is written,

$$T(\mathbf{r}, t) = \frac{1}{3}\langle |\mathbf{u} - \langle \mathbf{u} \rangle|^2 \rangle \tag{B.1}$$

From this definitions, plugging into a Boltzman equation and expanding to lowest order yields hydrodynamic equations for number density (or equivalently, volume fraction $\nu = \frac{\pi}{6}n\sigma^3$), momentum, and granular temperature.

$$\frac{\partial n}{\partial t} + \nabla \cdot (n\mathbf{u}) = 0, \tag{B.2}$$

$$n\left(\frac{\partial \mathbf{u}}{\partial t} + \mathbf{u} \cdot \nabla \mathbf{u}\right) = \nabla \cdot \underline{\mathbf{P}} - ng\hat{\mathbf{z}}, \tag{B.3}$$

$$\frac{3}{2}n\left(\frac{\partial T}{\partial t} + \mathbf{u} \cdot \nabla T\right) = -\nabla \cdot \mathbf{q} + \underline{\mathbf{P}} : \underline{\mathbf{E}} - \gamma, \tag{B.4}$$

where the components of the symmetrized velocity gradient tensor $\underline{\mathbf{E}}$ are given by: $E_{ij} = \frac{1}{2}\left(\partial_j u_i + \partial_i u_j\right)$. The components of the stress tensor $\underline{\mathbf{P}}$ are given by the constitutive relation:

$$P_{ij} = \left[-p + (\lambda - \frac{2}{3}\mu)E_{kk}\right]\delta_{ij} + 2\mu E_{kk}, \tag{B.5}$$

and the heat flux is calculated from Fourier's law:

$$\mathbf{q} = -\kappa\nabla T. \tag{B.6}$$

To calculate the pressure, the equation of state and radial distribution function at contact proposed by Goldshtein *et al.* [74] to include both dense gas and inelastic effects:

$$p = nT\left[1 + 2(1+e)G(\nu)\right], \tag{B.7}$$

$$G(\nu) = \nu g_0(\nu), \tag{B.8}$$

and the radial distribution function at contact, g_0, is:

$$g_0(\nu) = \left[1 - \left(\frac{\nu}{\nu_{max}}\right)^{\frac{4}{3}\nu_{max}}\right]^{-1}, \tag{B.9}$$

where $\nu_{max} = 0.65$ is the 3D random close-packed volume fraction.

We note that $g_0(\nu)$ is essentially a fit to reproduce a branch on the phase diagram for hard-spheres (Figure 9.4). As such, many different forms have been proposed. The standard Carnahan and Starling form [25] for well below onset is,

$$g_0(\nu) = \frac{2 - \nu}{2(1 - \nu)^3} \tag{B.10}$$

while recent authors [16] have used a form from Speedy [170] which works well near RCP,

$$g_0(\nu) = \frac{1}{1 - \dfrac{\nu}{\nu_{\text{RCP}}}} \tag{B.11}$$

Equations B.2–B.4 differ from those for a compressible, dense gas of elastic particles by the energy loss term,

$$\gamma = \frac{12}{\sqrt{\pi}}(1 - e^2)\frac{nT^{3/2}}{\sigma}G(\nu), \tag{B.12}$$

which arises from the inelasticity of collisions between particles. The bulk viscosity is given by

$$\lambda = \frac{8}{3\sqrt{\pi}}n\sigma T^{1/2}G(\nu), \tag{B.13}$$

the shear viscosity by

$$\mu = \frac{\sqrt{\pi}}{6}n\sigma T^{1/2}\left[\frac{5}{16}\frac{1}{G(\nu)} + 1 + \frac{4}{5}\left(1 + \frac{12}{\pi}\right)G(\nu)\right], \tag{B.14}$$

and the thermal conductivity by

$$\kappa = \frac{15\sqrt{\pi}}{16}n\sigma T^{1/2}\left[\frac{5}{24}\frac{1}{G(\nu)} + 1 + \frac{6}{5}\left(1 + \frac{32}{9\pi}\right)G(\nu)\right]. \tag{B.15}$$

Appendix C

Dispersion relation calculation

In this appendix we give details on the calculation of the dispersion relation for the normal modes found in Chapter 5.
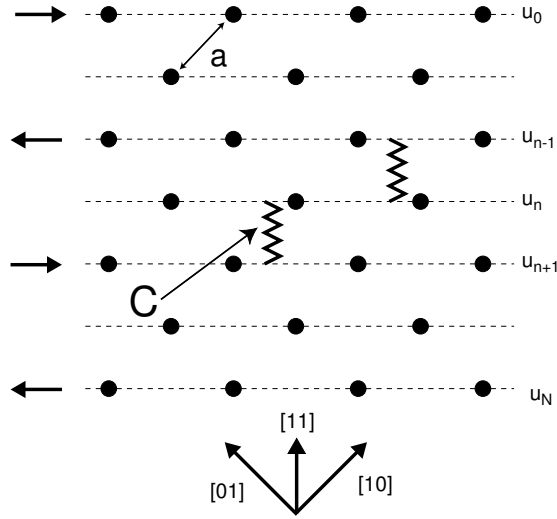
Figure C.1: The diagram showing the spring model used to calculate the $(1,1)_T$ normal modes.

We begin with a model for coupling of $(1,1)$ rows of the lattice in the same spirit of coupling planes in a crystal [102]. We will assume harmonic potential for coupling between the rows. The equation of motion describing the transverse motion of the displacement of a $(1,1)$ row from its equilibrium position can be written,

$$m\frac{du_n}{dt} = C_T(u_{n+1} + u_{n-1} - 2u_n) \tag{C.1}$$

Plugging in a trial wave solution,

$$u_n = e^{-\imath\left(\frac{kan}{\sqrt{2}} + 2\pi f_L t\right)} \tag{C.2}$$

with wavevector k in the $(1, 1)$ direction, and f_L the frequency of the wave, yields the dispersion relation,

$$f_L = \frac{1}{2\pi} \sqrt{\frac{4C_T}{m}} \sin(\frac{ka}{2\sqrt{2}}) \qquad \text{(C.3)}$$

where $k = \pi\sqrt{2}/a$ is the maximum wavevector on the lattice in the $(1, 1)$ direction, the wavevector at the edge of the Brillouin zone.

Assuming free boundary conditions gives the condition $k = \frac{n\pi\sqrt{2}}{aN}$ with $0 \leq n \leq N$. This sets the number of allowed modes.

Appendix D

Single inelastic ball model solver

The code listing for the single inelastic ball model solver. This code calculates the trajectory of a single completely inelastic ball boucing on an oscillating plate. This method was inspired by a similar code in [182].

```
#include <stdio.h>
#include <math.h>

#define PI 3.1415926
#define G 981.0
#define GAMMIN ((float)6.9)
#define GAMSTEP ((float).1)
#define GAMMAX ((float)6.9)
//#define F ((float)30)
#define BOUNCES 200
#define CUTOFF .01
#define PL .25
#define YACC .00000001
#define REST 0.0
#define YINIT ((float)1)
#define IMAX 10
#define PRINTBOUNCE 20
/* 0 printing to disk off. 1 printing on */
#define POSPRINT ((int)1)
#define TIMEPRINT ((int)1)
#define VELPRINT ((int)0)




main()
{
int i,j,k,bounce;
```

```
double e(double,double);
double yplate(double,double,double);
double vplate(double,double,double);
double aplate(double,double,double);
double yball(double,double,double);
double vball(double,double);
double sign(double);
double temp;
double sg,sl,sr;
int pflag;
int rtflag;
int aflag;
int changeflag; // wont change when =1


FILE *out_dat1;
FILE *out_dat2;
FILE *out_dat3;

double F;
double gam,w,yio,yin,y,yp,yl,ypl,yr,ypr,ap;
double vio,vin,v,vb,vp,t,tglobal;
double tl,tr,tm;
double vrel;
double rl,rr,rm;
double DT;

out_dat1=fopen("positout.dat","wb");
out_dat2=fopen("timesout.dat","wb");
out_dat3=fopen("velsout.dat","wb");

//for (F=20.0; F <= 34.0+.01 ;F+=1)
for (F=30.0;F<=30;F++)
{
fprintf(stderr,"freq=%f\n",F);
for (gam=GAMMIN;gam<=GAMMAX;gam+=GAMSTEP)
{
/* Initial conditions */
DT=1/(50*F);
yio=YINIT;
vio=0;
t=0;
```

224

```c
tglobal=0;
w=2*PI*F;
pflag=0;
rtflag=0;
aflag=0;
changeflag=1;
fprintf(stderr,"gamma=%f\n",gam);


for (bounce=0;bounce<=BOUNCES && aflag==0;bounce++)
{


/*printf("bounce=%d\n",bounce);*/
/* Calculate time to next hit */
/* Bound root*/
t=DT;
rtflag=0;
pflag=0;

/* Now we see where to see initial increment from t=0 */

for (i=0;i<IMAX && rtflag==0;i++)
{
/*
printf("tstart=%-.16f\n",t);

printf("i=%d\n",i);
*/
yl=yball(t,vio,yio);
ypl=yplate(gam,w,t+tglobal);
rl=yl-ypl;

if (rl<0.0) /* Still no bound, decrease initial step */
{
/*
printf("rl=%-.16f\n",rl);
*/
t=t/2;
}

else /* we have found a good initial step,
 break out of loop */
```

```
{
/*
printf("rl=%-.16f\n",rl);
*/
rtflag=1;
}
}


if (i==IMAX) /* Ball is stuck on plate for all
intents and purposes */
{
pflag=1;
/*
printf("Ball is resting comfortably on plate\n");
*/
/* Check to see if ball will ever leave the plate again */
if (gam<=1.0)
{
printf("Ball is stuck on plate forever at this gamma\n");
aflag=1;
}

else
{
/* Track ball on plate until it is ready to leave */
tglobal=tglobal+t;
while (aplate(gam,w,tglobal)>-G)
{
yp=yplate(gam,w,tglobal);

if ((BOUNCES-bounce)<PRINTBOUNCE && POSPRINT==1)
{
fprintf(out_dat1,"%f %f %f\n",tglobal,yp,yp);
/*printf("printing to disk\n");*/
}

tglobal=tglobal+DT/10;
}
yio=yplate(gam,w,tglobal);
vio=vplate(gam,w,tglobal);
```

```c
}
}

/* Ball isn't stuck on plate, so let's
   find the next hit position */
if (pflag==0)
{
/*
printf("Ball will undergo another collision\n");
*/

rtflag=0;
while (rtflag==0)
{
yl=yball(t,vio,yio);
ypl=yplate(gam,w,t+tglobal);
rl=yl-ypl;

yr=yball(t+DT,vio,yio);
ypr=yplate(gam,w,t+tglobal+DT);
rr=yr-ypr;

sl=sign(rl);
sr=sign(rr);
if (yl>ypl && yr<ypr) { rtflag=1;}
else
{
/*
printf("%f %f %f %f\n",yl,ypl,rl,rr);
*/

/* Can change plate accelertion suddenly here */
if (changeflag==0 && bounce>=5 && fabs(ypl)<.01)
{printf("Changed accel\n");
gam=3.3; changeflag=1;}

if ((BOUNCES-bounce)<PRINTBOUNCE && POSPRINT==1)
{
fprintf(out_dat1,"%f %f %f\n",t+tglobal,yl,ypl);
}
```

```
t=t+DT;
}
}
/*
printf("Bounded root lies between t=%f and t=%f\n",t,t+DT);
printf("With root values of %f and %f\n",rl,rr);
*/

/* Now that we have a bound, narrow it down */
/* Initialize */
tl=t;
tr=t+DT;

tm=.5*(tl+tr);
rl=yball(tl,vio,yio)-yplate(gam,w,tl+tglobal);
rr=yball(tr,vio,yio)-yplate(gam,w,tr+tglobal);
rm=yball(tm,vio,yio)-yplate(gam,w,tm+tglobal);
/* Start testing */
while (fabs(rm)>YACC)
{
if (rl*rm>0)
{
tl=tm;
}
else
{
tr=tm;
}

tm=.5*(tl+tr);
rl=yball(tl,vio,yio)-yplate(gam,w,tl+tglobal);
rr=yball(tr,vio,yio)-yplate(gam,w,tr+tglobal);
rm=yball(tm,vio,yio)-yplate(gam,w,tm+tglobal);
/*
printf("tm=%f rm=%f\n",tm,rm);
*/
}

/* Update final values */
```

```c
t=tm;
y=yball(t,vio,yio);
yp=yplate(gam,w,t+tglobal);
/*
printf("%f %f %f\n",t,y,yp);
*/


if ((BOUNCES-bounce)<PRINTBOUNCE && POSPRINT==1)
{
fprintf(out_dat1,"%f %f %f\n",t+tglobal,y,yp);
/*printf("printing to disk\n");*/
}




/* Printing for collision time */

if ((BOUNCES-bounce)<PRINTBOUNCE && TIMEPRINT==1)
{
fprintf(out_dat2,"%f %f\n",gam,t);
}




/* Found intersection time and point, or takeoff point */

/* Make a rebound */
yio=y;
vb=vball(t,vio);
ap=aplate(gam,w,t+tglobal);
/*
printf("t+tglobal=%f\n",t+tglobal);
*/
vp=vplate(gam,w,t+tglobal);
/*
printf("vb=%f vp=%f\n",vb,vp);
*/
vrel=vb-vp;
if ((BOUNCES-bounce)<PRINTBOUNCE && VELPRINT==1){
fprintf(out_dat3,"%f %f %f %f\n",gam,vb,vp,vrel);
}
```

```
vio=vp-e(vrel,REST)*vrel;

/*
printf("vrel=%f\n",vrel);
printf("New vb=%f\n",vio);
printf("takeoff y=%f\n",yio);
getchar();
*/
tglobal=tglobal+t;


}


pflag=0;
}


/* Prints final velocities */
vrel=vb-vp;
fprintf(out_dat3,"%f %f %f %f\n",gam,vb,vp,vrel);
fprintf(stderr,"%f %f %f %f\n",gam,vb,vp,vrel);



} /* End Gamma loop */



}  /* End Freq loop */
fclose(out_dat1);
fclose(out_dat2);
fclose(out_dat3);


}
/* functions*/
/* coefficient of restitution, flag=-1 for variable */
double yplate(double gam,double w,double t)
{
return ((gam*G)/(w*w)*sin(w*t));
}

double vplate(double gam,double w,double t)
{
return ((gam*G)/w*cos(w*t));
}
double aplate(double gam,double w,double t)
```

```
{
return (-gam*G*sin(w*t));
}
double yball(double t,double vi,double yi)
{
return (-.5*G*t*t+vi*t+yi);
}
double vball(double t,double vi)
{
return (-G*t+vi);
}

double e(double vrel, double corflag)
{
double er;
if (corflag==-1.0)
{
if (fabs(vrel) < CUTOFF)
{
er=1.0;
/*
printf("e=%-.16f",er);
*/
return er;
}

else
{
er=pow(CUTOFF,PL)*pow(fabs(vrel),-PL);
/*
printf("e=%-.16f\n",er);
*/
return er;
}
}
else
{
er=corflag;
/*
printf("e=%-.16f\n",er);
*/
return er;
```

```
}

}

double sign(double num)
{
if (num>=0.0){ return 1.0;}
else {return -1.0;}
}
```

Bibliography

[1] Bruce J. Ackerson, S. E. Paulin, Benjamin Johnson, William van Megan, and Sylvia Underwood. Crystallization by settling in suspensions of hard spheres. *Phys. Rev. E.*, 59:6903, 1999.

[2] Gerold Adam and Julian H. Gibbs. On the temperature dependence of cooperative relaxation properties in glass-forming liquids. *J. Chem. Phys.*, 43:139, 1965.

[3] B. J. Alder and T. E. Wainwright. Phase transition for a hard sphere system. *J. Chem. Phys.*, 27:1208, 1957.

[4] T. B. Anderson and R. Jackson. Fluid mechanical description of fluidized beds. Equations of motion. *Ind. Eng. Chem. Fundam.*, 6:527, 1967.

[5] J. P. Andrews. Theory of collisions of spheres of soft metals. *Phil. Mag.*, 9(58):593–610, 1930.

[6] C. A. Angell. Formation of glasses from liquids and biopolymers. *Science*, 267:1924, 1995.

[7] C. A. Angell, K. L. Ngai, G. B. McKenna, P. F. McMillan, and S. W. Martin. Relaxation in glassforming liquids and amorphous solids. *App. Phys. Rev.*, 88:3113, 2000.

[8] I. S. Aranson, D. Blair, W. K. Kwok, G. Karapetrov, U. Welp, G. W. Crabtree, V. M. Vinokur, and L. S. Tsimring. Controlled dynamics of interfaces in a vibrated granular layer. *Phys. Rev. Lett*, 82:731, 1999.

[9] Igor S. Aranson, Boris A. Malomed, Len M. Pismen, and Lev S. Tsimring. Crystallization kinetics and self-induced pinning in cellular patterns. *Phys. Rev. E*, 62:R5, 2000.

[10] Guy Barnocky and Robert H. Davis. Elastohydrodynamic collision and rebound of spheres: Experimental verification. *Phys. Fluids*, 31:1324, 1988.

[11] G. I. Batchelor. Sedimentation in a dilute dispersion of spheres. *J. Fluid Mech.*, 52:245, 1972.

[12] V.M. Bedanov, G.V. Gadiyak, and Yu. E. Lozovik. On a modified Lindemann-like criterion for 2D melting. *Phys. Lett. A*, 109A:289, 1985.

[13] B. Bernu and R. Mazighi. One-dimensional bounce of inelastically colliding marbles on a wall. *J. Phys. A: Math. Gen.*, 23:5745–5754, 1990.

[14] C. Bizon, M. D. Shattuck, J. B. Swift, W. D. McCormick, and H. L. Swinney. Patterns in 3-dimensional vertically oscillated granular layers: Simulation and experiment. *Phys. Rev. Lett.*, 80:57–60, 1998.

[15] C. Bizon, M. D. Shattuck, J. B. Swift, and H. L. Swinney. Transport coefficients for granular media from molecular dynamics simulations. *Phys. Rev. E*, 60:4340–4351, 1999.

[16] L. Bocquet, W. Losert, D. Schalk, T. C. Lubensky, and J. P. Gollub. Granular shear flow dynamics and forces: Experiment and continuum theory. *Phys. Rev. E*, 65:011307, 2001.

[17] Eberhard Bodenschatz, John R. de Bruyn, Guenter Ahlers, and David S. Cannell. Transitions between patterns in thermal convection. *Phys. Rev. Lett.*, 67:3078, 1991.

[18] D. Bonamy, L. Laurent, Ph. Claudin, J.-Ph. Bouchaud, and F. Daviaud. Electrical conductance of a 2D packing of metallic beads under thermal perturbation. *Europhys. Lett.*, 51:614, 2000.

[19] J. Bougie, Sung Joon Moon, J. B. Swift, and Harry L. Swinney. Shocks in vertically oscillated granular layers. *Phys. Rev. E*, 66:051301, 2002.

[20] J. F. Brady and G. Bossis. Stokesian dynamics. *Ann. Rev. Fluid Mech.*, 20:111–157, 1988.

[21] H. Brand and M. C. Cross. Phase dynamics for the wavy vortex state of the taylor instability. *Phys. Rev. A*, 27:1237, 1983.

[22] Michael P. Brenner. Screening mechanisms in sedimentation. *Phys. Fluids*, 11:754, 1999.

[23] Reha V. Cakmur, David A. Egolf, Brendan B. Plapp, and Eberhard Bodenschatz. Bistability and competition of spatiotemporal chaotic and fixed point attractors in Rayleigh-Bénard convection. *Phys. Rev. Lett.*, 79:1853, 1997.

[24] Alastair Cameron. *Basic Lubrication Theory*. Longman, 1970.

[25] N. F. Carnahan and K. E. Starling. Equation of state for nonattracting rigid spheres. *J. Chem. Phys.*, 51:635, 1969.

[26] G. F. Carnevale, Y. Pomeau, and W. R. Young. Statistics of ballistic agglomeration. *Phys. Rev. Lett.*, 64:2913, 1990.

[27] M. E. Cates, J. P. Wittmer, J.-P. Bouchaud, and P. Claudin. Jamming, force chains, and fragile matter. *Phys. Rev. Lett*, 81:1841, 1998.

[28] J. J. Christensen and A. J. Bray. Pattern dynamics of Rayleigh-Bénard convective rolls and weakly segregated diblock copolymers. *Phys. Rev. E*, 58:5364, 1998.

[29] S. Ciliberto, S. Douady, and S. Fauve. Investigating space-time chaos in faraday instability by means of the fluctuations of the driving acceleration. *Europhys. Lett.*, 15:23, 1991.

[30] E. Clément, J. Duran, and J. Rajchenbach. Experimental study of heaping in a two-dimensional "sandpile". *Phys. Rev. Lett.*, 69:1189–1192, 1992.

[31] P. Constantin, E. Grossman, and M. Mungan. Inelastic collisions of three particles on a line as a two-dimensional billiard. *Physica D*, 83:409–420, 1995.

[32] J.-P. Couderc. Incipient fluidization and particulate systems. In J. F. Davidson, R. Clift, and Harrison, editors, *Fluidization*, pages 1–44. Academic Press, second edition, 1985.

[33] P. Coullet and G. Iooss. Instabilities of one-dimensional cellular patterns. *Phys. Rev. Lett*, 64:866, 1990.

[34] M. L. Cowan, J. H. Page, and D. A. Weitz. Velocity fluctuations in fluidized suspensions probed by ultrasonic correlation spectroscopy. *Phys. Rev. Lett*, 85:453, 2000.

[35] M. C. Cross and P. C. Hohenberg. Pattern formation outside of equilibrium. *Rev. Mod. Phys.*, 65:851, 1993.

[36] M. C. Cross, D. Meiron, and Yuhai Tu. Chaotic domains: A numerical investigation. *Chaos*, 4:607, 1994.

[37] M. C. Cross and D. I. Meiron. Domain coarsening in systems far from equilibrium. *Phys. Rev. Lett.*, 75:2152, 1995.

[38] Gianfranco D'Anna and Gerard Grémaud. The jamming route to the glass state in weakly perturbed granular media. *Nature*, 413:407, 2001.

[39] Gianfranco D'Anna and Gerard Grémaud. Vogel-Fulcher-Tammann-type diffusive slowdown in weakly perturbed granular media. *Phys. Rev. Lett*, 87:254302–1, 2001.

[40] L. Daudet, V. Ego, S. Manneville, and J. Bechhoefer. Secondary instabilities of surface waves on viscous fluids in the faraday instability. *Europhys. Lett.*, 32:313, 1995.

[41] J. F. Davidson, R. Clift, and Harrison. *Fluidization.* Academic Press, second edition, 1985.

[42] J. F. Davidson and D. Harrison. *Fluidised particles.* Cambridge University Press, 1963.

[43] J. F. Davidson, D. Harrison, and J. R. F. Guedes de Carvalho. On the liquid behavior of fluidized beds. *Ann. Rev. Fluid Mech.*, 9:55, 1977.

[44] Pablo G. Debenedetti. *Metastable Liquids: concepts and principles.* Princeton University Press, 1996.

[45] Pablo G. Debenedetti and Frank H. Stillinger. Supercooled liquids and the glass transition. *Nature*, 410:259, 2001.

[46] Claudio Donati, Jack F. Douglas, Walter Kob, Steven J. Plimpton, Peter H. Poole, and Sharon C. Glotzer. Stringlike cooperative motion in a supercooled liquid. *Phys. Rev. Lett*, 80:2338, 1998.

[47] Claudio Donati, Sharon C. Glotzer, Peter H. Poole, Walter Kob, and Steven J. Plimpton. Spatial correlations of mobility and immobility in a glass-forming lennard-jones liquid. *Phys. Rev. E*, 60:3107, 1999.

[48] S. Douady, S. Fauve, and O. Thual. Phase diffusion in the vicinity of an oscillatory secondary bifurcation. *Europhys. Lett*, 10:309, 1989.

[49] Yunson Du, Hao Li, and Leo P. Kadanoff. Breakdown of hydrodynamics in a one-dimensional system of inelastic particles. *Phys. Rev. Lett.*, 74(8):1268–1271, 1995.

[50] M. Dubois, R. Da Silva, F. Daviaud, P. Berge, and A. Petrov. Collective oscillating mode in a one-dimensional chain of convective rolls. *Europhys. Lett.*, 8:135, 1989.

[51] James W. Dufty. Kinetic theory and hydrodynamics for rapid granular flow - a perspective. *cond-mat/0108444*, 2001.

[52] D. J. Durian. Influence of boundary reflection and refraction on diffusive photon transport. *Phys. Rev. E*, 50:857–866, 1994.

[53] Paul Duru, Maxime Nicolas, John Hinch, and Elisabeth Guazzelli. Constitutive laws in liquid fluidized beds. *J. Fluid Mech.*, 452:371, 2002.

[54] M. D. Ediger. Spatially heterogeneous dynamics in supercooled liquids. *Annu. Rev. Phys. Chem.*, 51:99, 2000.

[55] M. D. Ediger, C. A. Angell, and Sidney R. Nagel. Supercooled liquids and glasses. *J. Phys. Chem.*, 100:13200, 1996.

[56] S. F. Edwards and D. V. Grinev. Statistical phyisics of the jamming transition: The search for simple models. *cond-mat/9905114*, 1999.

[57] M. M. El-Kaissy and G. M. Homsy. Instability waves and the origin of bubble in fluidized beds, part 1: Experiments. *Int. J. Multiphase Flow*, 2:379, 1976.

[58] K. R. Elder, J. Vinals, and M. Grant. Dynamic scaling and quasiordered states in the two-dimensional Swift-Hohenberg equation. *Phys. Rev. A*, 46:7618, 1992.

[59] A. B. Ezerskii, M. I. Rabinovich, V. P. Reutov, and I. M. Starobinets. Spatiotemporal chaos in the parametric excitation of a capillary ripple. *Sov. Phys. JETP*, 91:2070, 1986.

[60] A. F. Fortes, D. D. Joseph, and T. S. Lundgren. Nonlinear mechanics of fluidization of beds of spherical particles. *J. Fluid Mech.*, 177:467, 1987.

[61] David R. Foss and John R. Brady. Brownian dynamics simulation of hard-sphere colloidal dispersions. *J. Rheol*, 44:629, 2000.

[62] U. Gasser, Eric R. Weeks, Andrew Schofield, P. N. Pusey, and D. A. Weitz. Real-space imaging of nucleation and growth in colloidal crystallization. *Science*, 292:258, 2001.

[63] D. Geldart. Types of gas fluidization. *Powder Technology*, 9:285–292, 1973.

[64] F. Giorgiutti, A. Bleton, L. Limat, and J. E. Wesfreid. Dynamics of a one-dimensional array of liquid columns. *Phys. Rev. Lett*, 74:538, 1995.

[65] F. Giorgiutti and L. Limat. Solitary dilation waves in a circular array of liquid columns. *Physica D*, 103:590, 1997.

[66] F. Giorgiutti, L. Limat, and J. E. Wesfreid. Phase diffusion in the vicinity of an oscillatory secondary bifurcation. *Phys. Rev. E.*, 57:2843, 1998.

[67] R. Glowinski, T.-W. Pan, T. I. Hesla, and D.D. Joseph. A distributed lagrange multiplier/fictitious domain method for particulate flows. *Int. J. Multiphase Flow*, 25:755, 1999.

[68] J. D. Goddard and A. K. Didwania. Computations of dilatancy and yield surfaces for assemblies of rigid frictional spheres. *Q. J. Mech. Appl. Math*, 51:15, 1998.

[69] I. Goldhirsch. Scales and kinetics of granular flows. *Chaos*, 9:659, 1999.

[70] I. Goldhirsch and G. Zanetti. Clustering instability in dissipative gases. *Phys. Rev. Lett.*, 70:1619, 1993.

[71] D. Goldman, M. D. Shattuck, C. Bizon, W. D. McCormick, J. B. Swift, and Harry L. Swinney. Absence of inelastic collapse in a realistic three ball model. *Phys. Rev. E*, 57:4831, 1998.

[72] Daniel I. Goldman, M. D. Shattuck, Sung Joon Moon, J. B. Swift, and Harry L. Swinney. Resonantly excited normal modes and shear melting of a nonequilibrium pattern. *To be submitted to PRL*, 2002.

[73] Daniel I. Goldman, M. D. Shattuck, Harry L. Swinney, and Gemunu H. Gunaratne. Emergence of order in an oscillated granular layer. *Physica A*, 306:180, 2002.

[74] A. Goldshtein, M. Shapiro, and C. Gutfinger. Mechanics of collisional motion of granular materials: 3. self-similar shock wave propagation. *J. Fluid Mech.*, 316:29, 1996.

[75] W. Goldsmith. *Impact*. Edward Arnold Ltd., London, 1960.

[76] P. Gondret, E. Hallouin, M. Lance, and L. Petit. Experiments on the motion of a solid sphere toward a wall: From viscous dissipation to elastohydrodynamic bouncing. *Phys. Fluids*, 11:2803, 1999.

[77] E. Grossman and M. Mungan. Motion of three inelastic particles on a ring. *Phys. Rev. E*, 53(6):6435–6449, 1996.

[78] E. L. Grossman and B. Roman. Density variations in a one-dimensional granular system. *Phys. Fluids*, 8(12):3218–3228, 1996.

[79] E. L. Grossman, Tong Zhou, and E. Ben-Naim. Toward granular hydrodynamics in two dimensions. *Phys. Rev. E*, 55(4):4200–4206, 1997.

[80] G. H. Gunaratne, D. K. Hoffman, and D. J. Kouri. Characterizations of natural patterns. *Phys. Rev. E*, 57:5146, 1998.

[81] G. H. Gunaratne, R. E. Jones, Q. Ouyang, and H. L. Swinney. An invariant measure of disorder in patterns. *Phys. Rev. Lett.*, 75:3281, 1995.

[82] G. H. Gunaratne, A. Ratnaweera, and K. Tennekone. Emergence of order in textured patterns. *Phys. Rev. E*, 59:5058, 1999.

[83] S. J. Haam and R. S. Brodkey. Motions of dispersed beads obtained by particle tracking velocimetry measurements, part II. *International Journal of Multiphase Flow*, 26, 2000.

[84] T. C. Hales. Sphere packings. I. *Discrete and Computational Geometry*, 17:1, 1997.

[85] B. I. Halperin and David R. Nelson. Theory of two-dimensional melting. *Phys. Rev. Lett.*, 41:121, 1978.

[86] John Happel and Howard Brenner. *Low Reynolds number hydrodynamics, with special applications to particulate media*. Prentice-Hall, 1965.

[87] H. G. E. Hentschel and I. Procaccia. The infinite number of generalized dimensions of fractals and strange attractors. *Physica D*, 8:835, 1983.

[88] K. M. Hill and J. Kakalios. Reversible axial segregation of rotating granular media. *Phys. Rev. E*, 52:4393, 1995.

[89] Scott A. Hill and Gene F. Mazenko. Nonlinear hydrodynamical approach to granular materials. *Phys. Rev. E*, 63:031303, 2001.

[90] D. K. Hoffman, G. H. Gunaratne, D. S. Zhang, and D. J. Kouri. A method to Fourier filter textured images. *Chaos*, 10:240, 2000.

[91] D. K. Hoffman and D. J. Kouri. Distributed approximating functionals: A new approach to approximating functions and their derivatives. In G. Cohen, editor, *Proc. Third Int. Conf. on Math. and Num. Aspects of Wave Propagation (SIAM)*, page 56, 1995.

[92] G. M. Homsy. Nonlinear waves and the origin of bubbles in fluidized beds. *Applied Scientific Research*, 58:251, 1997.

[93] G. M. Homsy, M. M. El-Kaissy, and A. Didwania. Instability waves and the origin of bubble in fluidized beds, part 2: Comparison with theory. *Int. J. Multiphase Flow*, 6:305, 1980.

[94] Q. Hou, S. Sasa, and N. Goldenfeld. Dynamical scaling behavior of the Swift-Hohenberg equation following a quench to the modulated state. *Physica A*, 239:219, 1997.

[95] Daniel Howell, R. P. Behringer, and Christian Veje. Stress fluctuations in a 2D granular couette experiment: A continuous transition. *Phys. Rev. Lett*, 82:5241, 1999.

[96] R. B. Hoyle. Phase instabilities of oscillatory standing squares and alternating rolls. *Phys. Rev. E.*, 49:2875, 1994.

[97] R. Jackson. *The Dynamics of Fluidized Particles*. Cambridge University Press, 2000.

[98] James T. Jenkins and Chao Zhang. Kinetic theory for identical, frictional, nearly elastic spheres. *Phys. Fluids*, 14:1228, 2002.

[99] G. G. Joseph, R. Zenit, M. L. Hunt, and A. M. Rosenwinkel. Particle-wall collisions in a viscous fluid. *J. Fluid Mech.*, 433:329, 2001.

[100] L. P. Kadanoff. Built upon sand: Theoretical ideas inspired by granular flows. *Rev. Mod. Phys*, 71:435, 1999.

[101] S. Kirsch, V. Frenz, W. Schärtl, E. Bartsch, and H. Sillescu. Multispeckle autocorrelation spectroscopy and its application to the investigation of ultraslow dynamical processes. *J. Chem. Phys.*, 104:1758, 1996.

[102] Charles Kittel. *Introduction to Solid State Physics*, page 82. Freeman, 6 edition, 1986.

[103] James B. Knight, E. E. Ehrichs, Vadim Yu. Kuperman, Janna K. Flint, Heinrich M. Jaeger, and Sidney R. Nagel. An experimental study of granular convection. *Phys. Rev. E.*, 54:5726, 1996.

[104] James B. Knight, Christopher G. Fandrich, Chun N. Lau, Heinrich M. Jaeger, and Sidney R. Nagel. Density relaxation in a vibrated granular material. *Phys. Rev. E*, 51:3957, 1995.

[105] James B. Knight, H. M. Jaeger, and Sidney R. Nagel. Vibration-induced size separation in granular media: The convection connection. *Phys. Rev. Lett.*, 70(24):3728–3731, 1993.

[106] J. P. Koeppe, M. Enz, and J. Kakalios. Phase diagram for avalanche stratification of granular media. *Phys. Rev. E*, 58:R4104, 1998.

[107] A. Kudrolli, M. Wolpert, and J. P. Gollub. Cluster formation due to collisions in granular material. *Phys. Rev. Lett.*, 78(7):1383–1386, 1997.

[108] G. Kuwabara and K. Kono. Restitution coefficient in a collision between two spheres. *Jap. Jour. App. Phys.*, 26(8):1230–1233, 1987.

[109] Mooson Kwauk. *Fluidization: idealized and bubbleless, with applications.* Ellis Horwood, 1992.

[110] L.D. Landau and E.M. Lifshitz. *Fluid Mechanics.* Pergamon Press, Oxford, England, 1959.

[111] X. Lei, B. J. Ackerson, and P. Tong. Settling statistics of hard sphere particles. *Phys. Rev. Lett*, 86:3300, 2001.

[112] Andrea J. Liu and Sidney R. Nagel. Jamming is not just cool anymore. *Nature*, 396:21, 1998.

[113] C. H. Liu. Spatial patterns of sound propagation in sand. *Phys. Rev. B*, 50:782, 1994.

[114] C. H. Liu, S. R. Nagel, D. A. Schecter, S. N. Coppersmith, S. Majumdar, O. Narayan, and T. A. Witten. Force fluctuations in bead packs. *Science*, 269:513, 1996.

[115] C. H. Liu and Sidney R. Nagel. Sound in sand. *Phys. Rev. Lett.*, 68:2301, 1992.

[116] C. H. Liu and Sidney R. Nagel. Sound in a granular material: Disorder and nonlinearity. *Phys. Rev. B*, 48:15646, 1993.

[117] W. Losert, L. Bocquet, T. C. Lubensky, and J. P. Gollub. Particle dynamics in sheared granular matter. *Phys. Rev. Lett*, 85:1428, 2000.

[118] W. Losert, J.-C. Géminard, S. Nasuno, and J. P. Gollub. Mechanisms for slow strengthening in granular materials. *Phys. Rev. E.*, 61:4060, 2000.

[119] Rodney Loudon. *The Quantum Theory of Light.* Oxford University Press, second edition, 1992.

[120] S. Luding, E. Clément, A. Blumen, J. Rajchenbach, and J. Duran. Anomalous energy dissipation in molecular-dynamics simulations of grains: The "detachment effect". *Phys. Rev. E*, 50(5):4113–4120, 1994.

[121] S. Luding, E. Clément, A. Blumen, J. Rajchenbach, and J. Duran. Studies of columns of beads under external vibrations. *Phys. Rev. E*, 49(2):1634–1646, 1994.

[122] S. Luding and H. J. Herrmann. Cluster-growth in freely cooling granular media. *Chaos*, 9:673, 1999.

[123] S. Luding, H. J. Herrmann, and A. Blumen. Simulations of two-dimensional arrays of beads under external vibrations: Scaling behavior. *Phys. Rev. E*, 50(4):3100–3108, 1994.

[124] L. Massimilla, G. Donsi, and C. Zucchini. The structure of bubble-free gas fluidized beds of fine fluid cracking catalyst particles. *Chem. Eng. Sci.*, 27:2005, 1972.

[125] Gregory McMillan. *Tuning and Control Loop Performance.* Instrument Society of America, Research Triangle Park, third edition, 1994.

[126] Sean McNamara and W. R. Young. Inelastic collapse and clumping in a one-dimensional granular medium. *Phys. Fluids A*, 4:496–504, 1992.

[127] Sean McNamara and W. R. Young. Inelastic collapse in two dimensions. *Phys. Rev. E*, 50(1):R28–R31, 1994.

[128] Sean McNamara and W. R. Young. Dynamics of a freely evolving, two-dimensional granular medium. *Phys. Rev. E*, 53:5089, 1996.

[129] F. Melo, P. B. Umbanhowar, and H. L. Swinney. Hexagons, kinks, and disorder in oscillated granular layers. *Phys. Rev. Lett.*, 75:3838, 1995.

[130] N. Menon and J.D. Durian. Particle motions in a gas-fluidized bed of sand. *Phys. Rev. Lett.*, 79:3407, 1997.

[131] S. Michalland and M. Rabaud. Localized phenomena during spatio-temporal intermittency in directional viscous fingering. *Physica D.*, 61:197, 1992.

[132] Brian Miller, Corey O'Hern, and R. P. Behringer. Stress fluctuations for continuously sheared granular materials. *Phys. Rev. Lett*, 77:3110, 1996.

[133] S. J. Moon, M. D. Shattuck, and J. B. Swift. Velocity distributions and correlations in homogeneously heated granular media. *Phys. Rev. E*, 64:031303–1 to 031303–10, 2001.

[134] Sung Joon Moon, Daniel I. Goldman, J. B. Swift, and Harry L. Swinney. Avalanche and shear driven convection and transport in oscillated granular layers. *To be submitted to Phys. Rev. Lett*, 2002.

[135] Sung Joon Moon, M. D. Shattuck, C. Bizon, Daniel I. Goldman, J. B. Swift, and Harry L. Swinney. Phase bubbles and spatiotemporal chaos in granular patterns. *Phys. Rev. E*, 65:011301, 2002.

[136] Daniel M. Mueth, Heinrich M. Jaeger, and Sidney R. Nagel. Force distribution in a granular medium. *Phys. Rev. E.*, 57:3164, 1998.

[137] Nicolas Mujica and Francisco Melo. Solid-liquid transition and hydrodynamic surface waves in vibrated granular layers. *Phys. Rev. Lett*, 80:5121, 1998.

[138] Corey S. O'Hern, Stephen A. Langer, Andrea J. Liu, and Sidney R. Nagel. Force distributions near jamming and glass transitions. *Phys. Rev. Lett*, 86:111, 2001.

[139] George Y. Onoda and Eric G. Liniger. Random loose packings of uniform spheres and the dilatancy onset. *Phys. Rev. Lett*, 64:2727, 1990.

[140] J. H. Page, M. L. Cowan, P. Sheng, and D. A. Weitz. Diffusing acoustic wave transport and spectroscopy. In R. C. McPhedran, L. C. Botten, and N. A. Nicorovici, editors, *IUTAM Symposium 99/4: Mechanical and Electromagnetic Waves in Structured Media*, page 121. Kluwer Academic, 2001.

[141] J. H. Page, M. L. Cowan, and D. A. Weitz. Diffusing acoustic wave spectroscopy of fluidized suspensions. *Physica B*, 279:130, 2000.

[142] H. K. Pak, E. Van Doorn, and R. P. Behringer. Effects of ambient gases on granular materials under vertical vibration. *Phys. Rev. Lett.*, 74:4643–4646, 1995.

[143] T.-W. Pan, D.D. Joseph, R. Bai, R. Glowinski, and V. Sarin. Fluidization of 1204 spheres: simulation and experiments. *J. Fluid Mech.*, 451:169, 2002.

[144] D. J. Pine, D. A. Weitz, P. M. Chaikin, and E. Herbolzheimer. Diffusing-wave spectroscopy. *Phys. Rev. Lett*, 60:1134–1137, 1988.

[145] P. N. Pusey and W. Van Megan. Phase behavior of concentrated suspensions of nearly hard colloidal spheres. *Nature*, 320:340, 1986.

[146] P. N. Pusey and W. Van Megan. Observation of a glass transition in suspensions of spherical colloidal particles. *Phys. Rev. Lett.*, 59:2083, 1987.

[147] C. V. Raman. The photographic study of impact at minimal velocities. *Phys. Rev.*, 12(6):442–447, 1918.

[148] Sriram Ramaswamy. Issues in the statistical mechanics of steady sedimentation. *Adv. Phys.*, 50:297, 2001.

[149] Richard H. Rand. Dynamics of a nonlinear parametrically-excited PDE: 2-term truncation. *Mech. Res. Comm.*, 23:283, 1996.

[150] E. C. Rericha, C. Bizon, M. D. Shattuck, and H. L. Swinney. Shocks in supersonic sand. *Phys. Rev. Lett.*, 88:014302, 2001.

[151] O. Reynolds. On the dilatency of media composed of rigid particles in contact. *Phil. Mag.*, 20:469–481, December 1885.

[152] J. F. Richardson and W. N. Zaki. Sedimentation and fluidization, part I. *Trans. Inst. Chem. Eng.*, 32:35, 1954.

[153] M. D. Rintoul and S. Torquato. Metastability and crystallization in hard-sphere systems. *Phys. Rev. Lett*, 77:4198, 1996.

[154] F. Rouyer, D. Lhuillier, J. Martin, and D. Salin. Structure, density, and velocity fluctuations in quasi-two-dimensional non-Brownian suspensions of spheres. *Phys. Rev. Lett*, 83:1058, 1999.

[155] F. Rouyer, J. Martin, and D. Salin. Non-Gaussian dynamics in quasi-2D noncolloidal suspensions. *Phys. Rev. Lett*, 83:1058, 1999.

[156] P. N. Rowe. The delayed bubbling of fluidised beds of fine particles. *Chemical Engineering Science*, 24:415, 1969.

[157] Srikanth Sastry, Pablo G. Debenedetti, and Frank H. Stillinger. Statistical geometry of particle packings. II. "weak spots" in liquids. *Phys. Rev. E*, 56:5533, 1997.

[158] Srikanth Sastry, Pablo G. Debenedetti, and Frank H. Stillinger. Signatures of distinct dynamical regimes in the energy landscape of a glass-forming liquid. *Nature*, 393:554, 1998.

[159] Klaus Schätzel. Single photon correlation techniques. In Wyn Brown, editor, *Dynamic Light Scattering: The method and some applications*, page 76. Clarendon Press, 1993.

[160] Adrian E. Scheidegger. *The Physics of Flow Through Porous Media*. The Macmillan Company, 1957.

[161] H. R. Schober, E. Allroth, K. Schroeder, and H. Müller-Krumbhaar. Dynamics of periodic pattern formation. *Phys. Rev. A*, 33:567, 1986.

[162] Thomas Schwager and Thorsten Pöschel. Coefficient of normal restitution of viscous particles and cooling rate of granular gases. *Phys. Rev. E*, 57:650, 1998.

[163] P. N. Segré, E. Herbolzheimer, and P. M. Chaikin. Long-range correlations in sedimentation. *Phys. Rev. Lett*, 79:2574, 1997.

[164] P. N. Segré, F. Liu, P. Umbanhowar, and D. A. Weitz. An effective gravitational temperature for sedimentation. *Nature*, 409:594, 2001.

[165] N. Sela and I. Goldhirsch. Hydrodynamics of a one-dimensional granular medium. *Phys. Fluids*, 7(3):507–525, 1995.

[166] W. Shockley, J. H. Hollomon, R. Maurer, and F. Seitz, editors. *Imperfections in nearly perfect crystals*. John Wiley, 1959.

[167] Jeffrey R. Smart and David T. Leighton. Measurement of the hydrodynamic surface roughness of noncolloidal spheres. *Phys. Fluids A*, 1:52, 1989.

[168] M. Smoluchowski. On the practical applicability of Stokes' law. *M. Proc. 5th Int. Congr. Math*, 2:192, 1912.

[169] F. Spahn, U. Schwarz, and J. Kurths. Clustering of granular assemblies with temperature dependent restitution under keplerian differential rotation. *Phys. Rev. Lett.*, 78(8):1596–1599, 1997.

[170] Robin J. Speedy. On the reproducibility of glasses. *J. Chem. Phys.*, 100:6684, 1994.

[171] Frank H. Stillinger. A topographic view of supercooled liquids and glass formation. *Science*, 267:1935, 1995.

[172] Katherine Strandburg. Two-dimensional melting. *Rev. Mod. Phys.*, 60:161, 1988.

[173] J. Swift and P. C. Hohenberg. Hydrodynamic fluctuations at the convective instability. *Phys. Rev. A*, 15:319, 1977.

[174] M. H. Jensen T. C. Halsey, L. P. Kadanoff, I. Procaccia, and B. I. Shraiman. Fractal measures and their singularities: The characterization of strange sets. *Phys. Rev. A*, 33:1141, 1986.

[175] M-L. Tan and I. Goldhirsch. Rapid granular flows as mesoscopic systems. *Phys. Rev. Lett*, 81:3022, 1998.

[176] P. Tong and J. Ackerson. Analogies between colloidal sedimentation and turbulent convection at high prandtl number. *Phys. Rev. E*, 58:R6931, 1998.

[177] S. C. Tsinontides and R. Jackson. The mechanics of gas fluidized beds with an interval of stable fluidization. *J. Fluid Mech.*, 255:237, 1993.

[178] N. B. Tufillaro, R. Ramshankar, and J. P. Gollub. Order-disorder transition in capillary ripples. *Phys. Rev. Lett.*, 62:422, 1989.

[179] P. B. Umbanhowar, F. Melo, and H. L. Swinney. Localized excitations in a vertically vibrated granular layer. *Nature*, 382:793, 1996.

[180] P. B. Umbanhowar, F. Melo, and H. L. Swinney. Periodic, aperiodic, and transient patterns in vibrated granular layers. *Physica A*, 249:1–9, 1998.

[181] P. B. Umbanhowar and Harry L. Swinney. Wavelength scaling and square-stripe and grain mobility transitions in vertically oscillated granular layers. *Physica A*, 288:344, 2000.

[182] Paul Umbanhowar. *Wave Patterns in Vibrated Granular Layers.* PhD thesis, University of Texas at Austin, 1996.

[183] Meint P. van Albada, Bart A. van Tiggelen, Ad Lagendijk, and Adriaan Tip. Speed of propagation of classical waves in strongly scattering media. *Phys. Rev. Lett*, 66:3132, 1991.

[184] W. van Megan and S. M. Underwood. Dynamic-light scattering study of glasses of hard colloidal spheres. *Phys. Rev. E*, 47:248, 1993.

[185] W. van Megan and S. M. Underwood. Glass transition in colloidal hard spheres: Measurement and mode-coupling theory analysis of the coherent intermediate scattering function. *Phys. Rev. E*, 49:4206, 1994.

[186] W. van Megan, S. M. Underwood, and P. N. Pusey. Nonergodicity parameters of colloidal glasses. *Phys. Rev. Lett*, 67:1586, 1991.

[187] T. P. C. van Noije, M. H. Ernst, R. Brito, and J. A. G. Orza. Mesoscopic theory of granular fluids. *Phys. Rev. Lett.*, 79(3):411–414, 1997.

[188] L. Vanel, Ph. Claudin, J.-Ph. Bouchaud, M. E. Cates, E. Clément, and J. P. Wittmer. Stresses in silos: Comparison between theoretical models and new experiments. *Phys. Rev. Lett*, 84:1439, 2000.

[189] S. C. Venkataramani and E. Ott. Spatiotemporal bifurcation phenomena with temporal period doubling: Patterns in vibrated sand. *Phys. Rev. Lett.*, 80:3495, 1998.

[190] Virgile Viasnoff, Francois Lequeux, and D. J. Pine. Multispeckle diffusing-wave spectroscopy: a tool to study slow relaxation and time-dependent dynamics. *arXiv:cond-mat/0203396*, 2002.

[191] Eric R. Weeks, J. C. Crocker, Andrew C. Levitt, Andrew Schofield, and D. A. Weitz. Three-dimensional direct imaging of structural relaxation near the colloidal glass transition. *Science*, 287:627, 2000.

[192] David A. Weitz and David J. Pine. Diffusing-wave spectroscopy. In Wyn Brown, editor, *Dynamic Light Scattering: The method and some applications*, pages 653–720. Clarendon Press, 1993.

[193] R. H. Wilhelm and M. Kwauk. Fluidization of solid particles. *Chem. Engng. Prog.*, 44:201, 1948.

[194] D. R. M. Williams and F. C. MacKintosh. Driven granular media in one dimension: Correlations and equations of state. *Phys. Rev. E*, 54(1):R9–R12, 1996.

[195] Apollo P. Y. Wong and P. Wiltzius. Dynamic light scattering with a ccd camera. *Rev. Sci. Instrum.*, 64:2547, 1993.

[196] Mingming Wu, Guenter Ahlers, and David S. Cannell. Thermally induced fluctuations below the onset of Rayleigh-Bénard convection. *Phys. Rev. Lett*, 75:1743, 1995.

[197] Mingming Wu and David Andereck. Phase dynamics in the taylor-couette system. *Phys. Fluids A.*, 4:2432, 1992.

[198] Richard Zallen. *The physics of amorphous solids*. Wiley, 1983.

[199] Wenbin Zhang and Jorge Vi nals. Secondary instabilities and spatiotemporal chaos in parametric surface waves. *Phys. Rev. Lett.*, 74:690, 1995.

[200] T. Zhou and L. P. Kadanoff. Inelastic collapse of three particles. *Phys. Rev. E*, 54(1):623–628, 1996.

[201] J. Zhu, M. Li, W. Meyer, R. H. Ottewill, STS-73 Space Shuttle Crew, W. V. Russel, and P. M. Chaikin. Crystallization of hard sphere colloids in μ-gravity. *Nature*, 387:883, 1997.

Vita

Daniel Ivan Goldman was born on January 24, 1972 in Richmond, VA to Stanley A. Goldman and Frances T. Goldman. In September 1990 he moved to Boston, MA to attend the Massachusetts Institute of Technology where he received an S.B. in physics in 1994. In September 1994 he moved to Austin, TX and enrolled in graduate school in physics. In December 1994, he withdrew and tried to establish himself in the pressure washer industry. However, the early morning life of breakfast tacos and motor oil was not always so pleasant, and he soon decided that physics was his true calling. He re-enrolled in graduate school in physics in September 1995 and joined the Center for Nonlinear Dynamics in June 1996.

Permanent address: 4505 Duval St. 172
Austin, Texas 78751

This dissertation was typeset with LaTeX† by the author.

---

†LaTeX is a document preparation system developed by Leslie Lamport as a special version of Donald Knuth's TeX Program.